UNIVERSITY OF SOUTHAMPTON

FACULTY OF NATURAL AND ENVIRONMENTAL SCIENCES

SCHOOL OF CHEMISTRY

High Throughput Optimisation of Functional Nanomaterials and Composite Structures for Resistive Switching Memory

By

Mabkhoot Abdullah Alsaiari

A thesis submitted in partial fulfilment

of the requirements for the degree of

Doctor of Philosophy

April 2018

UNIVERSITY OF SOUTHAMPTON

ABSTRACT

FACULTY OF NATURAL AND ENVIRONMENTAL SCIENCES

SCHOOL OF CHEMISTRY

Doctor of Philosophy

High Throughput Optimisation of Functional Nanomaterials and Composite Structures for Resistive Switching Memory

By Mabkhoot Abdullah Alsaiari

The Semiconductor industry is investigating high speed, low power consumption, high-density memory devices that can retain their information without power supply. Resistive Random Access Memory (ReRAM) is one of the most attractive candidates as an alternative to conventional flash memory devices due to of its simple metal-insulator-metal (MIM) structures. A compositional gradient of thin film materials produced by the simultaneous combination of elements provides a powerful tool for the combinatorial synthesis of materials. It was applied here to control the composition, structure and morphology of materials in composite devices of ReRAM. This allows the systematic high throughput screening of the intrinsic properties of the materials, as well as the high throughput optimisations of composite thin films that mimic memory device structures. Therefore, the focus of this project is to develop a novel capacitor for ReRAM application. We present here details of the preparation technique and the screening methodologies of this approach by applying the synthesis to various phases of titania, for which there is an extensive literature, as a prelude to the screening of more complex systems. Inert Pt electrodes and active Cu electrodes were deposited on TiO_2 as top electrodes using different mask sizes (50 micron and 250 micron). The bottom electrode is Si/ SiO_2/ TiO_2/ Pt (SSTOP) was constant throughout this project. TiO_2 was prepared using evaporative physical vapour deposition (PVD) with a variation of thickness between 10 nm and 300 nm on SSTOP. The synthetic conditions were chosen to produce TiO_2 oxygen stoichiometric and sub-stoichiometric amorphous, anatase and rutile materials. The oxides have been fully characterised by X-Ray Diffraction (XRD), X-ray Photo electron Spectroscopy (XPS), Raman Spectroscopy, Four Point Probe (4pp) and Atomic Force Microscopy (AFM). The electrical screening was carried out on capacitor-like structures produced using 250 micron diameter top electrodes deposited using a 14 x 14 array contact mask. Current-Voltage (I-V) measurements were conducted employing a variety of current compliances (IC). The typical I-V switching of the unipolar mode (both state in one polarity) was achieved on all titania phases, whereas the bipolar mode (each state in different polarity) was achieved only on the amorphous phase. The resistance differences between High Resistance State (HRS) and Low Resistance State (LRS) were clearly identified in each system. It was observed that for all the devices investigated, a lower forming field was required on the thicker layer of the active switching layers. Devices with copper electrodes, and composite devices with sub-stoichiometric titania adjacent to the stoichiometric titania could be formed at lower voltages and electric fields. The results obtained here confirm the feasibility of the high-throughput approach to optimise functional nanomaterials and composite device structures for resistive switching memory application.

Table of Contents

Declaration of Authorship

I, Mabkhoot Abdullah Alsaiari, declare that this thesis and the work presented in it are my own and has been generated by me as the result of my own original research.

High Throughput Optimisation of Functional Nanomaterials and Composite Structures for Resistive Switching Memory

I confirm that:

1. This work was done wholly or mainly while in candidature for a research degree at this University;
2. Where any part of this thesis has previously been submitted for a degree or any other qualification at this University or any other institution, this has been clearly stated;
3. Where I have consulted the published work of others, this is always clearly attributed;
4. Where I have quoted from the work of others, the source is always given. With the exception of such quotations, this thesis is entirely my own work;
5. I have acknowledged all main sources of help;
6. Where the thesis is based on work done by myself jointly with others, I have made clear exactly what was done by others and what I have contributed myself;
7. None of this work has been published before submission.

Signed: .....

Date: .....

Acknowledgements

الحمد لله رب العالمين

First, all praises due to God, the Most High, for His continuous blessings, mercies and sustenance.

I would like to express my sincere gratitude to my supervisor Prof. Brian Hayden for his gaudiness and supervision of this project. My sincere thanks and appreciation to him for his patience and humbleness during the time of this project. Without the constant encouragement and support in various ways, this project would not have been possible. I consider myself privileged to work with such outstanding and highly motivated professor who combines the knowledge of academia and industry.

I would like to also to than my second supervisor Prof. Philip Bartlett for his valuable suggestion and feedback.

Special thanks to former and present member of ACMF, my friends: Dr Jin Yao for his amiableness and willingness to help when I face problems (even at 11:40 pm). I really appreciate his help in Raman Spectroscopy. I'm thankful to Dr John for proofreading my thesis and also his critical discussion, Abdulrahman Alharbi for sharing the ups and downs moments, Dr. Jaffar for assisting me when I first arrived in my PhD, Dr Sandy who introduced me to the PVD system and helping me in the synthesis of the first system, and Carmen for her assistant of our need in the lab. Thank you all for the fruitful discussions during my stay at ACMF.

I should also thank ilika staff in the laboratory for their help and comments namely: Dr Sam, Dr Miklos, Dr Steve, Dr, Owain, Dr Rob and Dr Louise.

I would like also to thank the Mechanical Workshop member: Alan and Rob for keeping our work going smoothly by supplying repairs when things did not go well. I would like to thank Neil Sessions who introduced me to the clean room and trained me on the equipment. I also thank Dr Mark light for his help in XRD.

I am Pleased to thank Najran University for funding this project. I would like also, to thank the ministry of higher education of Saudi Arabia and the Saudi Culture Bureau in London for their support.

I'm very thankful to all the members of the Saudi Student Club in Southampton, particularly those we worked together during our turn:, Abdullaziz Abahussain, Abdullaziz Almohana, Dr Faisal Almalki, Fahad Algamdi, Mohammed Alomair and Khaled Alrzooqe. I truly appreciate my friends, who made my life at Southampton wonderful and memorable: Dr Khaled Alfahad, Dr Khaled Alothman, Dr Bader Alshammri, Ibrahim Almansor, Dr Abdulelah Alwabel, Dr Musaab Alnaim, Dr Fahad Almoqhim, Dr Abdullah Aljohani.

I'm entire grateful to my beloved parents and I hereby to express my apologies for being away from them for a few years, special thanks to my mum Fitnah Alkorbi for her prayer and Duaa. Thanks to all my brother and sisters for their love and motivation. Last, but not least, I hereby express my deep sense of gratitude and appreciation to my wife (Milhah), my son (Ziyad) and my daughter (Wateen) for their understating, patience and endless love through my studies.

I would like to thank my brother in law Mubarak and my sister Dr Riadhah for being with us and made our life in UK more pleasant.

Dedication

This work is dedicated to my brother Dr Saleh Alsaiari: words cannot express my deepest gratitude, love and indebtedness.

Abbreviations and Definitions

Abbreviations	Definition
A	Current
ACMF	Advanced Composite Materials Facility
AFM	Atomic Force Microscopy
ALD	Atomic Layer Deposition
C-AFM	Conductive Atomic Force Microscopy
CBRAM	Conductive Bridge Random Access Memory
CCD	Charge-coupled Device
CMOS	Complementary Metal Oxide Semiconductor
CVD	Chemical Vapour Deposition
DC	Direct Current
DRAM	Dynamic Random Access Memory
DUT	Device Under Test
EDS	Energy Dispersive X-ray Spectroscopy
E_f	Fermi Energy Level
E_g	Energy Gap
E-gun	Electron Beam Source
FeRAM	Ferroelectric Random Access Memory
FG	Floating Gate
FS	Forming Step
GCA	Growth Chamber A
GST	GeSbTe (Germanium-Antimony-Tellurium)
HRS	High Resistance State
HT-PVD	High-Throughput Physical Vapour Deposition
IC	Current Compliance

IoT	Internet of Things
IRS	Initial Resistance State
K_b	Boltzmann Constant
K-cell	Knudsen Cells
LRS	Low Resistance State
MBE	Molecule Beam Epitaxy
MEMS	Micro-electro Mechanical Systems
MIM	Metal Insulator Metal
Memristor	short form of memory resistor
MRAM	Magnetic Random Access Memory
NERSC	National Energy Research Scientific Computing Centre
NVM	Non-volatile Material
PCRAM	Phase Change Random Access Memory
PLD	Pulsed Laser Deposition
PMC	Programmable Metallisation Cell
PVD	Physical Vapour Deposition
QCM	Quartz Crystal Microbalance
R	Resistance
RAM	Random Access Memory
ReRAM	Resistive Random Access Memory
rf	Radio Frequency
ROM	Read Only Memory
RS	Resistive Switching
RT	Room Temperature
RTA	Rapid Thermal Annealing
sccm	Standard Cubic Centimetres Per Minute

SEM	Scanning Electron Microscopy
SMU	Source/Monitor Unit
SRAM	Static Random Access Memory
SSTOP	Substrate ($Si/SiO_2/TiO_2$/ Pt)
TEM	Transmission Electron Microscopy
t	Time
TiO_2	Titanium Dioxide
TMO	Transition Metal Oxide
UHV	Ultra-High Vacuum
V	Voltage
XPS	X-ray Photo Electron Spectroscopy
XRD	X-ray Diffraction
ρ	Resistivity
σ	Electrical Conductivity

Chapter 1: Introduction

1.1 Motivation

Information is valuable. As the world is flooded with data, several industries and academic institutions focus mainly on the collection and storage of information. There are billions of sensors in cars, cell phones, computers, and other technological devices that create huge amounts of data. For example, in 2014 the National Energy Research Scientific Computing Centre (NERSC) reported 100 petabytes of stored data. This is projected to increase by 40% annually.[1] It is estimated that humankind has stored over 295 billion gigabytes of data between 1986-2011.[2] To store this information, there is a growing need for computers with larger memory space and higher performance levels, especially when considering the next technological revolution; the Internet of Things (IoT). Small memory may be a part of modern life, but this was not always the case.[3] The original hard disk drive stored 5 megabytes of data on a 50 magnetic disk. Each disk was 24 inches in diameter and weighed 1 ton. The IBM hard disk storage unit was operational in 1965.[4] In 2017, memory is measured in micrometres as having a capacity of 256 gigabytes and a weight of 0.5g (**Figure 1.1**).

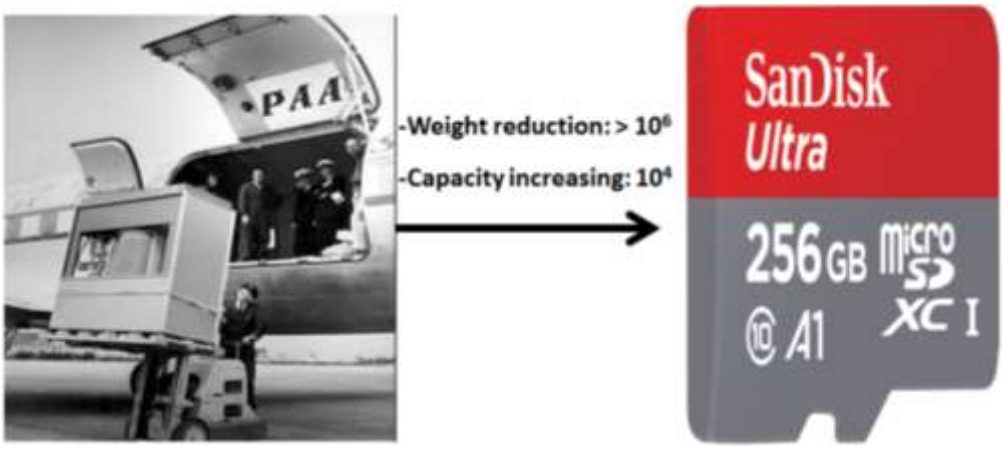

Figure 1.1. A representation of the evolution of the memory system between the years 1965-2017.[3, 4]

1.2 Project Aim

Research has focused extensively on the next generation of computer memory. In particular, resistive random-access memory (ReRAM) materials and composite structures have been reviewed as a method of searching for promising candidates to replace current

memory technologies. Despite a large number of publications which discuss ReRAM, the mechanism behind its switching nature is still relatively misunderstood. Understanding the effect of material composition, structure, and morphology in composite ReRAM devices is essential for a more complete mechanistic insight, as well as for the optimisation of next generation memory devices and logic applications. For this reason, the combinatorial synthesis of thin film materials using evaporative techniques provides an ideal tool for the control of the composition, structure, and morphology of complex materials.[5] This process allows for a systematic high-throughput screening of the intrinsic material properties, as well as a high-throughput optimisation of composite thin films which mimic memory device structures. The aim of this thesis is to investigate the trends and structural properties of titania in order to understand the key material properties that affect the switching behaviour of ReRAM devices. The phases, top electrodes, function of thickness, and structural modifications of titania will be evaluated in this work.

In order to achieve this aim, the following objectives have been set:

- Develop and design a high-throughput framework that will accelerate the discovery of ReRAM material and composite structures.
- Synthesise model thin film materials and structures using the high-throughput physical vapour deposition technique to compare our result against studies that have utilised differing preparation techniques. TiO_2 with Pt electrodes have been chosen as the benchmark for this project in order to verify this technique.
- Synthesise and characterise different titania phases with large variations in thickness so that the relationship between phase and thickness with the functional properties of ReRAM devices can be studied.
- Extend the synthesis and characterisation of Pt/ TiO_2/ Pt to Cu/ TiO_2/ Pt from a cost standpoint compared to Pt, as well as study the effect of heterogeneity of electrodes.
- Extend the synthesis and characterisation of TiO_2 to a composite structure with different stoichiometry and thicknesses of TiO_{2-x} (fixed thickness)/ TiO_2 (gradient thickness).

- Screen the devices obtained according to high-throughput characterisation techniques and primary electrical testing. This will be done using test device arrays and tools that will optimise functional materials and structure in order to shed light on ReRAM mechanisms.

1.3 Outline of the thesis

- Chapter **1** states the motivation for undertaking this project and outlines the aim and objectives.
- Chapter **2** provides an introduction on memory systems and the different types of memory that are commercially available. It also discusses the memory systems that are currently under investigation. This chapter focuses on the literature related to ReRAM in terms of dielectric material, electrode materials, the proposed mechanism, and the key properties of ReRAM application. The underlying physics behind the switching behaviour of ReRAM is also analysed. Finally, there is a brief overview of the current techniques employed in fabricating devices, as well as the promising high-throughput physical vapour deposition (HT-PVD) techniques that are utilised within this project.
- Chapter **3** explains the experimental systems and techniques used in the synthesis and characterisation of thin film ReRAM materials in this study.
- Chapter **4** provides the characterisation results for the structures which were obtained by X-ray powder diffraction XRD and Raman Spectroscopy, as well as the surface characterisation results obtained by XPS, 4pp, EDS and AFM.
- Chapter **5** describes the experimental work carried out for this project, as well as the results. This chapter is divided into three sections. The first section focuses on I-V characterisation (switching behaviour) across different systems: Pt/ TiO_2/ Pt, Cu/ TiO_2/ Pt and Pt/ TiO_{2-x}/ TiO_2/ Pt. The second section describes how switching as a function of polarity is investigated across each above mentioned system. Finally, the third section focuses on investigating the trends and structural properties of titania as a function of thickness, phases, top electrode and the modification of structure in conjunction with the available literature.
- Chapter **6** discusses current state of the art devices applied to other studies and compares them with our results. This chapter also investigates the key properties that affect the switching mechanism, providing suggestions for the appropriate mechanisms applicable to each system.
- Chapter **7** summarises the achievements of this project, and suggestions for further areas of improvement and testing.

Chapter 2: Introduction to Memory Systems

Memory structures play a basic role in providing integrated circuits of powerful processing capabilities. Even most powerful processors have nothing to offer without an accompanying memory. In addition to this, the development of mobile devices is dependent on the continual improvement of memory technology. Typical memory hierarchical design includes three main stages: an embedded on-chip Static Random Access Memory (SRAM) and embedded Dynamic Random Access Memory (DRAM), which is a cache memory directly related to the processor; a commodity DRAM as a main memory; and a storage memory, such as a hard disk drive.[3]

Semiconductor memories can be classified based on, for instance, possible write/erase cycles, re-programmability and volatility into several categories as shown in **Figure 2.1**. The three main conventional types of memory are SRAM, DRAM and flash memory. Generally, SRAM is the fastest, DRAM provides higher density, and flash memory is non-volatile. However, SRAM suffers from a large cell size, while power consumption in DRAM is high due to the required refresh cycle – and both are volatile. The main drawback of flash memory is that it is slow and suffers from scaling limitations. A specific comparison between emerging memory technology and conventional memory can be seen in **Table 2.1.** As shown in **Table 2.1**, as compared with SRAM, STT-MRAM has the advantage of a smaller cell area, low programming voltage, fast write/read speed and long endurance; thus, STT-MRAM is attractive for embedding memory on chips, e.g., an SRAM replacement in caches.[6] As compared with flash, RRAM is attractive due to its lower programming voltage and faster write/read speed, and thus the initial target of RRAM technology development is to replace flash for mass storage application.[7] It should be mentioned that different emerging memories may have different application spaces due to their various characteristics, and a hybrid system with emerging memory and conventional memory is also attractive.[3]

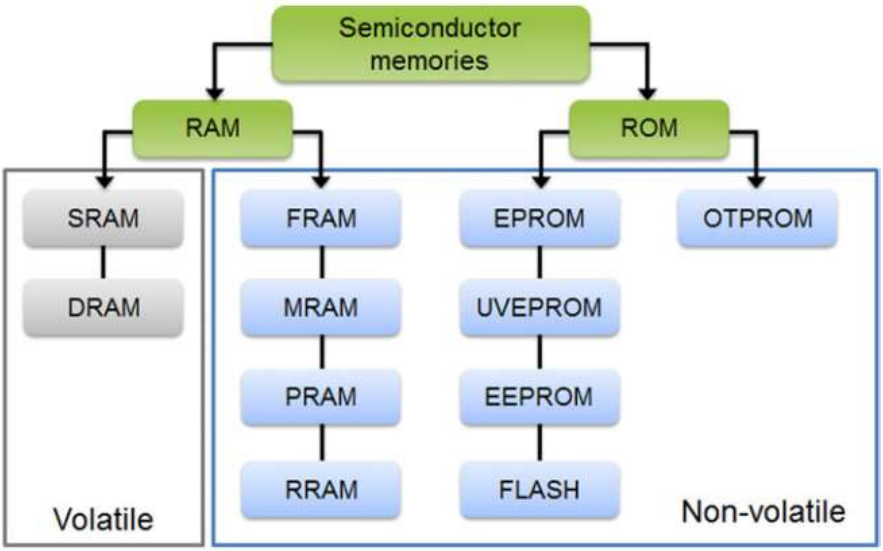

Figure 2.1. Diagram of semiconductor memory classification.[8]

DRAM and SRAM[9] are the most widely used forms of memory for fast write/read speed. Nevertheless, the SRAM storage bit, which is constructed from multiple transistors, is inevitably large; whereas DRAM has high endurance but low scalability. These memories are volatile: They can lose their data if electrical power is disabled. Thus, currently,[10,11,12] DRAM and SRAM have been replaced by flash memory, which is non-volatile and unaffected by power outages, yet has high scaling, a low write speed and a limited number of write/erase cycles.

Non-volatile RAM does not require a power supply to retain data. The most used type of non-volatile RAM is flash memory. However, despite being one of the most used memory types, flash memory still suffers from some drawbacks. These include slow access times compared to volatile RAM, either DRAM or SRAM, a limited number of write/erase cycles (around 100,000), and in some cases, limited random addressability. Due to these intrinsic drawbacks, many alternative approaches to flash memory are being developed. Therefore, present flash memory will not meet the size, speed and higher operational power requirements of future technologies.[8,13] Further improvement in processing capabilities requires a universal memory gathering of all preferable properties, rather than compromising between them. Research efforts are being made to realise the dream of ultimately non-volatile memory, which must also be fast and reliable, operate on low power with a high transfer rate, and have good endurance, a long retention time and a high density. Additionally, it must be compatible with CMOS technology.[14] For this reason, new (i.e., next generation) memory concepts are being investigated that combine non-volatility with high endurance and scalability,[10] such as Ferroelectric Random Access Memory (FeRAM), where the polarisation of ferroelectric materials is reversed; Magneto

Resistive Random Access Memory (MRAM), which uses magnetic tunnel junctions; Phase Change Random Access Memory (PCRAM), which uses the change in resistance between the crystalline and amorphous state of a chalcogenide compound; and more recently, Resistive Switching Random Access Memory (ReRAM), which uses a resistive switching phenomenon. Several RRAM technologies are currently under investigation, including phase-change materials (chalcogenides, perovskites, Ge sulphide and selenide) and, currently most promising, metal oxides (NiO, TiO_2, HfO_2) in which resistance is switched through the formation and destruction of conductive filaments. Work is moving rapidly from fundamental research to development. However, problems understanding the switching mechanism, device reliability and processing remain critical. The consensus is that switching is predominantly due to the migration of oxygen vacancies under the application of external fields, although Joule heating also plays an important role. Much about the microscopic details of the switching process is largely conjectural. However, some techniques have been suggested to explain the mechanism, such as conducting a filament model, trap charging and a discharging model.[12] Furthermore, many questions have not yet been answered, such as the number of write cycles that could be achieved and the write speed limit. Details of each type of emerging memory are presented in the following sections.

Table 2.1. Device Characteristics of Conventional and Emerging Memory Technologies.[7]

	Conventional Memories				Emerging Memories		
	SRAM	DRAM	FLASH		STT-MRAM	PCRAM	RRAM
			NOR	NAND			
Cell area	$140F^2$	$6F^2$	$10F^2$	$<4F^2$	$\sim 20F^2$	$4F^2$	$<4F^2$ if 3D
Multi-bit	1	1	1	3	1	3	2
Voltage	<1V	<1V	>20V	>20V	<2V	<3V	<3V
Read time	<1ns	~10ns	~10ns	~0.1ms	<10ns	~10ns	<10ns
W/E time	<1ns	~10ns	1µs/10ms	1/0.1ms	<10ns	~50ns	<10ns
Retention	N/A	~64ms	>10y	>10y	>10y	>10y	>10y
Endurance	>1E16	>1E16	>1E5	>1E4	>1E15	>1E9	>1E6~1E12
Write Energy (J/bit)	<fJ	~10fJ	~100pJ	<0.1fJ	~0.1pJ	~10pJ	~0.1 pJ

2.1 Memories

Generally, electronic storage systems are classified into two groups – random access devices and mass storage devices.[15] Random access devices are controlled in a parallel way, providing faster access. They have a matrix organisation. Every memory cell is addressed by appropriately addressing two address lines – a bit line and a word line. Mass storage devices are more suitable for storing larger amounts of data. In this case, data access is sequential. This means that the operational speed is slower and depends on the physical position of the accessed data. There is a clear trade-off between the operational speed and the overall storage capacity. Different types of memories are used for different purposes – from very fast, low capacity cache memories to much slower higher capacity permanent memories like hard disk drives. Matrix-based memories are further classified into two types – random access memories (RAM) and read only memories (ROM). The first type is used as a main memory in semiconductor devices, such as personal computers, mobile phones and portable electronics. The second type is used when the access time needs to be as short as possible. The memory capacity of ROM is lower compared to RAM. ROM is typically used for instruction storage. These two types of memories are further divided into several categories as shown in **Figure 2.1**.

When it comes to RAM, there are two types of matrix organisation: passive matrix organisation and active matrix organisation.[14] Matrix memory organisation is shown in **Figure 2.2.** The rows of address lines (called word lines – WL) are perpendicular to the columns of address lines (called bit lines – BL). At the node of every intersection, there is a memory unit/resistive switch (RS). In the case of passive organisation, there is no additional active switch. However, the nonlinear element (NLE), usually a diode, in series to RS is used. A passive memory matrix allows high device density, low fabrication costs and the possibility of 3D architectures – stacking of multi layers into a 3D configuration.[15] However, in the case of RRAM with passive matrix organisation, sneak currents through non-selected cells limit the maximum size of the matrix. An active memory matrix, as an addition to a memory cell, includes an active switch. This active switch is a selector device, usually a transistor,[14] that overcomes the problem of sneak paths and fractional stressing of non-selected cells. Although this greatly helps with respect to the maximum size of an individual matrix, it comes at the cost of an additional element.

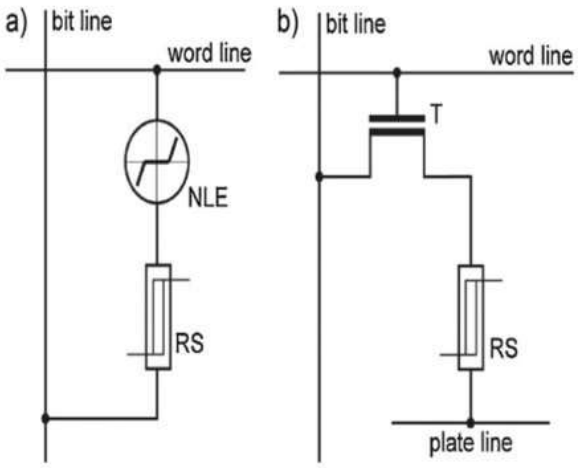

Figure 2.2. Diagram of a (a) passive memory matrix; (b) active memory matrix.[14]

RAM is further classified into two groups – volatile RAM and non-volatile RAM. In the case of volatile RAM, the memory state is lost once the power supply is removed. For the continuous retention of data, an external power supply is required. There are two types of volatile RAM – SRAM and DRAM.

2.1.1 Static Random Access Memory (SRAM)

SRAM is a volatile memory that uses bistable latching circuitry to store each bit, meaning no writing operation. SRAM has two stable states; these states represent the logical '1' or '0'. In this type of memory, when the power supply is removed, the data are lost.[17] The typical cell consists of six MOSFET transistors and has two stable states. The states are stored in four transistors – two cross-coupled inverters formed by transistors M1–M4 as shown in **Figure 2.3.** Transistors M5 and M6 provide access to the inverters.[17]

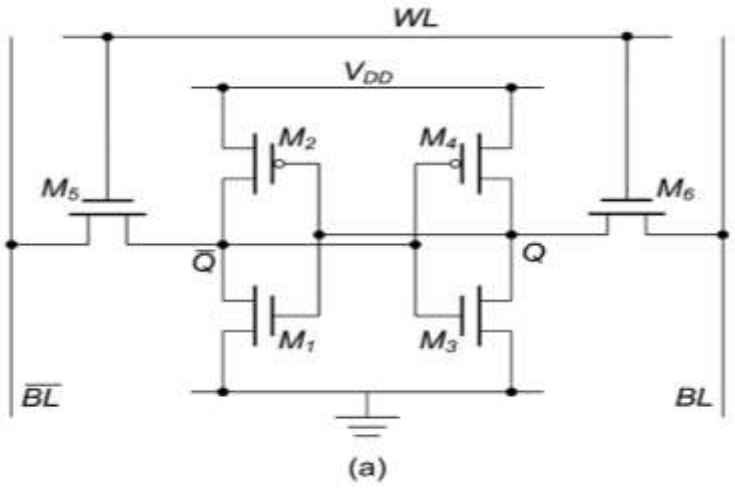

Figure 2.3. Diagram representation of a SRAM memory cell.[14]

2.1.2 Dynamic Random Access Memory (DRAM)

DRAM is a type of volatile memory that stores each bit of data in a separate capacitor within an integrated circuit; in contrast to static RAM, which requires periodic refreshment of data each time. The capacitor charger is used to represent a memory state in which every bit state ‘1’ or ‘0’ is represented by the charge or discharge of the capacitor. The density of DRAM is high. Also, it is much faster than flash memory as it operates on a nanosecond scale, while flash require tens of microseconds.[16,18] Although DRAM uses much less space than the equivalent SRAM (capacitor and selector in the case of DRAM, compared to six transistors in the case of SRAM), as shown in **Figure 2.4**, SRAM is still used for fast memory-like caching. The access time of SRAM is shorter than that of DRAM (approximately 50 ns in the case of DRAM and 10 ns in the case of SRAM).

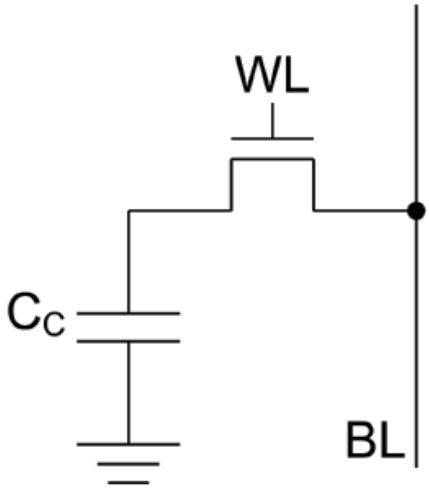

Figure 2.4. Diagram representation of a DRAM memory cell.[16]

2.1.3 Flash Memory

Flash memory is based on floating gate (FG) transistors, where the basic flash memory unit is the FG-MOSFET transistor. Flash memory still dominates the non-volatile memory market. The FG is isolated from the external control gate and drain, at which no resistive connection between the floating gate and the control gate. The charge stored in the floating gate can be modified by applying high voltage to the control gate. Charging and discharging of the floating gate can represent the logical memory state ‘0’ and ‘1’. A schematic of a MOSFET transistor is shown in **Figure 2.5.**[18,12]

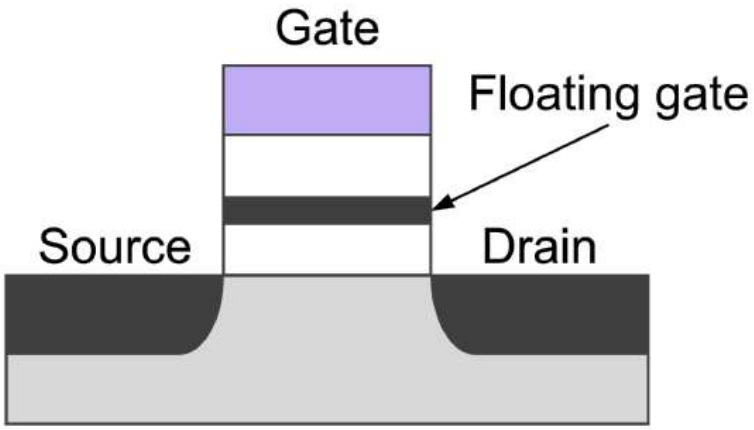

Figure 2.5. Diagram representation of a floating gate transistor.[16]

2.1.4 Magnetic Random Access Memory (MRAM)

MRAM is based on magnetic material that uses magnetic charges to store data. The memory cell consists of two ferromagnetic plates, each of which can hold a magnetization, separated by an insulating layer (one is pinned and the other can be change) as shown in Figure 2.6.[19] By applying an external magnetic field, the magnetic moment of the second plate can be changed. The magnetic moments of the two plates can be either parallel or anti-parallel to each other. These cases represent the logical states of the memory '1' and '0'. The anti-parallel arrangement of two magnetic moments provides a higher resistance to the cell (HRS), whereas the parallel arrangement represents a low resistance state (LRS).[20]

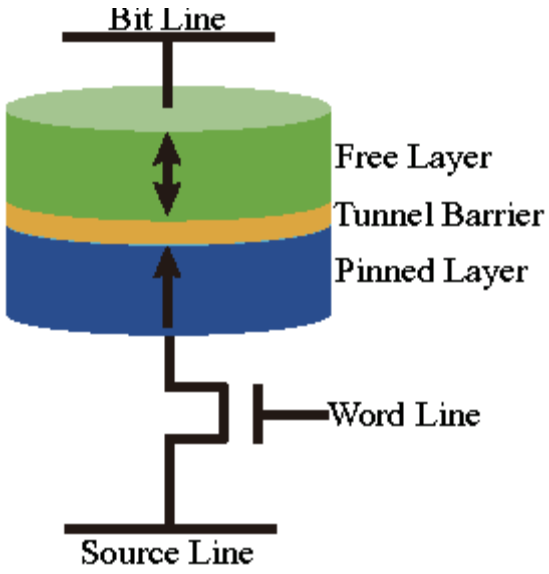

Figure 2.6. The structure of an MRAM cell with bit and word lines.[19]

2.1.5 Ferroelectric Random Access Memory (FeRAM)

Ferroelectric random access memory (FeRAM) has the same property as DRAM but uses a ferroelectric layer, such as lead zirconate titanate, $Pb(Zr_xTi_{1-x})O$, to form ferroelectric capacitors when placed between two metallic electrodes (**Figure 2.7.**). The difference between the polarisation states induced by switching the spontaneous polarisation of the materials represents the logical memory state. When an external electric field is applied, dipoles inside the ferroelectric align them with the field produced by small shifts in the electronic charge in the crystal structure. The dipoles retain their state even after the charge is removed. The reading process is destructive, and the state must be rewritten after reading. The main issue with FeRAM is lower storage density and higher cost compared to high volume memories that are already on the market.[21]

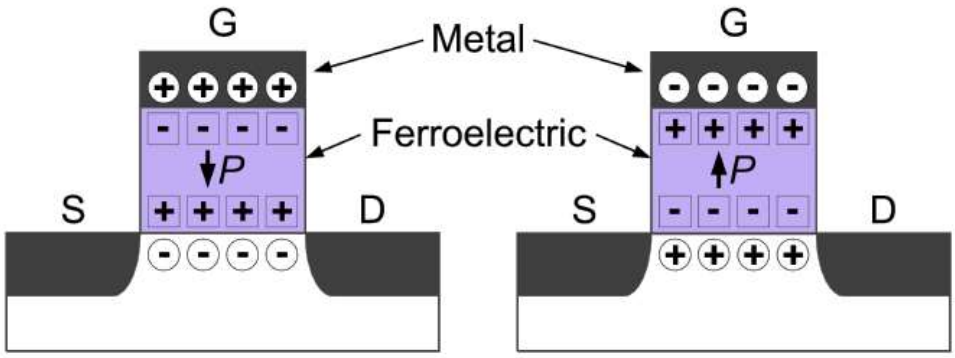

Figure 2.7. Diagram representation of an FeRAM memory cell.[7]

2.1.6 Phase Change Memories (PCM)

Phase change memories (PCM, or PCRAM) are based on chalcogenide materials, which can switch between an amorphous and crystalline phase when heat is applied. This heat is generated when a current pulse is applied through the device. The resistivity of the device will change with the phase. The amorphous titania has higher resistivity, and the crystalline phase, exhibiting a lower resistivity. The transition from an amorphous to crystalline phase corresponds to the SET operation, whereas the opposite transition, from a crystalline to an amorphous phase, corresponds to the RESET operation. This process needs relatively high power due to the intensity required to reach the melting point of the material. As this transition reversibly occurs, it represents the memory logic value '1' and '0'.[22] A schematic of a typical PCM cell is shown in **Figure 2.8**. Intense heating and abrupt cooling afterwards transition the material into the amorphous phase. Longer, weaker heating transitions the material into the crystalline phase. Although PCRAM can already

be found in volume production,[23] several challenges are still present. The high temperature sensitivity of PCM is still the main drawback. Moreover, existing commercial memories are proving to be more economical.

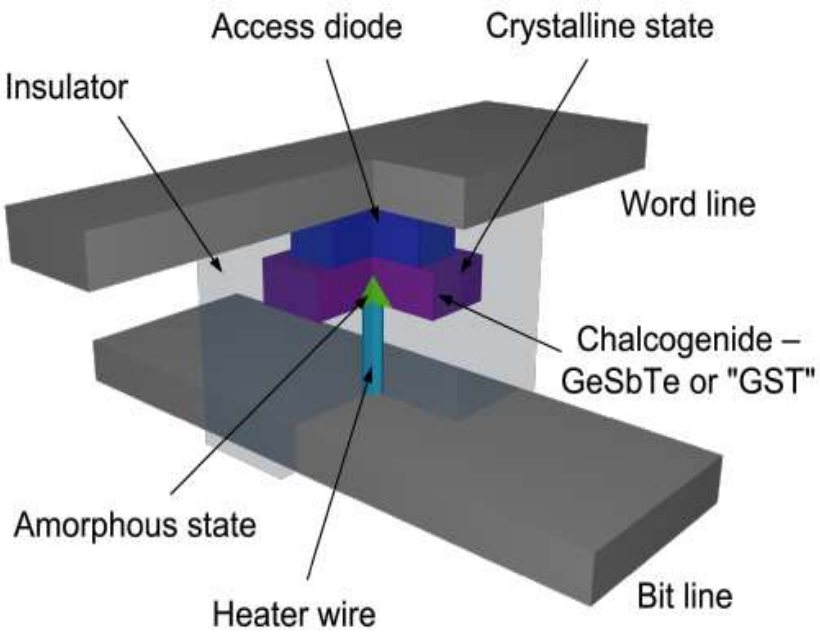

Figure 2.8. Cross-point Phase Change memory cell.[22]

2.1.7 Resistive Random Access Memory (ReRAM)

Resistive switching memory is based on the resistive switching phenomenon,[24] whereby materials can change their resistivity states under an electric field. More details about this type of memory have been addressed in this thesis.

2.2 Resistive Random Access Memory based on Metal Oxide

In 1962, the first reported study of ReRAM was carried out by Hickmott,[25] who studied hysteretic current-voltage (I-V) characteristics in MIM structures of $Al/Al_2O_3/Al$. He observed a resistive switching phenomenon as a result of an applied electric field. Since then, ReRAM has attracted a great deal of interest from researchers and semiconductor industries. In 2008, Williams et al.[26] came up with the 'missing' fourth circuit's element, the memristor (memory resistor), which is the milestone that led to investigating TiO_2-based ReRAMs.

Interest in this technology has increased in the last decade alongside the dramatic increase in the number of related publications, as shown in **Figure 2.9**. The statistics were obtained by a search term (ReRAM or resistive switching memory or resistive random

access memories) using the Web of Science indexing service. Additionally, the first commercially available ReRAM memory was [MN101LR05D-8bit] with embedded ReRAM, developed by Panasonic for portable healthcare and sensors,[27] followed by [RM24C32DS-32kbit] by Adesto[28] and then Sony-Micron.[29] However, despite such improvements, research focusing on the further development of ReRAM performance in areas such as materials, reproducibility, stability, variability and integration to 3D is still ongoing.

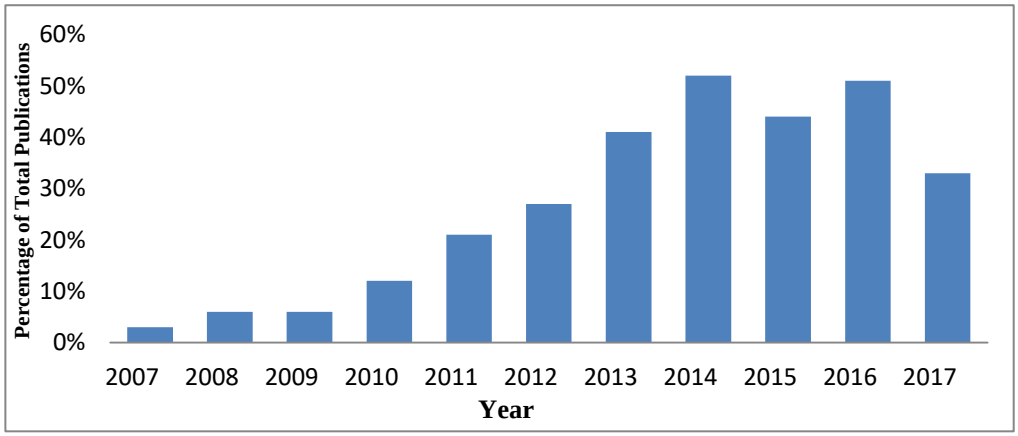

Figure 2.9. Number of publications per year as a percentage of the total for the 2007–2017 periods as cited in Web of Science. Search included the terms "Resistive Switching Memory OR Resistive Random Access Memory OR ReRAM.

The basic principle behind this kind of non-volatile memory is based on the resistive switching phenomenon,[24] whereby materials can change their resistivity states under an electric field. By applying the correct voltage or current, materials that are in an HRS or OFF state can switch to an LRS or ON state. Switching from OFF to ON is called the 'SET' process, while switching from ON to OFF is called 'RESET'. These two states represent the logic values 1 and 0, respectively. The change in resistance is reversible and can be used to store information: ReRAM depends on intrinsic materials that can switch reversibly between two different resistance values. A change in structure and/or composition is associated with these changes.

Resistive memory has its own excellent propitiates, such as lower operation voltage, high speed operation and high density 3D integration, as well as its own unique advantage of having a simple structure. Due to these advantages, ReRAM is favoured by many researchers and semiconductor industries as the most promising candidate for future technologies.[30]

ReRAM devices have a capacitor configuration with a structure consisting of insulator oxide materials inserted between two highly conductive electrodes, as shown in Figure 2.10. These electrodes can both be inert, or one can be inert and one can be active; the structure is referred to as a metal insulator metal (MIM) device. This device stores information '0' and '1' via two different resistance state levels: LRS and HRS. Two switching modes have been identified: unipolar and bipolar. In the unipolar mode, SET and RESET voltages have the same bias polarity. Usually, in the unipolar mode, the RESET voltage is less than the SET voltage; whereas in the bipolar mode, SET and RESET voltages have opposite polarities. In both modes, switching from HRS to LRS is called the SET process, while switching from LRS to HRS is called the RESET process.[31]

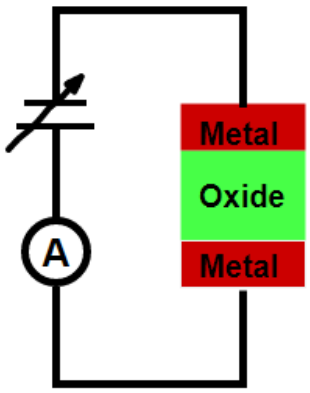

Figure 2.10. Diagram of a ReRAM memory cell with a capacitor-like structure in which an insulating oxide is sandwiched between two metal electrodes.

One of the most important factors in ReRAM is current compliance (IC), which is applied to the device to prevent any damage from large current (hard breakdown), usually in the SET process or the forming process. In both operation modes, there is a pre-switching step called the 'forming step', which is an initial step that switches from an initial resistance state (IRS) to a low resistance state (LRS). Usually, this step requires higher voltage than the SET and RESET process. However, ReRAM today is still being investigated (Figure 2.11) due to the fact that no materials or structures have been confirmed to meet the memory device's requirements.[31]

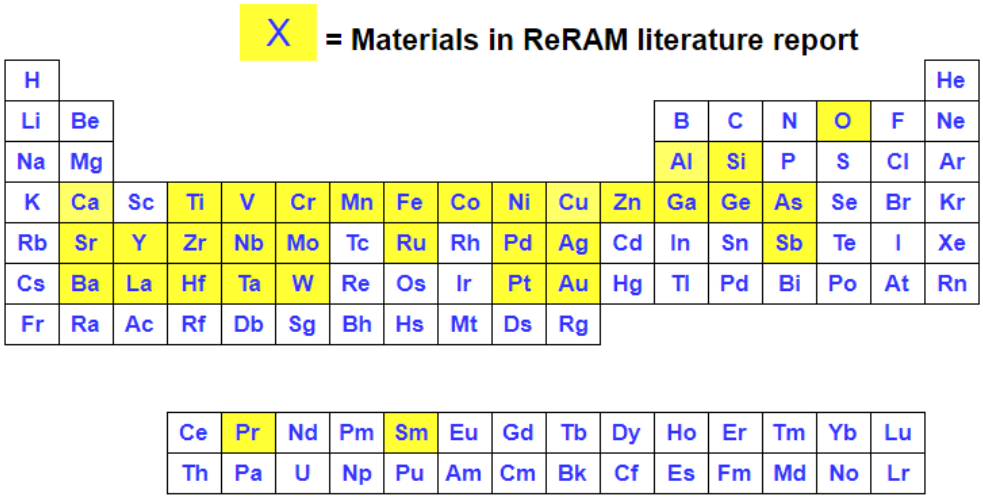

Figure 2.11. Diagram shown the elements (mostly in an oxide) that are used for ReRAM in literature (collected from different reviews) [8-9, 14,32-33]

2.3 Dielectric Materials

The materials used for ReRAM are very important, as the ReRAM mechanisms vary from one cell to another depending on the nature of the materials used for resistive switching.[32,34] One of the key successes of future ReRAM technology will be the ability to integrate materials/switch structures into a conventional material that can switch reversibly between two different resistance values. Therefore, the selection of materials should depend on whether the material has a high dielectric constant and a different oxidation state.[35]

Reversible resistive switching has been observed in various oxide materials, including binary metal oxides such as TiO_2,[36,37,38,39,40,41] NiO,[42-43] HfO_2,[44,45] AlO_x[46]; perovskite oxides (e.g., Cu-Doped ZrO_2,[47] $SrTiO_3$,[48,49,50] Fe-Doped $SrTiO_3$,[51] Cu-doped TiO_2,[52,53] Cr-Doped TiO_3,[54] Nb-Doped $SrTiO_3$[55]; chalcogenide materials (e.g., GST)[56]; and complex oxides materials like (Pr,Ca) MnO_3,[57] amorphous silicon (a-Si),[58] carbon-based materials,[59] and amorphous zinc-doped silicon oxide.[60] Composite oxides, such as TiO_2/TiO_{2-x}[61,62] and HfO_2/TiO_2[63] have been considered for ReRAM application. Among these resistive switching materials, binary metal oxides are of great interest, especially TiO_2, the most commonly reported oxide in ReRAM. Titanium oxide has been chosen as a benchmark material for this high-throughput research project in order to establish a reliable screening of ReRAM material. Furthermore, TiO_2 has been studied as a high-k capacitor oxide.[64] It is intrinsically an insulator, meaning it has a very high resistance. The conductivity of film occurs by making the oxide richer with oxygen vacancies, which

behave like positively charged species. By applying an external voltage bias in a stoichiometry film, it is possible to drift the oxygen vacancies. In addition, due to the simplicity of its fabrication, ReRAM shows both unipolar and bipolar RS, which makes it easier to study both mechanisms.[41] Moreover, TiO_2 is compatible with CMOS, a cheap, non-toxic material, and is chemically stable; its electrical properties, on the other hand, are unstable, which leads to either more insulation or conduction through the appropriate choice of impurities.[37] TiO_2 is widely used in different areas of research under various forms, such as single crystals and ceramics, or as thin films, such as optical application[65] and photocatalysis.[66,67,68] TiO_2 is also used as a support material due to its high conductivity in the sub-stoichiometric or doped form.[69]

2.4 Electrode Materials

Electrode materials have been found to impact the switching behaviour of ReRAM.[41] Therefore, electrode materials should be carefully selected, as improper materials, especially top electrodes (TE), can lead to degradation, which occurs via the formation of bubbles underneath the contact.[70,71] This will affect the endurance of the device. It is important to highlight that a selection of electrode materials should be taken into account for a metal with high oxidation resistance. Furthermore, active top electrodes have been reported,[72] as they have unique features, such as bipolar resistive switching, long switching time and opposite cycling direction in contrast to inert electrodes.

There are many studies in the literature that have tested a variety of electrode materials. Chen et al.[71] studied the effect of top electrode materials (Pt, Al and Ti) for ZrO_2, with Pt as the bottom electrode; it was concluded that Ti can be reproducibly switched over 1000 times with a slight decrease in the resistance ratio between the ON/OFF states. In addition, the write/erase operation was found in 10 cycles without degradation where good stability for the ON/OFF state has high potential for non-volatile memory (NVM). However, it was reported that the conductive channel is formed by the nearest Ti ions in the presence of an oxygen vacancy chain.[73]

Another study by Kang et al.[42] examined NiO thin film using Al, Pt and Ta. They observed that Al and Ta lose their switching characteristics within 24 hours, which results in irreversible breakdown. In contrast, Pt still exhibits repetitive resistive switching. Resistive switching at a slower sweep rate is more stable than at a faster sweep rate, which might be due to the higher energy required in the RESET process.[71] However, Chen et al.[71]

have confirmed that the resistive switching characterisation of Ti/ZrO_2/Pt is more stable than that of Al/ZrO_2/Pt and Pt/ZrO_2/Pt devices. The oxygen ion comes from the ZrO_2 matrix, which reduces variation in resistive switching and provides an oxygen source from the Ti/ZrO_2 interface layer. In addition, it enhances endurance performance. Wang et al.[74] have reported that substantial power is consumed in the transition from LRS to HRS (RESET step). In addition, voltage across the device will drop as soon as a conductive path is created, and most of the applied current will follow from this path. The Cu top electrode has been studied and its diffusivity in TiO_2 confirmed, showing bipolar behaviours.[75] Another study was conducted by Jaewan et al.[76] using the Cu top electrode, in which it was concluded that Cu/TiO_2/Pt exhibited high fluctuation of the current in HRS compared to Ni and Al.

2.5 Operation Mode in ReRAM

In ReRAM, there are two switching schemes, which can be classified as unipolar switching and bipolar switching; for both switching schemes, there is a pre-switching step called the forming step.[13]

2.5.1 Forming Step (FS)

The FS, which is the initial process for resistive switching measurement, is performed by applying an appropriate voltage until the materials are in an initial resistance state (IRS), sufficiently stressed to cause a breakdown (Vset), at which point the current flows; the current is limited by the set IC.[34] Then, heat is generated, causing a major modification of materials whereby the device switches to low resistance state (LRS) (ON). On sweeping the voltage back, the current remains on IC until it falls to zero. This step usually involves enormous hysteresis in (I-V) behaviour at several orders of magnitude greater than that observed before the breakdown,[31] as shown in **Figure 2.12**. Basically, there are two types of breakdown – hard breakdown and soft breakdown – depending on the possibility of recovery from a degraded resistance state. In hard breakdown, there is a hard decrease in resistance such that the cell cannot be switched back to HRS[77]; whereas in soft breakdown, the FS activates resistive switching between HRS and LRS. It is important to highlight that HRS is generally lower after the FS than in its pristine state (before the FS), indicating that once the FS is switched, HRS cannot be switched back to a pristine state.[32] One of the main parameters in the FS is oxide thickness, as it determines the forming voltage, which is the highest voltage needed. It is important to indicate that the

SET and RESET operations are not dependent on oxide thickness, as they have lower voltages than FS. The forming voltage can be reduced by thinning the oxide layer; however, a thin film would lead to greater breakdown than a thick film. In addition, the forming voltage can be compared to SET voltage, and so the forming voltage becomes unnecessary.[41] However, some devices do not require this step, especially non-stoichiometric devices, as they are low in oxygen.[62]

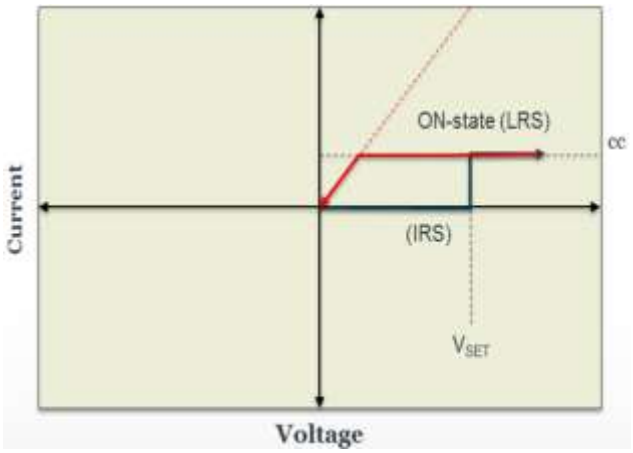

Figure 2.12. Diagram of forming step. CC: compliance current. Dashed line indicates that the real voltage in the system is different from the control voltage.

2.5.2 Unipolar mode

Unipolar resistive switching behaviours do not depend on the polarity of applied voltage. After the FS, the voltage is increased until the switch from LRS to HRS occurs, at which point a thermal dissolution of the filament takes place (Vreset), as shown in **Figure 2.13a**. By sweeping the voltage, the materials switch to LRS (Vset), as shown in **Figure 2.13b**. It is important to mention that the RESET process requires higher current than the forming and SET steps. In addition, the SET step is quite similar to the forming process. However, the forming process requires a higher voltage than both the SET/RESET processes. During this process, a continuous reversible switching sequence should be observed, as shown in **Figure 2.15**.[13,31,77] Unipolar types have been observed in many highly insulating oxides, such as binary metal oxides.[13,31,34]

a RESET **b SET**

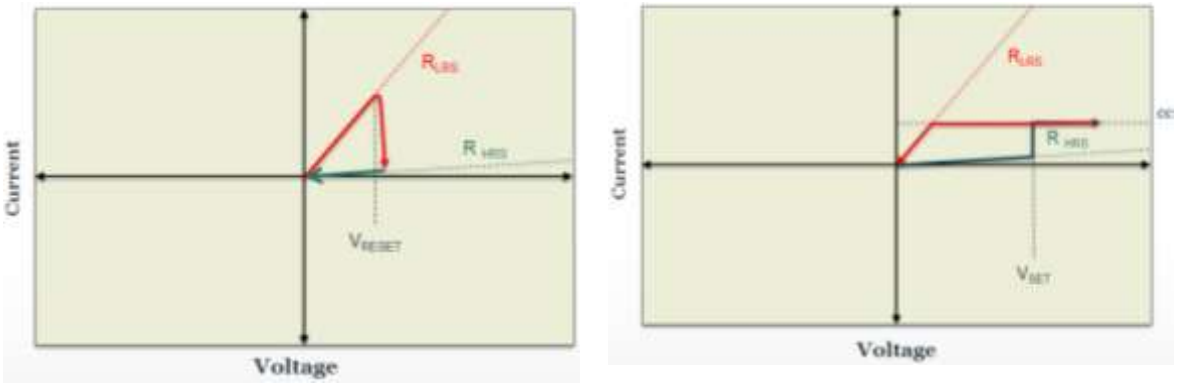

Figure 2.13. I–V curves for unipolar switching. CC denotes the compliance current. The dashed lines indicate that the real voltage in the system will differ from the control voltage because of the CC in action. (a) RESET step. (b) SET step where the voltage is higher than the RESET voltage, and the RESET current is always higher than the CC during SET operation.

2.5.3 Bipolar mode

Bipolar resistive switching is based on the polarity of the applied voltage, as shown in **Figure 2.14**.[34] As mentioned, after the FS and by applying the opposite polarity of voltage, the device switches to HRS (Vreset), as shown in **Figure 2.14** (positive polarity), at which point there is a recombination of oxygen vacancies. The oxygen diffuses in the filament by applying voltage with an opposite polarity (result in higher resistance of the device), after which the device switches to LRS (Vset),[35] as presented in **Figure 2.14** (negative polarity). As this process continues, a reversible switching sequence should be observed, as shown in **Figure 2.15**. For the bipolar type, the switching can be very abrupt, which makes the device suitable for digital memory applications. These types of switching behaviours are observed with many semiconducting oxides, such as complex perovskite oxides.[35,31,34]

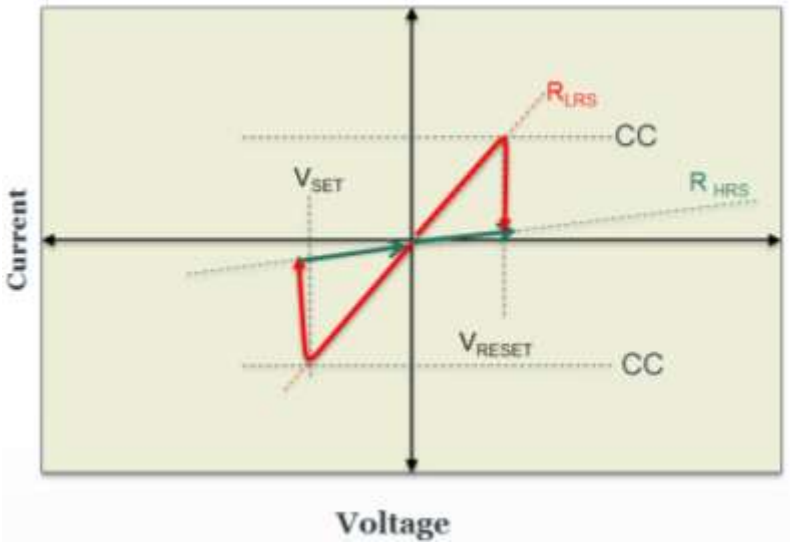

Figure 2.14. I–V curves for bipolar switching. cc denotes the compliance current. Dashed lines indicate that the real voltage in the system will differ from the control voltage because of the cc in action. The SET operation occurs on one polarity of the voltage, the RESET operation requires the opposite polarity.

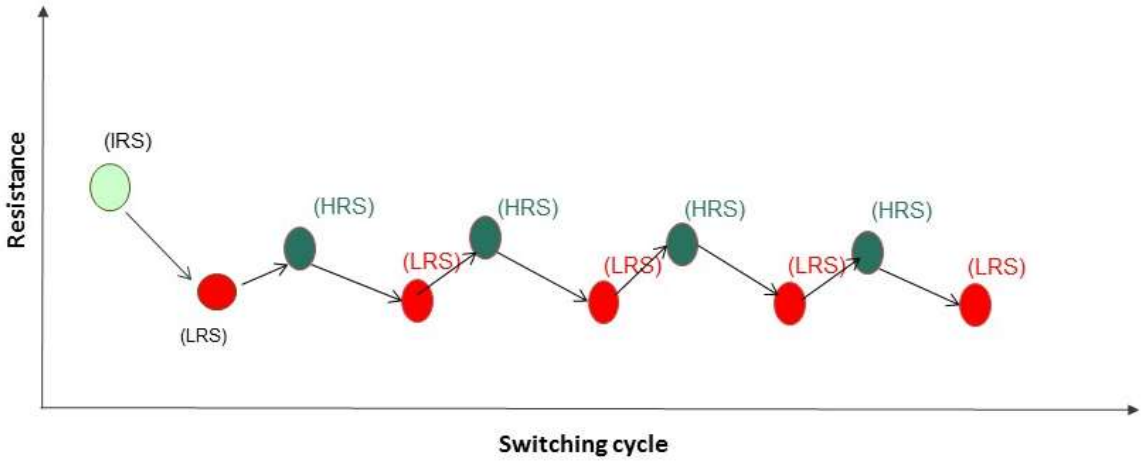

Figure 2.15. Reversible switching sequence: (IRS, initial resistance state; LRS, low resistance state; HRS, high resistance state).

2.6 Switching Mechanisms

One of the main challenges in the optimisation of ReRAM is the need for a better understanding of the mechanism. Although there has been extensive research on ReRAM, the mechanism behind the switching phenomenon is still not fully understood. However, it has been reported that the ReRAM mechanism can be broadly classified into the filament model and the interface model,[31] as well as conductive bridge RAM (CBRAM).[78]

In a filament model, resistive switching originates from the formation and rupture of conductive filaments of dielectric oxide under thermal effect, as shown in **Figure 2.16a** below. This model can be linked to bipolar and unipolar switching behaviours.[31,79] Oxygen vacancies in TiO_2 are known to act as n-type dopants, transforming the insulating oxide into an electrically conductive-doped semiconductor. The vacancy dopants drift in the electric field via diffusion paths, such as grain boundaries, which form channels with electrical conductivity (σ). When the conductance channels infiltrate the electronic barrier, the device is in a switched ON state. After that, voltage with reverse polarity is applied, which takes the vacancies in the conducting channel away from the top interface where the electronic barrier is recovered, and the device is switched to an OFF state; whereas in the unipolar switching mode, the device is switched back by the rupture of the conduction filament by the generated heat.[74]

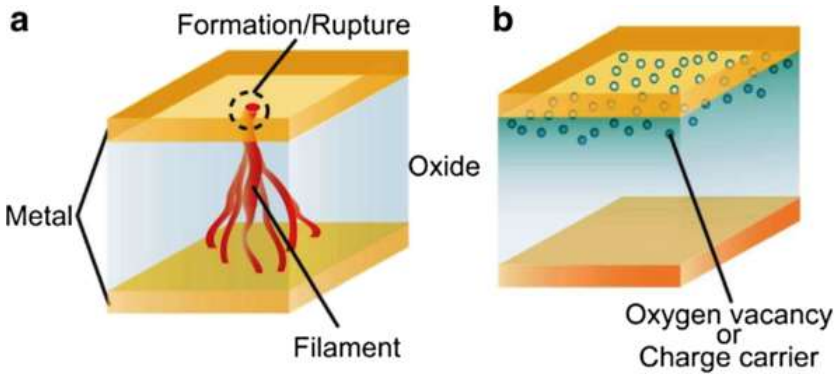

Figure 2.16. Switching mechanisms: (a) Filamentary conducting path model and (b) an interface-type conducting path model.[31,79]

On the other hand, with the interface model, resistive switching takes place at the interface between the metal electrode and the oxide, as shown in **Figure 2.16b** above.

Figure 2.17 summarises the switching process of the filament model, which considered by joule heating. The forming process creates filaments consisting of oxygen vacancies, and the RESET process occurs when local oxidation takes place, and is then SET take place when local reduction occurs.

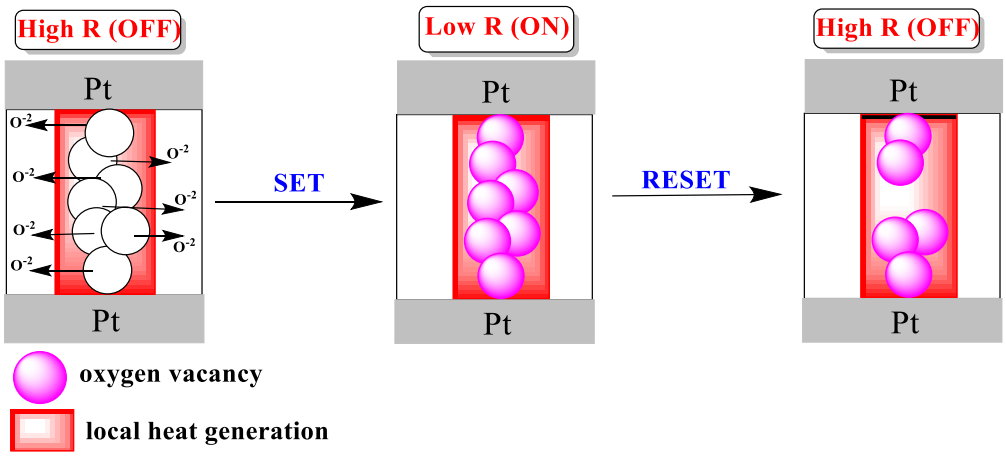

Figure 2.17. Switching process of filamentary model (forming, reset and set)

Furthermore, the switching process of the interface model occurs through the migration of oxygen under an electric field, as seen in **Figure 2.18**. The conduction filament takes place in the forming process, after which oxidation of the filament resettles the device before the generation of oxygen vacancies occurs (SET).

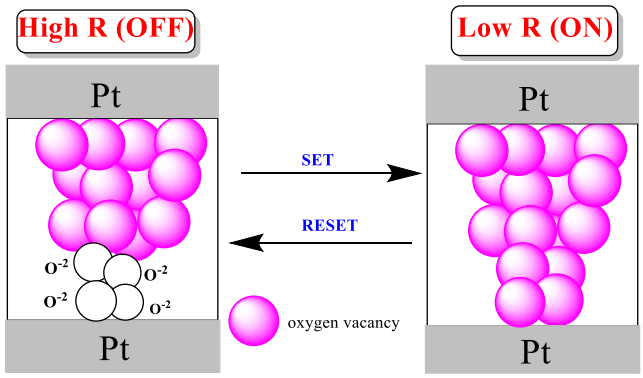

Figure 2.18. Switching process of the interface model.

Another suggested mechanism[78] is conductive bridge RAM (CBRAM) (**Figure 2.19**), in which the electrolyte layer is inserted between an oxidizable anode and inert cathode. The conductive formation involves certain steps. First, when positive voltage is applied to the oxidizable anode, an electrochemical reaction occurs in the anode that oxidises the anode's metal atom into a metal ion. Next, the highly mobile cation drifts in the ion conductive layer under the electrical field. Finally, the metal ions are deoxidised back to metal atoms at the inert cathode. As this process continues, a metallic filament is established between the two electrodes, and the device switches from HRS to LRS. By changing the polarity of the bias voltage, an electrochemical dissolution of the conductive

bridge takes place, which resets the device to HRS.[35,80] The switching process of this mechanism can be seen in **Figure 2.20**.

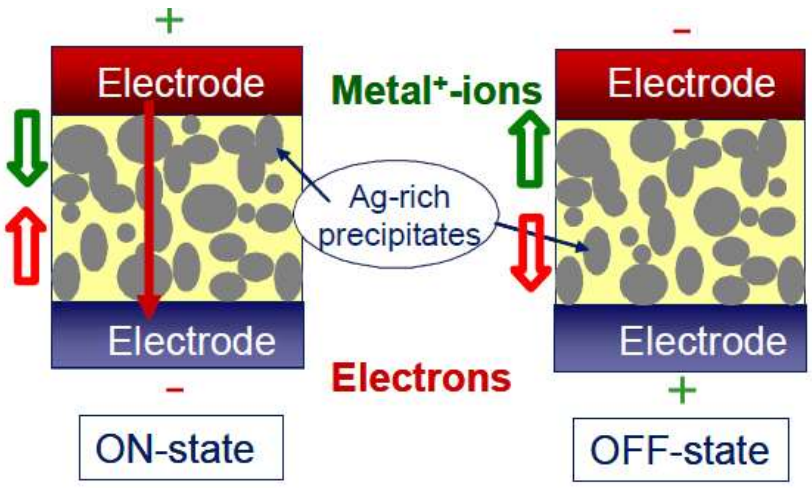

Figure 2.19. Illustration of the CBRAM switching mechanism: ON state: Redox reaction drives Ag ions in chalcogenide glass, resulting in a conductive bridge; OFF state: Size and number of Ag-rich clusters is reduced, breaking of the conductive bridge.[78]

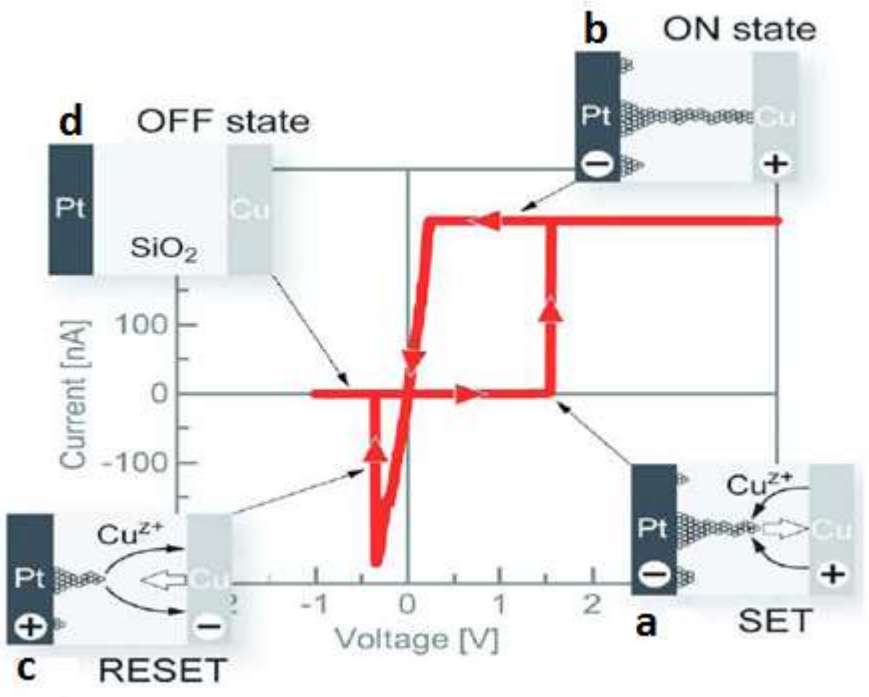

Figure 2.20. Switching process of conductive bridge mechanism.[81]

Nevertheless, Direct current (DC) characterisation provides statistical information on ReRAM switching parameters (such as desired voltage, leakage current and compliance current), while dynamic information (such as retention and endurance) can be obtained via Pulse I-V, where time is controlled during the applied voltage to test the device. In DC instruments, IC is used to limit the maximum current flowing through the test device, with

the goal of limiting the amount of current to reduce the stress on the cell and improve the quality of the switching process.[82] However, at this stage of the project, the Pulse I-V characteristics could not be obtained, as the equipment had only just arrived at our laboratory. **Figure 2.21**shows an example of a Pulse I-V experiment in which the y-axis (blue curve) is the applied pulse voltage, the y-axis (red curve) is the current response, and the x-axis is the time in nanoseconds, where the SET and RESET switches are on the same time scale.

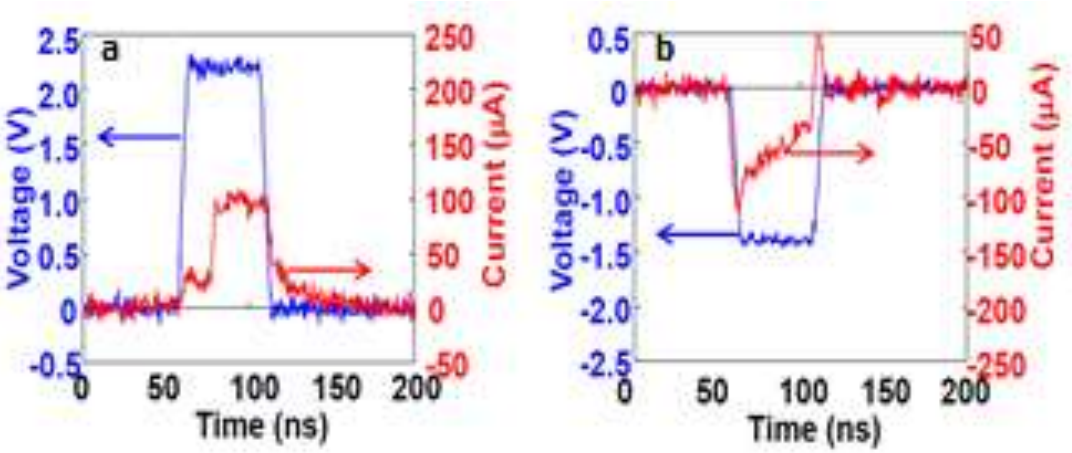

Figure 2.21. Applied pulse voltage and writing current waveforms of Ta/CoO/Pt for (a) SET and (b) RESET. SET and RESET conditions are 2.2 V 50 ns and -1.4 V 50 ns, respectively.[83]

A range of materials has been applied to ReRAM applications in the literature. The materials can be classified in terms of their application to ReRAM relevant to the switching mechanism – that is, ion migration or the redox system. This literature is summarised in **Table 2.2** and **Table 2.3** and contains information on some of the key parameters of the device studied, including material thickness, applied voltages, phase and the metal contact electrodes. Important features reported for TiO_2-based ReRAM, such as forming voltage, thickness and electrodes, are shown in **Table 2.4**.

Table 2.2. Various Binary Metal Oxide Materials Utilised in ReRAM Devices in Ion Migration. Top (left) and Bottom (right) Electrodes Compressing the Oxide Layer; N/S is 'Abbreviation Not Specified'.

Materials	Phase	Electrodes	Thickness	Voltage	Company Involved	Year	Ref
ZnO_2	N/S	Ti, Pt	40–70	-3,+1	Taiwan Semiconductor Manufacturing Company Ltd	2007	[53]
TiO_2	amorphous	Pt, Pt	27	-6.1, +1.1	Centre of Nano Electronic Systems for Information Technology, Germany	2007	[36]
ZrO_2	crystalline	Au, Si	25	-4, +3	Institute of Microelectronics, Chinese Academy of Sciences, Beijing	2007	[47]
ZnO_2	amorphous	Tin, Pt	30	-4, +4	Institute of Microelectronics, Peking University, Beijing	2008	[84]
CU doped ZrO_2	N/S	Cu, Pt	20	-2, +2	Institute of Microelectronics, Chinese Academy of Sciences, Beijing	2008	[85]
ZnO_2	N/S	Pt, Tin	20	-2, +1.5	Institute of Microelectronics, Peking University, Beijing	2009	[86]
ZnO_2	N/S	ITO, Ag (BE)- ITO	50	+0.6, +3.4	Korea Advanced Institute of Science and Technology	2009	[45]
TiO_2	amorphous	Al, Al	10	-3, +3	Yang Kyu Choi (Hyinx Company)	2009	[11]

TiO_2	amorphous	Pt, Pt	60	-2, +1.5	Inter-University Semiconductor Research Centre, Seoul National University, Korea	2010	[12]
ZrO_2	N/S	Au, Ag	150	0, +0.5	Institute of Microelectronics, Chinese Academy of Sciences, Beijing	2010	[54]
TiO_2	amorphous	Pt, Tin	100	+2, -2	Institute of Science and Technology, South Korea	2011	[13]
ZnO_2	crystalline	Cu, Pt	50	-1, +1	Ningbo Institute of Material Technology and Engineering	2012	[87]
TiO_2	crystalline	Pt, Ti	60	-2, +4	Inter-University Semiconductor Research Centre, Seoul National University, Seoul, Korea	2011	[39]
NiO	amorphous	Ag, Pt	40	0, +2.5	Samsung	2008	[16]
HfO_2	N/S	Au, Pt	10	-10, +10	Inter-University Microelectronics Centre, Belgium	2010	[44]

Table 2.3. Various Binary Metal Oxide Materials Utilised in ReRAM Devices in Redox System. Top (left) and Bottom (right) Electrodes Compress the Oxide Layer; N/S is 'Abbreviation Not Specified'

Materials	**Phase**	**Active Electrodes**	**Thickness**	**Voltage**	**Company Involved**	**Year**	**Ref**
TiO_2	amorphous	Ru- (Pt, Al)	20–57	+2, -2.5	Institute of Electronic Materials, Germany	2005	[40]
TiO_2	crystalline	Pt, Pt	N/S	1-2 (set) 0.5 (reset)	Samsung Advanced Institute of Technology, Korea	2005	[41]
ZnO_2	crystalline	ITO, ITO	100	3.2	Korea Advanced Institute of Science and Technology	2008	[88]
$Ge_2 Sb_2 Te_2$	amorphous	Ag, Pt	135	-1, +1	Samsung	2012	[56]
$Ta_{2,} O_2$	amorphous	Cu, Pt	50	+0.65	Samsung	2007	[90]
Cr -doped $SrTiO_2$	crystalline	Cr, Pt	N/S	-2, +2	IBM Research, Zurich Research Laboratory	2007	[54]
$Mg_{0.2} Zn_{0.2}$	crystalline	Pt, Pt	350	+0.65	State Key Laboratory of Optoelectronic Materials and Technologies, China	2008	[91]
$Pr_{0.7} Ca_{0.3}$ Mn_{03}	amorphous	Pt, W	50	-1.5, +1.5	Gwangju Institute of Science and Technology, Korea	2011	[57]
$SrTiO_3$	crystalline	Au, Pt	300	-1.2, +1	IMEC	2011	[50]
WO_3	N/S	Cu, Pt	50	-0.44, +0.1	Institute of Microelectronics, Chinese Academy of Sciences, Beijing	2011	[92]
HfO_2	amorphous	Ti, Pt	N/S	N/S	Department of Materials Science and Engineering, Korea	2012	[93]

Table 2.4. Important Features Reported for TiO_2-based ReRAM, such as Forming Voltage, Thickness, Electrodes and Area; N/S is 'Abbreviation Not specified'.

Thickness of TiO_2 / nm	Top Electrode	Bottom Electrode	Electrode Thickness(Top)/ nm	Pad Size	Phase	Ref
27	Pt	Pt	10	10-100 um	N/S	36
10	Pt	Pt	10	NS	amorphous	94
10	Pt	Pt/Ir (AFM tip)	N/S	2um	amorphous	95
30	Al	Pt	200 um (Al)	N/S	amorphous	96
70	Pt	Pt	100	100 um	N/S	97
40	Pt	Pt	NS	46 um	amorphous	98
50	Pt	Pt	30	40 um	N/S	99
5	Ni	Ni	30	NS	amorphous	100
50	Pt	Pt	30	40 um	N/S	101
20–57	Pt	Ru	NS	NS	rutile	102
30	Cu	Pt	NS	100 nm	anatase	75
120	Al	Pt	NS	200 um	anatase	52
40	Cu	Pt	185	100 um	amorphous	76

2.7 Screening Materials for ReRAM Application

The challenge is to implement the statistical and dynamical measurements necessary to assess the performance of material in an ReRAM device, which should be compatible with the synthesis of high-throughput methodology. However, the electrical

parameters listed below are key to indicating the behaviour of the materials compatible with ReRAM devices.

2.7.1 Operating Voltages

Operating voltages for a ReRAM device should only be a few volts for both programming and erasing voltages. High operating voltages mean high consumption of power. In addition, reliability can be a problem with high operating voltages.[34,105]

2.7.2 Resistance Ratio

The ratio of resistance for HRS to LRS is an important factor in ReRAM applications as it affects the accuracy of programming and erasing. Generally, a resistance ratio greater than 10 is required to distinguish the two resistance states in circuit design.[34,40]

2.7.3 Write Operation

To be compatible with scaled CMOS, the write voltage should be in the range of a few hundred mV, which can also provide an advantage over flash memory, which suffers from high programming voltage.[34,35]

2.7.4 Read Operation

Read voltage must be smaller than write voltage to prevent a change in resistance during read operation. In the ON state, the read current should not be less than 1 mA to allow fast detection of the state by reasonably small sense amplifiers.[34]

2.7.5 Retention Time

The length of time a memory cell will stay in one state after programming or erasing is called retention time, which means the ability of a memory cell to retain its content. The ideal retention time is 10 years, as most of the commercially available devices are guaranteed to retain whether the power is ON or OFF.[34]

2.7.6 Operating Speed

The shortest time for programming and erasing device cells is defined as the operating speed. It has been found that the best operating speed for ReRAM devices is between 5 ns and 100 ns.[34,35]

2.7.7 Multilevel Storage

The ability of a memory cell to exhibit reproducible resistive switching between multiple resistance states is defined as multilevel storage, which can enhance storage density. Each resistance state remains stable over 104 seconds and is predicted to have a lifetime of 10 years.[34,35]

2.7.8 Size Dependence

It has been reported that[104] small device areas exhibit good resistive switching properties compared to large-sized areas investigated using TEM (0.15 um versus 8 um) because of the higher resistance of the pristine device. On the other hand, small-sized devices exhibit switching at lower compliance, 50 um, and lower voltages, +/-2V, without the need for a FS.

2.7.9 Thickness Dependence

The thickness of TiO_2 should be small to obtain a current density that is in agreement with the current density of ReRAM devices. In addition, to keep the voltage as low as possible, the thickness should be on the order of a nanoscale to meet the device's manufacturing requirements. When oxygen vacancies increase, the Fermi level of TiO_2 becomes closer to the conduction band.[105]

2.8 Physical Properties toward Resistive Switching Memories

The physics and chemistry of TiO_2 play a critical role in the relationship between atomic surface structure and other physical and chemical properties, as there is mixed ionic and covalent bonding in metal oxide systems.

2.8.1 Bulk Structure of TiO_2

Titanium oxide can crystallize into different structures, such as anatase, rutile and brookite.[106,107,108] The most common and studied structures are anatase and rutile. In this project, TiO_2 anatase and rutile were produced using physical vapour deposition (PVD) by molecule beam epitaxy (MBE). In addition, amorphous TiO_2 thin films have been prepared at low temperature.

Titanium dioxide occurs as two important polymorphs, the stable rutile and metastable anatase, and their crystalline phases are shown in **Figure 2.22**. Rutile can be formed at any temperature between 600 °C –1800 °C, at which point TiO_2 becomes liquid.[108] Whereas at temperatures above 600 °C, irreversible transformation of the anatase structure to rutile structure occurs.[106] The elementary cells of the TiO_2 crystal structures are presented in **Figure 2.22**. Rutile and anatase phases show inherently different particle sizes, which might differentiate their electrical proprieties. The most stable crystal face is rutile (110). However, it can be restructured and reconstructed under a reducing or oxidising condition under high temperature. Furthermore, the anatase face (101) is more thermodynamically stable than rutile (110) at which, rutile (110) can be easily reduced than anatase (101).[105]

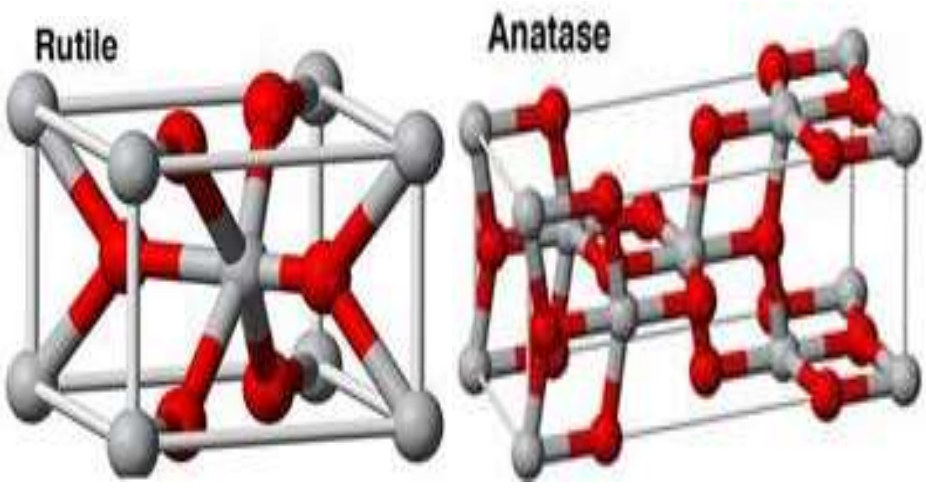

Figure 2.22. Elementary cells of the TiO_2 crystal structures. White ball denote the titanium atoms and red balls the oxygen atoms.[109]

2.8.2 Surface Defect

Ideally, controlling TiO_2 defects, such as oxygen vacancies, is required, which could be created by annealing in the UHV. Changes in oxygen vacancies cause changes in electronic structures. The order of oxygen vacancies would increase the conductivity of

TiO_2 if the electronic configuration and bonding characters around the vacancies were changed.[105]

2.8.3 Bulk Defect

The region of oxygen deficiency where the defect is located is still under investigation. However, most studies have shown that Ti interstitials are the most dominant type in ReRAM. The thermal annealing that occurs in the bulk of TiO_2 crystals causes loss of oxygen, which might lead to crystallographic shear planes. On the other hand, non-stoichiometric TiO_{2-x} contains Ti interstitials in addition to O, which results in higher diffusivity at RT which can in turn form additional TiO_2 structures.[105]

At elevated temperatures of TiO_2 crystals, oxygen vacancies form defect states (occupied) below the conduction band. Moreover, the occupied defect states provide electrons as charge carriers (n-type). If other atoms are doped to form unoccupied states just above the valence bands, then p-type crystals will be formed.[110] Oxygen vacancies in TiO_2 are known to act as n-type dopants, transforming insulating oxide into electrically conductive doped semiconductors. In both crystal structures, these defects give rise to states in the band gap corresponding to electrons localised at Ti^{3+} centres.[37]

There is no ideal crystal. At any temperature, crystals contain various structural imperfections or defects. The greatest point defects of pure rutile TiO_2 are oxygen vacancies and interstitial titanium atoms, which are formed by the transfer of an oxygen atom on a normal site to the gaseous state[111]; the chemical reaction is written in the following manner:

$$O^{-2}_{\text{lattice}} \leftrightarrow V^{-2}_{\text{lattice}} + \tfrac{1}{2} O_2 \qquad \text{Equation (2.1)}$$

Where O^{-2}_{lattice} is an oxygen ion on a normal lattice site, and V^{-2}_{lattice} is oxygen vacancy. Two trapped electrons (e´) associated with the vacancy may, depending on the temperature, be excited and freed from the vacancy. In this case, the vacancy acts as a donor and becomes singly or doubly charged,[112] as follows: $Ti^{+4}O_2^{-2}$

$$V^{-2}_{\text{lattice(0)}} + Ti^{+4}_{\text{lattice(Ti)}} \leftrightarrow Ti^{+3}_{\text{lattice(Ti)}} + V^{-}_{\text{lattice(0)}} \qquad \text{Equation (2.2a)}$$

Or

$$V^{-2}_{\text{lattice(0)}} + 2Ti^{+4} \leftrightarrow 2Ti^{+3} + V^{0}_{\text{lattice}} \qquad \text{Equation (2.2b)}$$

Where $V^{-2}_{\text{lattice (0)}}$ are two trapped electrons, and $Ti^{+4}_{\text{lattice (Ti)}}$ is a titanium ion in a normal lattice.

The Ti ion can relax in the lattice and become interstitial as follows:

$$Ti^{+3} \leftrightarrow V_{\text{lattice(Ti)}} + Ti^{+3}_{\text{interstitial}} \qquad \text{Equation (2.3)}$$

A clear description of these equations is outlined in the schematic presented in **Figure 2.23**.

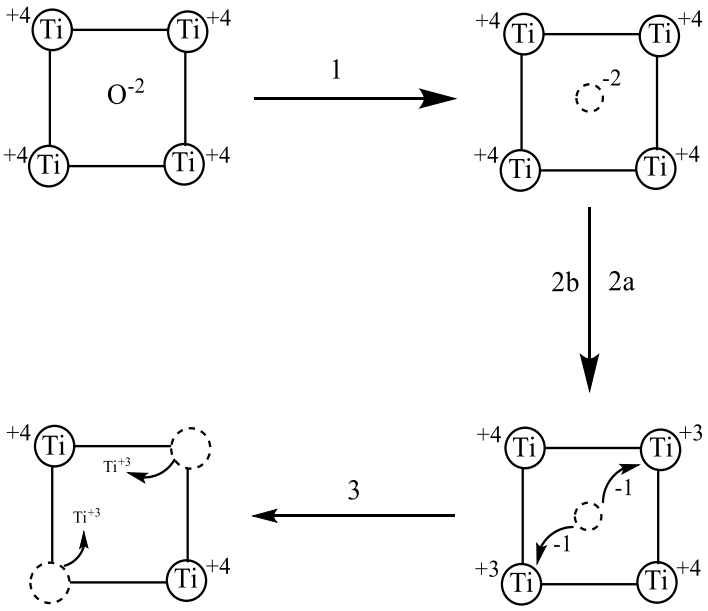

Figure 2.23. Schematic display the defect mechanism in TiO_2

Point defects can contribute to electrical conductivity (σ) in different ways. First, they can provide mobile charge carriers (ionisation); second, they can move in response to an electric field, which means producing an ionic current. Hence, it is important to know the concentration of defects, since when the concentration of oxygen vacancies crosses the upper limit boundary, the phase instability of original TiO_2 becomes high, and phase transition leads to the second phase: the 'magneli phase'.[77] The oxygen vacancies act as electron donors; thus, TiO_{2-x} is an n-type semiconductor, in contrast with p-type semiconductors, which contain electron acceptors and where the charge carriers are holes rather than electrons.[113]

2.8.4 Band Structure

Band gap energy differences between the top valance state and the bottom conductance state determine the electrical conductivity of solid materials, with large band

gaps comprising insulators and smaller band gaps comprising semiconductors. Electrons are able to jump from one band to another, from valance to conductance, by absorbing phonons (heat) or photons (light).[114] The conductivity of intrinsic semiconductors depends on band gaps, The only available charge carriers for conduction are electrons that have enough thermal energy to be excited across the band gap and the electron hole left off when such an excitation occurs.[113]

The energy band diagram of pure semiconductors is characterised by an energy gap (E_G) at which no electronic states are encountered.[113] Electrical conductivity can be measured using the following formulas:

$$\sigma = \sigma_n + \sigma_p = q\,\mu_n\,n + q\,\mu_p\,P \qquad \text{Equation (2.4)}$$

$$n = N_c \exp(-Ec\text{-}E_F/kT) \qquad \text{Equation (2.5)}$$

Where n is the electron density in the conduction band and σ electrical conductivity

$$P = Nv \exp(-E_F\text{-}Ev/Kt) \qquad \text{Equation (2.6)}$$

Where p is the hole density in the valance band

$$E_F = (Ec + Ev/2) + (\kappa T/2 \ln(Nv/Nc)) \qquad \text{Equation (2.7)}$$

Where E_F is the Fermi energy

K is Boltzmann's constant; T is the absolute temperature; q is the electronic charge; μ_n is the electron mobility; μ_p is the hole mobility; Nc and Nv are the effective densities of the conduction and valence bands states, respectively; Ev is the energy at the top of the valance band; and Ec is the energy at the bottom of the conduction band, as indicated in **Figure 2.24**.

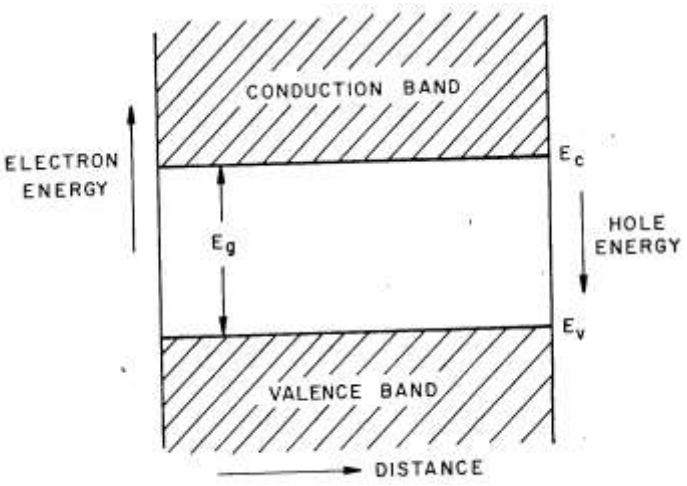

Figure 2.24: Simplified band diagram of a semiconductor.[113]

2.8.5 Fermi level

The Fermi level, which is located in the middle of the band gap (**Figure 2.25a**), is the highest occupied level at absolute zero. If the Fermi level is near the bottom of the conduction band (top of the band gap), then the current transport is due to electrons, and the semiconductor is the n-type, since electrons are the majority charge carriers (**Figure 2.25b**). In the other case, if the Fermi level is near the top of the valence band (bottom of the band gap), then the semiconductor is p-type, since holes are responsible for the current transport: 'holes are the majority charge carriers' (**Figure 2.25c**).[113]

There are different types of defects, which can be classified into three groups: point defects, line defects and plane defects. Point defects include empty sites (oxygen vacancies), where constituent atoms are missing in the structure, and interstitial atoms occupy interstices between the regular atomic sites. Line defects 'dislocation' is analysis and displacements in the periodic structure in certain directions. Plane defects include the grain boundary.

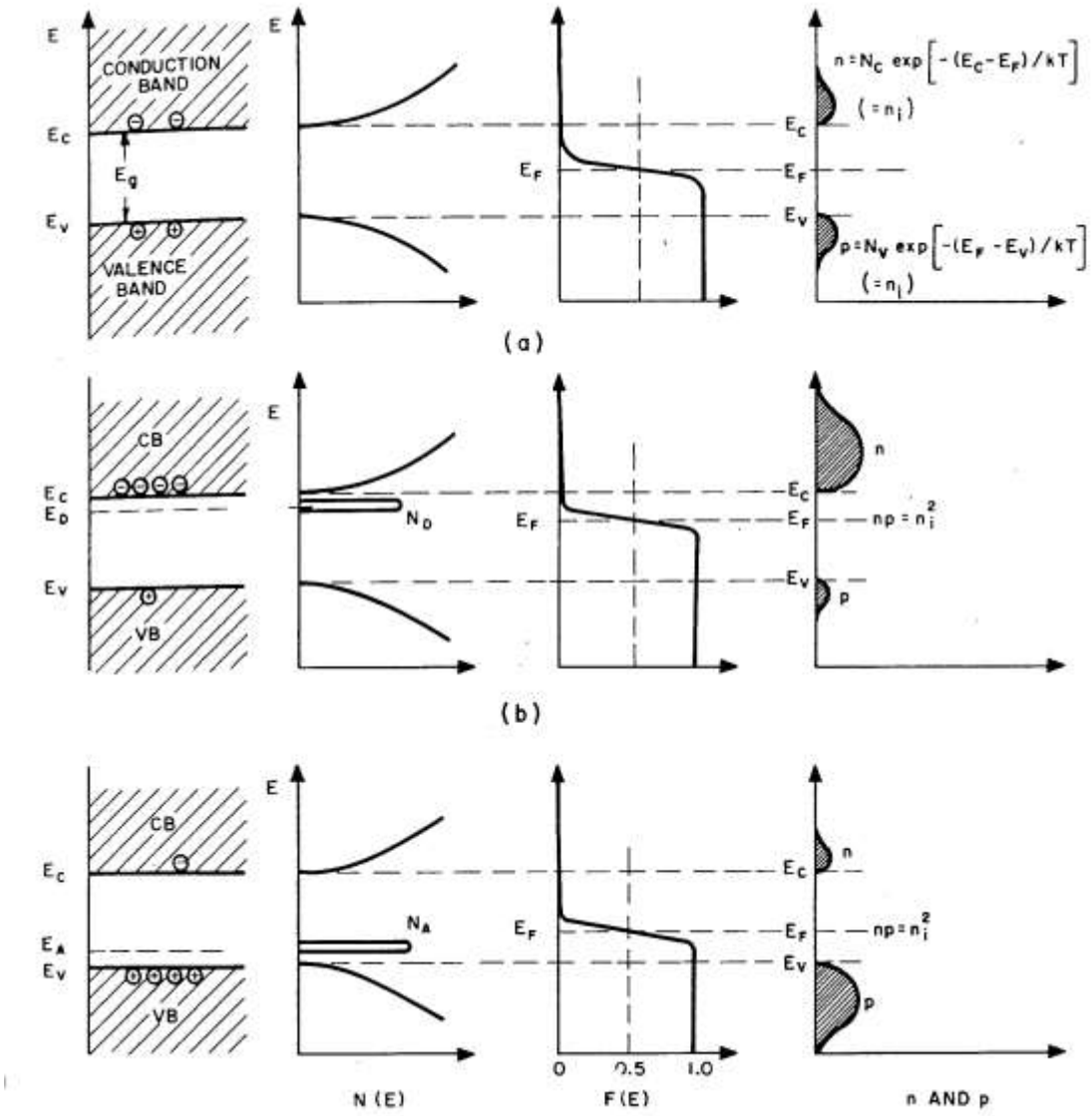

Figure 2.25. Band diagram and the carrier concentration for (a) intrinsic, (b) n-type, and (c) p-type semiconductors at thermal equilibrium.[113]

As this work is strongly related to electrical properties, it is important to highlight that titanium oxide is easily reducible due to the variety of stable phases available,[105] depending on thermodynamic variables, such as temperature and pressure. This is attributed to the transition metal Ti, which might have various valence states. In the phase diagram,[115] shown in **Figure 2.26**, the stoichiometric titania, which is essentially an insulator due to the wide band gap and has a resistivity on the order of 10^7 Ω[116], is shown; the reduced form is where a variety of defects can form as the resistivity drops significantly, and, for example, the magneli phase titania exhibits small resistivties,[117] which therefore means it is ideal as a conductive phase in ReRAM applications. Rutile and anatase structures are compatible with stoichiometries higher than 1.95 only (**Figure 2.26**). It has been reported[108,118] that titanium oxide is regarded as an n-type semiconductor, whereas $TiO_{2-n/2}$, (>1.5) is regarded as metal. Therefore, the change in the stoichiometry of

the magneli phase leads to a large change in electrical properties.[118] Depending on σ, the solid state materials can be classified into three groups: Low electrical conduction materials are insulators; materials with high σ are metals; and materials in between are semiconductors. The electrical conductivity in semiconductors increases when temperatures decrease, while the reverse phenomenon usually occurs in the case of metals.

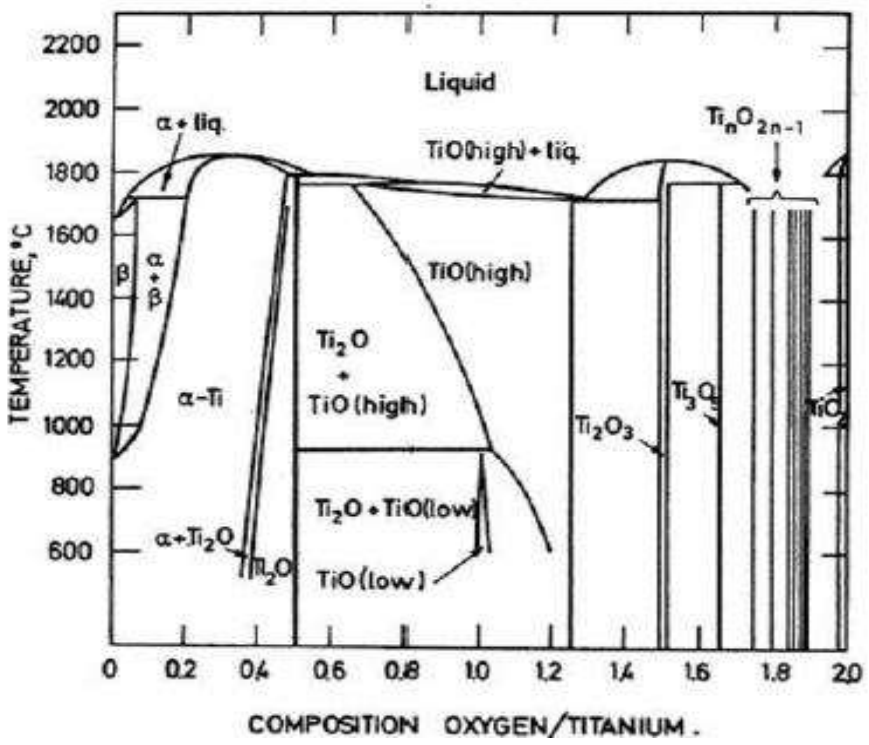

Figure 2.26. Phase diagram of titanium oxides (the magneli phase is located between TiO_2 and Ti_3O_5).[115]

2.9 Combinatorial Synthesis and High Throughput Screening of Solid State Materials

2.9.1 Introduction

Combinatorial chemistry and high-throughput techniques have emerged during the last decade due to the challenge of developing materials for different applications. These techniques aid in the design and rapid synthesis of a variety of material libraries. Such methods also allow the screening of libraries in a parallel manner. Control of the chemical composition of thin-film arrays and their desired thickness can also be achieved, which helps in finding suitable materials for each individual application.[5,119] These advantages have centred these techniques at the heart of industrial and academic research interest due to their cost and time effectiveness.[120,121]

Combinatorial methods were first used for drug discoveries.[122] Since then, they have been considered a very efficient tool for revealing the relationship of quantitative activity structures to establish the criteria for designing novel functional materials used for electronic thin film materials. Recently, extensive research has focused on the development of combinatorial and high-throughput methods for the discovery of new materials that can be used in different applications.[121,123] In addition to the adaptation of conventional methods of solid state synthesis to combinatorial synthesis, significant progress has been made in using thin film combinatorial synthesis combining sputtering or laser ablation of elements or precursors. More recently, a promising method for controlled synthesis was carried out using evaporative physical vapour deposition (PVD) to produce libraries of thin-film materials.[124] Combinatorial libraries with a high level of control over material composition gradients across the substrate can be developed through the simultaneous deposition of more than one element.[68] More recently, combinatorial methods have been successfully applied to ReRAM.[125]

Various experimental methods have been employed for the fabrication of ReRAM devices. They usually involve a layer-by-layer deposition of the different structural components that make up the device – namely, the bottom electrode, the TMO layer and the top electrode. The experimental conditions during ReRAM fabrication determine the structure of the thin-film layer as well as the performance of the devices. For example, Lee et al.[63] reported that annealing TiO_2-based ReRAM devices, under an oxygen environment, improved their resistive switching properties. This is related to the distribution of defects, oxygen vacancies specifically, introduced during synthesis. Consequently, defects are postulated to play an important role in determining the resistive switching mechanisms.

A range of ReRAM fabrication methods have been reported in the literature. They usually involve a combination of the following deposition techniques: pulsed laser deposition (PLD),[126] thermal oxidation and low pressure chemical vapour deposition (CVD),[127] photolithography and reactive ion etching,[128] electron-gun evaporation under high vacuum,[64] RF magnetron sputtering at room temperature under a low oxygen environment,[129] RF coupled with DC magnetron sputtering or thermal evaporation, atomic layer deposition (ALD)[61] and rapid thermal annealing (RTA).[130] A common limitation of the fabrication methods described in the literature is that they only allow for the synthesis of a defined composition and thickness of the TMO layer at a time. Additionally, its involve the use of a variety of instruments for each step, thus making it a relatively time-

consuming and costly process. This represents a drawback of the materials design and optimisation of ReRAMs.

2.9.2 Metal Oxide Materials

A combination of PVD and high-throughput material screening techniques[131] has started a revolution in the discovery of materials for different applications. This is based on the number of patents and papers that have been published by the Hayden research group.[68, 124, 131, 132, 133, 134,135, 136, 137, 138] It has been mentioned that metal oxides play an important role in ReRAM mechanisms.[49,74,77,130,139] More importantly, Hayden et al.[133] have demonstrated the capability and feasibility of the evaporative PVD technique in terms of producing libraries for non-volatile memory materials, where stoichiometric and sub-stoichiometric oxide can be achieved using electron beams or Knudsen sources, combined with a plasma atom source.[140] This unique technique, in which the films are deposited through the condensation of a vaporised form of the source material onto a substrate, allows the co-deposition of multiple elements (up to six elements) across the substrate.

2.9.3 High-Throughput Physical Vapour Deposition (HT-PVD)

The PVD system consists of four chambers with a base pressure of $1x10^{-8}$ **torr**: growth chambers A and B, the sputtering chamber, and the surface analysis chamber. Base pressure is achieved through a combination of pumps for the different chambers of the PVD system, including a rotary (Varian), turbo molecular (Pfeiffer), ion (Varian), titanium sublimation (Varian) and cryogenic (CTI Cryogenics) (DCA Instruments). These chambers are connected via an ultra-high vacuum (UHV) transfer line, as shown in **Figure 2.27**. The chambers are interconnected via a series of buffer lines, which are isolated from the chambers by gate valves. Each chamber also features a transfer arm for inserting and removing samples from within them. Growth chambers use a combination of Knudsen cells (K-cells), which use a heating filament that surrounds the crucible to evaporate the source materials, and electron beam sources (E-gun), which use a beam of electrons to evaporate the source materials. Samples are loaded onto named specimen holders sitting on a trolley, and a load lock allows the insertion and removal of samples from the system. This load lock is used to vent atmospheric pressure before subsequent pumping down to the UHV pressure, independent of the rest of the buffer line. The samples are delivered to chamber A by a trolley inside the buffer line. Then, the sample is picked up from the trolley and placed in the chamber by use of a transfer arm. The sample is then held by the

chamber manipulator and positioned at a pre-defined deposition height relative to the source. Several manipulators are also present in the transfer line for moving samples between the trolleys and transfer arms. Additional manipulators inside the growth chambers allow the samples to be picked up from the transfer arms and held in a constant or rotated position during deposition. The manipulators in the two growth chambers can also be heated to 1100 C°, allowing deposition onto heated substrates or post-deposition annealing. A schematic of the high-throughput system detailing the important features of each chamber is shown in **Figure 2.27**. In this work, an E-gun source was used to evaporate Ti (E-gun 1) and Pt and Cu from E-gun 3, while a plasma atom source, located at the position of K-cell 2 in the chamber (**Figure 2.28**), was used to supply a flux of atomic oxygen during deposition. All samples presented in this work were prepared using growth chamber A (GCA) as shown in **Figure 2.29**

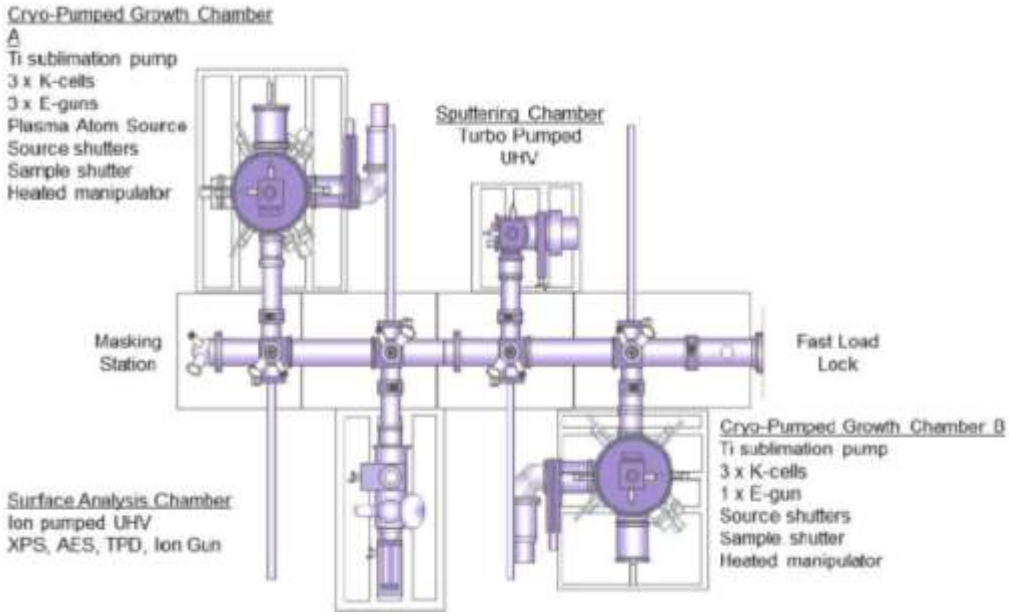

Figure 2.27. Layout of the HT-PVD system showing thin film growth chambers A and B, the sputtering chamber and surface analysis chamber.[141]

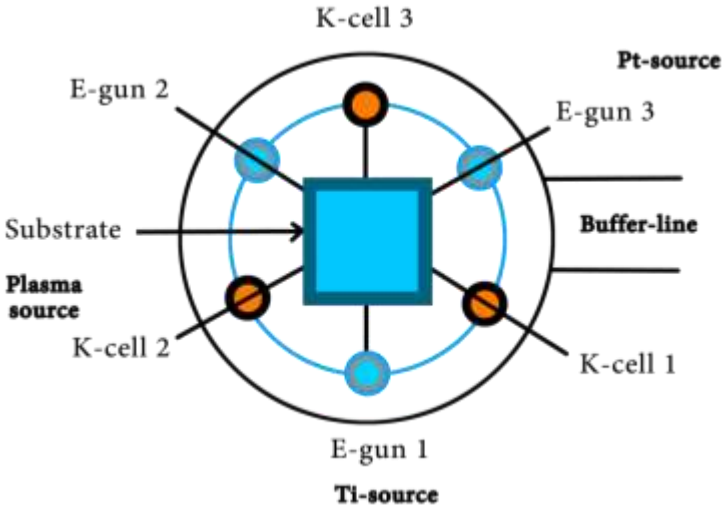

Figure 2.28. Layout of the evaporative sources and location of the evaporation source used in system.[69]

Figure 2.29. Photograph of the PVD system enables the co-deposition of up to six elements (chamber A).[142]

There are three types of shutters in the chamber: main, source and wedge shutters. The source shutter controls the beginning of the deposition and either fully shields or exposes the substrate to the vapour beam. This shutter can allow one to commence or terminate deposition to produce accurate and reproducible deposition times. The wedge shutter, which is located just above each source, moves directly into the elemental flux and

can partially obscure the substrate from the vapour to create a controlled material gradient.[124] **Figure 2.30** shows the effect of varying shutter placement on the deposition profile.

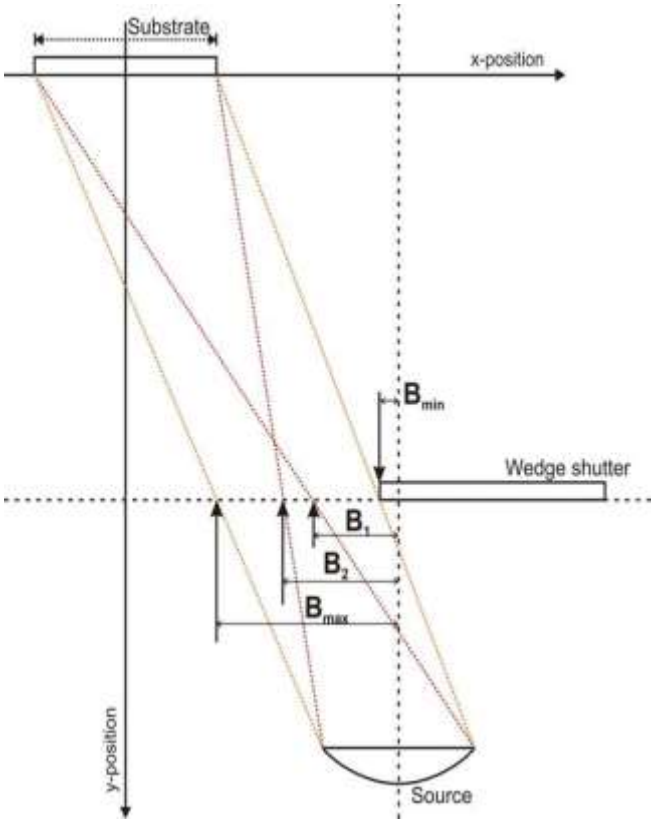

Figure 2.30. Schematic describing the effect of shutter position on the deposition profile for an off-axis source. B_{min} and B_{max} represent the positions at which the substrate is fully exposed and fully shielded from the source respectively. B_1 and B_2 show the origin of the shadow effect created from the wedge.[124]

Generally, when at positions B_1 and B_2, the substrate is partially shielded from some areas of the source (**Figure 2.30**). This therefore limits the flux of material capable of reaching the substrate and creates a gradient in thickness. Simultaneous evaporation from opposite sources can then create a compositional gradient across the substrate via a combination of opposing thickness gradients (**Figure 2.31**). The movement of the shutter allows for a wide range of compositional variations across the array. The co-deposition of elements also ensures good mixing on an atomic level. This mixing also removes the need for annealing and allows the synthesis of metastable phases.

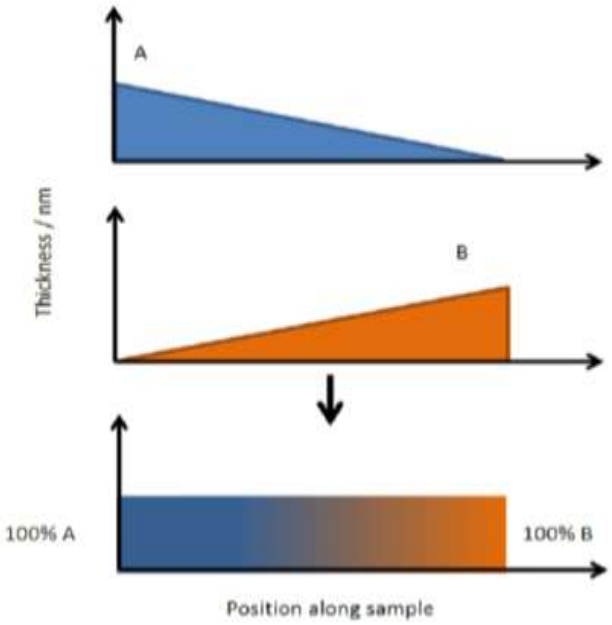

Figure 2.31. Deposition profiles for two opposite off-axis sources with the use of a wedge shutter. The top and middle pictures show the constituent deposition profiles of each element, which form the thin film in the bottom picture when co-deposited**.**[141]

2.9.3.1 Summary of the advantages of the PVD system

The PVD technique has successfully confirmed its feasibility and suitability for the synthesis and screening of thin-film material libraries. This has been achieved through the following strengths of the technique:

- The complete control of material libraries by using main and wedge shutters and source evaporation rates.
- Growth of material libraries over a small area, *ca.* 28 mm x 28 mm.
- Capacity to be combined with micro-fabricated chips for the high-throughput screening of materials.
- The reproducibility of the materials obtained when using the same conditions for subsequent depositions.
- Ability to synthesise thin films and nanoparticle samples as well as complex compound materials easily with well-controlled size distribution
- The system can be combined with an atom plasma source that allows direct synthesis of stoichiometric oxide, mixed or doped oxides, nitrides and hydrides.
- Direct synthesis of the amorphous phase and control of the crystallisation.
- Compatibility with micro-electro mechanical systems (MEMS) array chip screening.
- High purity material synthesis.

Chapter 3: Experimental Procedure and Characterisation Techniques

In this chapter, the methods used to synthesise and characterise resistive switching memory materials and structures will be presented. Synthesis of thin films was achieved by means of physical vapour deposition techniques, particularly the HT-PVD system discussed in **section 2.9.3.**

3.1 Thin Film Synthesis

As discussed in **section 2.9.3**, the HT-PVD system is a highly effective technique for the synthesis of combinatorial material libraries. This system was used to deposit the libraries of titania studied in this project.

Thin films for this project were deposited as 28 × 28 mm films. All samples were marked with a reference dot to keep track of their orientation during deposition and later screening. The reference dot can be found at the bottom right corner of the film, and as such, this will be the orientation used for data presentation throughout this thesis. Elements were deposited within growth chamber A (**Figure 2.29**) using electron beam evaporators (E-guns): E-gun 1 deposited Ti, while E-gun 3 deposited Pt as well as Cu (**Figure 2.28**). The source shutter was required to control the growth of the TiO_2 film, while the main shutter was used to control the thickness gradients of titania. In addition, an HD25 RF atom source (Oxford Applied Research), located at the position of K-cell 2 and aimed at sample substrate, was used to ionise a flow of molecular oxygen gas during deposition using different power. The oxygen flow was controlled via a mass-flow controller.

Source calibration, in which the optimum deposition rate and position of the wedge shutter needed to produce the thin-film materials over the desired composition range are calculated for all systems fabricated, is an essential step in every deposition plan. The deposition rate was varied for the E-guns by altering the source power and using data from a Quartz Crystal Microbalance (QCM) to determine the rate of deposition. However, the rate from the crystal is proportional to the real deposition rate. The actual rate was calculated from the deposition time and the film thickness, as will be shown later in this chapter.

During the source calibration, the elemental deposition sources in chamber A of the HT-PVD system were filled with ultra-pure materials. Ti (99.995%, Alfa Aesar metals) from E-gun 1, Pt (99.999%, Testbourne Ltd), Cu (99.999%, Testbourne Ltd, metals) from E-gun 3, and oxygen (Air Products, special gases, 99.999%) were supplied from a plasma source, which was used to break down molecular O_2 to atomic O to react with Ti and subsequently obtain the desired material: stoichiometric TiO_2. Substrates of glass and Si/SiN (Nova Electronic Materials) were used for Atomic Force Microscopy (AFM) and X-ray diffraction (XRD) measurements, respectively. When optimum deposition conditions were found, the SSTOP ($Si/SiO_2/TiO_2/Pt$) substrate was used for the deposition of TiO_2. It is necessary to emphasise that the substrate is important as it can influence the structure and electrical properties of the thin film. As an ideal case, all electrical measurements in this thesis were made on the same kind of substrate to ensure that a good correlation could be established between the results. The substrate was cleaned in an ultrasonic bath for 10 minutes in isopropanol alcohol, then cleaned with deionised water and dried before being inserted into the system.

3.1.1 Synthesis of Pt/ TiO_2/ Pt

The samples were rotated during the deposition to obtain a homogeneous film across the substrates with an average thickness of 250 nm. TiO_2 deposition was carried out following the same deposition conditions achieved in the calibration stage (see Appendix B). These conditions were based on a constant chamber pressure of 10^{-5} **torr** at a flow rate of 5 sccm, a plasma power of P_{rf} = 400 W and a deposition rate of 4 Å/s (measured by QCM). The actual deposition rate was calculated from the deposition time and the film thickness. The conditions used match those in a paper published using the same preparation methods of TiO_2.[140]

The main shutter was only employed for the second system to fabricate a thickness gradient (10–60 nm) across the substrate of different phases of stoichiometric TiO_2. All samples were deposited at room temperature, and a constant chamber pressure (Appendix B 2.2) with a flow rate of 1 sccm of oxygen and a plasma source power of P_{rf} = 300W was used to obtain the desired material with a deposition rate of 2 Å/s (measured by QCM). It is important to highlight that the crystalline materials were obtained after annealing the sample at 200 °C in the chamber under a 1-sccm oxygen flow rate for 60 minutes. Subsequently, Pt contact pads were deposited on top of the TiO_2 samples after heating the substrate to 100 °C for 15 minutes using a variety of deposition masks. Finally, the

experiment finished with a metal insulator metal (MIM) structure, as shown in **Figure 3.1**. **Figure 3.2** shows an amorphous titania picture using different masks size of Pt top electrode as continues growth of Titania. The rest of the sample pictures are shown in Appendix A.

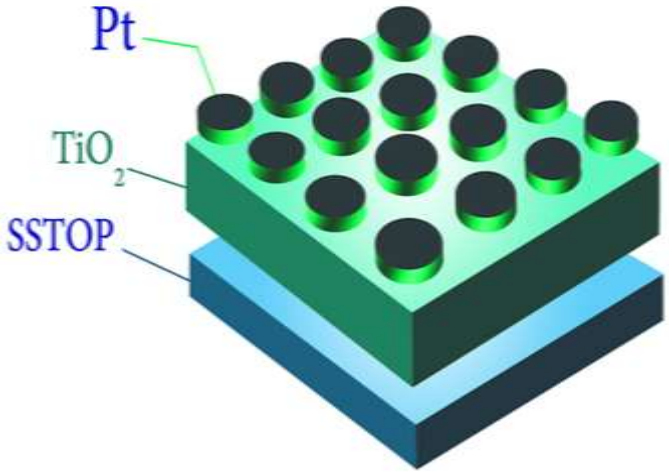

Figure 3.1. Diagram shown the final design of experiment. Top electrode is Pt. Oxide layer TiO_2 deposited on SSTOP substrate (bottom electrode)

Three oxide samples for each phase (amorphous, anatase and rutile) were prepared. Three samples, one for each phase, were deposited with a 250-micron pad, three samples used a 50-micron pad, and the last three samples had no pad deposited on them (see Appendix A 3.2). Preparation conditions of TiO_2, stating the deposition condition and the evaporation sources of Ti and Pt are summarised in Appendix B.

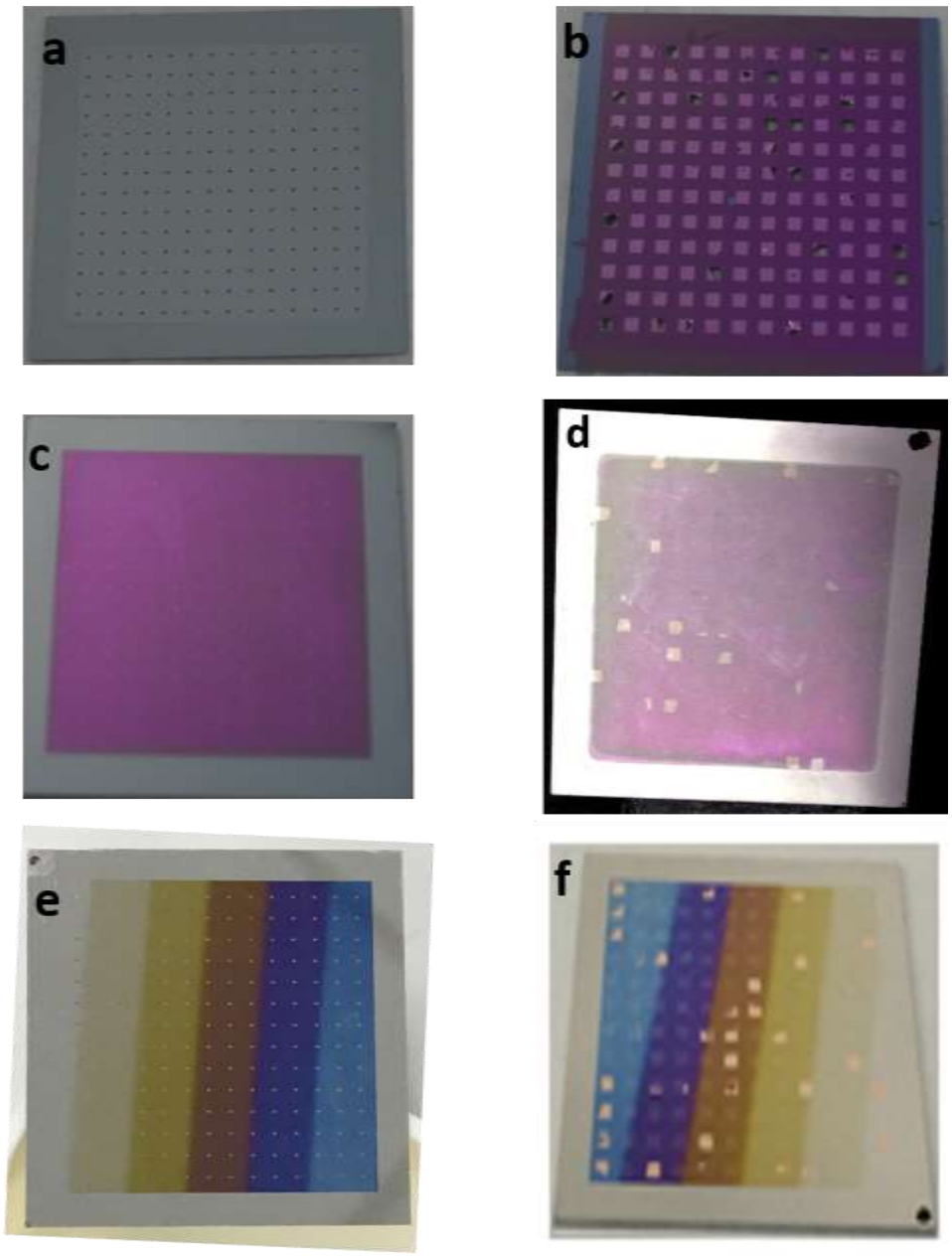

Figure 3.2. Photograph of fabrication masks. (A) 250 micron mask, (B) 50 micron mask, (C), (D), (E) and (F) sample prepared using such masks.

3.1.2 Synthesis of Cu/ TiO_2/ Pt

In this system, we used exactly the same conditions used in Pt/ TiO_2/ Pt, at which the main shutter was employed to fabricate a thickness gradient (10–60 nm) across the substrate of different phases of stoichiometric TiO_2. Different masks were (as described in section 3.1.1) used to deposit Cu 80–100-nm thick. The experiment ended with an MIM structure, as shown in **Figure 3.3** (See Appendix A for sample pictures).

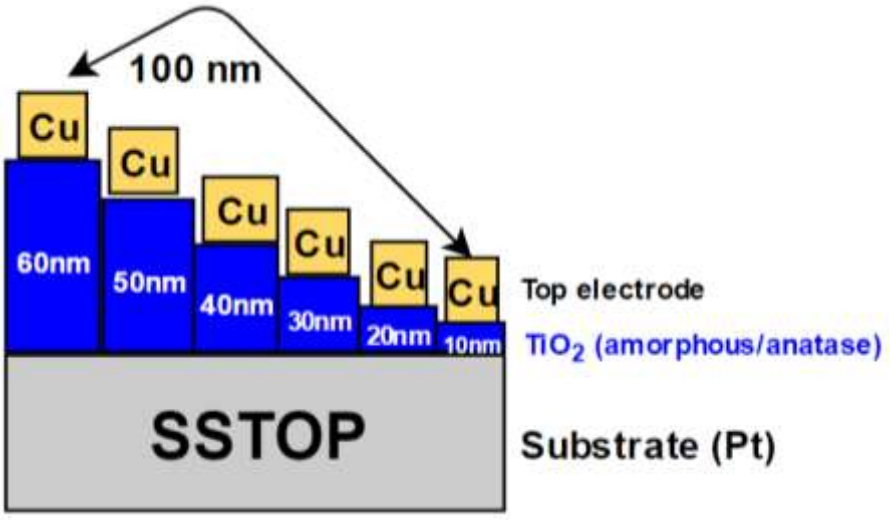

Figure 3.3. Diagram representing the final design of the experiment. Top electrode Cu/gradient thickness of oxide layer of TiO_2 deposited on SSTOP substrate (bottom electrode) with different phase structure (amorphous/anatase).

3.1.3 Synthesis of Pt/ TiO_{2-x}/ TiO_2/ Pt

In this composite system, the main shutter was employed to fabricate a thickness gradient (10–60 nm) across the substrate of different phases of stoichiometric TiO_2. All samples were deposited at room temperature and at a constant chamber pressure (see Table 4 in Appendix B) of 1-sccm oxygen flow rate, and a plasma source of P_{rf} = 300W was used to obtain the desired material with a deposition rate of 2 Å/s (measured by QCM). It is important to highlight that the crystalline materials were obtained after annealing the sample at 200 °C in the chamber under 1-sccm oxygen flow rate for 60 minutes. Then, a 50-nm layer of TiO_{2-x} was deposited on top of TiO_2 using molecular oxygen with a flow rate of 1 sccm. Thickness was calibrated using the same procedure as that used in the case of TiO_2. Subsequently, Pt contact pads were deposited on top of TiO_{2-x}/TiO_2 after heating the substrate to 100 °C for 15 minutes using a variety of deposition masks (described in section 3.1.1). Finally, the product was a composite structure as stated in **Figure 3.4**. Samples prepared using different mask sizes of Pt are shown in Appendix A. Fabrication conditions are listed in Appendix B.

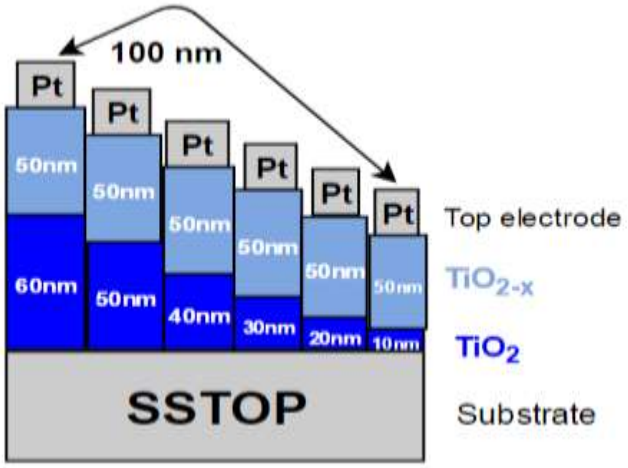

Figure 3.4. Diagram of the final design of the composite systems. Top electrode = Pt, multioxide layer TiO_{2-x} (light blue)/ TiO_2 (dark blue) deposited on SSTOP substrate (bottom electrode) with different phase structure.

3.2 Characterisation Techniques

Different microstructural, chemical and electrical properties were obtained using different characterisation techniques. X-ray diffraction and Raman spectroscopy were used to confirm the synthesis of the targeted phase. SEM and AFM were used to study the surface morphology, while X-ray photoemission spectroscopy as well as a four-point probe were used for chemical analysis and stoichiometry of TiO_2. A probe station was used for electrical testing to assess the different behaviours of the different layer structures electrically.

3.2.1 X-ray Diffraction (XRD)

XRD is commonly used to identify the atomic structure of a crystal. In general, an X-ray thin-film diffractometer instrument consists of an X-ray source, an incident optical system, a goniometer, a receiving optical system and a detection system. When the incident X-ray beam impinges onto the surface, a diffraction pattern is obtained as a result of reflections (produced by detectors) from the crystal lattice planes of the sample. The diffracted rays will interfere either constructively or destructively depending on the d atomic spacing in the crystal. For polycrystalline materials, including thin films, a powder diffractometer configuration is used to produce the 2θ diffraction conditions. For thin-film samples, to increase the sensitivity of the measurements, the incident beam may also be kept at a grazing angle. The detector is scanned in 2θ configurations to record diffraction

intensities.[143] For ordered crystalline lattices, X-rays are diffracted constructively according to the Bragg's law given in Equation 3.1:

$$2d \sin\theta = n\lambda \qquad \text{(Equation 3.1)}$$

Where n is the order of diffraction, λ is the wavelength of the X-ray radiation, d is the spacing between crystal planes, and θ is the incident angle.

X-ray penetration can be controlled, which allows a high diffraction intensity from thin-film samples as well as the suppression of strong signals from substrates (highly orientated along a single crystal plane). The smaller the incident angle, the smaller the penetration depth.[144] The diffracted X-rays are detected and then processed and counted by the instrument's software, where they are converted into a diffraction pattern. The peaks observed in the pattern correspond to the individual planes in the material and their geometric separation, and each material has a unique diffraction pattern. A crystalline sample is considered a series of stacked parallel planes at each of which a beam diffraction takes place, as shown in **Figure 3.5**.

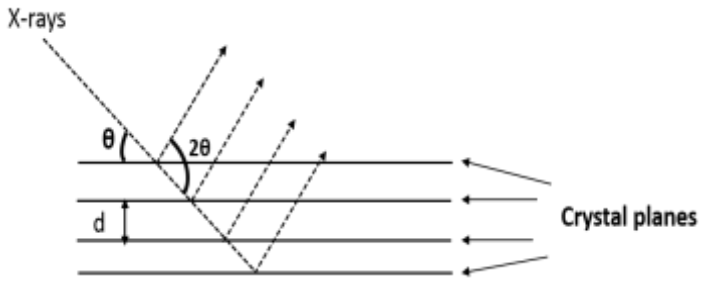

Figure 3.5. Schematic of two parallel X-rays being diffracted at parallel crystal planes.[144]

For this project, X-ray patterns were recorded on a Rigaku smart lab 9KW SN JD3604N. The X-rays were generated by a Cu Kα1 source; the X-ray wavelength was 1.54 angstrom. The scans passed through a specified 2θ range by moving both the X-ray source and the detector. All measurements were done at a grazing incidence angle of 1°. A typical 2θ range was between 10° and 60°. Samples deposited on SSTOP substrates were positioned on a stage with X-Y-Z control.

3.2.2 Raman Spectroscopy

When a beam of monochromatic light is introduced to a sample, typically using a laser as the source, the light interacts with the sample by either being absorbed or scattered. There are two types of scattering: elastic scattering (Rayleigh scattering), in which the light

is scattered without changing the photon energy; and inelastic scattering (Raman scattering), where energy is lost (known as Stokes shift) or gained (known as anti-Stokes shift) in the scattering process (**Figure 3.6**) with energy transfer to or from rotational or vibrational transitions (in the solid state, these modes can couple to give frustrated rotational states). For a rotational or vibrational mode to be Raman-active (this energy transfer to take place), the rotational or vibrational mode must result in a change in the polarizability component of the system. In order to predict the polarizability of a rotational or vibrational mode, one must consider the symmetry of the structure together with the irreducible representation to which the polarisation is associated.[145]

The group theory defines the symmetry behaviour of every vibration of a system belonging to a specific point group. There are four possible vibration assignments – A, B, E and T – that can assign a vibration to a particular irreducible representation in a particular point group. A and B mean that the mode is singly degenerate. E and T mean the mode is doubly and triply degenerate, respectively. The symbols odd (u) and even (g) denote the type of the mode.[146] Most explanation of Raman is usually about the identification of Raman active modes for molecules which work in case of gas or liquid. However, in the case of solid state materials (crystal) for which may be no molecules species such as TiO_2, a unit cell and the atoms located at specific sites is considered. The factor group consists of symmetry operation and symmetry elements that when applied to the unit cell leave it in distinguishable from its original position.[147]

In a typical Raman microscope experiment, an optical microscope is used to focus the laser onto a small spot of the sample. The emitted photons pass back through the microscope and into the spectrometer, where the Raman-shifted radiation is detected by a charge-coupled device (CCD) sensor. A computer connected to the instrument is used for data collection and processing. The result is a Raman spectrum of signal intensity versus the Raman shift of the material. It is a suitable technique for studying the evolution of the local structure across combinatorial thin-film libraries due to its high lateral resolution and high sensitivity to change in chemical composition. The confocal nature of the microscope also allows the volume (hence the depth) of the materials to be defined in the measurement. Because of the weakness of the Raman effect, multiple scans are required to achieve a good signal to noise ratio.

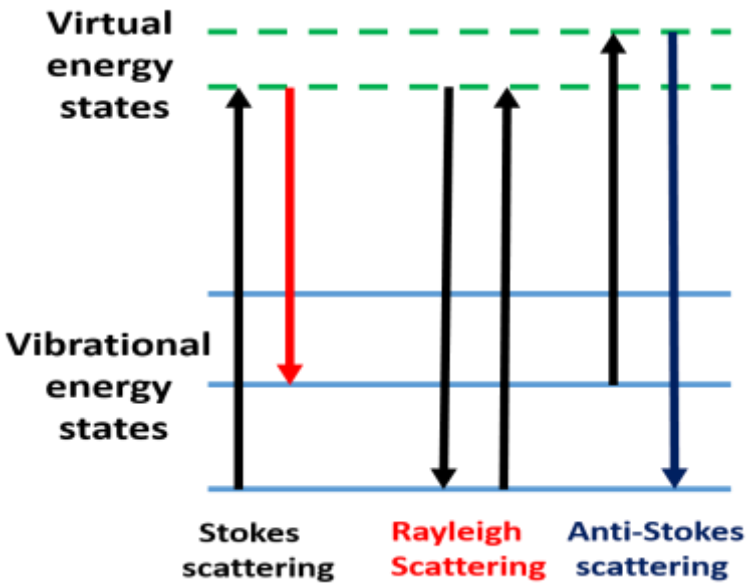

Figure 3.6. Diagram of energy levels showing the states involved in Raman spectra. In Stokes, a photon gives some energy to a system in the process of interaction. Because of this process, the system moves from a lower energy level to a higher energy level, and the energy of the scattered photon decreases. In anti-Stokes, because of interaction with an excited-state system, the photon energy increases and the system goes into a lower energy state. For comparison, in Rayleigh scattering (in the centre), there is no energy exchange between the photon and the system.[145]

For this project, Raman spectra were collected at room temperature using an XploRA confocal Raman microscope (Horiba Jobin Yvon, Inc.) coupled to an Olympus BX41 optical microscope. The spectrometer was equipped with a 532-nm, 25-mW solid-state laser. The spot size of the laser on the samples was approximately 1 μm. The experiment was repeated three times on each sample in order to obtain a good signal and confirm the expected phase. The laser power was kept sufficiently low in order to minimise any localised heating of the material.

3.2.3 Atomic Force Microscopy (AFM)

Atomic force microscopy (AFM) is a scanning probe technique used to obtain high resolution images of samples' surfaces. A silicon nitride tip attached to a cantilever is scanned across the surface. The cantilever is deflected due to van der Waals forces between the tip and the surface. The degree of deflection is measured by reflecting a laser off the back of the cantilever onto a two-dimensional photodetector, as shown in **Figure 3.7**. Afterwards, the control software translates the degree of deflection into topographic information. Samples are typically measured under standard ambient conditions. Imaging under a liquid medium or a high vacuum is also possible.[148,149]

The measurements can be performed under one of three operating modes: contact, non-contact and tapping. In contact mode, the tip is positioned close enough to the sample to experience repulsive forces, which deflect the cantilever. In the non-contact/tapping mode, the cantilever oscillates at its resonance frequency (kHz range). When the tip approaches the sample's surface, the amplitude and resonance frequency change significantly, acting to dampen the oscillation, and the feedback loop acts to maintain the resonance frequency by moving the tip up, therefore providing feedback to the scanner. The tapping mode may be advantageous, since it does less damage to both the surface and the tip.

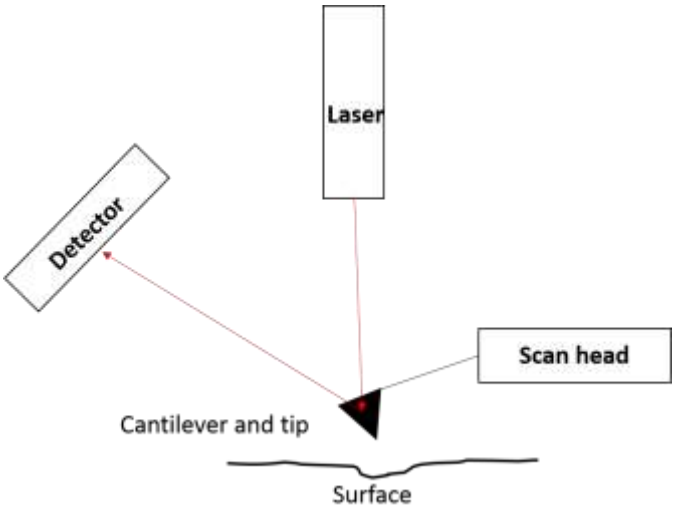

Figure 3.7. Diagram of the AFM measurement process: The tip interacts with the surface of the sample, and the laser beam reflects off the back of the cantilever at different angles, which can be detected by a two-dimensional position-sensitive photodiode.[150]

The AFM used in this project was a Keysight Technologies 5600LS Atomic Force Microscope. Measurements of thin-film thickness were carried out in tapping mode using a Nanosensors Point probe-Plus n-doped Si tip with a resonant frequency range of 146 kHz to 236 kHz. The topography at the edges of the thin-film samples was measured over a space of approximately 50 μm at a 0:5 lines/s scan rate and a resolution of 512 points/line. The proportional and integral gain parameters of the feedback loop had to be adjusted manually for each measurement point. Once the measurement was completed, a topography cross-section was obtained three times at each point using the AFM control software, and the height difference between the substrate and the top of the film was measured as shown in section 4.2. Once the thickness of the different edges of the sample was known, the values were imported into the Paradise software, where the thickness was interpolated at each intermediate point, for a 14 × 14 grid, assuming a linear change in thickness between points. The same procedure was applied for samples with a gradient of

thickness using a 10 × 10 grid. Surface topography scans on amorphous and crystalline samples were also performed in order to observe surface features at each strip of thickness on the films. These were done in tapping mode using the same probe type used for thickness measurements. Scans were carried out over a 5 × 5 μm area, at different points of the films, at a 0:5 lines/s scan rate and 512 points/line resolution.

3.2.4 X-ray Photoelectron Spectroscopy (XPS)

Electrons can be ejected from their bound state with kinetic energy E_{kE} by electromagnetic radiation, after which these electrons can be analysed, and the chemical and physical nature of the atom can be derived from their distribution and chemical shift. The ejection of these electrons by primary radiation sources with energy in the X-ray region of the electromagnetic spectrum is called X-ray photoelectron spectroscopy (XPS).[151] The fundamental processes occurring in XPS are described in **Figure 3.8** (a), where an X-ray of known excitation energy impinges on a sample at an angle θ, exciting electrons from core atomic levels which have kinetic energies given by (Equation 3.2):

$$Eke = h\nu - BE - ø \qquad \text{(Equation 3.2)}$$

Where hν is the energy of X-rays impinging on the surface, BE is the binding energy of the ejected electrons with respect to Fermi level (E_f), and ø is the work function of the sample.

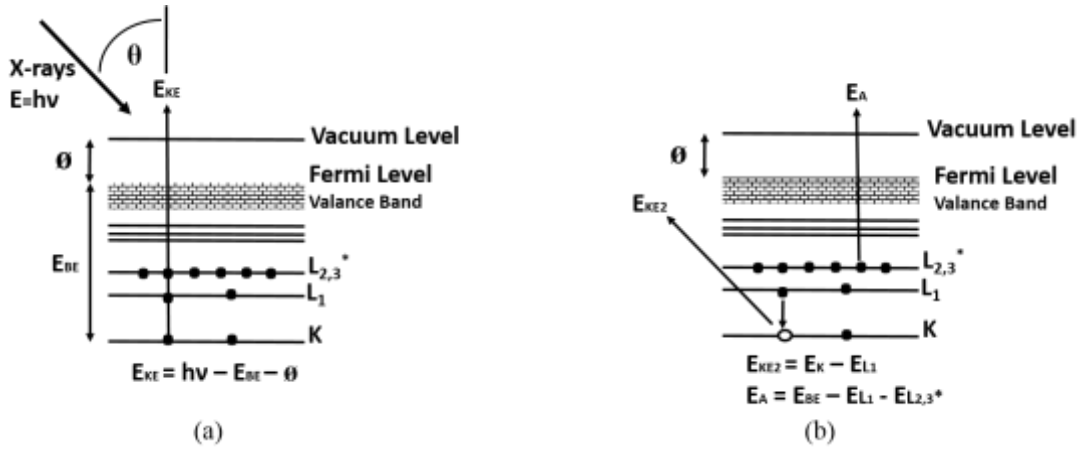

Figure 3.8. Energy level diagram showing the effect of X-ray radiation impinging at angle θ to the surface normal on core level electrons, (a) initial ejection of an electron from core level K, and (b) possible secondary process that can occur.[151]

As shown in **Figure 3.8** (b), the creation of a core level hole following the ejection of a core electron by X-ray radiation allows for the recombination of the hole by an Auger process. The hole in core level K is filled by an electron in lower level L_1, releasing energy $E_k - E_{L1}$. The electron presented in the $L_{2,3}^*$ shell can be ejected, providing $E_k - E_{L1} -$

$E^{*}_{L1,2,3}$ positive. Therefore, the XPS spectrum also contains peaks due to electrons ejected by Auger emissions.[151]

Due to relaxation and chemical shift effects, the exact position of the photoelectron peak might be different from that predicted by Equation (3.2) at which when a hole is created in an atom by photoemission (**Figure 3.8** b), the remaining electrons relax at lower energy to partially screen the hole.[152] Additionally, the energy of photoejected electrons is determined by the local electronic and chemical environment of an atom, there would be a difference in the environment of atoms of the same elements, which can be shown in different ways, such as differences in the oxidation state.[153]

In-situ XPS was used in this project to evaluate the stoichiometry of TiO_2 films for different phases of titania using a base pressure of 8.2×10^{-9} **torr**. The XPS measurements were performed on films with different thicknesses on a platinised silicon substrate. All data were collected on an area approximately 5 mm × 5 mm. The X-ray source was operated at a 10 mA emission current and an accelerating voltage of 10.5 kV. All spectra were corrected for any charge shift by aligning them to the C 1s core level at 285.0 eV.

3.2.5 Four-point Probe (4pp)

Resistivity (ρ) is an intrinsic property of semiconductor materials. The four-point probe is used to measure the sheet resistance of thin-film samples using the methods developed by Van der Pauw.[153] Once the thicknesses are known, it is possible to calculate the resistivity. Resistivity depends on the free electron and hole densities in n- and p-type conductors, respectively, and their mobility. The probe is made of four evenly spaced, spring loaded, conductive tips loaded onto a stage that permits contact between the tips and the sample's surface. When in contact, a current is passed through two adjacent probes, and the resulting voltage is measured across the two opposite probes, as shown in **Figure 3.9**. The conductivity type measurement (if not known) can be achieved by choosing the test needed, whether n-type or p-type. In n-type, the majority carrier are the electrons; while in the p-type, the majority carrier are the holes.[154] The sheet resistances can be calculated using the following Equation 3.3:

$$R_{Sh} = \rho/t \qquad \text{(Equation 3.3)}$$

Where R_{Sh} is sheet resistance, ρ is resistivity and t is the thickness of the sample studied.

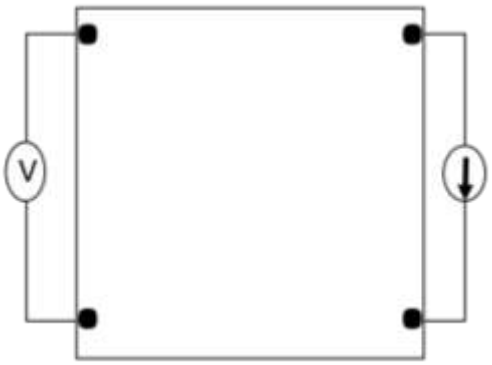

Figure 3.9. Resistivity measurement setup using the van der Pauw method on a square sample with a four point square probe.

In this project, since TiO_2 is known as an n-type material, the focus was only on n-type conductivity measurements. The sheet resistance was measured at room temperature using a Four Dimensions Inc. Model 280DI four-point probe. The probe had four tungsten carbide tips in a square arrangement, each with a diameter of 25 μm and 0.635-mm spacing. Prior to measurement, the tips were repeatedly cleaned by placing them on an alumina substrate. All samples were deposited on an insulating silicon nitride substrate, thus ensuring that conduction was a result of the thin-film conductivity. The instrument is equipped with a rotary translational stage, and its control software allows for the automated measurement of a defined matrix of points across the thin-film sample.

3.2.6 Energy-Dispersive X-ray Spectroscopy (EDS)

Energy-dispersive X-ray spectroscopy (EDS) is an analytical technique that provides elemental analysis or chemical information about materials. An EDS system is normally coupled with an electron microscope that can generate the excitation beam necessary to achieve the emission of X-rays from the sample.

Each element has a unique atomic structure, allowing X-rays that are characteristic of an element's atomic structure to be identified in a mutually unique order. The sample under study was characterised by an incident beam that can excite an electron in an inner shell and eject it from the shell, creating a vacancy that can be filled later by another electron from an outer (higher energy) shell. The difference in energy between the higher and lower energy shells may be released in the form of an X-ray. **Figure 3.10** illustrates the Rutherford-Bohr atomic model, which shows how an X-ray ejects an inner shell electron, leaving a vacancy that filled by an outer shell electron, and then releasing a photon. Since X-ray energy is characteristic of the difference in energy between adjacent shells and the atomic structure of the element from which it is emitted, the elemental

composition of the specimen can be measured. This technique is limited to elements above Be, at which needs to be carefully analysed the data, as several atoms have overlapping peaks at a particular energy.[155]

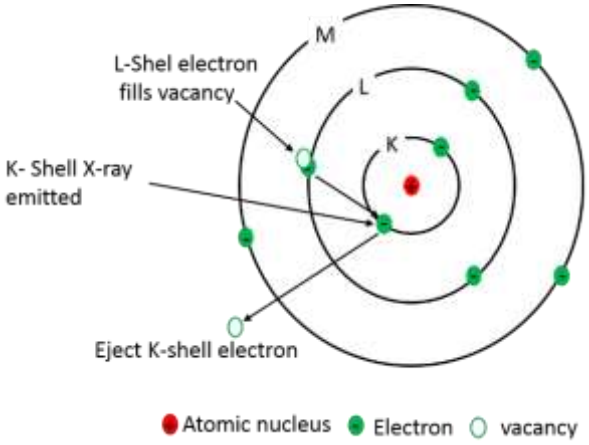

Figure 3.10. Emission of X-ray when outer L shell electron fills the K shell electron vacancy.[154]

For this project, all measurements were performed on a JEOL JSM-5910 scanning electron microscope, fitted with an Oxford Instruments x-act 51-ADD0006 EDS silicon drift detector. The Oxford Inca 300 EDS software was used for analysis. The composition of top electrode and oxide before and after the electrical test was achieved by means of EDS coupled with SEM. Samples that were tested electrically were introduced into the analysis chamber and placed under vacuum. The working distance of the measurement was 10 mm, with a magnification of 500x and accelerating voltage of 12V.

3.2.7 Electrical Test

The tests involved direct current (DC) measurements of current versus voltage (I-V). The measurement resource for parametric tests was the source/monitor unit (SMU). The SMU can force either voltage or current through the device under test (DUT) and simultaneously measure the corresponding parameter. The I-V sweeps used to determine $V_{\mathbf{Forming}}$ and switching voltage for the materials in this project were performed using a B1500A Semiconductor Device Analyser in corporation with probe station.

Parametric tests were performed on titania deposited on platinised silicon substrates. These substrates consisted of a series of layers on top of which a 100 nm-thick Pt layer was deposited. The layers consisted of Si, SiO_2, TiO_2 and Pt, hence the SSTOP shorthand used throughout this text. The conductive Pt layer functioned as a bottom contact onto which a probe was connected

Chapter 4: Characterisations of Materials and Composite Structures

In this chapter, the microstructural and chemical properties of different phases of TiO_2 with different thickness gradients are presented. X-ray diffraction and Raman spectroscopy were used to confirm the synthesis of the targeted phase; SEM and AFM were used to study the surface morphology; X-ray photoemission spectroscopy as well as a four-point probe were used for chemical analysis and stoichiometry of TiO_2. A probe station was used for electrical testing to assess the different behaviours of the different layer structures electrically.

4.1 Microstructure Characteristics

X-ray diffraction (XRD) analysis was performed after synthesis of the samples and after annealing to identify the crystalline property of materials using thin-film X-ray powder diffractometer measurements (Rigaku smart lab 9KW SN JD3604N). **Figure 4.1** shows the deposited titania film on the SSTOP substrate at a 5-sccm oxygen flow rate, a plasma source of P*rf* = 400 W and a deposition rate of 4 Å/s. It was noticed that the titania was in the amorphous phase. Two methods were followed to synthesise crystalline samples. First, for thicker samples (150 nm–300 nm), the sample (**Figure 4.2**) was deposited at room temperature, followed by annealing for one hour at 450 °C under an oxygen atmosphere in a tube furnace to obtain anatase phase. The other sample (**Figure 4.3**) was prepared by deposition at a substrate temperature of 600 $^{\circ}$C, followed by annealing for one hour at 600 °C under an oxygen atmosphere in a tube furnace to obtain rutile phase. Second, thinner TiO_2 samples (10–60 nm) were annealed after deposition inside the chamber for one hour at 200 $^{\circ}$C under a flow rate of 1 sccm of oxygen to produce an anatase structure. Alternatively, the rutile was annealed at 1100 °C in a tube furnace for two hours under an oxygen atmosphere.

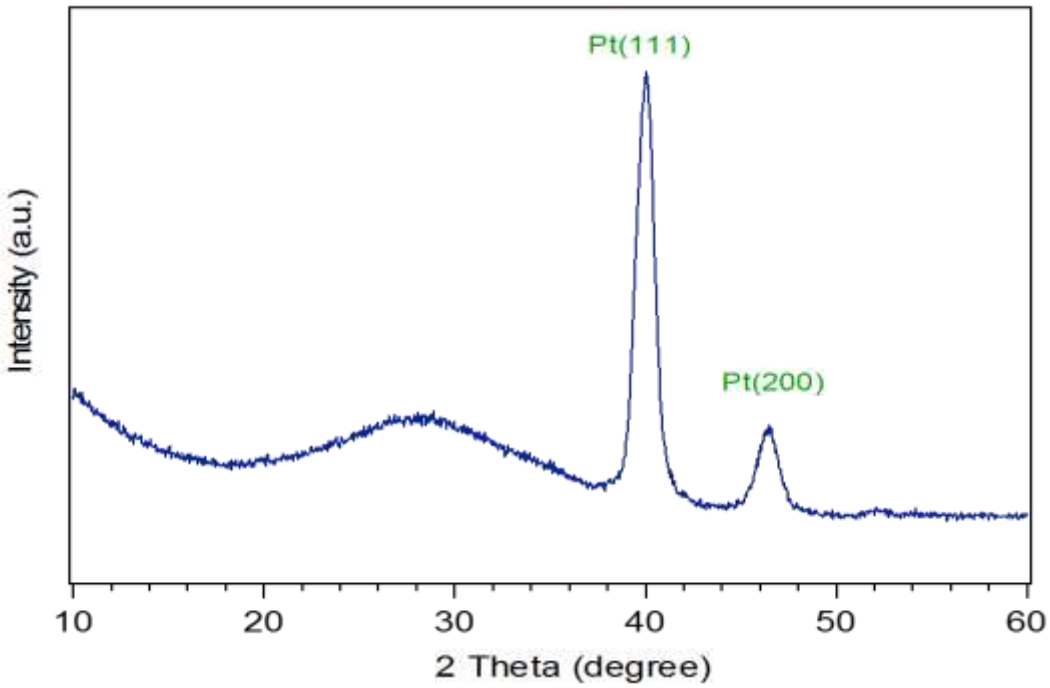

Figure 4.1. XRD on as deposited film of TiO_2. Peaks at 40° and 46° from the Pt substrate only.

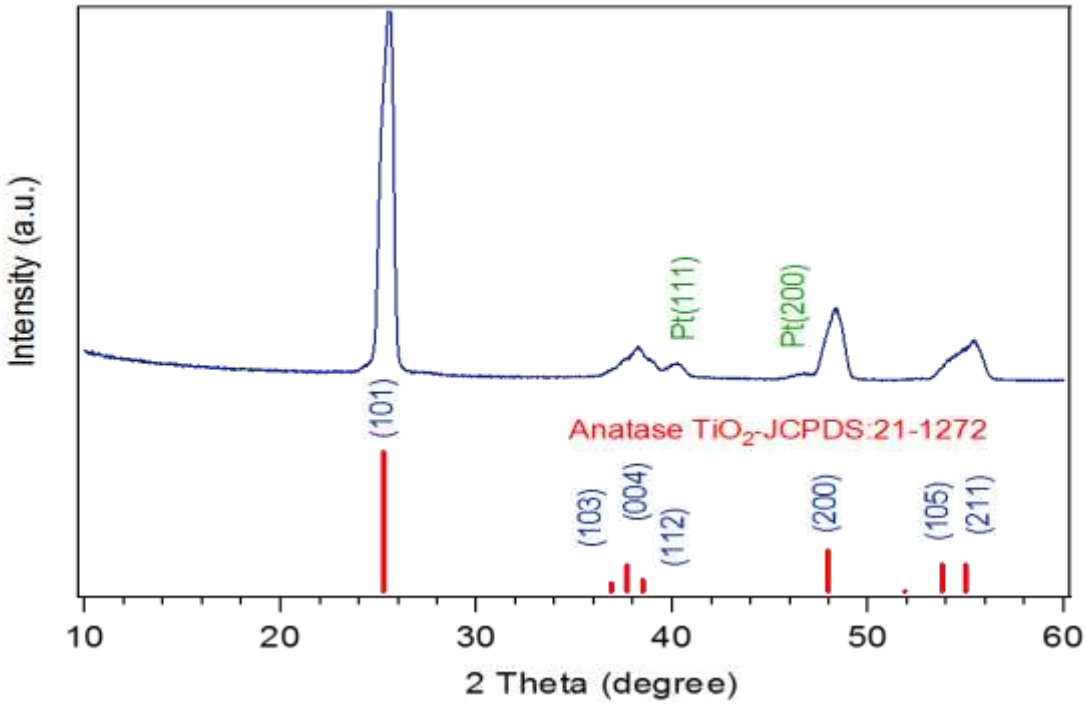

Figure 4.2. XRD patterns of TiO_2 annealed at 450℃. TiO_2 anatase and Pt peaks are visible.

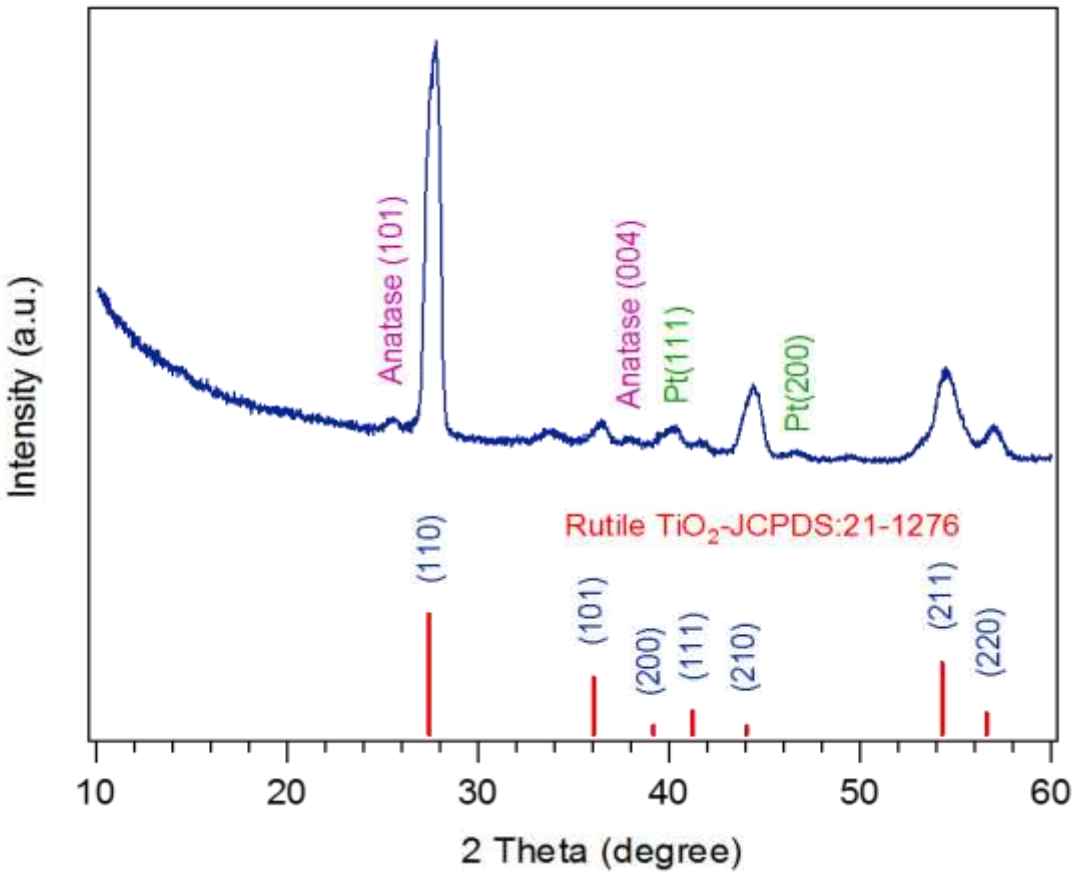

Figure 4.3. XRD patterns of TiO_2 deposited at 600℃ using an atomic oxygen plasma source. TiO_2 rutile and Pt peaks are visible

All diffraction peaks were identified. **Figure 4.2** shows the XRD characterisation of anatase sample #8008. The diffraction pattern corresponds to anatase TiO_2. Two peaks on the SSTOP substrate corresponding to Pt can be observed (at 40° and 46°). The patterns were compared to the Pdf card and were in good agreement. Sample #8025 represents the XRD characterisation of rutile TiO_2 as shown in **Figure 4.3**. The XRD pattern clearly exhibits rutile peaks with additional small peaks of anatase as compared to the reference card.

XRD data were also collected for gradient film thickness (10–60 nm) for the TiO_2 anatase phase on the SSTOP substrate. The XRD measurements were taken in each individual strip of thickness. It is clear that the peaks at 40° and 46° correspond to Pt peaks (substrate) as comparison with as deposited sample in **Figure 4.1,** which shows a very broad diffraction pattern of TiO_2 confirming that the sample is very amorphous anatase. **Figure 4.4,** on the other hand, shows several peaks that confirm the samples are clearly anatase (no rutile peaks); these peaks are at 25°, 38°, 48° and 56°, at 50 nm of thickness. The remaining diffraction patterns are shown in Appendix A. The intensity of TiO_2 peaks

decrease with decreasing thickness of TiO_2: On a 10-nm thin film, it is hard to see the TiO_2 diffraction peaks.

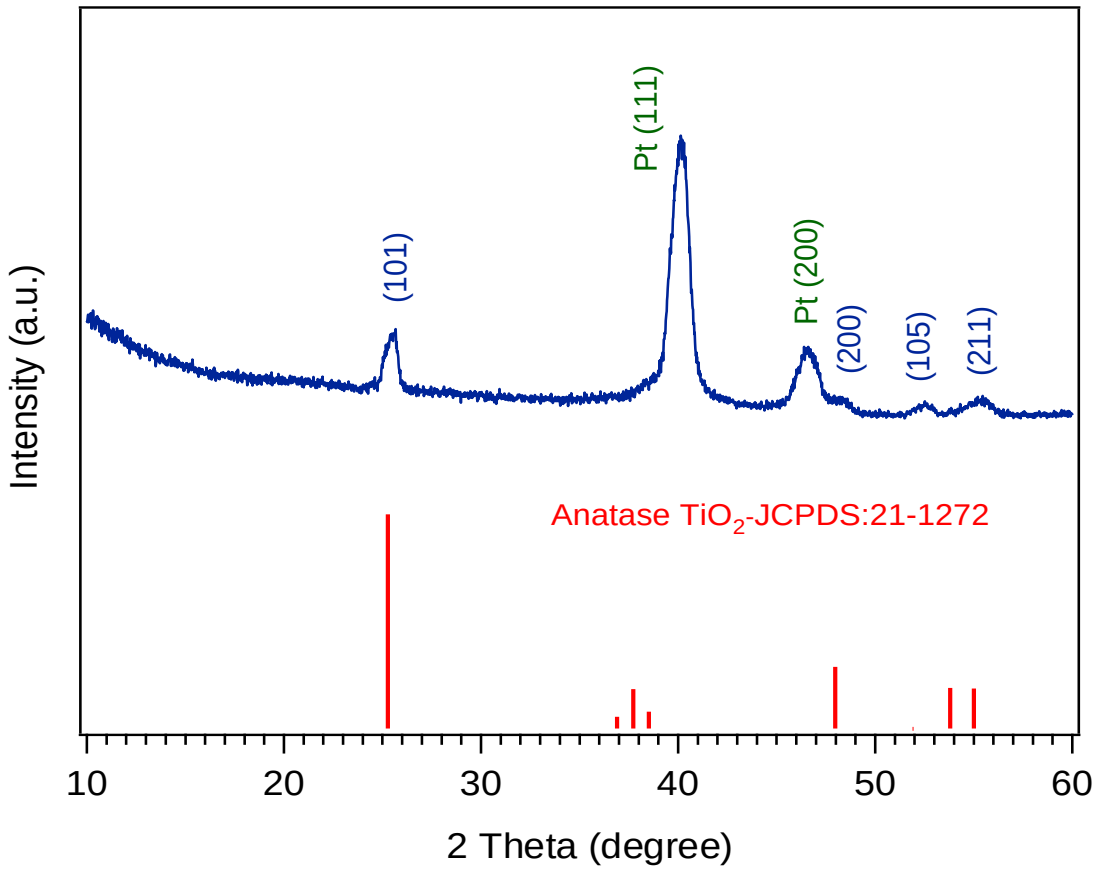

Figure 4.4. XRD data of anatase TiO_2 film with thickness 50 nm.

Furthermore, Raman scattering was used to confirm the synthesised TiO_2 phases and, more specifically, for structure identification of annealed samples with an average sample thickness of 270 nm. **Figure 4.6** shows the Raman spectrum of different phases of amorphous, anatase and rutile TiO_2. In the case of anatase, which has a space group symmetry of D^{19}_{4h} ($I_{41/amd}$), the only vibration mode that predicted to be oxygen pure in anatase is A_{1g} whereas, B_{1g} mode is pure Ti- atom vibration and the remaining vibration are mixture of both O atoms and Ti atoms motions. The symmetric bending vibration O-Ti-O is associated with the E_g and B_{1g} modes. The A_{1g} mode is associated with the anti-symmetric bending vibration of O-Ti-O.[147] In the case of rutile, which has a space group symmetry of D^{14}_{4h} ($P_{42/mnm}$), all Raman modes are purely oxygen-atom vibration (Ti-atom not moving). The symmetric bending vibration of O-Ti-O is associated with the B_{1g} and E_g modes, while the A_{1g} mode is associated with the symmetric stretching vibration. In the case of these crystalline structures, each is associated with the corresponding phonon mode of the long-range ordered structure. In the case of the amorphous materials, any vibrational

mode will be more localised since there is no long-range order. These modes in the amorphous structure appear to be very weak.[155] The displacement of each atom for the Raman-active vibration of rutile/anatase was reported.[146] These Raman-active modes (**Figure 4.5**) comprised motions of O^{2-} anions with respect to stationary central Ti^{4+} cations, either perpendicular to the c axis or along the c axis.[147] the arrows shows the actual displacement of the corresponding atoms.

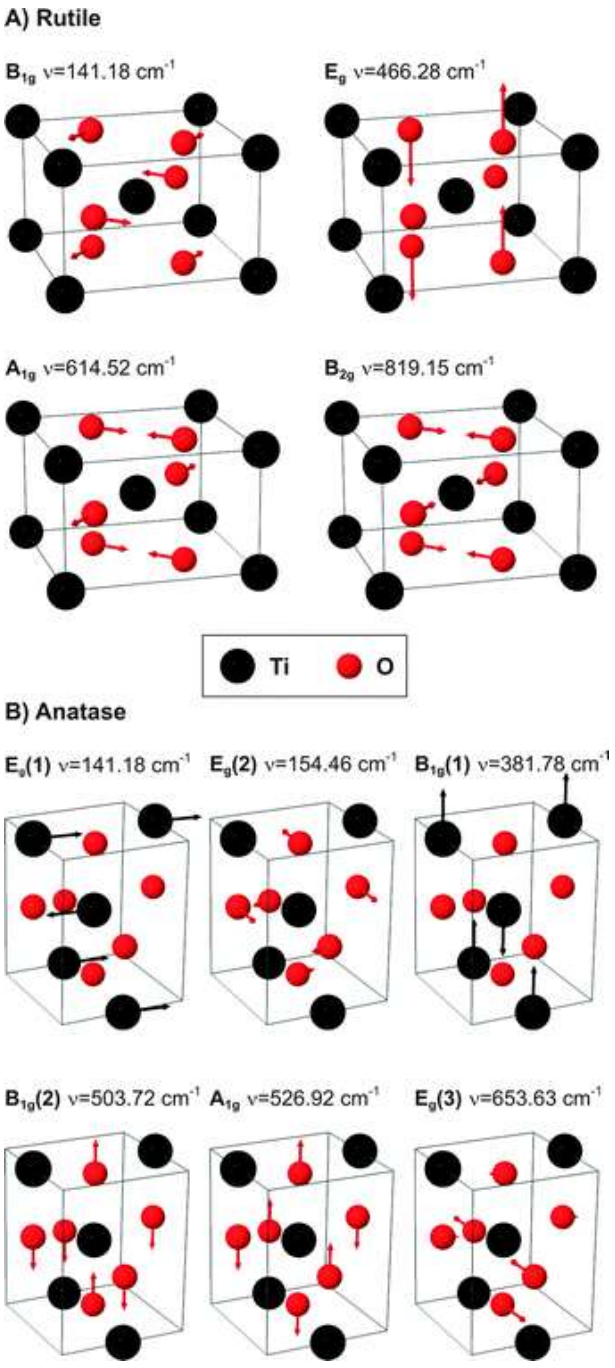

Figure 4.5. Illustration of the displacement of each atom for the Raman-active lattice vibrations in rutile/anatase TiO_2. black balls denote the titanium atoms, and red balls denote the oxygen atoms.[146]

The anatase and rutile structures can be confirmed through the allocation of the peaks in the Raman spectra (**Figure 4.6**). The anatase phase has five Raman-active "lattice vibration" assigned as follows: a peak with a strong signal appears at 162 cm^{-1} (E_g), followed by low intensity peaks at 210 cm^{-1} (E_g), 414 cm^{-1} (B_{1g}), 533 cm^{-1} (A_{1g}+B_{1g}) and 657 cm^{-1} (E_g). The rutile phase has three Raman active "lattice vibration" assigned as follows: a peak at 162 cm^{-1} (B_{1g}), 445 cm^{-1} (E_g) and 632 cm^{-1} (A_{1g}). In anatase TiO_2, E_g was the most intense vibrational mode, and B_{1g} was the weakest. In rutile TiO_2, E_g and A_{1g} were the most intense vibrational modes, and B_{1g} was the weakest. These findings are in general agreement with the literature.[156,157,158] A similar procedure was applied to thinner devices (average thickness of 50 nm) using Raman spectroscopy, yielding additional evidence that the expected phases were successfully synthesised (see Appendix A**)**. Detailing the peak position and the assignment of the peaks is also shown in Appendix B.

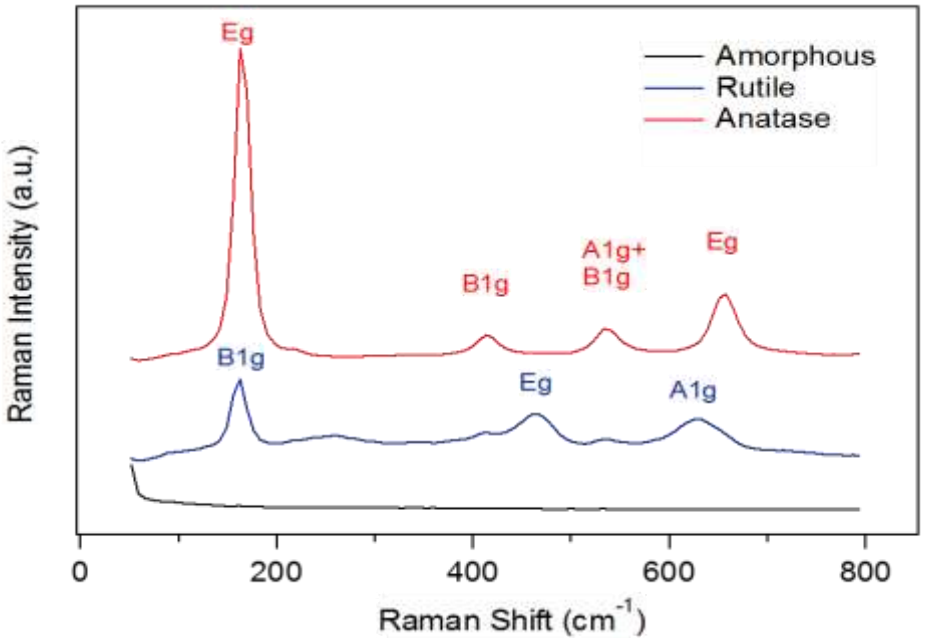

Figure 4.6. Raman spectra of three TiO_2 phases with average thickness of (270 nm) being synthesis using HT-PVD.

The microstructure of the switching device can significantly affect the performance of resistive switching memory. Defects in crystalline materials tend to accumulate around the grain boundaries and dislocation.[159] External or intrinsic defects, such as active electrode ions, can easily bond to these structures. In amorphous, for example, the oxide films at which the extensive oxygen vacancies or the injected foreign active electrode ions were homogenously distributed, and the position of the formation of filaments was random, as was the growth direction. As a result, according to the literature, [160] the shape of the filaments (in amorphous) is always like a tree with many branches. Crystalline films

seem to exhibit better performance and stability. It was found that with an increase of crystallinity – decreased density of grain boundaries – the switching voltages become low.[161]

4.2 Atomic Force Microscopy

Atomic force microscopy (AFM) was taken for different phases of TiO_2. As expected, the surface morphology changed with increasing temperature, as shown in **Figure 4.7** (Frequency scans and AFM for other systems are shown in Appendix A). It was observed that the amorphous phase (**Figure 4.7 A)** was flatter than the rutile phase (**Figure 4.7 C)**. Furthermore, the thickness of TiO_2 films, which affects the colour of the growing film, is shown in **Figure 4.8.**

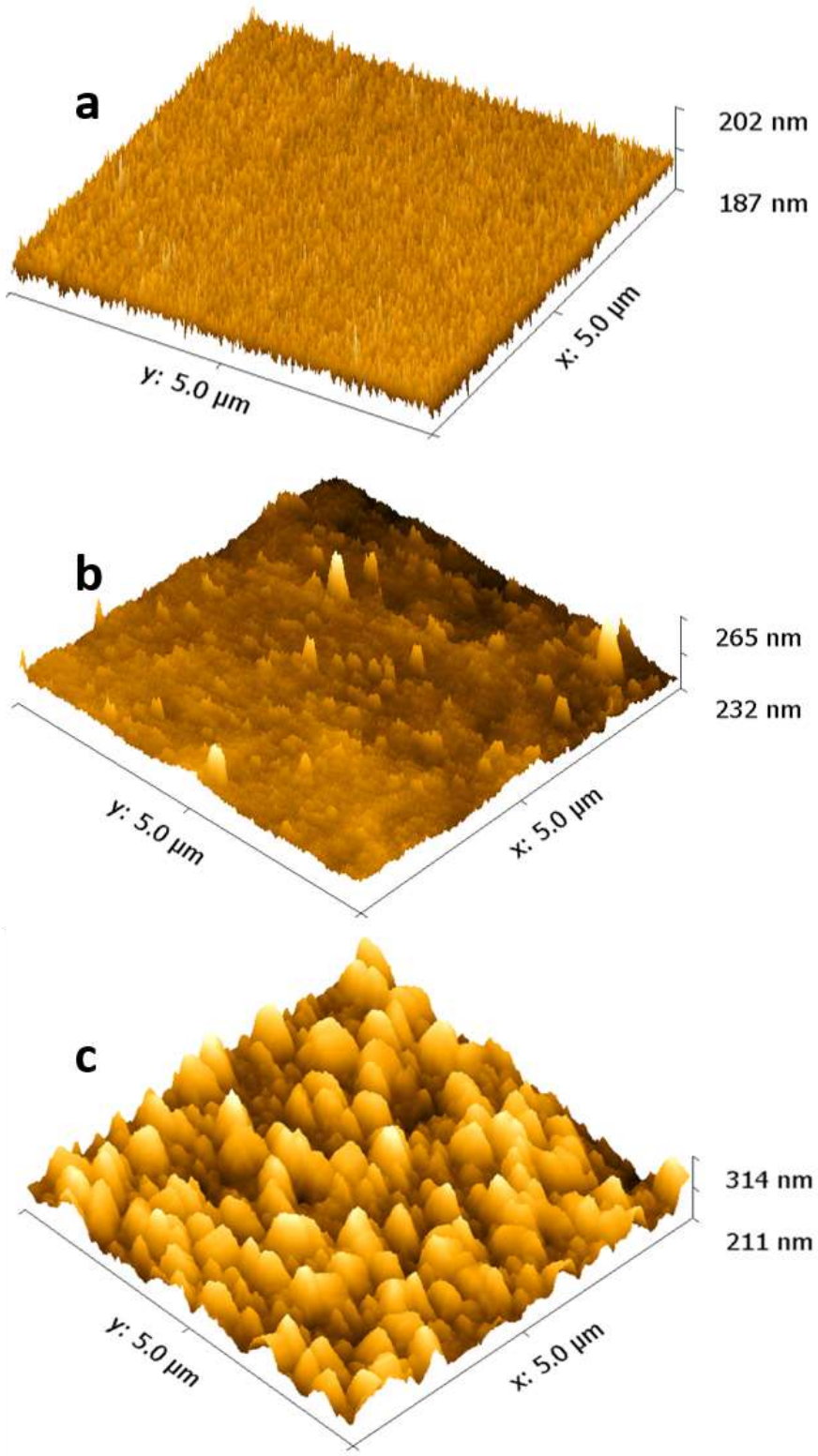

Figure 4.7. AFM topography of three phases of TiO_2 (a), (b) and (c) belong to amorphous, anatase and rutile, respectively.

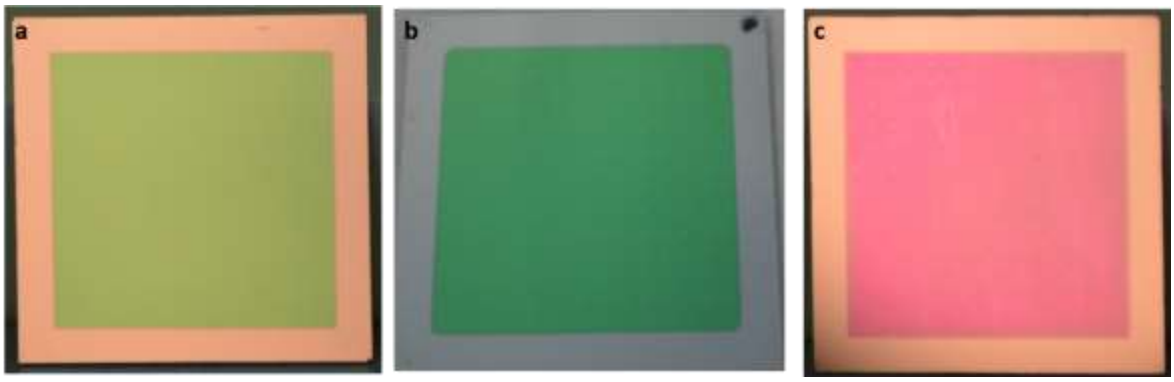

Figure 4.8. Thin film samples across different phases of TiO_2. (A): amorphous phase, (B) anatase phase and (C) rutile phase.

4.3 Chemical Characteristics

In-situ XPS was used to evaluate the stoichiometry of TiO_2 films for different phases of titania using a base pressure of 8.2×10^{-9} **torr**. The XPS measurements were performed on films with different thicknesses on a platinised silicon substrate. All data were collected on an area approximately 5 mm × 5 mm. The X-ray source was operated at a 10-mA emission current and an accelerating voltage of 10.5 kV. All spectra were corrected for any charge shift by aligning them to the C 1s core level at 285.0 eV. By fitting the obtained spectrum with Ti 2p spectra of different Ti valence states, it was found that only a valence state of Ti^{4+} could be detected at a binding energy of 464 eV (2p1/2) and 458 eV (2p3/2). An O 1s spectrum was shown at a binding energy of 530 eV, corresponding to the lattice oxygen. Amorphous TiO_2 prepared using a plasma atom source exhibited the expected stoichiometry (**Figure 4.9** and **4.10**). However, other phases are shown in Appendix A (anatase and rutile). The sub-stoichiometric titania was the main target for the growth of composite structures at which amorphous sub-stoichiometric titania obtained using molecular oxygen (**Figure 4.11** and **4.12**), and the rest of the sub-stoichiometric spectra are shown in Appendix A. All spectra were charge-corrected to the C 1s peak that resulted in a shift of the same magnitude in Ti 2p3/2, Ti 2p1/2 and O 1s.

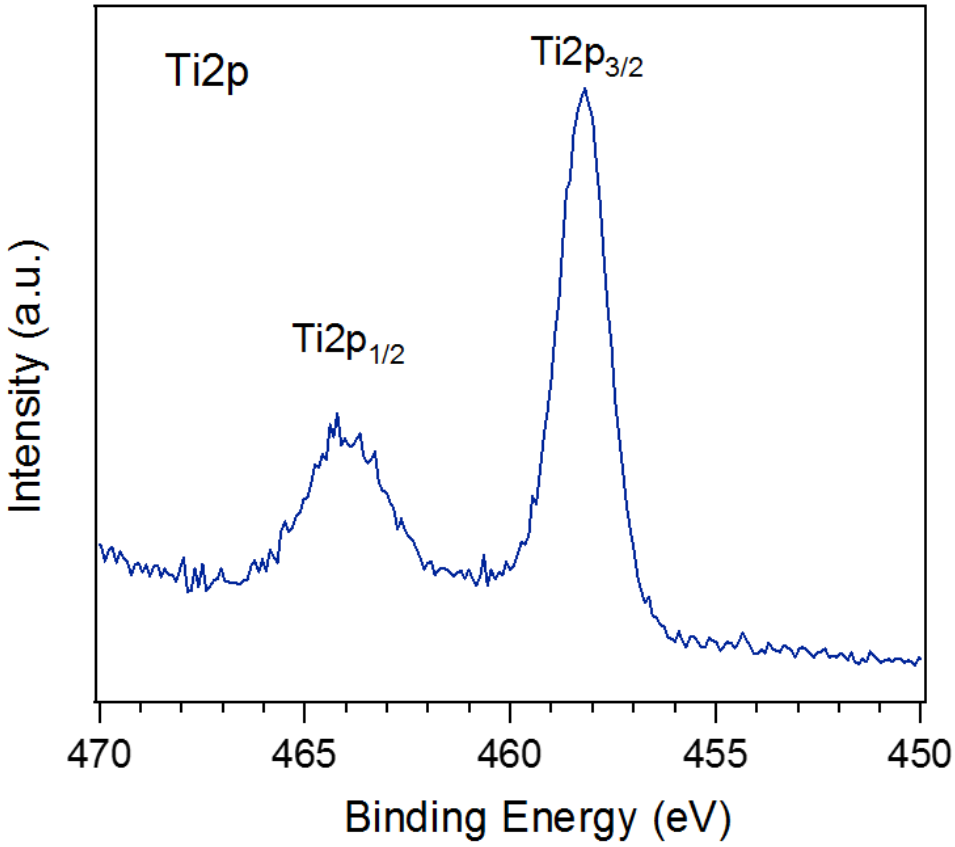

Figure 4.9. XPS spectra for thinner stoichiometric amorphous (50nm) Ti 2p.

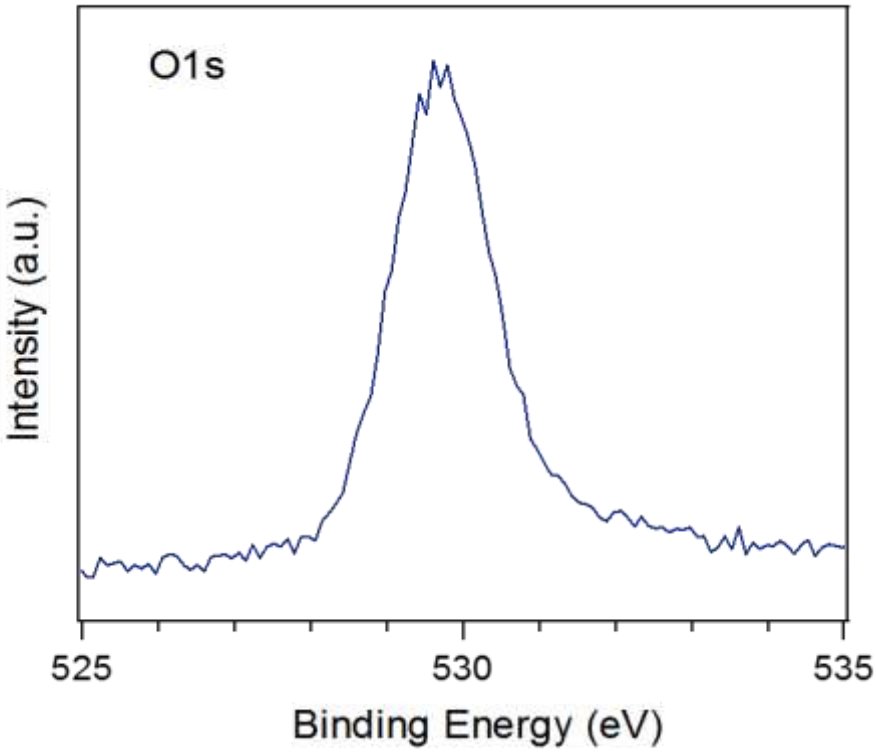

Figure 4.10. XPS spectra for thinner stoichiometric amorphous titania O 1s.

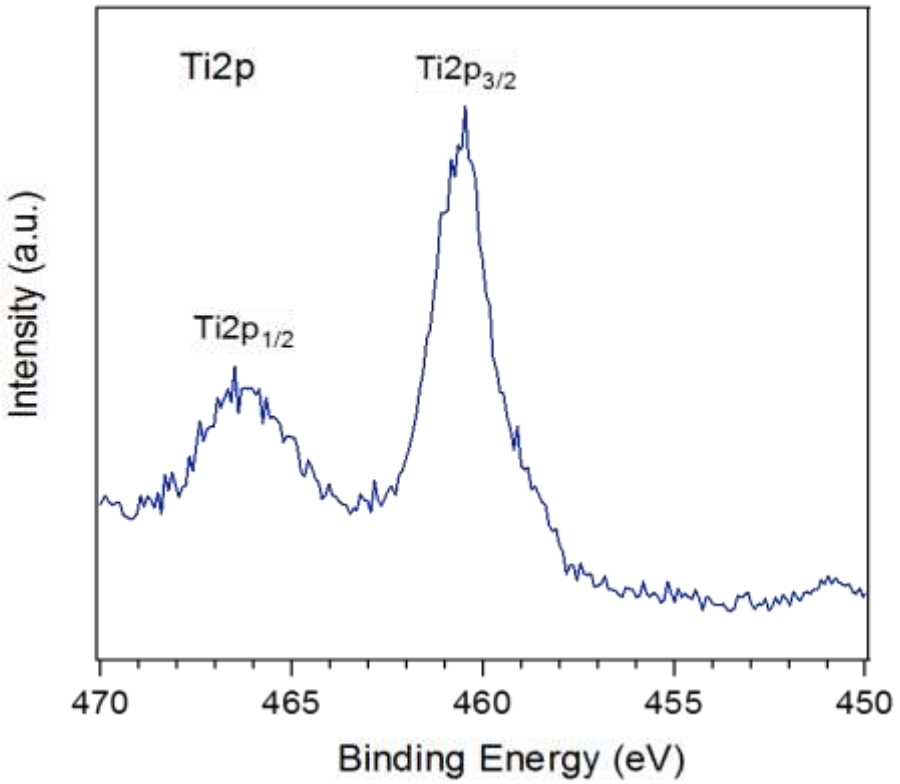

Figure 4.11. XPS spectra for thinner sub-stoichiometric amorphous (50nm) Ti 2p.

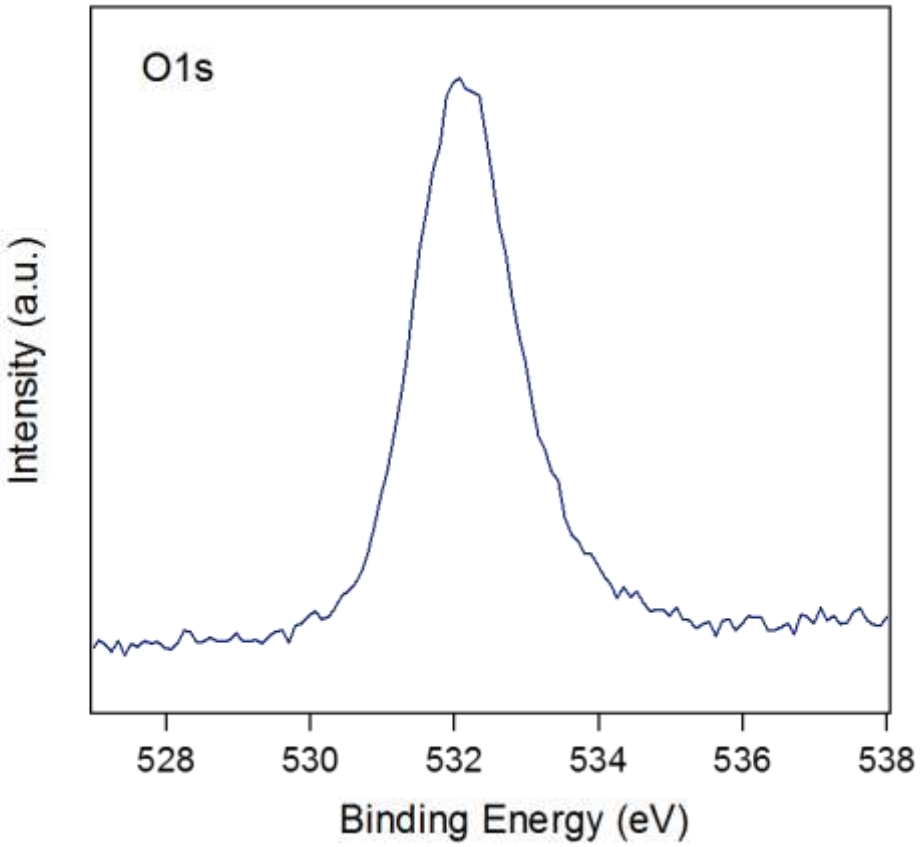

Figure 4.12. XPS spectra for thinner sub-stoichiometric amorphous titania O 1s

For the TiO_{2-x}, the value of x was calculated from the XPS data by calculating the ratio of Ti^{3+} to Ti^{4+} using Equation 4.1 as shown in **Table 4.1.** The analysis of these data is shown in Appendix A.

$$\frac{A}{A+B} \times 100 = \text{Ratio } \%$$

(Equation 4.1)

Where A is the peak area of Ti $^{3+}$ and B is the peak area of Ti^{4+}.

Table 4.1. Calculation of the Ratio Ti^{+3} to Ti^{+4} (from XPS data)

Number of measurement	Peak area (Ti^{+3})	Peak area (Ti^{+4})	Ratio in percentage %	TiO_{2-x}
1	114	716	14	$TiO_{1.93}$
2	222	833	20	$TiO_{1.90}$
3	82	338	20	$TiO_{1.90}$
4	248	684	26	$TiO_{1.87}$

In addition to XPS, 4pp was employed for comparison between stoichiometric and sub-stoichiometric titania and to illustrate the resistivity of titania structures synthesised in this investigation. Two structures were prepared with and without a plasma atom source. **Figure 4.13** shows sub-stoichiometric TiO_2. It is clear that the resistivity varied across the sample. The resistivity of stoichiometric TiO_2, exceeded the limit of 4pp (25,000 Ω) and could not be displayed.

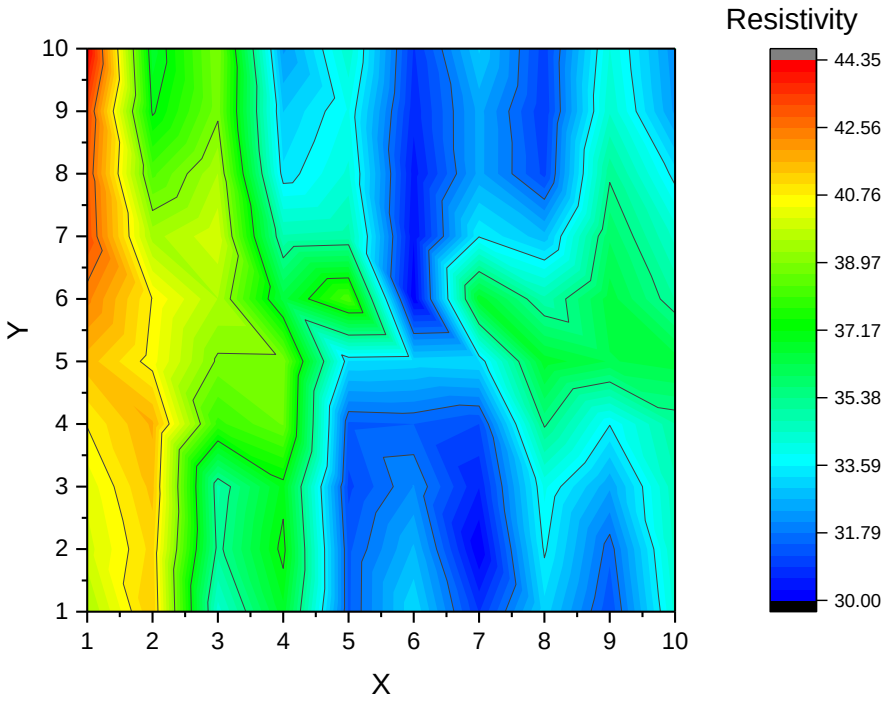

Figure 4.13. Resistivity of sub-stoichiometric TiO_2. (Resistivity of stoichiometric TiO_2 could not be plotted as it is over scale of 4pp).

4.4 Thickness Characterisation

AFM was employed for thickness measurements using a tapping mode with an Si tip at a resonant frequency range of 146 kHz to 236 kHz. Thicknesses were calibrated by measuring the height between substrate and film, as shown in **Figure 4.14.** Calibration of thicker and thinner film is shown in **Figure 4.15** and **Figure 4.16,** respectively.

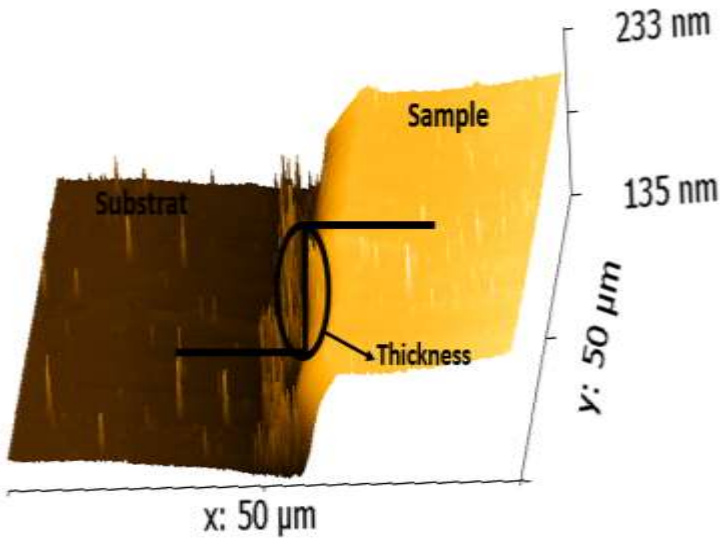

Figure 4.14. AFM topography shown the thickness calibration process.

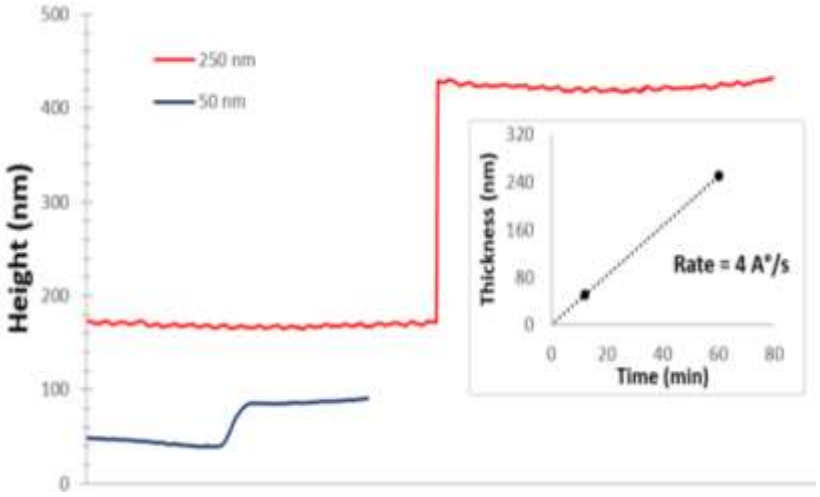

Figure 4.15. Thickness calibration of thicker Titania films. Data taken from AFM by measuring the height of sample and substrate. Subfigure represent the relationship between time and thickness for the presented data.

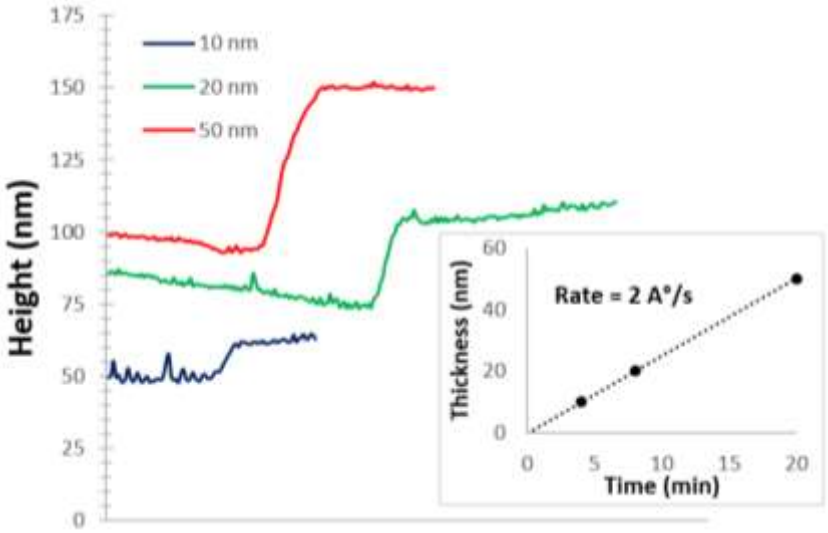

Figure 4.16. Thickness calibration of thinner Titania films. Data taken from AFM by measuring the height of sample and substrate. Subfigure represent the relationship between time and thickness for the presented data.

Figure 4.17 shows the AFM data on each corner of the sample of the continuous film, which were then modified to cover the whole region of the sample. The gradient of thickness for amorphous titania is shown in **Figure 4.18**. Other phase measurements and maps of thickness for all phases, which were evaluated using Paradise software (in-house software), are shown in the appendix A.

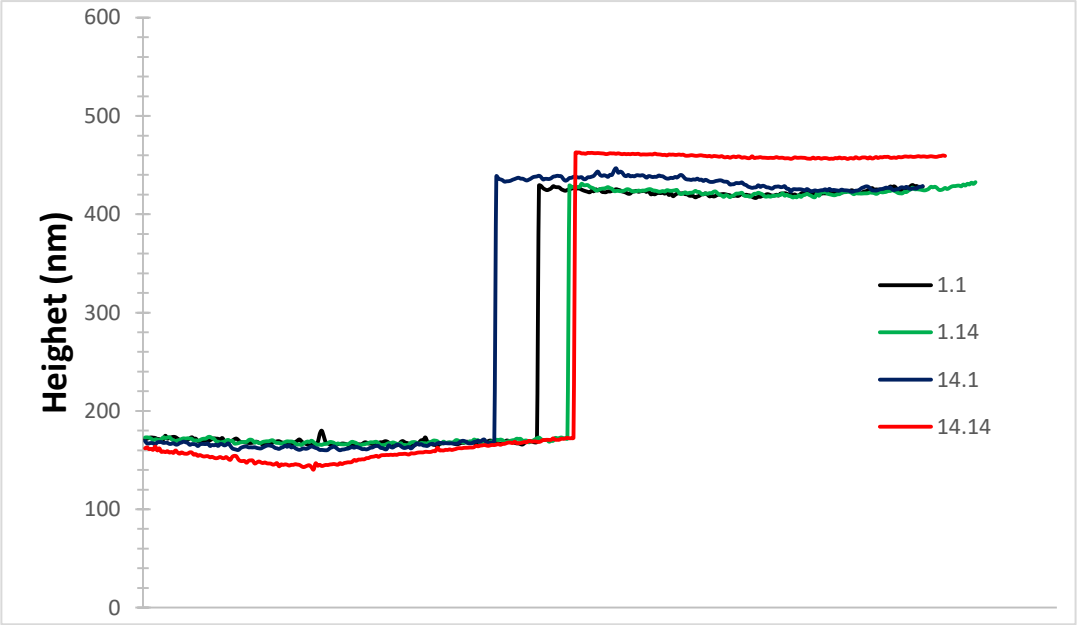

Figure 4.17. Multiple measurement on sample edges for thicker TiO_2 films. Data taken from AFM.

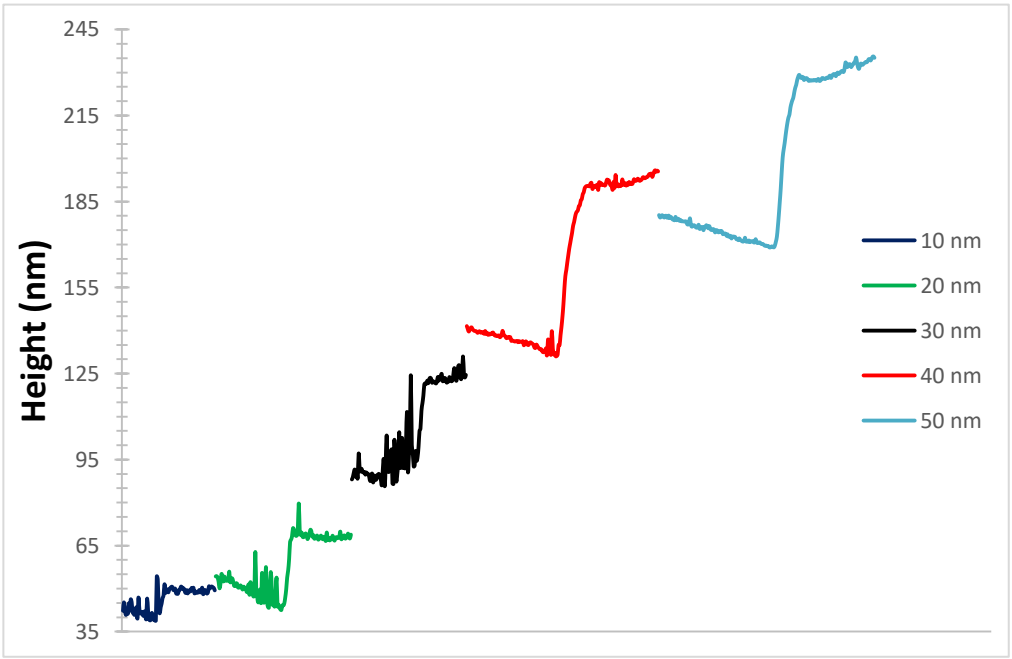

Figure 4.18. Distribution of gradient of thickness for thinner TiO_2 films.

Chapter 5: Results

This chapter focuses on specific electrical results obtained throughout the project. The aim was to investigate trends and structure properties of titania as a function of thickness, phases, top electrode and structure modification to understand the key materials properties effecting the switching behaviour of ReRAM devices. Three titania-based systems were divided into three sections: the first section described the I-V characteristics, and the second section described switching as a function of polarity. Finally, high-throughput screening of all systems was investigated.

5.1 I-V Characteristics of Titania across Different Electrode and Structure.

5.1.1 I-V Characteristics of the Pt/ TiO_2/ Pt Device

Pt/TiO_2/Pt structures of three phases (amorphous, anatase and rutile) were swept with a positive/negative voltage on the top electrodes, while the bottom electrodes were grounded, and then swept back to zero. At the beginning, all devices were swept to a high voltage (E > 3.5 V), as it was believed that the step required higher voltage for the 'forming process',[38,162,62] and then the subsequent voltage was decreased. The sweep rate was constant in all measurements, presented here at 50 mV/s. The diameter of the circular-shaped top electrode (TE) was 250 μm. The thickness of all devices presented in this section was 50 nm. The unipolar switching behaviour took place regardless of the polarity of the applied voltage, meaning that SET and RESET processes can be achieved under both positive and negative voltage, whereas bipolar behaviour was found to depend on the voltage polarity.

The devices were swept to positive voltage and then swept back to zero. The IC in all forming measurements was constant (1 mA). It is worth noting that in every measurement, read voltage was applied in the initial state (**Figure 5.1 B**); then, the voltage was increased slowly until the device switched state: Since this took place at different voltages, the maximum voltage of the sweep varied. For amorphous titania, the voltage was swept to 6 V and there was an increase in the current at 5.1 V, with a sudden jump in current observed at around 5.45 V, at which point the device formed (**Figure 5.1 A**): A conductive path was created between the top and bottom electrode through the oxide, and the device remained in the conductive state (ON) as the voltage was swept back to zero.

The read voltage after this forming was obtained (**Figure 5.1 C**). After forming the device (LRS), the IC value was set higher (double) than that for the forming process, and the voltage swept with the same polarity: A RESET process took place at 0.75 V (**Figure 5.2 A**), where the conductive path was apparently disconnected, and the device returned to the HRS (OFF). The voltage was swept again with the same polarity using the same IC of the forming step (1 mA), at which the device switch at 1.4 V from the HRS to the LRS (**Figure 5.2 B**) (this is a lower voltage than that required in the forming process), where the conductive path reconnected.

5.1.1.1 Pt/ amorphous TiO_2/ Pt

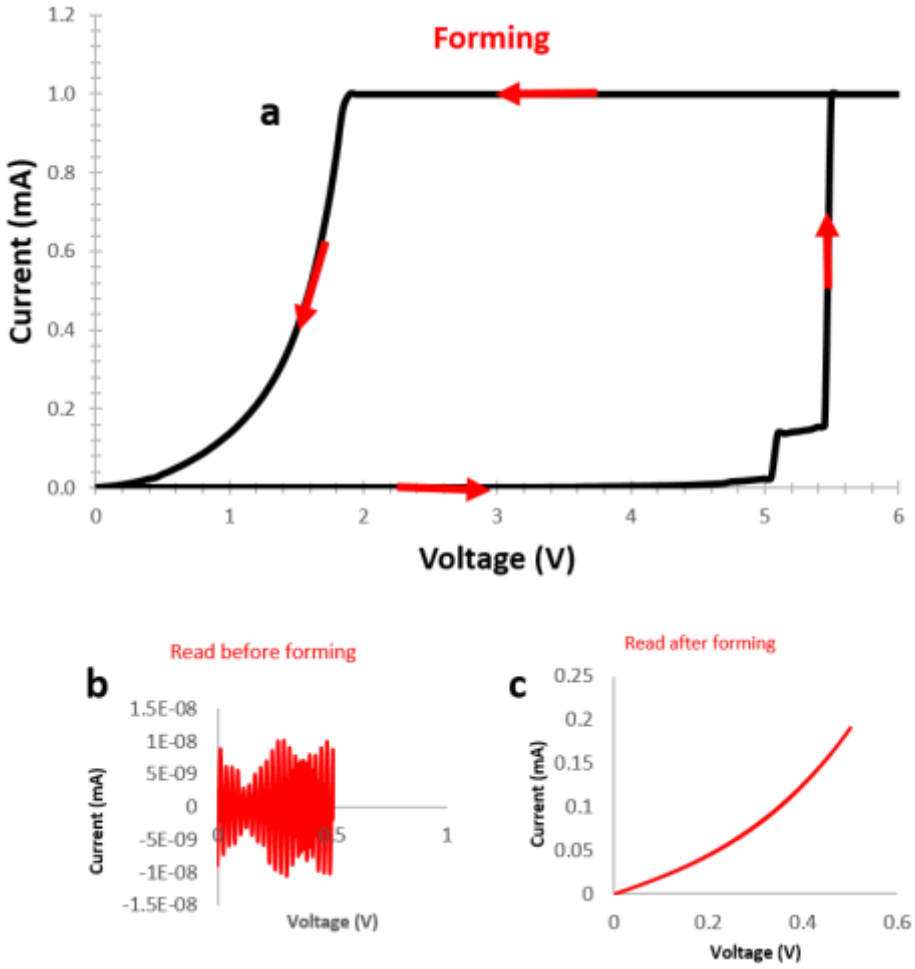

Figure 5.1. Forming process of amorphous titania. Initial state (as-prepared sample), and (B) read before forming, (C) read after forming. (Thickness 50nm).

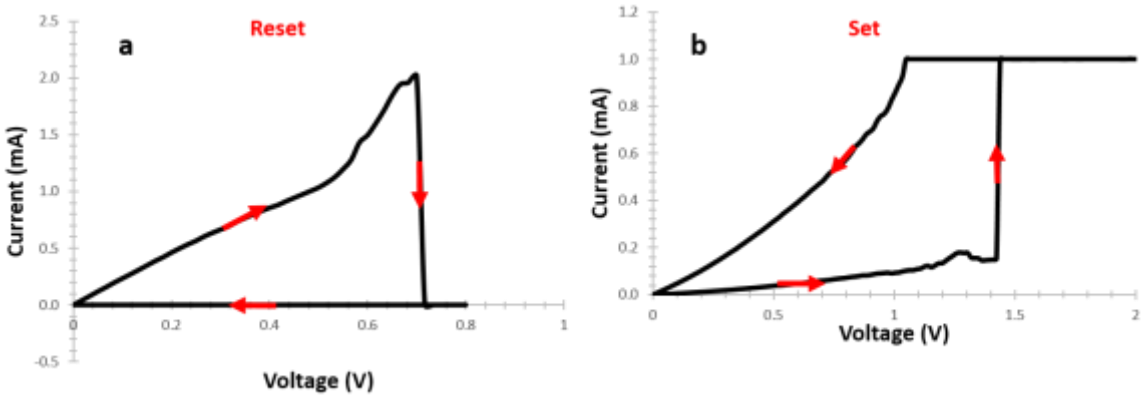

Figure 5.2. I-V sweeps of unipolar resistive switching behaviour of amorphous titania. (A) reset process and (B) set process. (Thickness 50nm).

The same test strategy was followed for crystalline titania (both anatase and rutile phases). For anatase, the voltage was swept in a positive direction at which the device had high resistance. However, at 5.2 V, there was a gradual increase of the current, and conductivity increased until 7.1 V, where a sudden jump of current was observed and the device was formed, as shown in **Figure 5.3 A**. The device switched from irreversible state IRS (HRS) to LRS. Read voltages were taken before and after the FS, as displayed in **Figure 5.3 B** and **5.3 C**. After setting IC to a higher target than the forming process (8 mA), the voltage was swept to 1.5 V, where it switched to 1.3 V from LRS to HRS (reset process), at which point the conductive path was broken (**Figure 5.4 A**). The voltage was swept again in order to set the device from HRS to LRS on the same polarity where the switching took place at 3.4 V, as shown in **Figure 5.4 B**. Rutile titania was formed at 9.4 V (**Figure 5.5 A**), at which point it was in a very high resistance state, as shown in read voltage before forming (**Figure 5.5 B**) at an IC of 1 mA. Read voltage after forming is displayed in **Figure 5.5 C**. In order to reset the device and disconnect the conductive path, the voltage was applied to 2 V with a higher IC compared to the forming process (7.5 mA), and the device switched at 1.4 V, at which point the device returned from LRS to HRS (RESET) as shown in **Figure 5.6 A**. The voltage was swept again in positive 6 V, at which point the conductivity increased gradually from 1.5 V until 5.4 V, where the device switched from HRS to LRS (SET) as shown in **Figure 5.6 B**. The time dependence of voltage sequences applied to the amorphous phase was obtained and is displayed in **Figure 5.7**. The time dependence of crystalline titania was obtained and is displayed in Appendix A for crystalline devices, respectively. Reversible switching sequences for all titania phases (IRS, initial resistance state; LRS, low resistance state; HRS, high resistance state) were obtained and are displayed in **Figure 5.8**.

5.1.1.2 Pt/ anatase TiO_2/ Pt

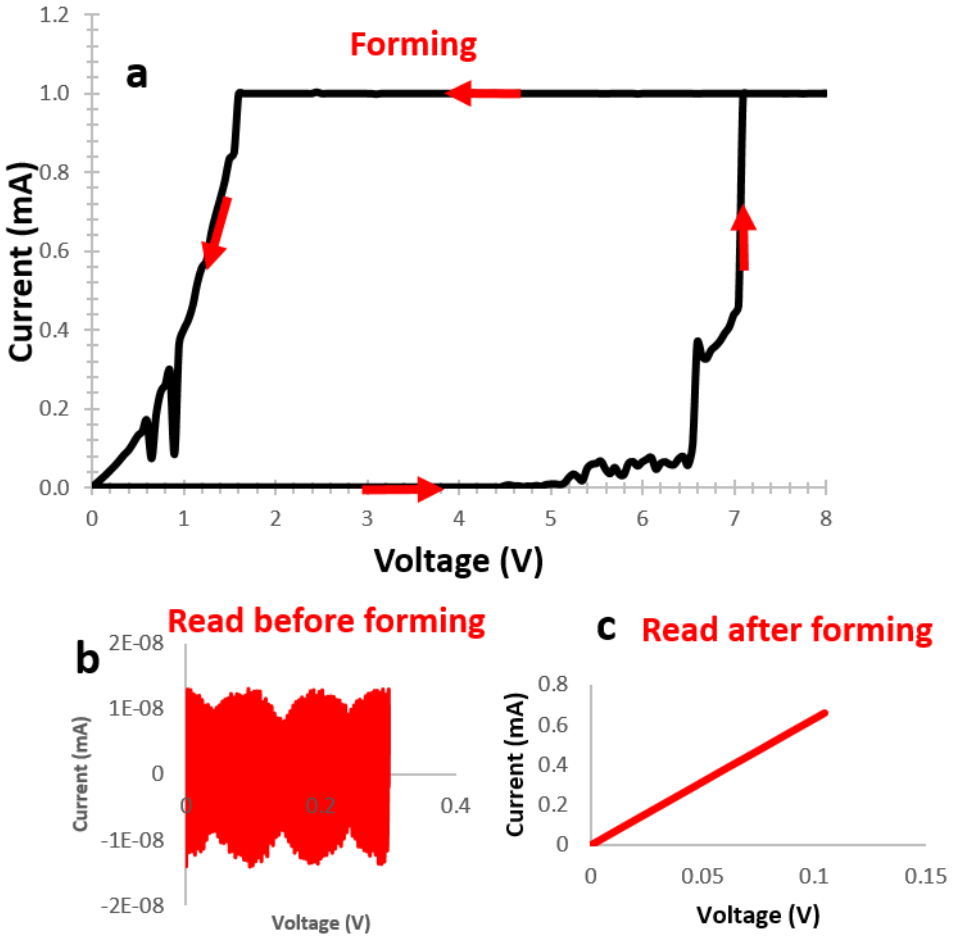

Figure 5.3. (A) Forming process of anatase titania. (B) read before and after (C) forming. (Thickness 50nm).

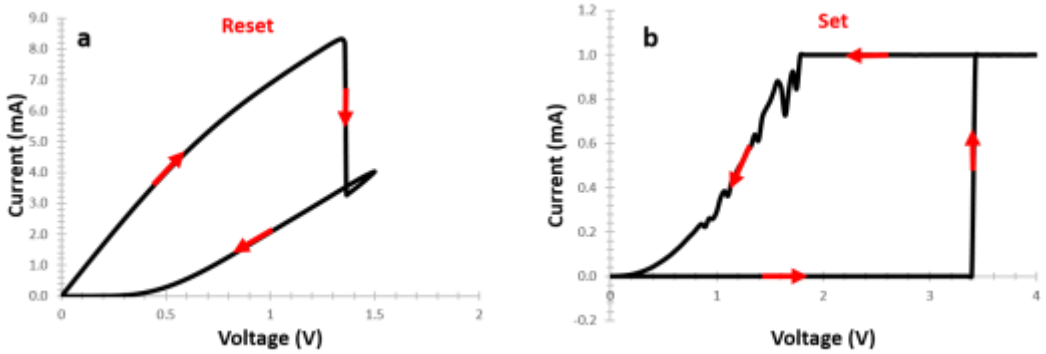

Figure 5.4. I-V sweeps of unipolar resistive switching behaviour of anatase titania. (A) reset process, and (B) set process. (Thickness 50nm).

5.1.1.3 Pt/ rutile TiO_2/ Pt

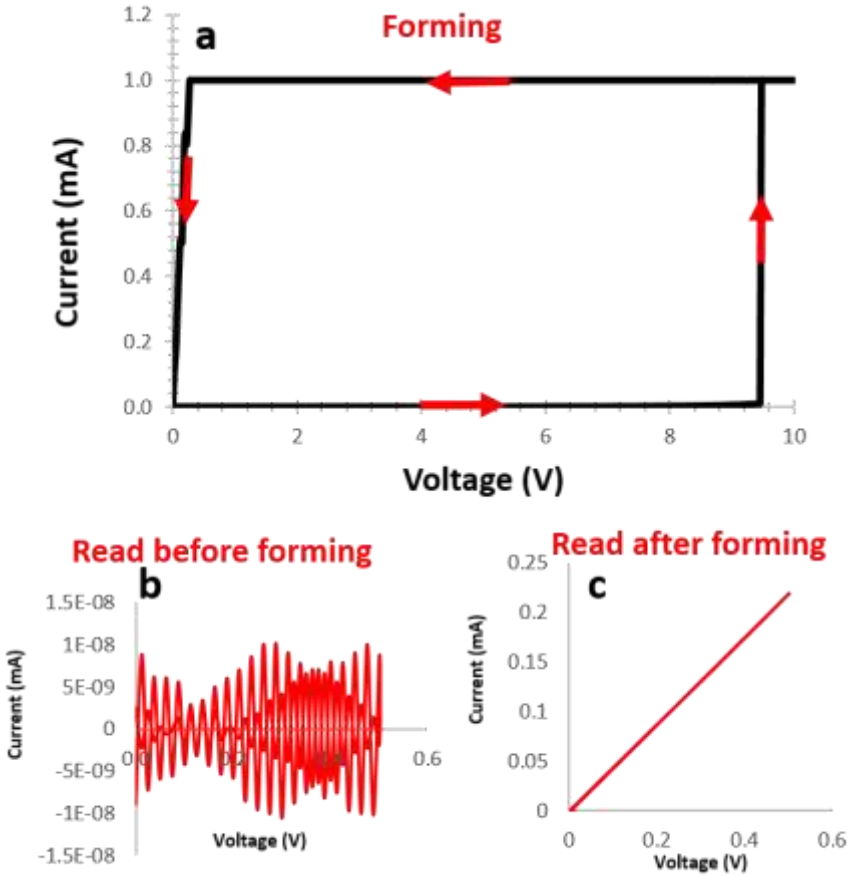

Figure 5.5. (A) Forming process of rutile titania. (B) read voltage before and (C) read after forming step. (Thickness 50nm).

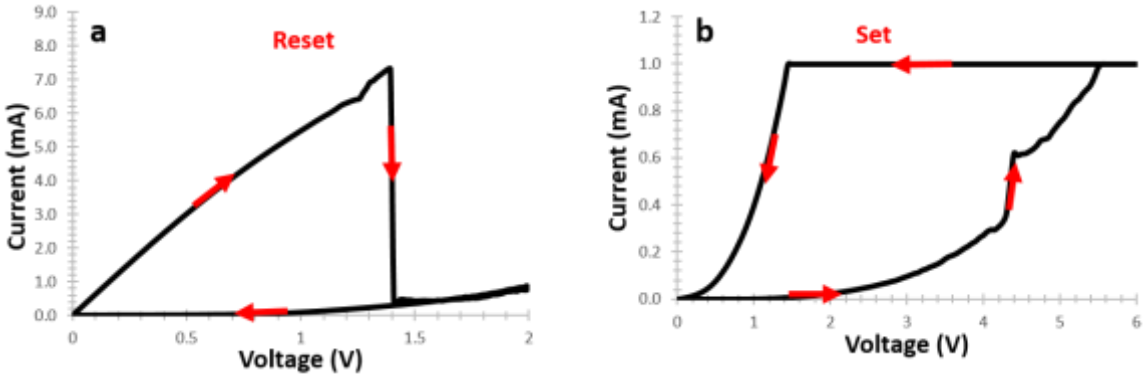

Figure 5.6. I-V sweeps of unipolar resistive switching behaviour of rutile titania. (A) reset, and (B) set processes. (Thickness 50nm).

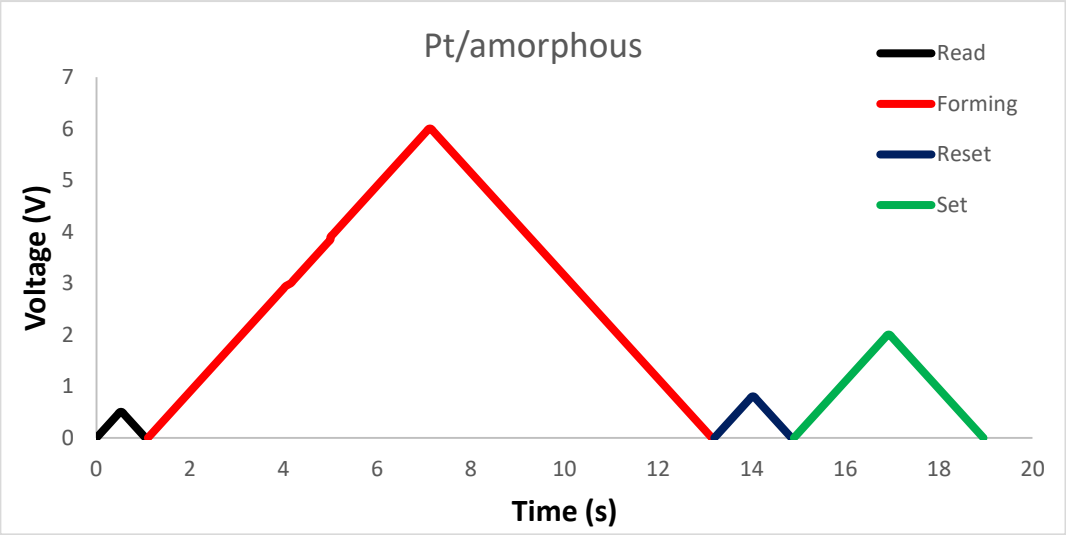

Figure 5.7. Time dependent of the voltage sequence applied to the device with amorphous titania, shown in **Figure 5.1.**

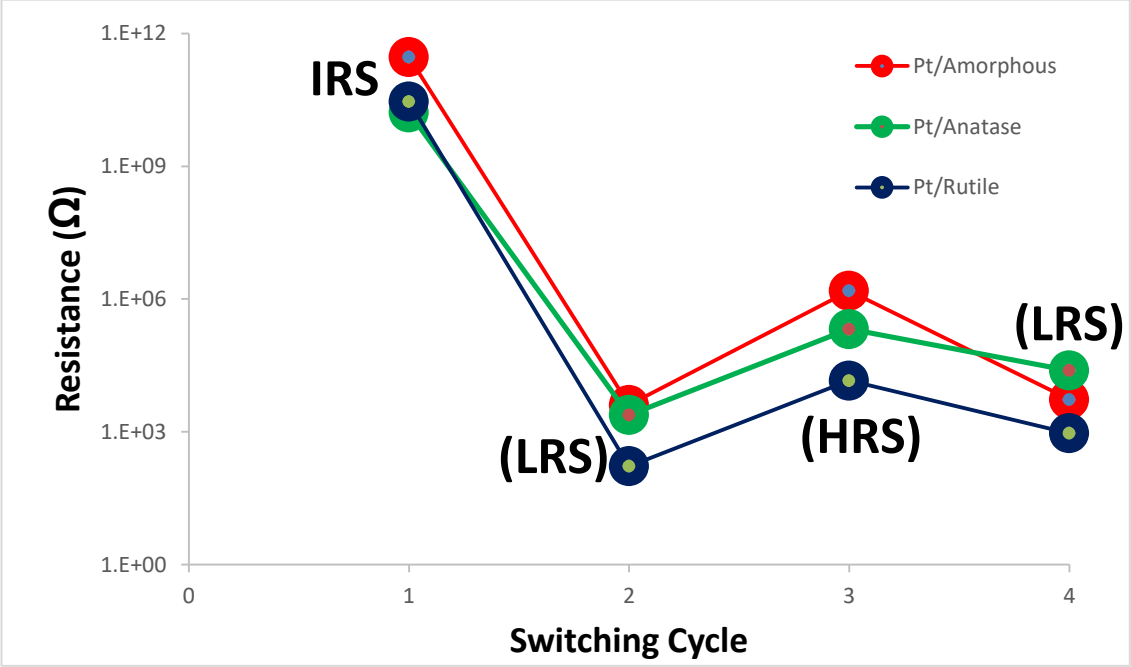

Figure 5.8. Reversible switching sequence for all titania phases. (IRS; initial resistance state, LRS; low resistance state, HRS; high resistance state).

A scanning electron microscope (SEM) image of a Pt/TiO_2/ Pt capacitor-like structure and energy dispersive X-ray spectroscopy (EDX) analysis were taken before and after dielectric breakdown (forming process). EDX analysis indicated that the Pt signal was lowered after breakdown (**Figure 5.9 D**) compared to **Figure 5.9 B**, and the Si signal in the inner circle increased, meaning the Pt was nearly peeled off in the outer circle. After the dielectric breakdown, many holes were formed on the surface of the Pt, which partially destroyed the electrode as well as the TiO_2 layer.

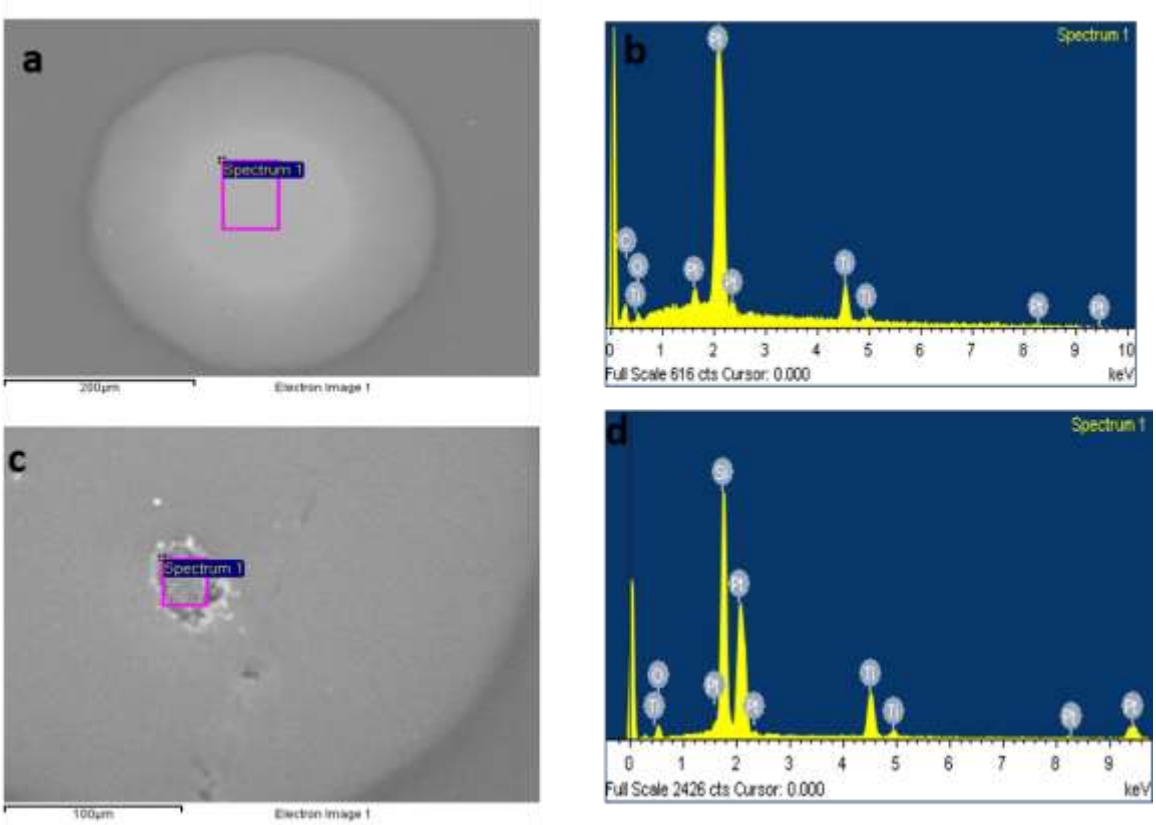

Figure 5.9. (A) SEM topography of a Pt top electrode before an electrical test, (B) signal of Pt before an electrical test, (C) top electrode after an electrical test, and (D) signal of Pt after an electrical test.

Only the amorphous titania device exhibited bipolar switching behaviour in the Pt/TiO_2/Pt structure. The voltage was swept first to negative (already formed in **Figure 5.1**) and subsequently to positive polarity. In the device with the amorphous phase of titania (**Figure 5.10**), the device switched at -2.8 V after the SET step (**Figure 5.2 B**) but at a higher IC (10 mA). The RESET process took place at 1.6 V, where the device switched to the HRS once again.

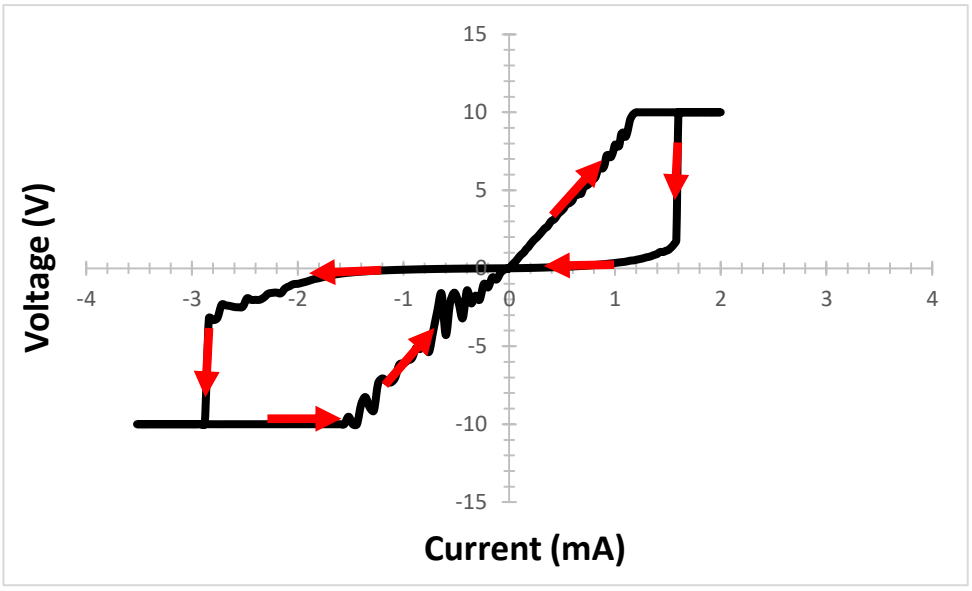

Figure 5.10. I-V sweeps of bipolar resistive switching behaviour of amorphous titania with thickness of 50 nm prepared using HT-PVD.

The results obtained above clearly reveal the diversity of titania phases toward switching phenomena in TiO_2, which may induce some confusion and dispute over an accurate understanding of the resistive switching mechanisms. However, the result obtained shows a typical unipolar/bipolar behaviour of TiO_2 as reported in the literature.[102,98,36] Crystalline titania has higher forming voltage (FV) than the amorphous phase: The order observed here is $FV_{rutile} > FV_{anatase} > FV_{amorphous}$. This, however, is not always the case, as described in the following **section 5.3**.

5.1.2 I-V Characteristics of the Cu/ TiO_2/ Pt Device

The choice of contact electrode metal influences device switching properties depending upon (i) symmetry of the anode and cathode, (ii) metal/TiO_2 contact, (iii) thickness, (iv) geometry and (v) nature of metal electrode (inert/active).[160] Hence, the aim of this section is to investigate the effect of the top electrode on the switching behaviour of ReRAM devices. Noble metals (preferably Pt) are widely employed for making Schottky contact with TiO_2, owing to their unique qualities, such as their non-oxidising and non-reactive nature.[13] Pt has a high cost, and thus reducing manufacturing cost is essential before ReRAM can be commercialised as a practical application; therefore, efforts to select an electrode for affecting switching properties must be considered an important factor.

Cu/TiO_2/Pt structures of amorphous/crystalline were swept to a positive/negative voltage on the top electrodes, while the bottom electrodes were grounded and then swept back to zero. In all devices, at the beginning, a read voltage was applied, after which the

devices were swept to a voltage (E > 2 V) at which the forming process took place, at 1.65 V. Subsequently, the voltage was decreased. The sweep rate was constant, at 50 mV/s, in all measurements presented here. The diameter of the circular-shaped top electrode (TE) was 250 µm. The thickness of the titania presented here was 30 nm. For amorphous titania, the voltage was swept to 2 V after reading the state of the device; the device clearly had high resistance at the beginning until its reached 1.65 V, at which point resistance decreased and the device switched from HRS to LRS, as shown in **Figure 5.11**. On the return sweep to zero, there was a jump in current to 1 mA before dropping to zero. Read voltage was applied to read the status of the device after forming, which showed the device in stay LRS (ON). After the forming process, the voltage was swept to negative (E ≤ -1 V), where the device switched at around -0.5 V from LRS (ON) to HRS (OFF). Then, the voltage was swept to positive (E ≤ 1 V), at which it stayed in HRS (OFF) until 0.4 V, where the device switched to LRS (ON) as shown in **Figure 5.12**.

5.1.2.1 Cu/ TiO_2 amorphous / Pt

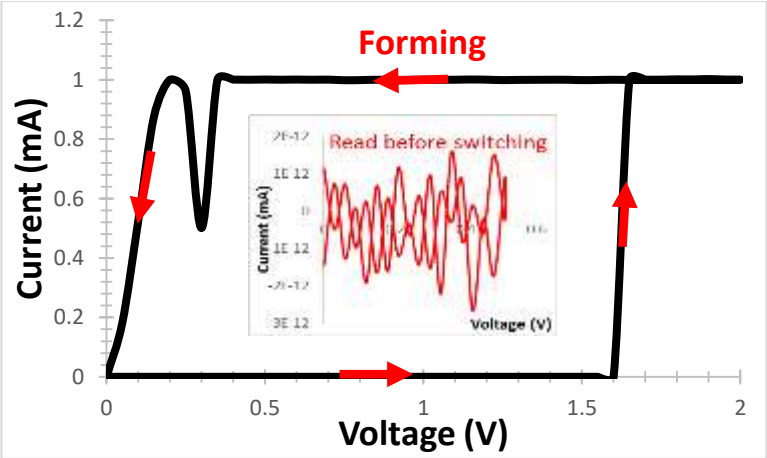

Figure 5.11. I-V sweep of forming process of Cu/ amorphous TiO_2 (30 nm)/ Pt. read voltage (subfigure) before the forming process at 0.5 V.

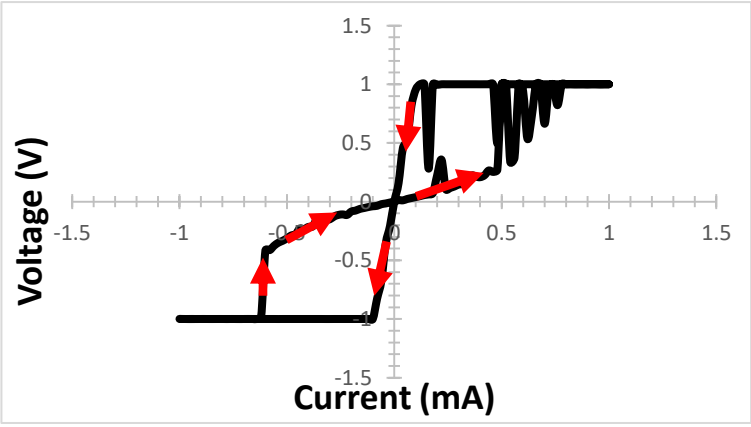

Figure 5.12. I-V sweeps of bipolar characteristics of Cu/ amorphous TiO_2/ Pt.

5.1.2.2 Cu/TiO_2 anatase /Pt

A similar behaviour was observed on Cu/anatase TiO_2 (30 nm)/Pt, at which the device was swept to positive (E > 2 V), then formed at around 1.5 V, as shown in **Figure 5.13**. There was degradation when sweeping the voltage back to zero. Read voltage before the forming process was obtained and is displayed in **Figure 5.13**. The device was swept to negative after forming, at which the device stayed in LRS (ON) until around -0.6, when it switched from LRS (ON) to HRS (OFF). The voltage was kept continuously increase until 0.5 V, where the device switched again from HRS (OFF) to LRS (ON), as shown in **Figure 5.14**. The time dependence of voltage sequences applied to amorphous was obtained and is displayed in **Figure 5.15,** while the time dependence for anatase titania was obtained and is displayed in Appendix A 4.3. The switching sequence for Cu/TiO2/Pt (IRS, initial resistance state; LRS, low resistance state; HRS, high resistance state) is displayed in **Figure 5.16.**

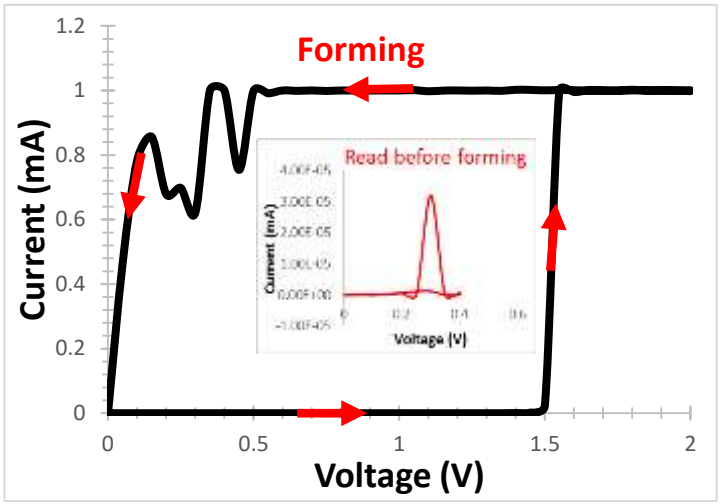

Figure 5.13. Forming process of Cu/ anatase TiO_2 (30 nm)/ Pt. read voltage (subfigure) before the forming process at 0.5 V.

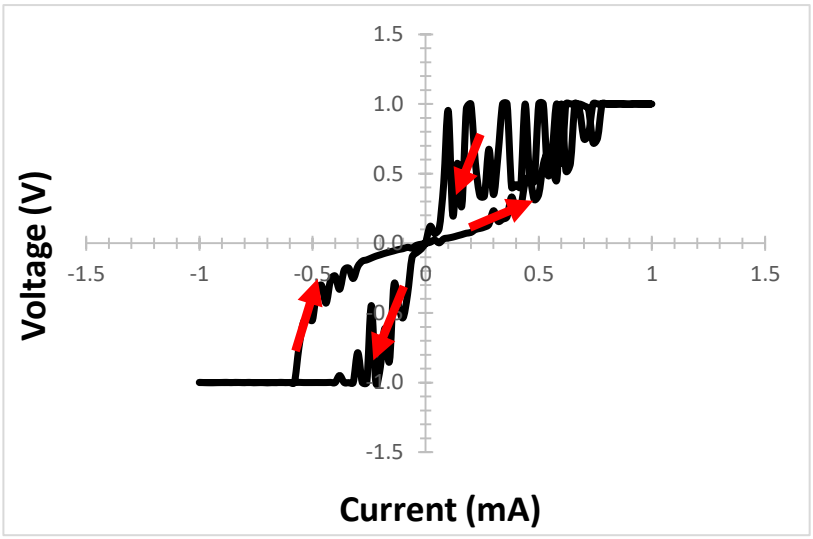

Figure 5.14. I-V sweeps of bipolar characteristics of Cu/ anatase TiO_2/ Pt.

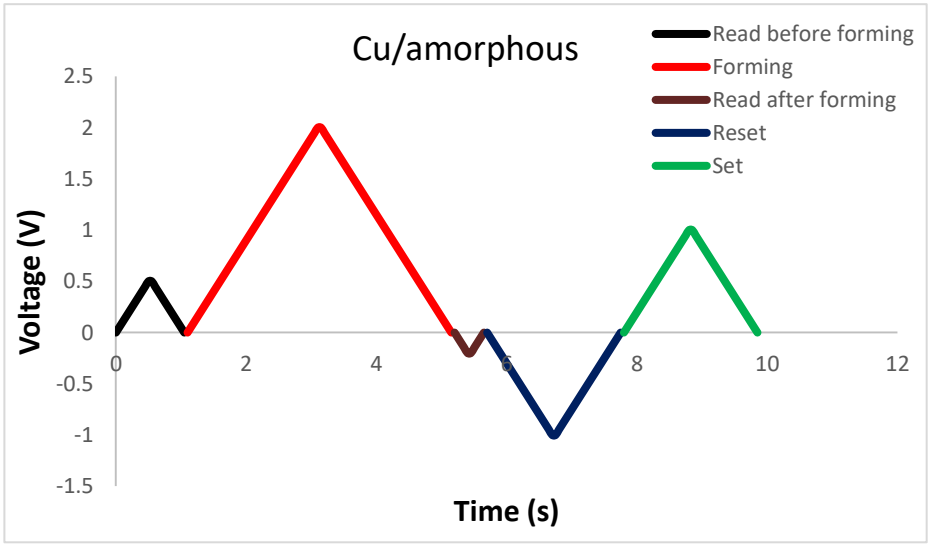

Figure 5.15. Time dependent of the voltage sequence applied on amorphous described in

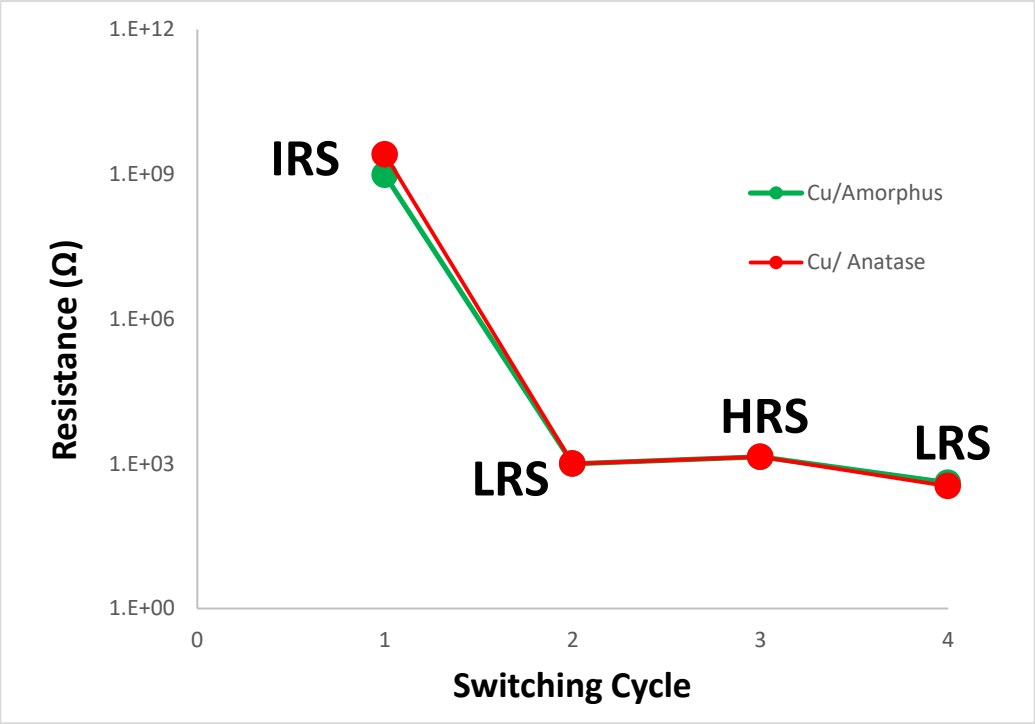

Figure 5.16. Reversible switching sequence for Cu/TiO_2/Pt. (IRS; initial resistance state, LRS; low resistance state, HRS; high resistance state).

The result obtained shows that anatase titania has lower forming and reset voltage than amorphous titania. In Cu-based titania, there was degradation during forming voltage for amorphous and anatase, which could be due to weak filaments created and broken quickly when the voltage swept back to zero. The subsequent sweep was not stable for either phase. This was mostly affected by the forming process. At the initial state, both devices had high resistance (10^{-11} Ohm), which was irreversible after forming. However, it was observed that some devices did not hold their resistance. This may be due to the creation of a new filament with lower resistance.

5.1.3 I-V Characteristics of the Pt/ TiO_{2-x}/ TiO_2 / Pt (composite) Device

The aim of this section is to investigate the effect of a composite structure of TiO_2 (oxygen rich) and TiO_{2-x} (oxygen poor) across thickness variations and different phases of titania. There is general agreement that the migration of oxygen ions or vacancies under an applied electric field plays a key role in resistive switching.[163,159] **Figure 5.17** describes the details of the structures demonstrated in this study.

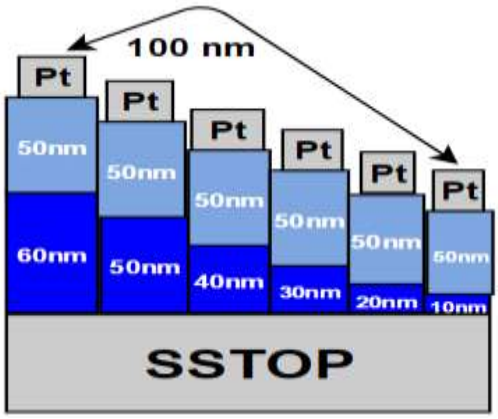

Figure 5.17. Diagram of composite structures demonstrated in this section: TiO_2 amorphous/ anatase (dark blue), TiO_{2-x} amorphous (light blue)

$Pt/TiO_{2-X}/TiO_2/Pt$ structures of amorphous/amorphous and amorphous/crystalline were swept to a positive/negative voltage on the top electrodes, while the bottom electrodes were grounded, and then swept back to zero. In all devices, at the beginning, a read voltage was applied, after which the devices were swept to a positive voltage. Subsequently, the resistance was decreased. The step voltage was constant in all measurements presented here, at 50 mV/s. The diameter of the circular-shaped top electrode (TE) was 250 μm. The thickness of the devices presented here were 50 nm and 25 nm for TiO_{2-x} and TiO_2, respectively, with a 100-nm Pt top electrode. For amorphous composite titania, the voltage was swept to 2.5 V after reading the state of the device under current limitation at 1 mA, in voltage sweep mode. The device had high resistance at the beginning, until its reached 1.2 V, at which point the resistance started decreasing gradually until 2.2 V, where a jump of current was clearly observed and the device switched from HRS (OFF) to LRS (ON), as shown in **Figure 5.18**. Then, the device stayed in the IC until it dropped to zero. Read voltage was applied to read the status of the device before and after forming, and is shown in **Figures 5.18 A** and **5.18 B**. After the forming process, the voltage was swept to negative (-2.5 V), where the device switched at around -1.65 V from LRS (ON) to HRS (OFF). Then, the voltage was swept to positive (2.5 V), at which it stayed in HRS (OFF) until 1.9 V, where the device switched to LRS (ON), as described in **Figure 5.19**. Anatase composite titania, on the other hand, was also swept to positive (4 V), with the forming process obtained at around 3.8 V, as shown in **Figure 5.20**. There was degradation in the voltage sweep back to zero. Read voltage before and after are displayed in **Figures 5.20 A** and **5.20 B**. The device was swept to negative after forming, at which the device stayed in LRS (ON) until around -2.2 V, where it switched from LRS (ON) to HRS (OFF) (defined as the RESET process). The voltage swept back to positive across zero, and the status of resistance was maintained until 1.9 V, where the

device switched again from HRS (OFF) to LRS (ON) (defined as the SET process), as shown in **Figure 5.21**. The time dependence of voltage sequences applied to the amorphous composite was obtained and is displayed in **Figure 5.22,** while the time dependence of anatase composite titania is displayed in Appendix A). The reversible switching sequence for Pt/TiO_{2-x} /TiO_2/Pt is shown in **Figure 5.22**.

5.1.3.1 Pt/ TiO_{2-x}/ TiO_2 (amorphous)/ Pt

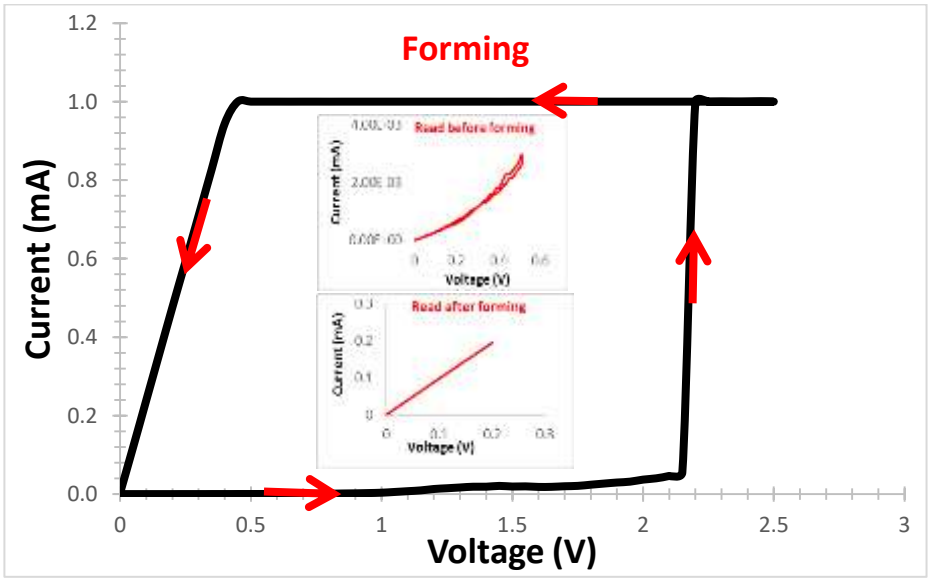

Figure 5.18. I-V sweep of forming process of Pt/ amorphous (50 nm)/ amorphous (25 nm)/ Pt (at read voltage (subfigure) at 0.5 V and 0.2 before and after forming process.

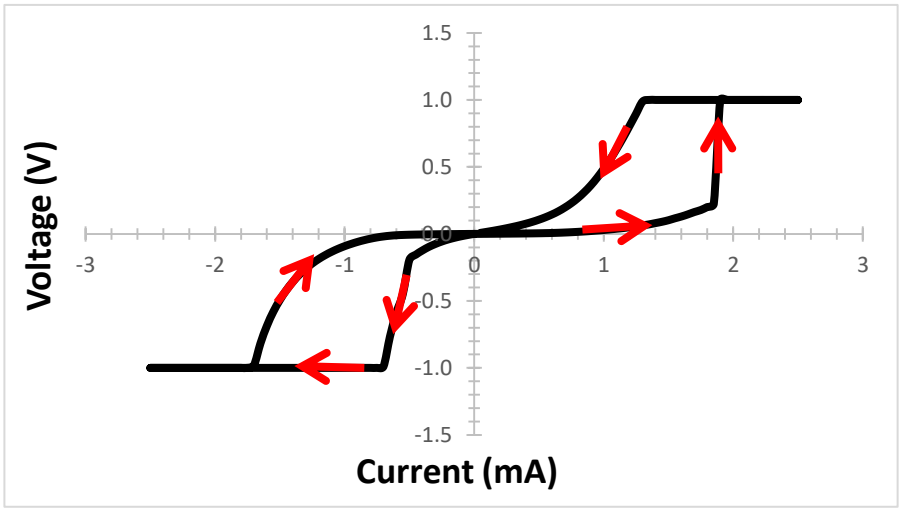

Figure 5.19. I-V sweeps of bipolar characteristics of Pt/ amorphous TiO_{2-x} (50nm) / amorphous TiO_2 (25nm) / Pt.

5.1.3.2 Pt/ TiO_{2-x}/ TiO_2 (anatase)/ Pt

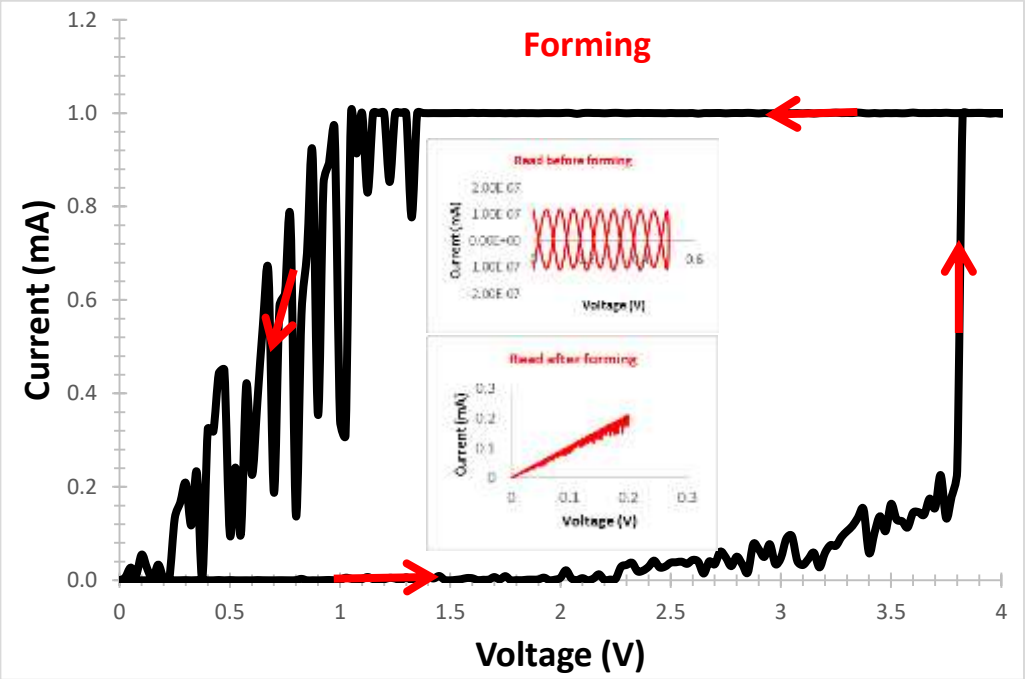

Figure 5.20. I-V sweep of forming process of Pt/ amorphous (50 nm)/ anatase (25 nm)/ Pt (at read voltage (subfigure) at 0.5 V and 0.2 before and after forming process.

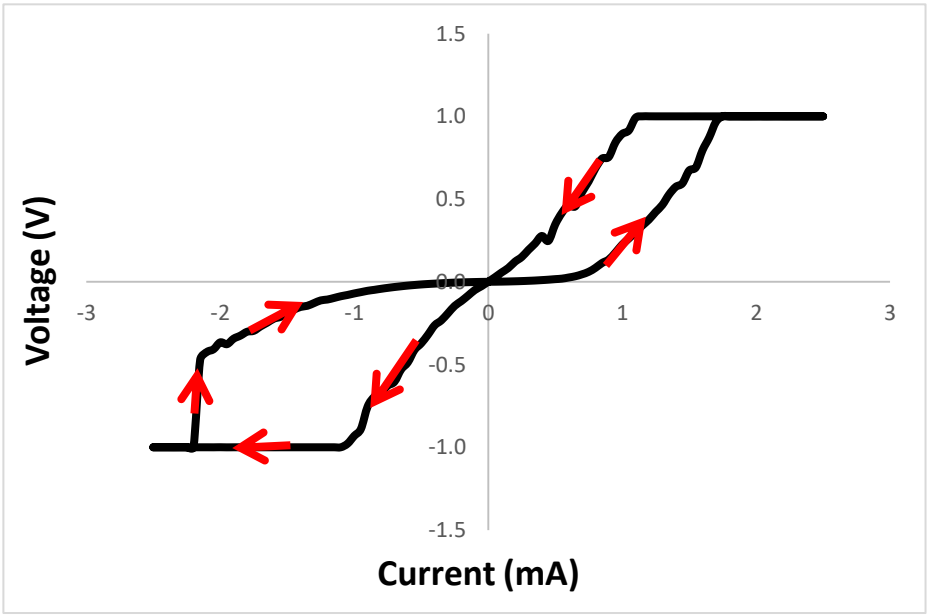

Figure 5.21. I-V sweeps of bipolar characteristics of Pt/ amorphous TiO_{2-x} (50 nm)/ anatase TiO_2 (25 nm)/ Pt.

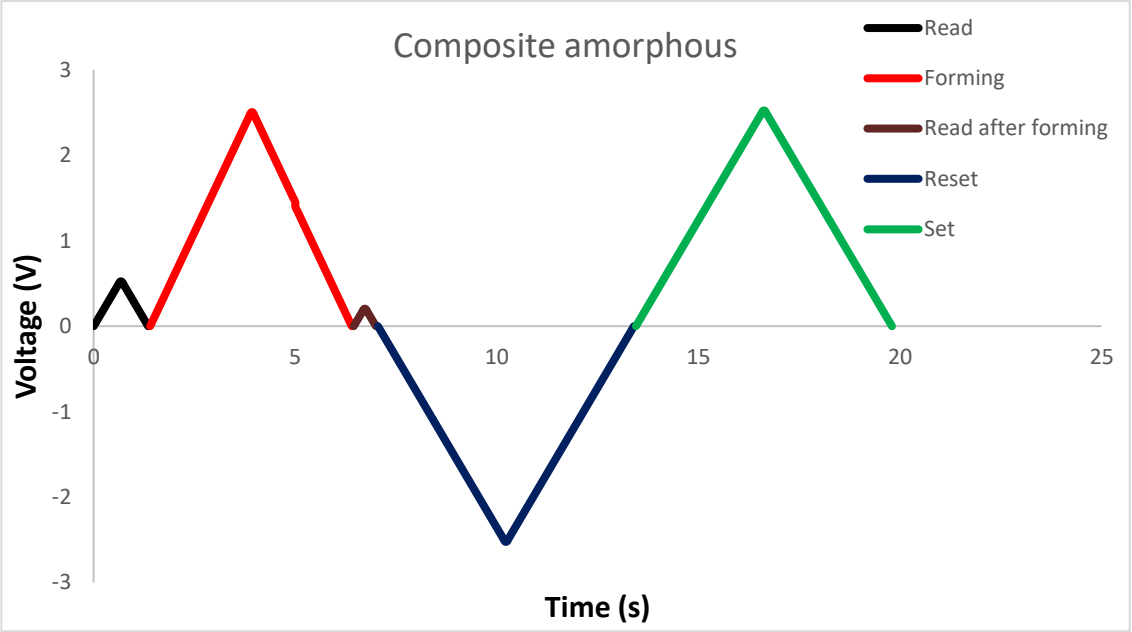

Figure 5.22. Time dependent of the voltage sequence applied on amorphous composite described in **Figure 5.13.**

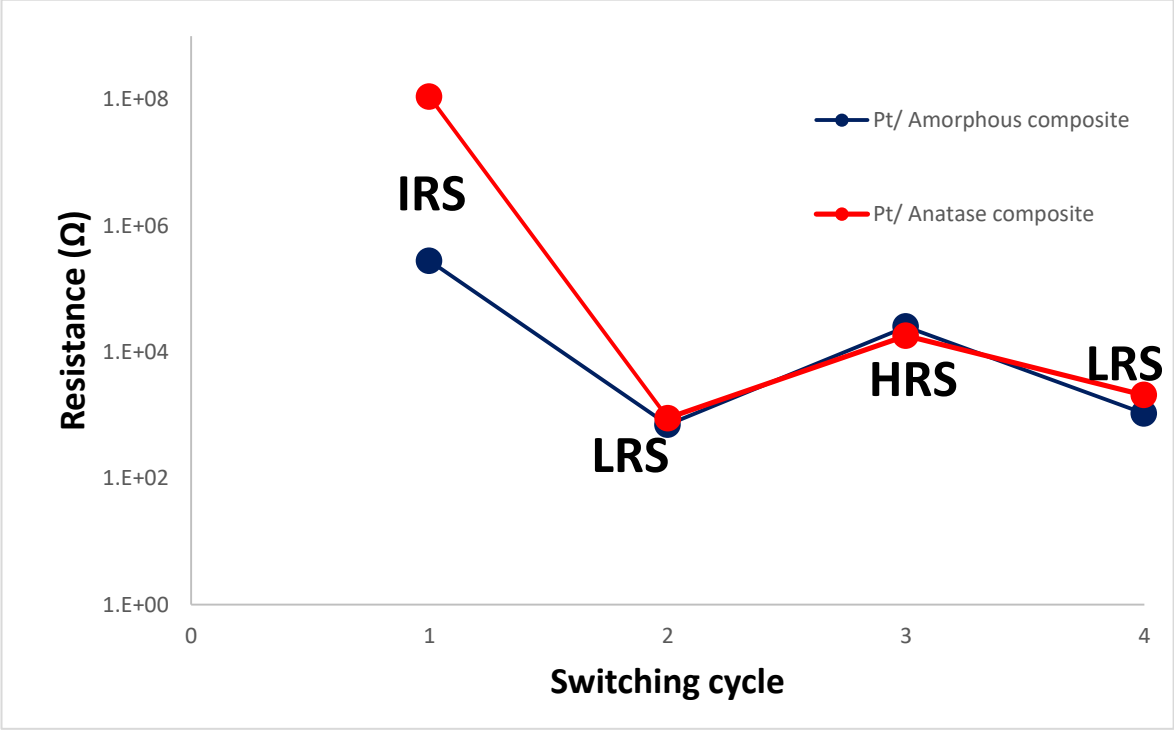

Figure 5.23. Reversible switching sequence for Pt/TiO_{2-x} /TiO_2/Pt (IRS, initial resistance state; LRS, low resistance state; HRS, high resistance state).

The result obtained from the composite structure shows typical I-V characteristics of the bipolar switching phenomenon. It was found that the amorphous phase has much lower resistance at its initial state when compared to anatase. It is important to note that in the case of thicker TiO_{2-x} and thinner TiO_2, the forming voltage becomes lower. The switching time of amorphous composite was found to be shorter than that of anatase. The

switching phenomenon obtained seems to be a combination of the redox and conduction paths resulting from ions drifting between the oxygen rich and oxygen poor regions in the composite structures.

5.2 Forming as a Function of Polarity

Several factors affect the switching mechanism in ReRAM. Among these are forming voltage. Therefore, this section focuses on the electrical forming of the device as a function of polarity for different structures of titania. **Figure 5.24** shows the test conducted on the effect of forming in a positive/negative direction on two different samples with the same structure of Pt/TiO_2/Pt at 50 nm. The voltage was swept to (E ≥ 5 V), at which the device switched at 4.6 V. On the other hand, a fresh sample was formed in the negative direction at 4.8 V. There was little difference in this symmetrical structure in terms of forming voltage or sweeping behaviour. The structure of Cu/TiO_2/Pt also formed in a different direction of polarity, as shown in **Figure 5.25**. Finally, the composite structure of Pt/TiO_{2-x}/TiO_2/Pt is displayed in **Figure 5.26**.

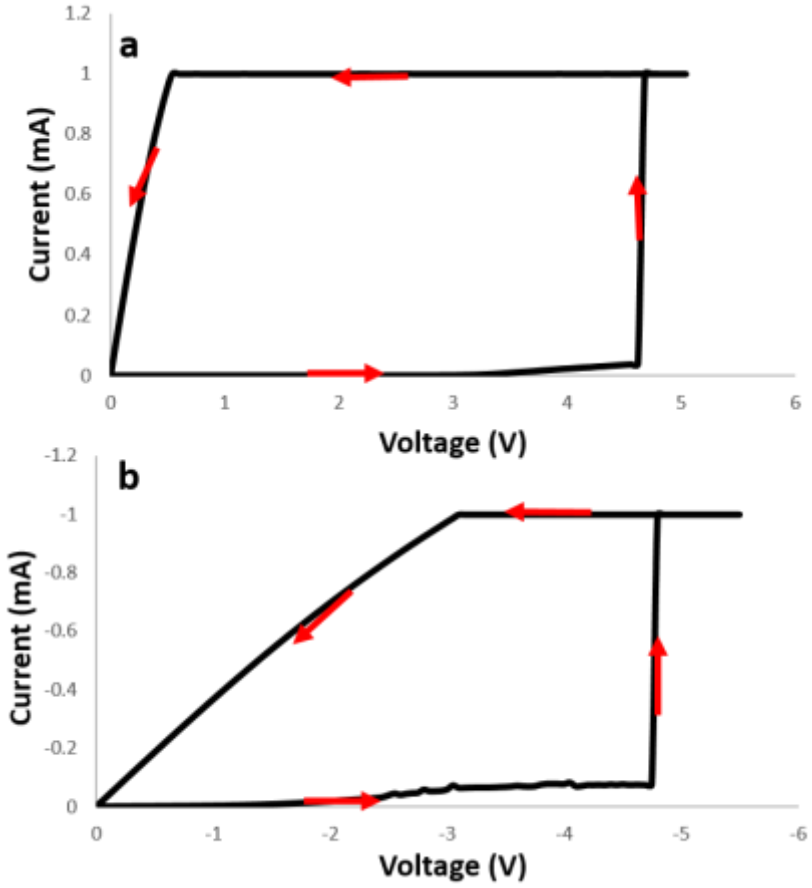

Figure 5.24. I-V sweeps represents the polarity dependent of Pt/ TiO_2 (50nm)/ Pt (A) positive forming and (B) negative forming.

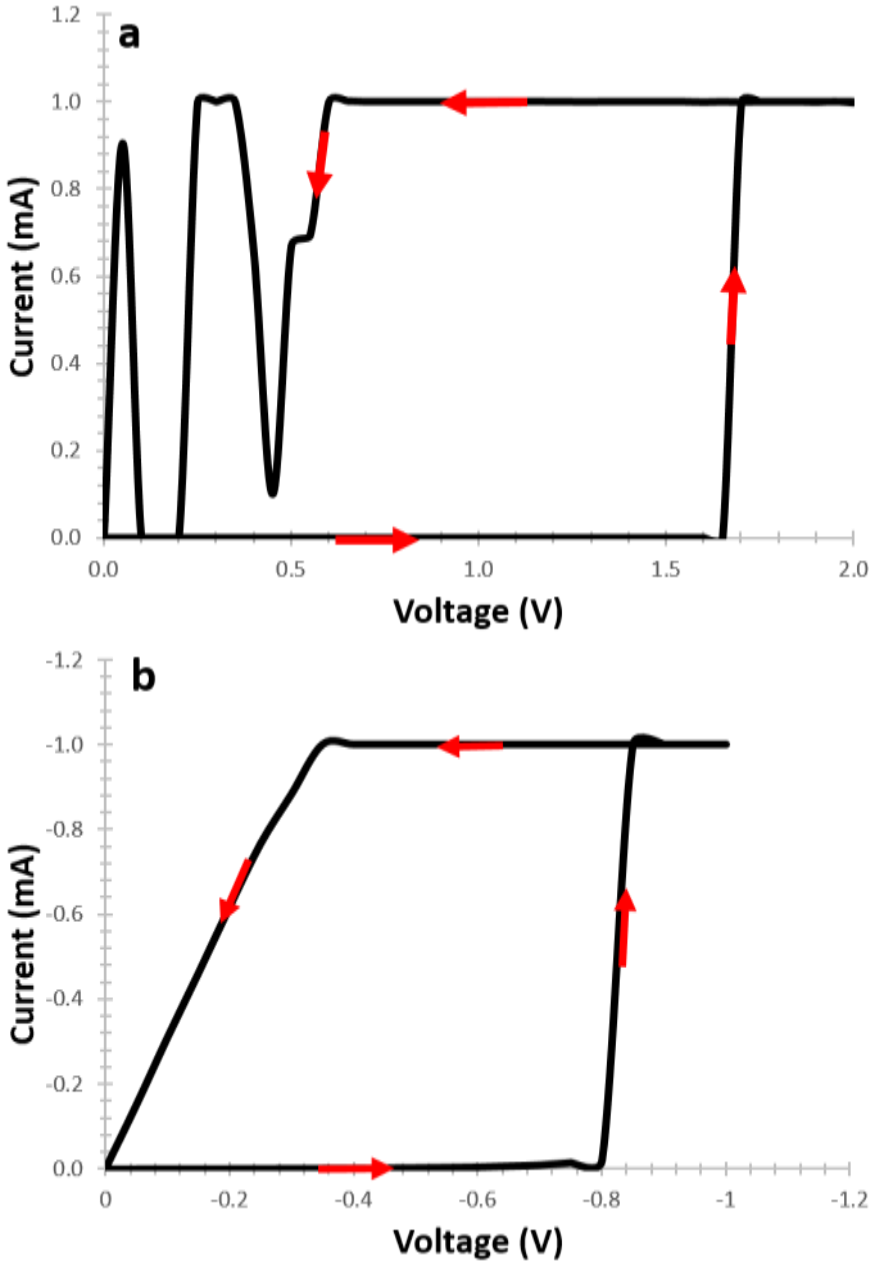

Figure 5.25. I-V sweeps represents the polarity dependent of Cu/ TiO_2 (40nm)/Pt (a) positive forming and (b) negative forming.

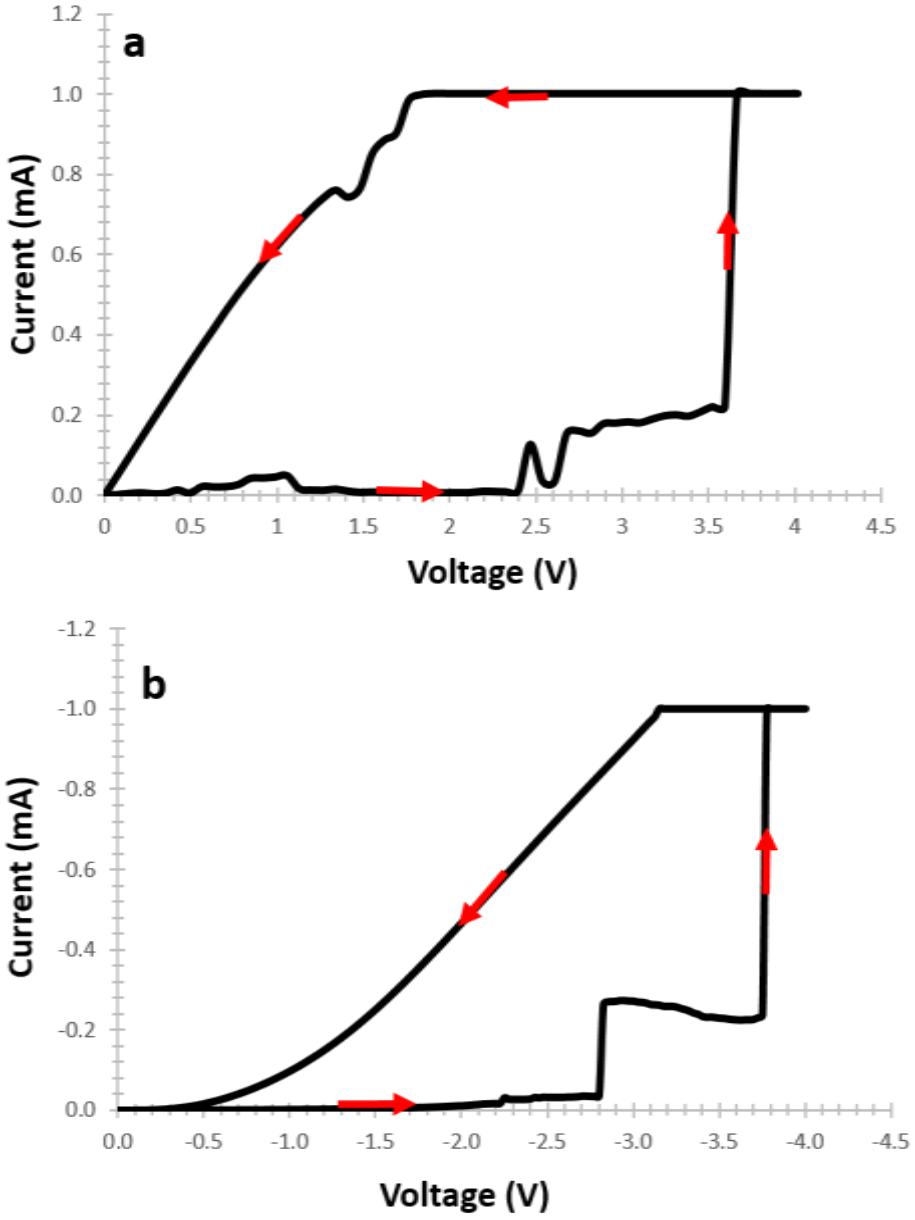

Figure 5.26. I-V sweep represents the polarity dependent of Pt/ TiO_{2-x} (50nm)/ TiO_2 (20nm)/ Pt. (A) positive forming and (B) negative forming.

It was found that in the symmetric structure of Pt/TiO_2/Pt, the forming process is not polarity dependent. This indicates that the presence of air at the platinum top electrode, or its absence at the bottom electrode, did not influence the switching behaviour (**Figure 5.24**). On the other hand, unsymmetrical structures of Cu/TiO_2/Pt and Pt/TiO_{2-x}/TiO_2/Pt were found to behave differently. In the Cu-based titania system, it was observed that forming in the positive direction requires higher voltage, which may also cause degradation in switching compared to negative polarity, which requires stable low voltage (**Figure 5.25**). In the composite system, as shown in **Figure 5.26**, it was found that when the device formed in the positive direction, its initial state had lower resistivity; whereas when it formed in the negative direction, the device started with very high resistance (four

orders of magnitude higher compared to positive) and then achieved high resistance again before dropping to zero. It was observed that for the same thickness of the switching stoichiometric TiO_2 layer, the forming voltage was much smaller when combined in the composite structure (with TiO_{2x}) than in the simple structure.

5.3 High Throughput Screening of Titania across Different Thicknesses and Structures

In this section, trends and structure properties of titania phases as a function of thickness are presented: The focus here is on understanding the voltage and field dependence of the forming and switching behaviour of devices as a function of the thickness of the active switching material.

5.3.1 Pt/ TiO_2/ Pt

Devices were formed electrically from different phases of TiO_2 – namely, amorphous, anatase and rutile. The study was focused on switching as a function of forming voltage and electric fields. The forming voltage and electric field were calculated for each device across thicknesses (Appendix A). Each strip of thickness was tested and calculated individually. **Figure 5.27** displays a schematic of forming voltage across gradient thicknesses of titania. Statistics of forming voltage and electric field gradients of different phases of TiO_2 are displayed in Appendix A. Electric fields across a 20–300-nm gradient of thickness of different phases of titania were obtained and are described in **Figure 5.28**.

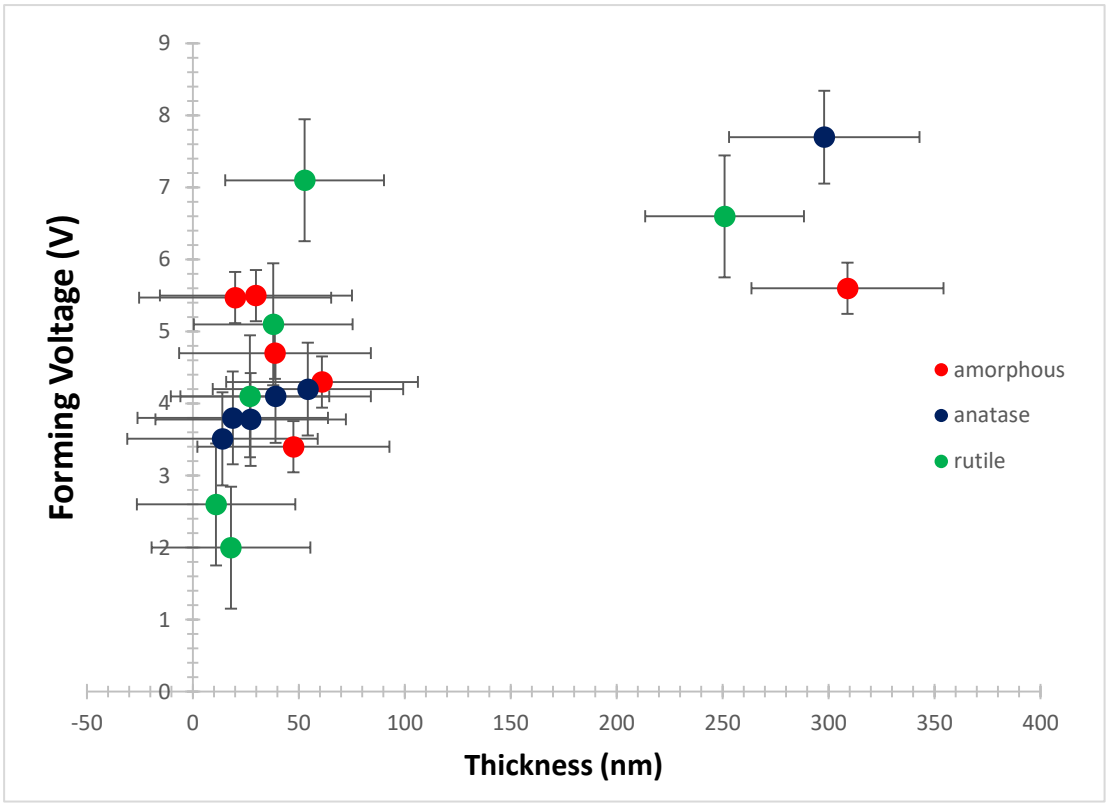

Figure 5.27. Data points of average forming voltage as function the thickness across phases of TiO_2

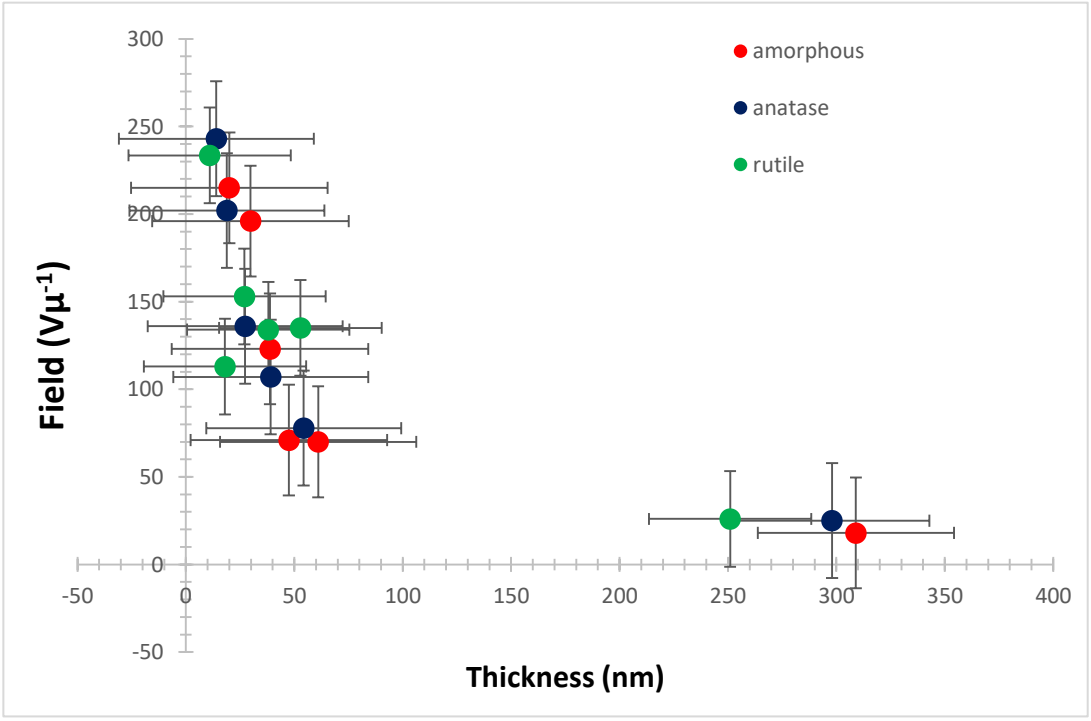

Figure 5.28. Data points of average electric field as function the thickness across three phases of TiO_2

A typical combinatorial library of $Pt/TiO_2/Pt$ devices was evaluated, and the statistics for switching are summarised in **Figure 5.29**. The switching operation was performed on a number of devices after the forming process with different voltages. The dark blue fields

indicate the number of devices that formed successfully. The green fields indicate the number of devices that subsequently, successfully switched in an ReRAM application (reset/set). The number of devices that were tested but failed to work are indicated by white fields. Light blue fields indicate devices that were not tested. Similar statistical representations of the testing of other libraries of devices are shown in Appendix A.

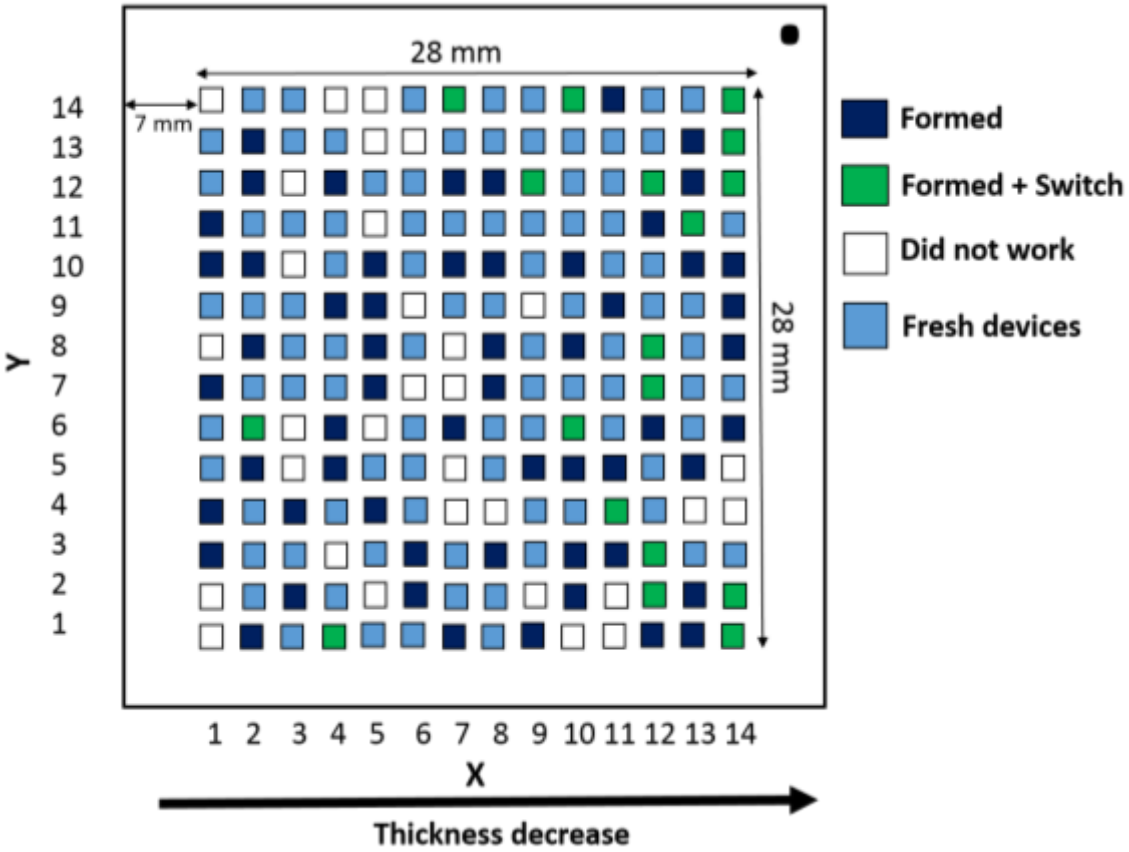

Figure 5.29. High-throughput statistics of device yields of Pt/TiO_2 amorphous/Pt. Dark blue indicate how many device were formed; green indicates how many devices were formed and tested and set again; white boxes indicate the number of devices that did not form; and light blue represents devices that were not tested.

By excluding the untested devices and combining all Pt/TiO_2/Pt systems, a clear comparison was achieved, as shown in **Figure 5.30**. It is important to mention that the data presented here – the data for the thicker devices (200–300 nm) and the thinner devices (10–50 nm) – were combined to give general statistics of device performance. Nearly 140 (red colour) devices were formed in the amorphous phase, whereas 130 and 95 devices were formed in the anatase and rutile phases, respectively. The lower number formed in crystalline devices could be due to different densities of defects at which, in addition to oxygen vacancies, the crystalline grain may play an important role in enhancing the conductivity of the device and thereby leading to its failure. This depends on the switching region at which the grain boundaries of the device should be formed at lower voltage;

switching in the middle of forming requires higher voltage. As mentioned in Chapter 2, the forming process is one critical success factor for ReRAM application, as the subsequent switching cycle depends on it. However, the subsequent cycle (reset/set) was performed on the devices that already formed. Pt/TiO_2 (all phases)/Pt showed the device performance (blue colour). The number of cycled devices for all phases was nearly the same (average of 25 devices). It is important to note that not all formed devices were cycled, since the focus was mainly on the forming process, a critical factor for the switching cycles. The number of devices that did not work (DNW) are indicated (green).

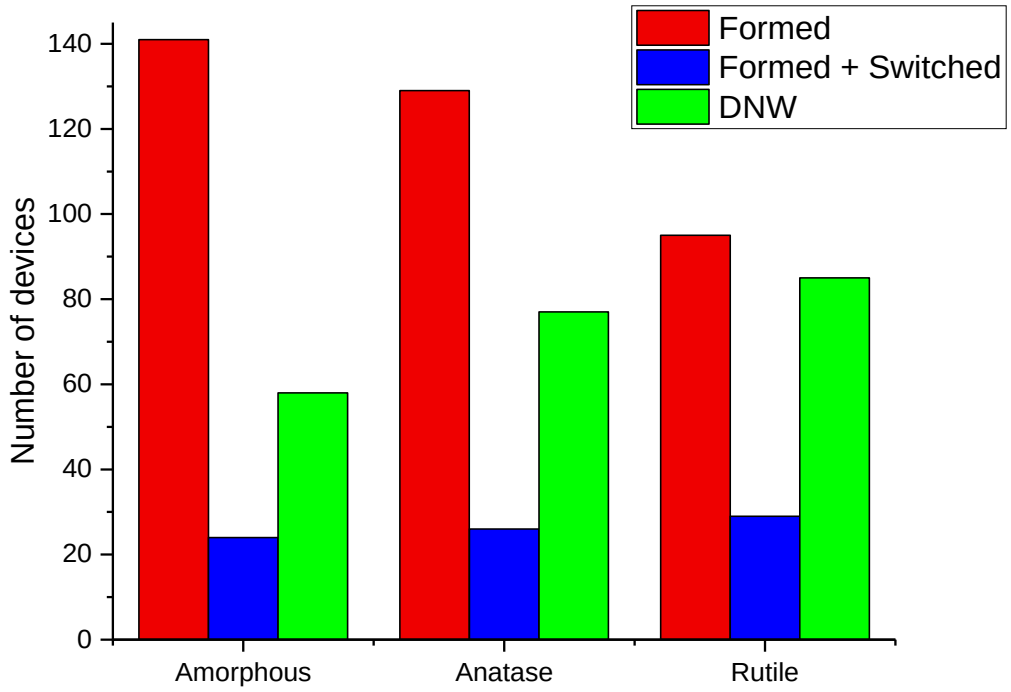

Figure 5.30. High-throughput statistics of device yields of all Pt/TiO_2/Pt-synthesised systems: a red colour indicates the number of devices formed; blue indicates the number of devices being switched; and green indicates the number of devices that did not work (DNW).

Multiple switching on one device (device No (9, 12)) across different behaviours was performed and is displayed in **Figure 5.31**. It is clear that the forming process requires higher voltage to create a conductive path through the oxide. The device exhibited much lower voltage in the subsequent cycle. After that, there was nearly stable switching until cycle 15, where the behaviour started changing and looked like a unipolar occurrence. On the 28th switching cycle, the hysteresis loop was not observed, and the device became very conductive. This could be due to an O atom becoming excited and leaving an O_2 poor film, resulting in increasing conductivity.

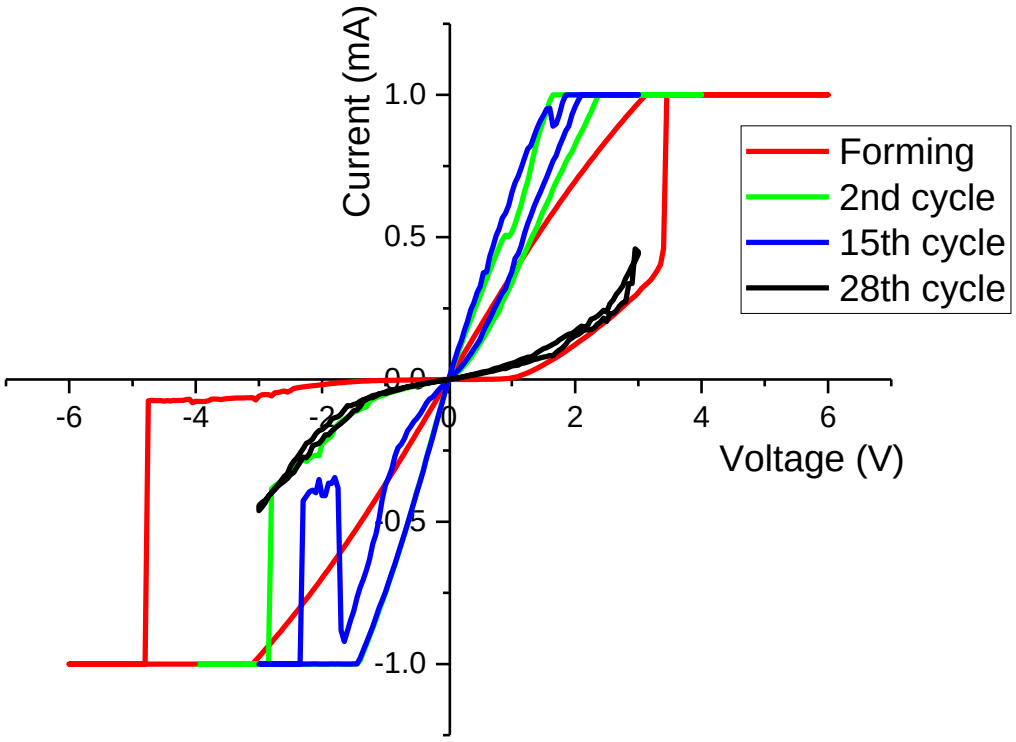

Figure 5.31. Multiple bipolar switching of Pt/TiO_2 (amorphous)/Pt. Forming (red), 2nd cycle (green), 15th cycle (blue) and 28th cycle (black).

Amorphous titania shows no dependency on forming voltage, whereas crystalline titania (anatase and rutile) shows slight dependency. By calculating the field of the device, it was found that all phases showed dependency on the field, which decreased with increasing thickness of the devices, as shown in **Figure 5.28**. The crystalline phases showed higher fields than the amorphous phase. Statistics of all devices showed that most of the devices tested formed successfully with a variation of voltage. This variation was due to different densities of defects. Multiple switching showed that the device lost oxygen with the time of the switching cycle.

5.3.2 Cu/ TiO_2/ Pt

An average of 100 fresh devices were formed electrically with different top electrodes across amorphous/crystalline titania with variations of thickness. The study was focused on switching as a function of forming voltage and electric fields. The forming and electric fields were calculated for each device across thicknesses for amorphous and crystalline titania (Appendix A). Each strip of thickness was tested and calculated both individually and by averaging each strip and plotting it as shown in **Figure 5.32**; in addition to the forming voltage of Cu-based titania, the forming voltage of Pt-based titania as well as literature results were described in the same figure in order to make a

comparison and validate the work done. As shown in **Figure 5.32**, it is clear that thinner devices require higher voltage. It was found that the electric field increased with a decreasing thickness of thin-film across all phases and electrodes, as shown in **Figure 5.33**. The Cu-based titania was found to have a lower forming voltage and electrical field than Pt. This might be due to the high diffusion rate of Cu. It was clear that the amorphous Cu phase had the lowest forming voltage and electrical field, while the Pt-based amorphous phase had the highest forming voltage. The field gradient obtained was in the order Pt/amorphous TiO_2 > Pt/anatase TiO_2 > Cu/anatase TiO_2 > Cu/amorphous TiO_2, as shown in **Figure 5.33**. The result obtained is consistent with the literature results (see data points in **Figure 5.32** and **5.33**), although our finding had a lower forming voltage than that reported using ALD[75] and Sputtering[76] despite having the same thickness.

When a switchable voltage was applied for switching, the resistance of the device lowered dramatically due to the formation of conduction filaments between the two electrodes.[97,164] On the other hand, if one electrode was active, such as Cu, the OFF state resistance was not significantly high compared to when it was inert.[75] Pt makes a Schottky contact with TiO_2 due to its high work function (6.32 eV) compared to TiO_2 (3.4 eV), which shows the stability of switching.[165] It is not predominantly governed by work function/barriers highest due to the fact that oxygen has high diffusivity through Cu.[96] Hence, Cu has some involvement as it has natural diffusion as well as oxygen diffusivity. Cu/TiO_2 exhibited only bipolar switching, whereas Pt/TiO_2 exhibited both modes of switching (unipolar and bipolar), specifically in amorphous devices. It was reported that a large ion diffusion coefficient leads to lower switching voltage.[73,166]

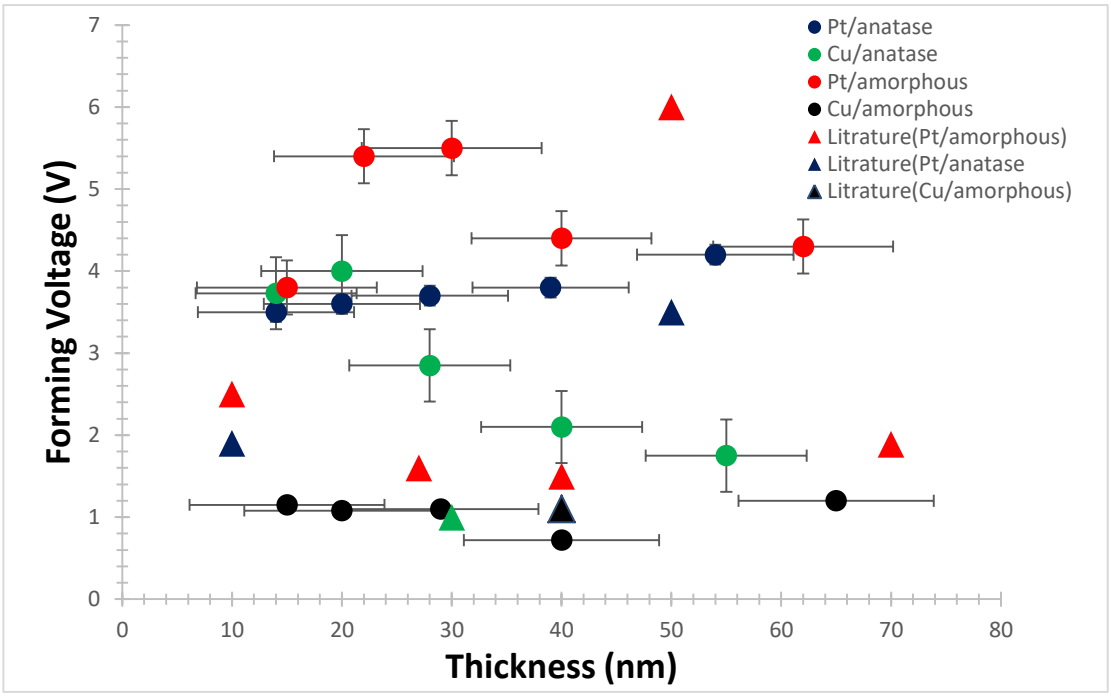

Figure 5.32. Data points of average forming voltage as a function of the thickness of Pt and Cu top electrodes across amorphous/anatase TiO_2/Pt with similar system studies in the literature (literature references [36,75,77,94,95,97,98,101,167]).

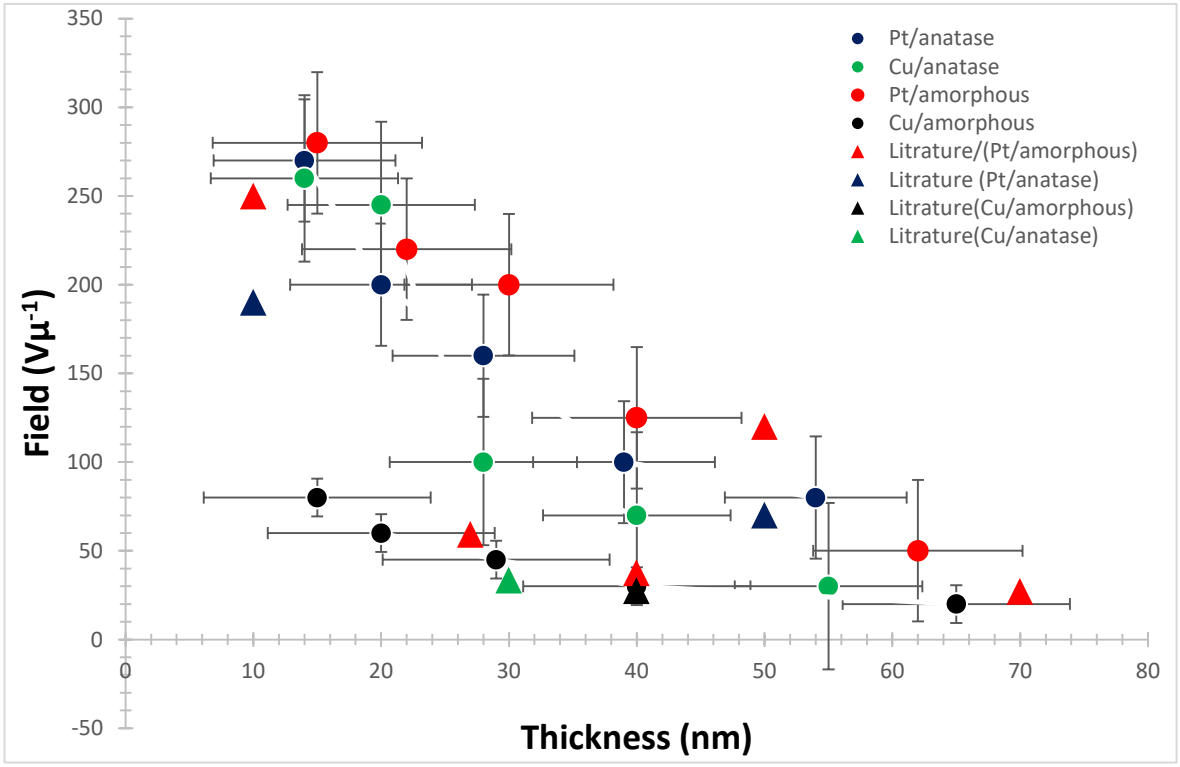

Figure 5.33. Data points of the average electric field as a function of the thickness of Pt and Cu top electrodes across amorphous/anatase TiO_2/Pt (literature references [36,75,77,94,95,97,98,101,167]).

Nearly 45 devices were formed (red colour) in each phase of amorphous and anatase Cu/TiO_2/Pt systems. The system was not reproducible at which approximately four

devices were exhibiting the subsequent switching cycles as indicated by the blue colour in **Figure 5.34**. The number of DNW devices was the highest among all systems presented in this thesis. The top electrode Cu plays an important role here since the phases (as shown in the previous system) do not show high impact on the device yield. This could be due to the higher diffusivity rate of Cu, which diffuses into TiO_2. Taking one of these switched devices (device No 5, 7) as multiple switching is shown in **Figure 5.35**. As can be seen, the switching was not stable during each cycle, and this phenomenon was observed on all devices of the Cu system. The unstable I-V curve of the thin-film with Cu electrodes was caused by the diffusion of Cu into the surface of the TiO_2 film, which formed a Cu-Ti-O interface that increased resistance during the sweeping voltage back.

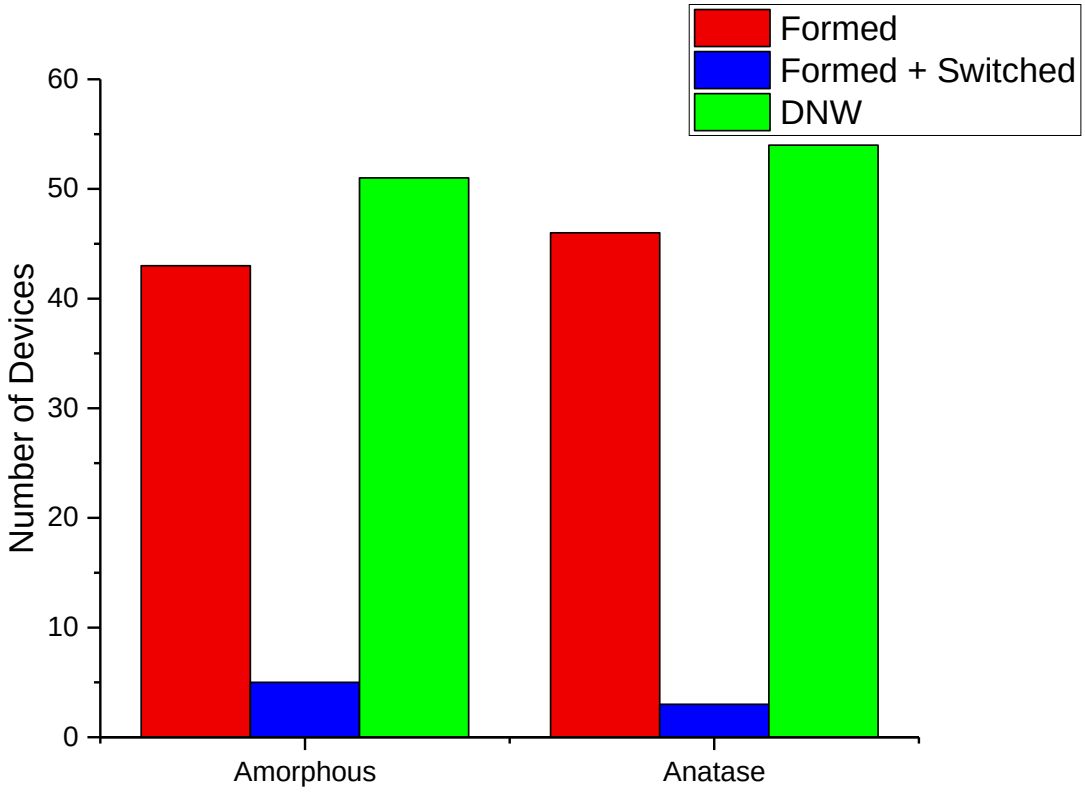

Figure 5.34. High-throughput statistics of device yield of all Cu/TiO_2/Pt-synthesised systems: red colour indicates the number of devices being formed; blue indicates the number of devices being switched; and green indicates the number of devices that did not work (DNW).

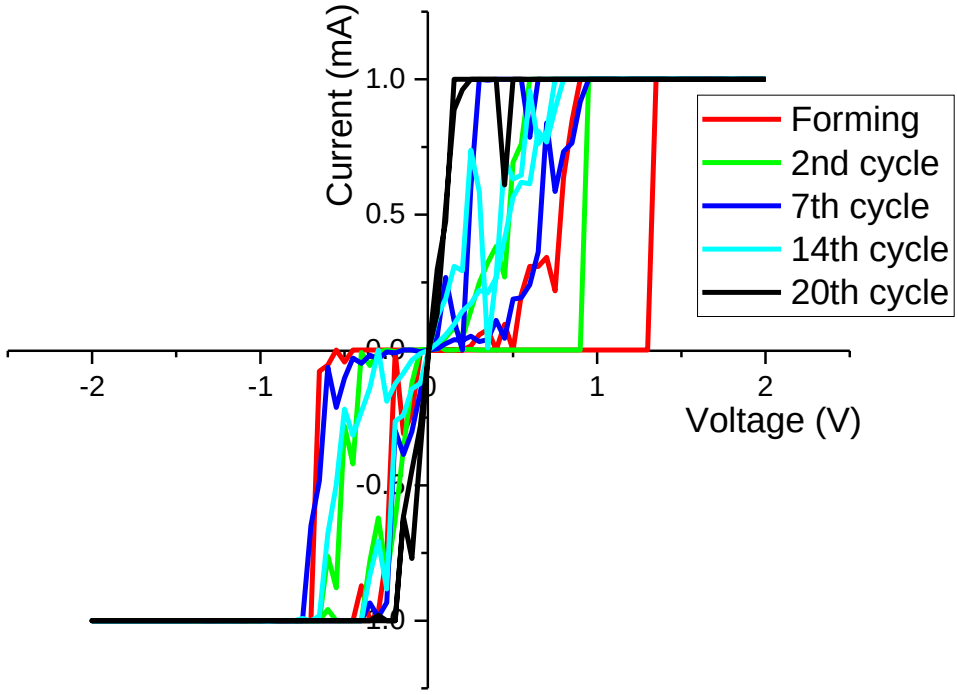

Figure 5.35. Multiple bipolar switching of Cu/TiO_2 (amorphous)/Pt. Unstable switching behaviour due to diffusion of Cu into TiO_2.

5.3.3 Pt/ TiO_{2-x}/ TiO_2/ Pt

An average of 120 fresh devices were formed electrically across amorphous/amorphous and amorphous/crystalline titania with variations of thickness. The study was focused on switching as a function of forming voltage and electric fields in contrast with the simple structure Pt/TiO_2/Pt. Each strip of thickness was tested and calculated both individually and by averaging each strip. **Figure 5.36** shows forming voltage across each strip of thickness for both composite and simple structures as well as limited results found in the literature using the same composite structure. An electric field was obtained for all phases and is displayed in **Figure 5.37**. A comparison between amorphous/amorphous and amorphous/crystalline structures determined that amorphous/amorphous had a lower voltage and electric field than crystalline (Appendix A). It is important to highlight that in order to make a clear comparison between simple/composite structures, the TiO_{2-x} thickness was substituted in the graph. It was found that composite structure had lower forming voltage and a lower electric field. Crystalline TiO_2 prepared by sputtering with a thickness of (TiO_2 = 25 nm and TiO_{2-x} = 25 nm) and TE/BE has been reported[61] in the literature and was compared with our finding. It was shown that our device had a lower forming voltage despite having the same thickness. In addition, device performance was enhanced. This is in general agreement with work done by Lee et al.[168] This improvement could be due to either the fabrication or annealing

process. Another study by William et al.[62] used Pt/TiO_2 (5 nm)/TiO_{2-x} (30 nm)/Pt at which reported an electroforming free, meaning that the initial virgin state was nearly equivalent to the subsequent OFF state. On the other hand, the same structure was reported in Hong et al.,[61] at which the forming process took place in both oxide layers. Our finding shows that a forming process took place on composite structures with lower voltage compared to the simple structure Pt/TiO_2/Pt.

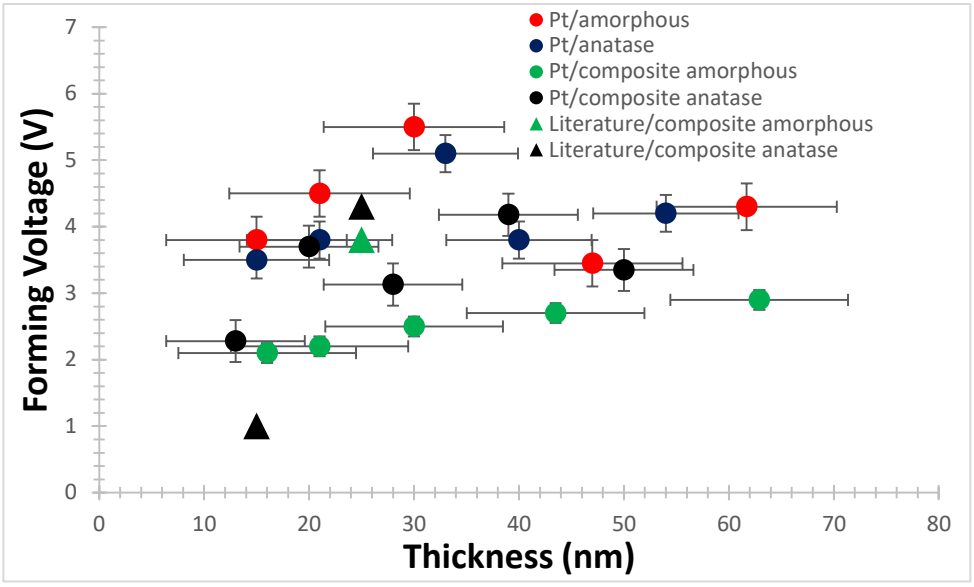

Figure 5.36. Data points of average forming voltage as a function of the thickness of composite and simple structure of titania with similar system studies in the literature (literature references [61,62,169]).

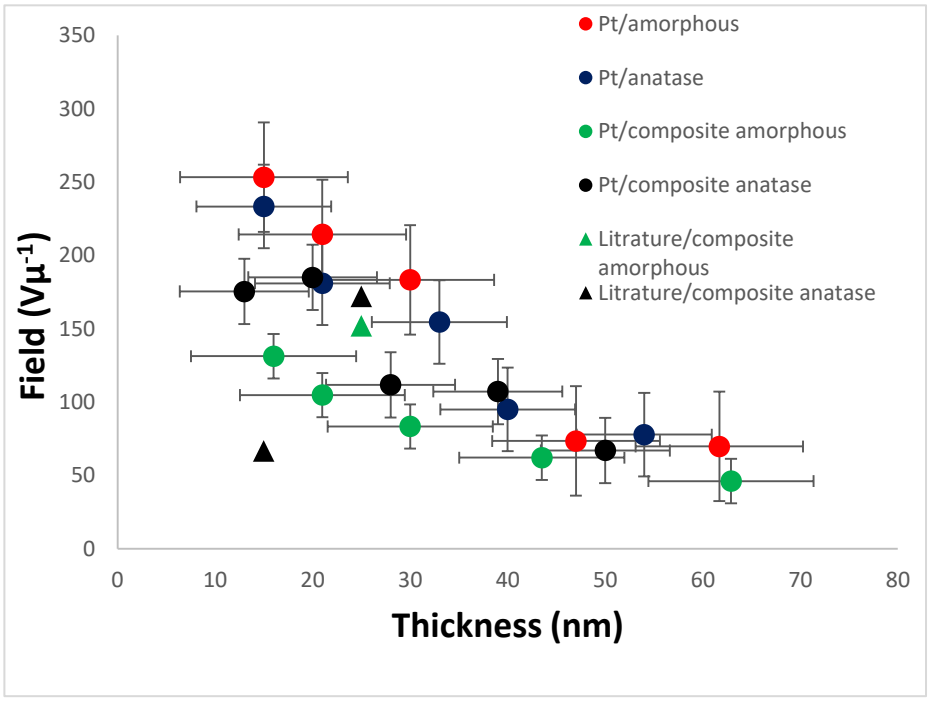

Figure 5.37 Data points of the average electric field as a function of the thickness of composite and simple structures of titania (literature references [61,62,169]).

An average of 60 devices were formed (red colour) in both amorphous and anatase $Pt/TiO_{2-x}/TiO_2/Pt$ systems. The forming voltage was lower in the simple system structure ($Pt/TiO_2/Pt$), while the device yield was higher than in simple systems, as shown in **Figure 5.38**. The stability of devices in this system showed a higher number of stable switching cycles. Devices (8, 12) were cycled as shown in **Figure 5.39**. It is clear that the switching voltage (1^{st} cycle) was nearly similar for the subsequent switching voltage. In addition, it was lower than in the simple structure of $Pt/TiO_2/Pt$. The device exhibited switching (distinguish HRS/LRS) nearly 50 times. After that, as cycle 50^{th} shows, the device became very conductive, and the hysteresis loop was hardly observed. This might be due to the interface between TiO_{2-X}/TiO_2, where both layers lost equilibrium and the oxygen released resulted in increased conductivity.

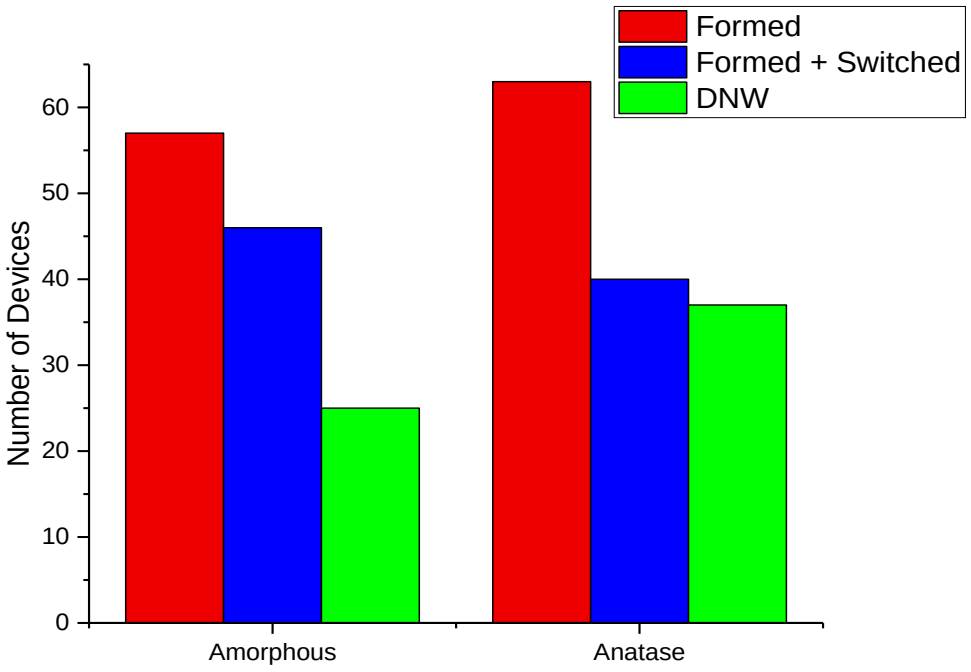

Figure 5.38. High-throughput statistics of device yield of all $Pt/TiO_{2-x}/TiO_2$ /Pt-synthesised systems: red colour indicates the number of devices being formed; blue indicates the number of devices being switched; and green indicates the number of devices that did not work (DNW).

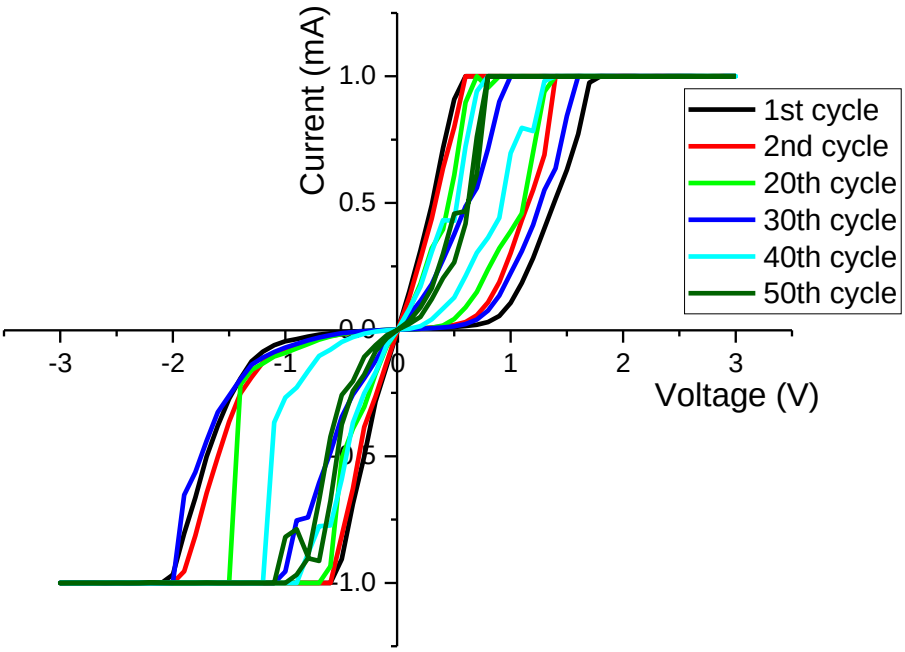

Figure 5.39. Multiple bipolar switching of Pt/TiO_{2-x}/TiO_2/Pt. stable switching and low voltage required comparing to simple structure Pt/TiO_2/Pt.

The insertion of a sub-stoichiometric layer enhanced the device yield and lowered the forming voltage by creating a higher density of oxygen vacancies, which can accelerate the conductivity of the devices without damaging their performance.

Chapter 6: Discussion

6.1 Pt/ TiO_2/ Pt

Generally, there are two dominant types of defects suggested (Chapter 2) to be responsible for the formation of the conducting path, namely titanium interstitials and oxygen vacancies. Marucco et al.[170] reported that the dominating defect of TiO_2 appears thermodynamically controlled, and at a lower temperature, oxygen vacancies are the likely dominating defect. Only at a high temperature will titanium interstitials dominate. Even if the oxygen vacancy defect in TiO_2 is thermodynamically favoured, there is a certain upper limit of concentration of these defects that can be accommodated in TiO_2 if its crystal structure is to be sustained.[171] Once the concentration of oxygen vacancies crosses the upper limit, the phase instability of the original TiO_2 structure becomes high, which might lead to phase transition (Magneli phase). Oxygen vacancies serve as donors in TiO_2, which means an increase in their concentration, resulting in an increase in the concentration of delocalised electrons; therefore, the conductivity of the electrical insulator titania will increase. Rutile has received great interest as a strong candidate for ReRAM applications because it has the highest value for the dielectric constant among the titania phases.[172,105] The high value of the dielectric constant comes from the highly effective charges of Ti and O ions and the soft optical phonon mode in the crystal structure.[105] However, there are many other properties of the phases, such as point defect and grain boundaries, which may strongly influence the effectiveness of the phase as a reversible switch. Hence, these properties also play a role in determining the forming voltage.

6.1.1 Forming Step (HRS ─ LRS)

The underlying mechanism of switching in a device can be inferred from characteristic switching behaviour and variations in device construction, such as thickness and the active switching layer. The forming process plays an important role in changing electrical conductivity, oxygen ion migration and physical deformation, which influences the subsequent resistive switching characteristics. The forming process is a partial breakdown of the material. During the forming process, a conducting path forms as a ‘soft’ (or partial) breakdown in the dielectric material, with oxygen vacancies introduced in the TiO_2 that result in a reduced conducting phase. Joule heating is a voltage-induced thermal dielectric breakdown process enhanced by moving oxygen from an equilibrium state to a

non-equilibrium state that causes excessive power dissipation.[160] It is well established that Joule heating is proportional to resistance and increases as the square of the current.[173] Thus, at high IC, memory performance might be affected due to large heat generation. For this reason, in this work, the IC was as low as 1 mA in all devices in the initial pristine state. The accumulation of oxygen vacancies inside the TiO_2 layer forms a conducting path that connects two separate electrodes, which eventually initiate this transition. There are studies in the literature which have experimentally identified that the conductive filament in TiO_2 is composed of the so-called Magneli phase Ti_nO_{2n-1}.[31,157,32] It can be assumed that the Magneli phase is responsible for forming the filament.[33,34] To form the initial filament (conducting bridge) comprising the Magneli phase, a large concentration of oxygen vacancies must be generated in the oxide in the FS, as shown in **Figure 6.1,** at which stoichiometric TiO_2 is reduced to sub-stoichiometric TiO_{2-x} and the conductive path is created. Even though a lower IC was applied (1 mA), physical deformation during the forming process was observed, which might be due to oxygen gas evolution, as shown in **Figure 5.9**. The same observation was reported by Yang et al.[174] The energy needed in the thermochemical reaction is provided by Joule heating from the flowing current (**Figures 5.1, 5.3** and **5.5 A**) for amorphous, anatase and rutile, respectively. The conduction of HRS in all phases of Pt/TiO_2/Pt structures shows thermally activated behaviour that suggests filament-type resistive switching as already reported.[13, 24,30]

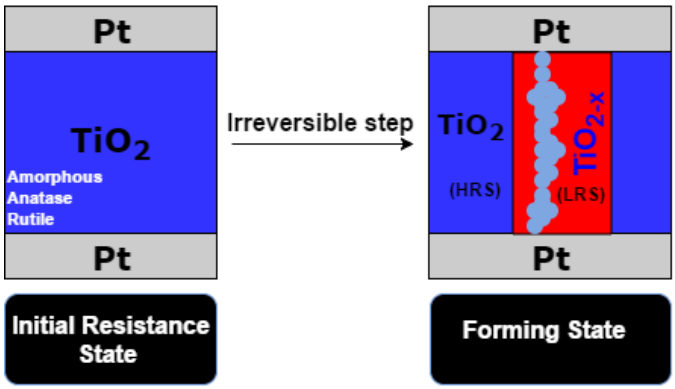

Figure 6.1. Diagram presenting the forming process and creation of conductive path of Pt/ TiO_2/ Pt structures.

6.1.2 RESET Step (LRS ─ HRS)

One detail of the RESET mechanism is still unclear: It requires higher current each time to RESET the device.[41,74] However, it can be suggested that RESET could be attributed to local power dissipation due to high current density in the conductive path, where power dissipation induces high temperature in the conductive path, causing either

the diffusion of vacancies out of the path or the diffusion of other impurities into the path, or even phase transition.[31] Therefore, the locally ruptured part of the conductive channel becomes insulating so that the overall resistance of the channel increases. This ruptured part may consist of a more insulating phase, the formation of which is again thermally activated through localised Joule heating.[107] A thermally induced redox process near the interface between the metal electrode and the oxide (**Figure 6.2**) is widely accepted and reported as the mechanism behind the formation and rupture of the conductive filaments.[24,31] The resistance of the RESET state is generally much lower than that of the pristine sample but is still far higher than that of the SET state. The promising aspect of this model (filamentary type) is that it does not require the unidirectional motion of oxygen ions during repeated set/reset switching. The material simply changes its phase from metallic (or highly conductive semiconducting) magneli to less conducting defective TiO_{2-x}. In this symmetric binary system, as the electrode material is inert, it could be assumed that oxygen vacancies diffuse out the conductive path due to Joule heating, at which point an oxygen atom diffuses into the conductive path and is exchanged with an oxygen vacancy, which therefore decreases the conductivity of the system; meanwhile, resistance is significantly increased due to the diffusion of oxygen atoms, which would be the major factor for switching from the ON state to the OFF state. It was reported that it does not matter how many oxygen vacancies are needed for reset: Only one oxygen vacancy exchanged with one oxygen atom would be enough to change the state of the device.[109]

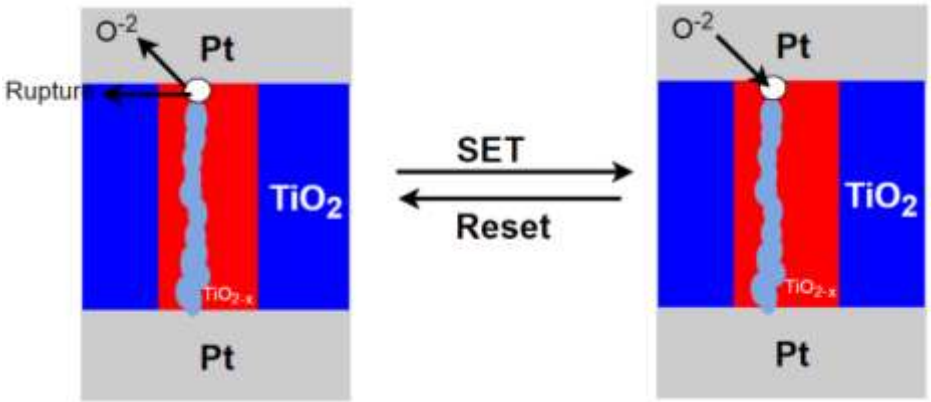

Figure 6.2. Diagram presenting RESET and SET process of $Pt/TiO_2/Pt$ structures.

6.1.3 SET Step (HRS ─ LRS)

In the RESET process described in section 6.1.2, localised heat is suggested to occur in the RESET step; and in the subsequent cooling, recrystallization in a more oxygen stoichiometric anatase or rutile phase takes place,[169] (Magneli phase) as shown in **Figure**

5.2, 5.4 and **5.6 A** for amorphous, anatase and rutile, respectively: This process is propagated by the adjacent crystalline phase around the filament. These re-formed (set process), defective anatase or rutile phases will likely have greater electrical conductivity than pristine stoichiometric TiO_2 (**Figure 5.2, 5.4** and **5.6 B**) for amorphous, anatase and rutile, respectively. However, it still has higher electrical resistance than the Magneli phase.

All the mechanisms mentioned above focused on the unipolar switching mode; bipolar behaviour was observed only on amorphous titania, as described earlier in **Figure 5.10.** The mechanism here was considered to be due to the electronic or ionic effect, in which electronic and ion migration play an important role in this type of switching. When a substantial Schottky potential barrier is present at the Pt/TiO_2 interface, electronic/ionic bipolar resistive switching (BRS) occurs, which lowers the Schottky barrier due to the low oxygen vacancy concentration near the electrode. Jeong et al.[164] have reported that an increase in the concentration of oxygen vacancies leads to a decrease in the Schottky barrier height at the Pt/TiO_2 interface.[180,181] Sawa et al.[31] reported that the filament was due to the localised drift of oxygen vacancies. It was also found that localised drifting of oxygen vacancies along the direction of the electric field is highly likely to occur with favourable defect migration pathways, such as grain boundaries.[172] The result obtained suggests that the RESET process is due to ruptured filaments (**Figure 6.2**) when reversed voltage is applied to the device.

It was reported that[160] stable resistive switching is due to the formation of the crystalline TiO_2 layer, but such annealing can modify the barrier highest at the Pt/TiO_2 interface,[175] causing unreliable switching performance; as the temperature increased, the grain size increased, and therefore the current path through the grain boundary became unstable, as found by Kim et al.[175] They found that upon crystallisation at high annealing temperatures, the titania exhibited only unipolar behaviour. On as deposited titania (most likely to be amorphous), bipolar switching was observed.

It was observed that thinner devices required higher voltage (**Figure 5.27**) and therefore a higher electrical field (**Figure 5.28**). This could be explained by a lower density of defect, which requires higher voltage. It was also observed that the distribution of forming voltage and the electrical field of thicker devices ($D > 150$ nm) was stable as compared to the random distribution of thinner devices ($D \leq 60$ nm). This could be due to the defect size and the physical region of switching: In the case of the thinner device, the defect size was small, which in turn provided a variety of forming voltage. In an

amorphous material (in general), there is no band structure. Nevertheless, notions such as 'band gap' or 'band structure' are still applied, but in a broader sense, as compared to crystalline materials.

The forming voltage of amorphous was less affected by thickness, which might be due to the point defect presented in amorphous titania. Whereas in crystalline (anatase and rutile), the forming voltage mostly depended on thickness. This, again, depends on the physical region of switching: In crystalline, both the point defect and grain boundaries were presented. If the switching region is on the boundaries of the grain, the voltage will be low. On the other hand, if the switching region is far from the boundaries, then the voltage will be higher. This could explain why higher voltage is required in anatase, as shown in **Figure 5.27**.

6.2 Cu/ TiO_2/ Pt

One of the factors that might affect the resistive switching properties of the MIM structure is contact between the metal electrode and the oxide material. The interface between the metal electrode and the oxide material affects the carrier injection. This interface determines the Schottky barrier height induced by the metal work function and the Fermi level of the oxide material.[97]

6.2.1 Forming Step (HRS ─ LRS)

There are two different filament formation mechanisms involved with different major carrier sources that make up filaments: the foreign atom and intrinsic defects. The first only relies on the cation from electrode materials, such as Cu, which is electrochemically active. This can be easily oxidised to metal ions followed by drifting from anode towards cathode with the accumulation of these metal atoms. It was reported that[75] the filaments will grow parallel to the direction of the applied electric field. As soon as these metal filaments are connected, the two terminal electrodes of the device switch. The conductive filament of the forming process shown in **Figures 5.11** and **5.13** involves the following steps: (i) When voltage is applied to Cu, an electrochemical reaction occurs in the Cu top electrode (**Figure 6.3**), which oxidises the Cu metal atoms to metal ions; (ii) the highly mobile cations drift in the ion conductive layer under the electrical field; then, (iii) the metal ions are deoxidised back to metal atoms at the Pt bottom electrode. As this

process continues, metallic filaments are established between the two electrodes and the device switches to LRS, as shown in **Figure 6.3**.

The second type is related to anions, such as oxygen ions. Under a high electrical field, oxygen ions will migrate from the lattice positions; defects like single oxygen vacancies are generated by the assistance of thermal effects. This will change the stoichiometry of the film and lead to an increase of its electronic conductivity due to defect creation (oxygen vacancies). When these vacancies form a local path, the device can be switched from HRS (OFF) to LRS (ON) (**Figure 6.3**).

It can be gleaned from many published papers[41,75,160,172,] that the choice of electrode materials is predominantly governed by thermodynamic aspects like Gibbs free energy and the free energy of oxide formation. Cu has slightly higher free energy than Ti has, which make it difficult to reduce Ti. Due to high diffusivity, Copper, could migrate into the TiO_2 bulk from the top electrode and affect the switching characteristics. The migrated atom can connect to Ti in the conducting path after the forming or SET process (**Figure 6.3)**. This could demonstrate that the conduction path of Ti is shorter due to the migrated portion.[42,110] A similar consideration was reported by Kim et al.[42] The Gibbs energy of Cu is smaller than it is for Ti. Hence, few oxygen ions drift to the top electrode from the TiO_2 thin film; in this case, the change in resistance is mainly affected by Joule heating.[76]

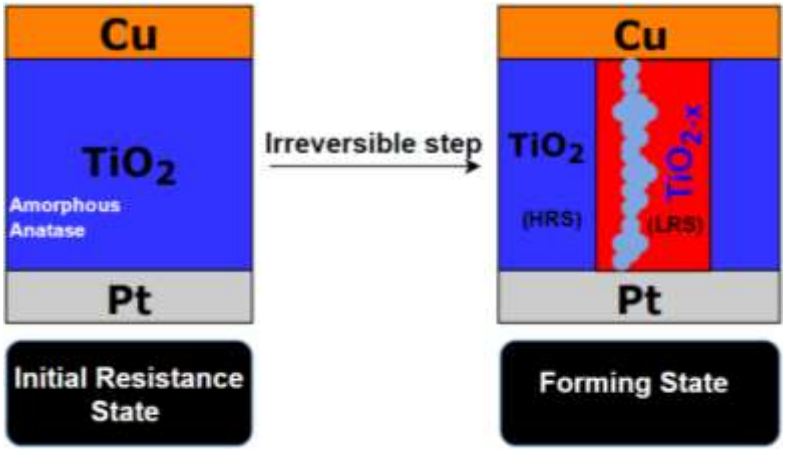

Figure 6.3. Diagram presenting the forming process and creation of the conductive path of $Cu/TiO_2/Pt$ structures.

6.2.2 RESET Step (LRS ─ HRS)

The rupture of the filament that led to switching the device to HRS (OFF) is called the RESET process. Filament rupture processes can also be divided into two classes, one involving electrochemical reactions and one involving thermal effects. By changing the polarity of the bias voltage, an electrochemical dissolution of the conductive bridges takes place which may cause the device to RESET to HRS (**Figure 6.4**). Joule heating could also cause the rupture of the filament and the resetting of the device to HRS. This is not the case for an inert electrode such as Pt, for which the RESET process has only a thermal effect and a higher IC than that applied to the forming and SET processes is required, which means that a large amount of heat is generated to repture the filament and switch the device to the HRS (OFF) state.

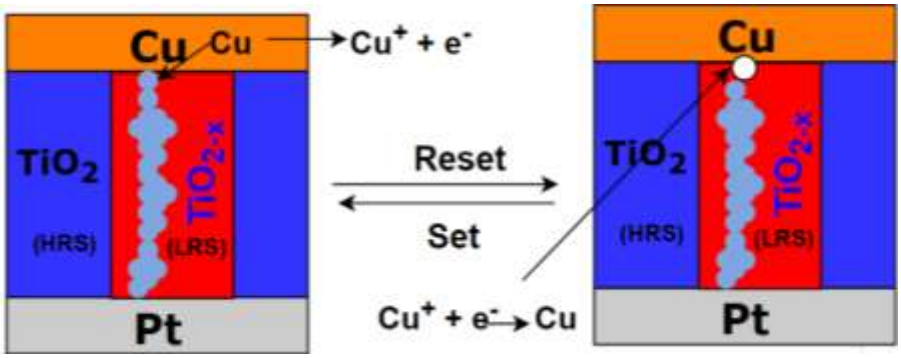

Figure 6.4. Diagram presenting RESET and SET processes of Cu/TiO_2/Pt structures.

6.2.3 SET Step (HRS ─ LRS)

After resetting the device to HRS, and by changing the polarity of bias voltage, the same process mentioned in the forming process (section 6.2.1) take place, at which point the device switches from HRS to LRS. However, the SET process had higher conductivity than the forming process, as shown in **Figures 5.12** and **5.14**. A degradation of the hysteresis loop was observed, which may be due to a weak filament being created and then broken quickly when the voltage swept back to zero.

Electrode materials and oxidation reactions at the interface of the TE and TiO_2 affected the resistive switching characteristics and therefore the reliability of the devices. Therefore, proper selection of the materials used for the top electrode is very important: The chosen metal must not be easily oxidizable and must be cost effective. From both literature results and our results, it seems feasible that Cu migrating rapidly into TiO_2 to form a conductive path makes the device switch. Accordingly, it can be concluded that for

reliable and stable device performance, the electrode metal should have higher Gibbs free energy than Ti. During high temperature processes, such as annealing or Joule heating, and owing to the higher Gibbs free energy, electrode metals are more prone to oxidation than Ti. The higher Gibbs free energy of these metals ensures a lower probability of electrode metal reduction during high temperature operation. Moreover, metals with a high Schottky junction with TiO_2 exhibit better switching behaviour as well as metal has higher work function to make Schottky contact with TiO_2.

The forming voltage and electric fields across devices, shown in **Figures 5.32** and **5.33**, reveal that Cu-based amorphous titania did not show dependency on thickness, whereas Cu-based anatase titania was affected by variations of thickness, with thinner titania requiring higher forming voltage and a higher electric field. This is consistent with Pt-based titania. However, Cu-based titania showed a much lower forming voltage and electric field compared to the Pt-based system. This could be attributed to the high diffusion rate of Cu. The results were validated with literature reporting different methods for preparing such devices.

6.3 Pt/ TiO_{2-x}/ TiO_2/ Pt

TiO_{2-x} (oxygen poor)/TiO_2 (oxygen rich) multilayer homojunctions were studied as alternative resistive switching structures for both high and low resistance transitions.

6.3.1 Forming Step (HRS ─ LRS)

TiO_2 prepared by sputtering with a thickness of (TiO_2 = 25 nm and TiO_{2-x} = 25 nm) and Pt as TE/BE has been reported[61] in the literature. It has been shown that a forming process is required at the pristine stage of the device. Another study by William et al.[62] using Pt/TiO_2 (5 nm)/TiO_{2-x} (30 nm)/Pt reported an electroforming free device, meaning that the initial virgin state was nearly equivalent to the subsequent OFF state. On the other hand, the same structure was reported in Hong et al.,[61] in which a forming process took place in both oxide layers. Our findings showed that a forming process took place on composite structures with lower voltage in the device with a thicker layer of TiO_{2-x} (**Figure 5.18** and **5.20**). However, it is not as low as free forming as reported by William et al.[62] Based in literature reports and our findings, it is believed that during the forming stage (**Figure 5.18** and **5.20**), there is a possibility that the oxygen ions could be trapped and un-trapped within the TiO_{2-x} layers under the applied bias, making a conductive path that

switches the device from HRS to LRS. As shown in **Figure 6.5**, the conducting paths were generated inside the TiO_2/TiO_{2-x} homojunctions during the forming process. The TiO_2 layer can act as an oxygen ion reservoir, while the TiO_{2-x} layer has a lower oxygen ion concentration. Therefore, the TiO_{2-x} layer is more sensitive to the movement of oxygen ions than the TiO_2 layer.

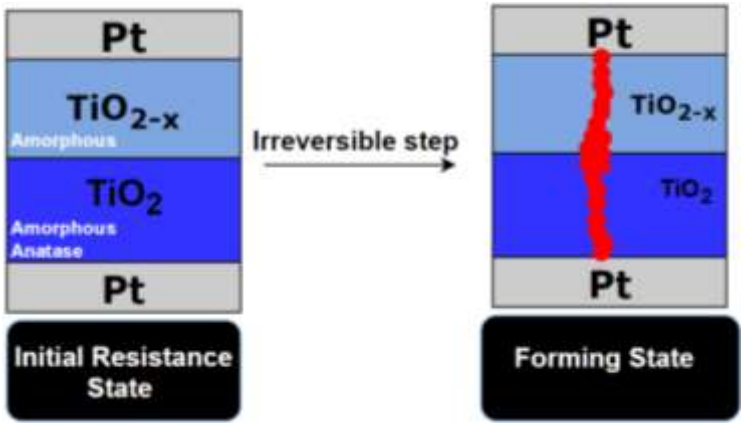

Figure 6.5. Diagram presenting the forming process and creation of conductive path of Pt/ TiO_{2-x}/ TiO_2/ Pt structures.

6.3.2 RESET Step (LRS ─ HRS)

After forming the device, and when reverse bias was applied, oxygen ions drifted from the TiO_2 layers to the TiO_2/TiO_{2-x} interface; oxidation then occurred at the interface region of the TiO_{2-x} layer, forming a fully oxidised layer. In addition, partial oxygen ions went into the TiO_{2-x} layer for ion trapping. As shown in **Figure 6.6 A**, this oxidised layer and ion trap in the TiO_{2-x} layer caused the device to switch into the HRS state (likely due to the rupture of filaments at the interface layer by preventing the movement of conducting electrons).

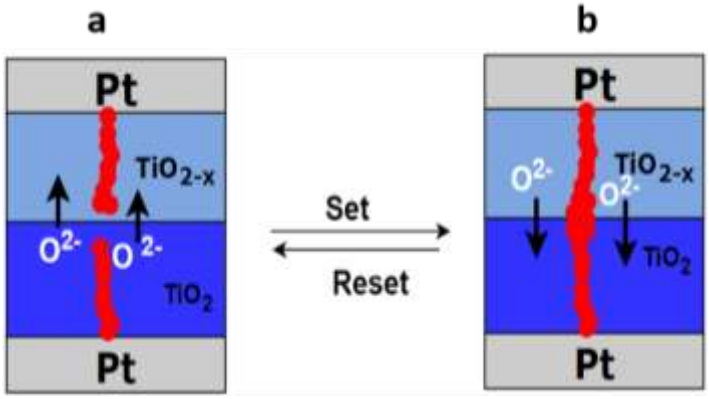

Figure 6.6. Diagram of RESET and SET processes of $Pt/TiO_{2-x}/TiO_2/Pt$ structures.

6.3.3 SET Step (HRS ─ LRS)

When a forward bias was applied, as shown in **Figure 6.6 B**, the oxidised oxygen ions at the interfaces and trapped ions in the TiO_{2-x} layer moved back towards the TiO_2 layer, likely due to the formation of filaments at the interface layer, switching into the LRS state.

The result obtained from the resistive switching phenomenon in composite structures seems to be a combination of the redox and conduction paths, resulting from ions drifting between the oxygen rich and oxygen poor regions in the composite structures; whereas the conduction path was obtained from bipolar switching behaviour (**Figure 5.19** and **5.21**). It shows typical I-V characteristics of bipolar switching phenomenon. The thickness of TiO_{2-x} (oxygen poor) plays an important role in forming voltage, which decreases with increasing thickness of TiO_{2-x} compared to simple structures of $Pt/TiO_2/Pt$. The improvement (low voltage) could be attributed to the ability of Ti to absorb oxygen atoms.

The result obtained in this system suggests that the incorporation of TiO_{2-x} into the composite structures plays an important role in lowering forming voltage: low forming voltage results in a higher yield of switching devices.

Chapter 7: Conclusions and Future Work

7.1 Conclusion

An average of 430 devices were synthesised and tested using physical vapour deposition and high-throughput screening methodologies towards ReRAM application. After studying the results and comparing them with the literature, it was possible to validate the use of a first-time methodology applied to ReRAM applications. Such a methodology had the power to produce different titania phases (amorphous, anatase and rutile). Most of the anatase devices were obtained without post annealing in a tube furnace. Characterisation techniques were employed to demonstrate that the phases and structures were successfully synthesised, which also suggests that higher oxygen content during synthesis converts the nanocrystalline film to a rutile structure, as shown in **Figure 4.3** and **Figure 4.4**. These characterisation results were consistent with the literature.[155,156,157,158] One of the contributions of this project, which is directly linked to the aims discussed in section 1.2, was the synthesis of the largest gradient of thickness reported to date. It is clear from XPS and 4pp characterisation that the sub-stoichiometric and stoichiometric phase were produced as required. The Cu system and the composite system showed a much lower forming field than the simple structure of Pt-based titania.

The results obtained throughout this high-throughput research suggests that in general, for all the systems studied, the forming voltage was slightly dependent on the thickness of the switching layer of TiO_2, but it was much more dependent on the electric field across the layer. It was also confirmed that thinner devices require higher voltages and higher electric fields due to the lower density of defects. Based on our results, there was no phase dependent on the devices, as all the titania phases behaved in relatively the same way. The type of electrode materials has an impact on resistive switching characteristics. The incorporation of TiO_{2-x} into the composite structures played an important role in lowering the forming voltage: Low forming voltage results in a high yield of switching devices.

7.2 Future Work

This project has demonstrated the validity and utility of high-throughput methodologies in the synthesis of ReRAM functional nanomaterials and structures. Hence, it should be a feasible system for the synthesis of any structure of materials (oxide, nitride or carbide). Despite the project's achievements, there are still limitations due to the time period of this thesis and the complexity of the circuit integration in our laboratory.

For this project, two fabrication masks, with a diameter of 250 μm and 50 μm, were made to investigate the dependency on pad size. Unfortunately, the small mask was not tested electrically during the project for a number of reasons. First, the camera and optics employed resulted in low image resolution, which made it difficult to image the smaller contact pads and therefore align the needle on them. In addition, the probe measurements were made manually (one by one). Following the completion of this work, the probe station was automated and the camera resolution increased, allowing the automation of high-throughput screening. A significant number of device libraries were prepared in the course of this work, and these should be measured using the high-throughput probe station in order to further improve the statistics of the datasets. An alternative approach to the electrical screening method would be to synthesise compositional gradient materials on a chip and apply multiplexing electronics in order to obtain the switching characteristics. This approach would have the advantage of using smaller node sizes in the device (down to tens of nm), closer to the dimensions in ReRAM memory. It is worth noting that an automated screening system already exists in the market.[184] However, this screening system is designed for crossbar arrays, as shown in **Figure 7.1**, which makes it difficult to test the system in a combinatorial fashion using such an approach. Therefore, the development of a new chip design is required for testing and adaption with an HT-PVD screening workflow. Such a chip should be designed so that each device (through either the top or bottom electrode) is separated from each other to allow independent tests of devices across gradients of thickness or compositions, as shown in **Figure 7.2**. This would have the advantage of reducing the leakage current from adjacent devices in a crossbar configuration, since each device would be tested independently. Achieving this will greatly reduce the time and cost in the research environment and will accelerate the discovery of materials applicable for ReRAM application.

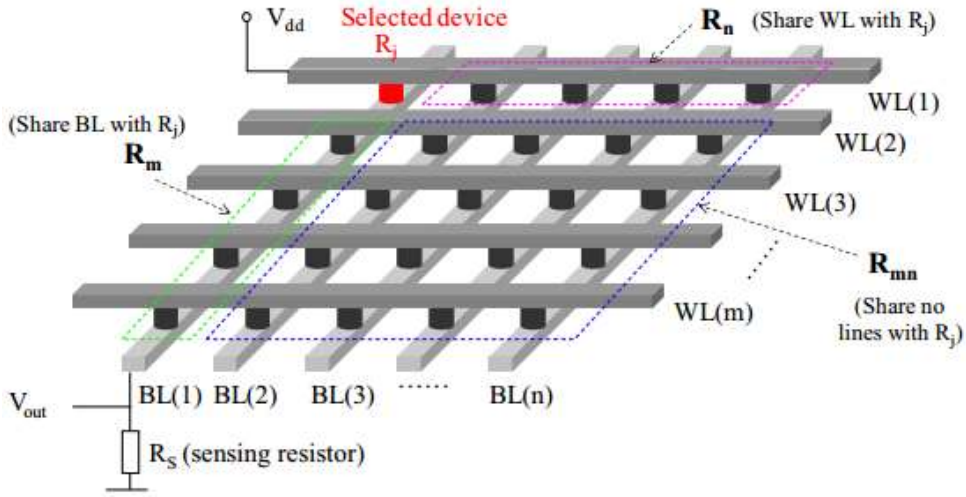

Figure 7.1. A schematic of a crossbar array with a horizontal word line (WL) on the top and a vertical bit line (BL) at the bottom. The upper left corner is the selected device (Rj) at which some device is half-selected (Rm, Rn) with Rj, and this makes it difficult for the HT-PVD approach to move from one electrode to another and test them independently.[185]

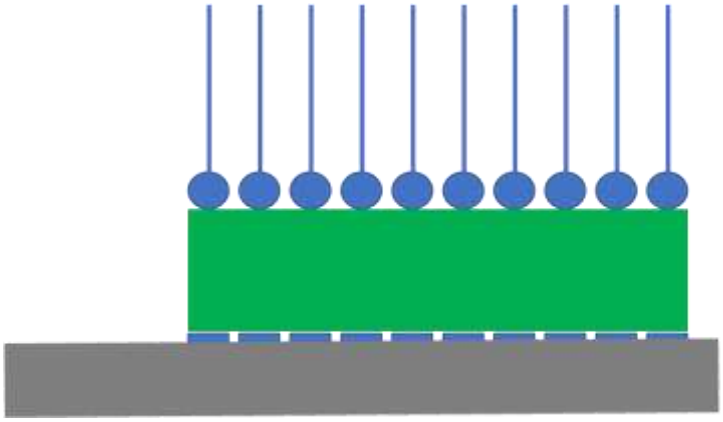

Figure 7.2. Diagram of a potential ReRAM testing chip. The cell with a capacitor-like structure in which a compositional gradient-insulating oxide (green) is inserted between two metal electrodes allows devices to be tested independently from each other across combinatorial libraries. The top electrode is a single bar, with the bottom electrodes being independently addressable.

One of the difficulties of this project was that we have not been able to study the filament (conductive path) in depth, though doing so would lead to a better understanding of the configuration needed for the right mechanism for each system prepared. Hence, it is worth considering high resolution TEM to study the filament. Such experiments for HfO_2 have shown that the filament changes with reversible switching.[186]

A high-throughput memory-testing platform should be developed by evaluating and connecting a Keysight 5600LS AFM as a microelectrode and a Keysight B1500A semiconductor analyser as a signal source and measuring device. Development of such a

system would open the door for new ways of investigating the location of filaments and their shape.

IC plays a key role in switching behaviour, especially in the forming process. As mentioned in Chapter 5, IC in this project was kept at 1 mA to minimise any deformation in the systems during the forming process. More focus should be placed on studying the effect of variations in IC during the forming process. This could be addressed in a more high-throughput screening probe station or chip.

Pulsed I-V testing is ideal for preventing device self-heating or minimising charge trapping effects when characterising devices. By using narrow pulses and/or low duty cycle pulses rather than DC signals, important parameters are extracted while maintaining the device under test performance. It also provides time control before and during the forming process. During this project, we were not able to perform Pulse I-V measurement to obtain dynamic characterisation. although it has been used to evaluate the switching speed[84] for TiN/ZnO/Pt devices (**Figure 7.3**). Endurance and retention can also be obtained using such a test.

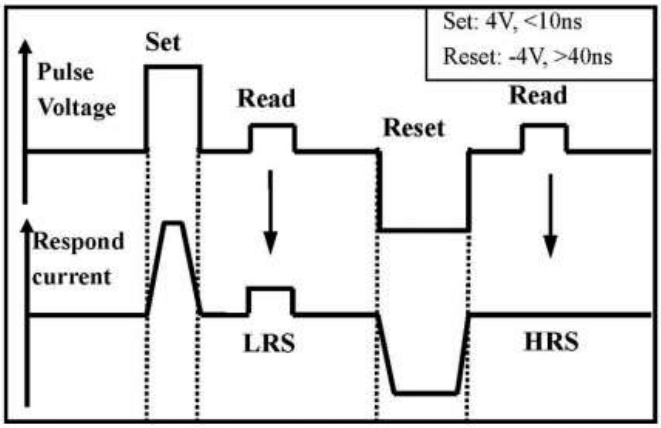

Figure 7.3. Sequences of set/reset voltage pulses used to study the electric pulse-induced reversible effect and the corresponding respondent current.[84]

Future ReRAM projects should consider a doping system which enhances conductivity and reduces the forming voltage. An example of such a system would be Pt/TiO_2/Pt with a low doping concentration of Cu (1–5%). By achieving this and combining it with the data already obtained, the system would greatly improve understanding of the mechanism involved. Improvement in endurance and reduction of forming voltage were already observed.[187]

It is known that during the forming process, a large number of oxygen vacancies are introduced to the system.[162] It is necessary to quantify the oxygen vacancies in the TiO_2

system during the forming process to clarify the relationship between the density of oxygen vacancies and the forming voltage. This would help increase control of the forming process, which is one of the major issues with ReRAM application. Studying the shape differences and chemical compositions between HRS and LRS gave us more detailed data about the RS phenomenon.

Perovskite materials (ABO_3, where A and B are two cations, O is an anion) have been prepared using the HT-PVD method, employing MBE in many fields, such as electrocatalysts[188] and battery application,[134,189] due to their interesting properties. The method has shown the ability to provide bistable switching of conductance between non-metallic and metallic in memory devices.[48] Perovskite-structured oxides can accept considerable substitutions in one or both cationic sites (i.e., A and B sites) while retaining their original crystal structures. Such a feature provides chemical tailoring of the materials via partial replacement of the cationic site(s) with foreign metal ions, hence modifying their properties.[137] The compositional gradient of perovskite has been determined,[136,137] revealing dielectrics properties, such as dielectric constants and dielectric losses. Dielectric losses refer to the dissipation of electrical energy resulting in deviations from ideal capacitor behaviour that might affect the reversibility of switching ReRAM devices. Dielectric losses should be as minimal as possible (**Figure 7.4**) in order to obtain reversible switching. The feasibility of such materials in ReRAM applications is high considering the areas in which they have been applied.

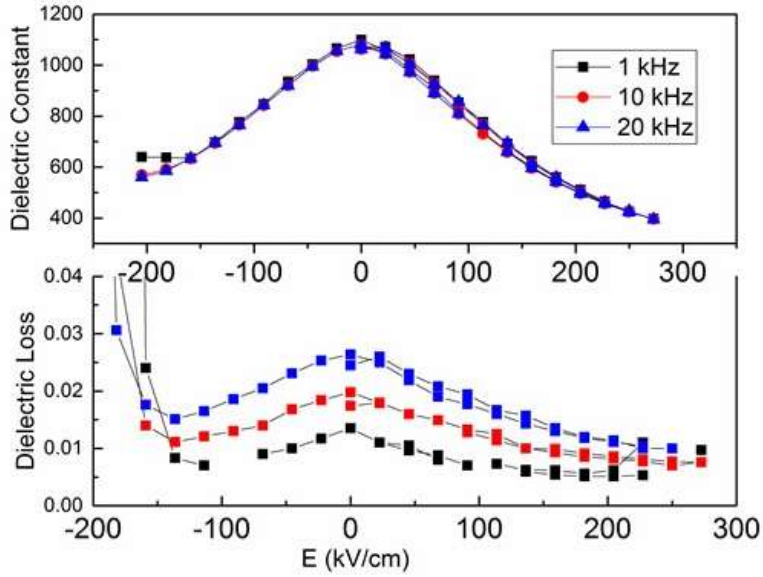

Figure 7.4. Electric field of dielectric constant and loss tangent of $BaSrO_3$ thin film, measured at different frequencies.[190]

Appendices

Appendix A Figures

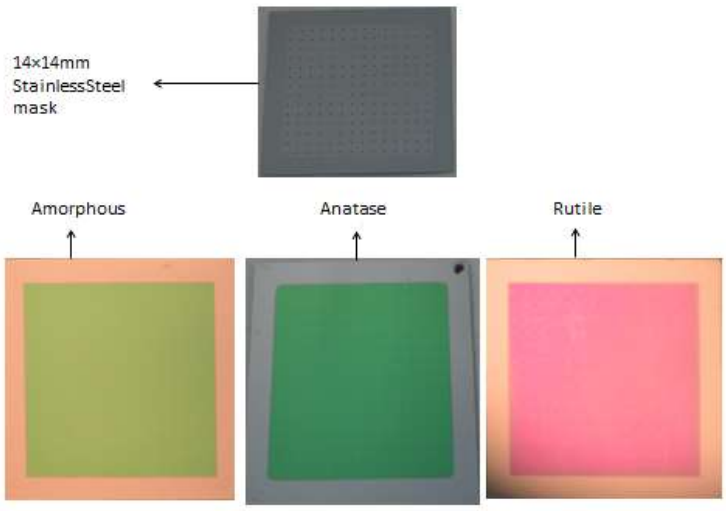

Figure 3.1. Photograph of samples prepared using A 14 × 14 matrix stainless-steel masks (250 micron).

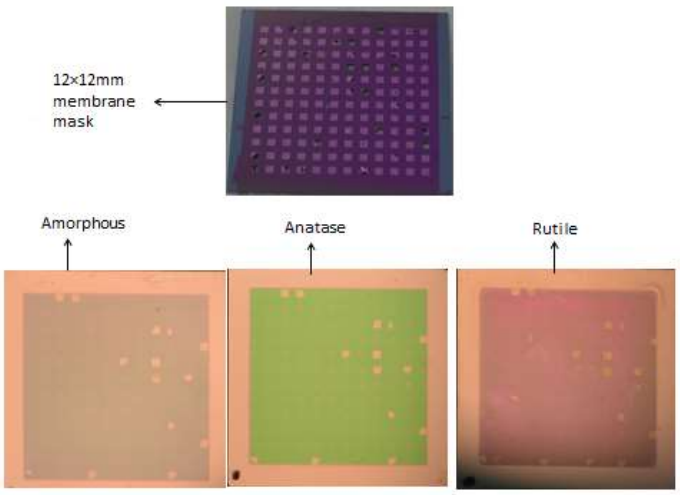

Figure 3.2. Photograph of samples prepared using A 12 × 12 membrane mask, fabricated by a member of our group.

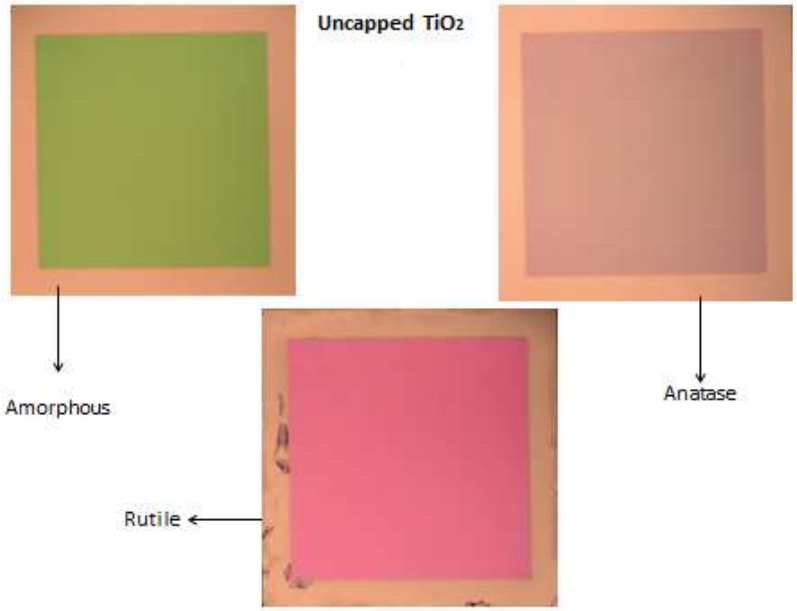

Figure 3.3. Photograph of thin-film oxide without Pt contact pad.

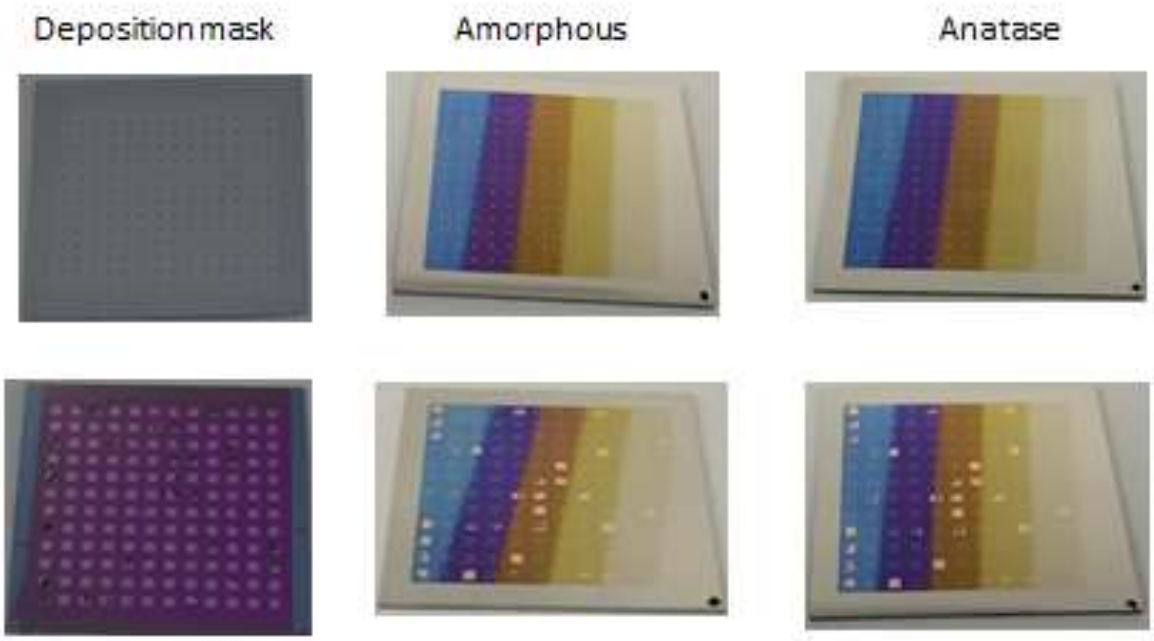

Figure 3.4. Photograph of samples prepared by Cu/TiO2/Pt using a variety of masks.

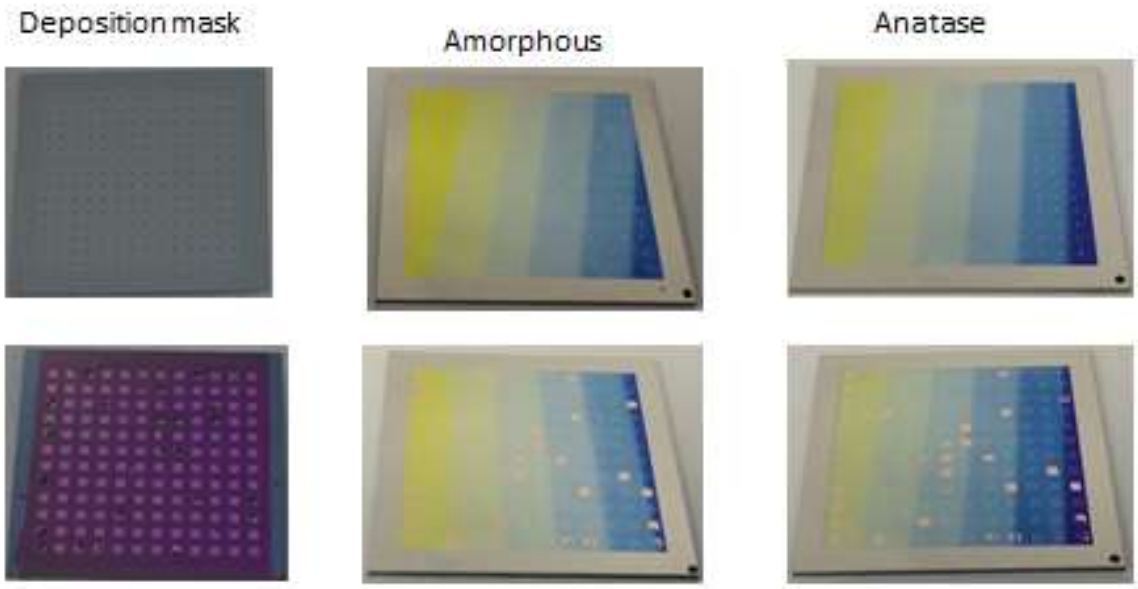

Figure 3.5. Photograph of samples prepared by $Pt/TiO_{2-x}/TiO_2/Pt$ using a variety of masks.

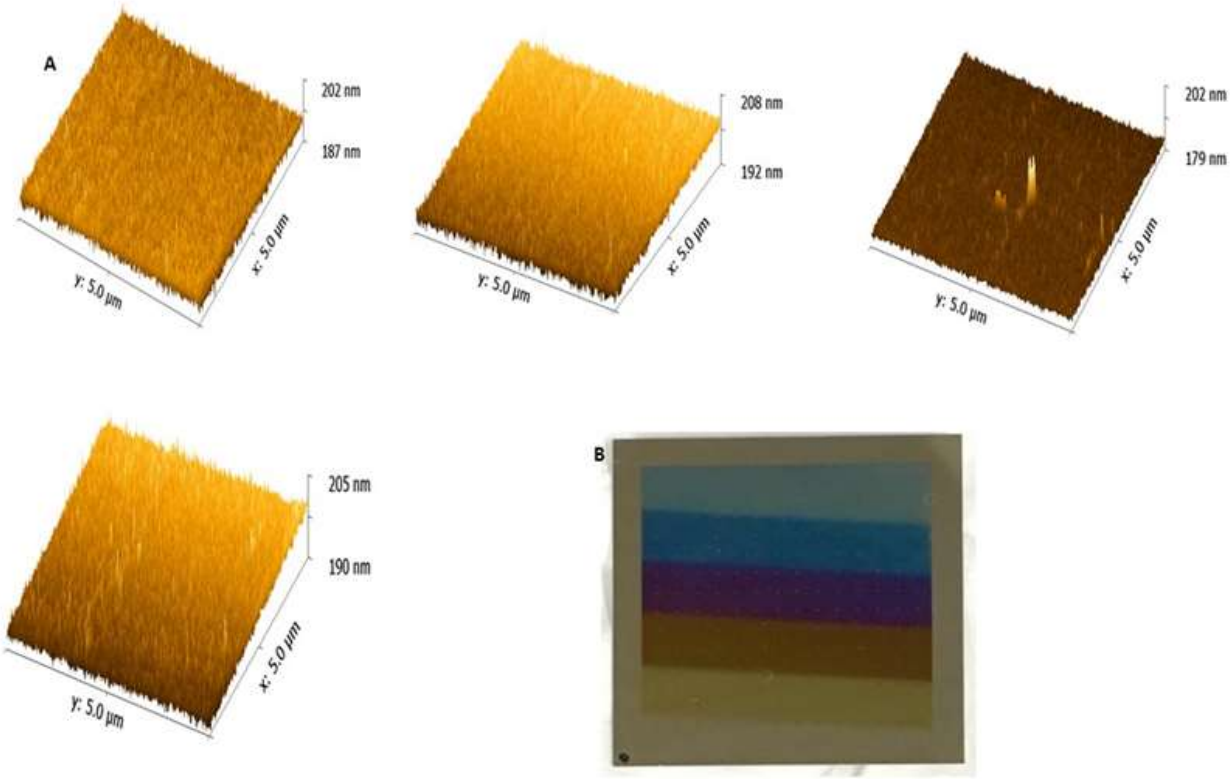

Figure 4.1. (A) AFM topography of amorphous titania across different thicknesses (10 to 50 nm, respectively). (B) Sample picture.

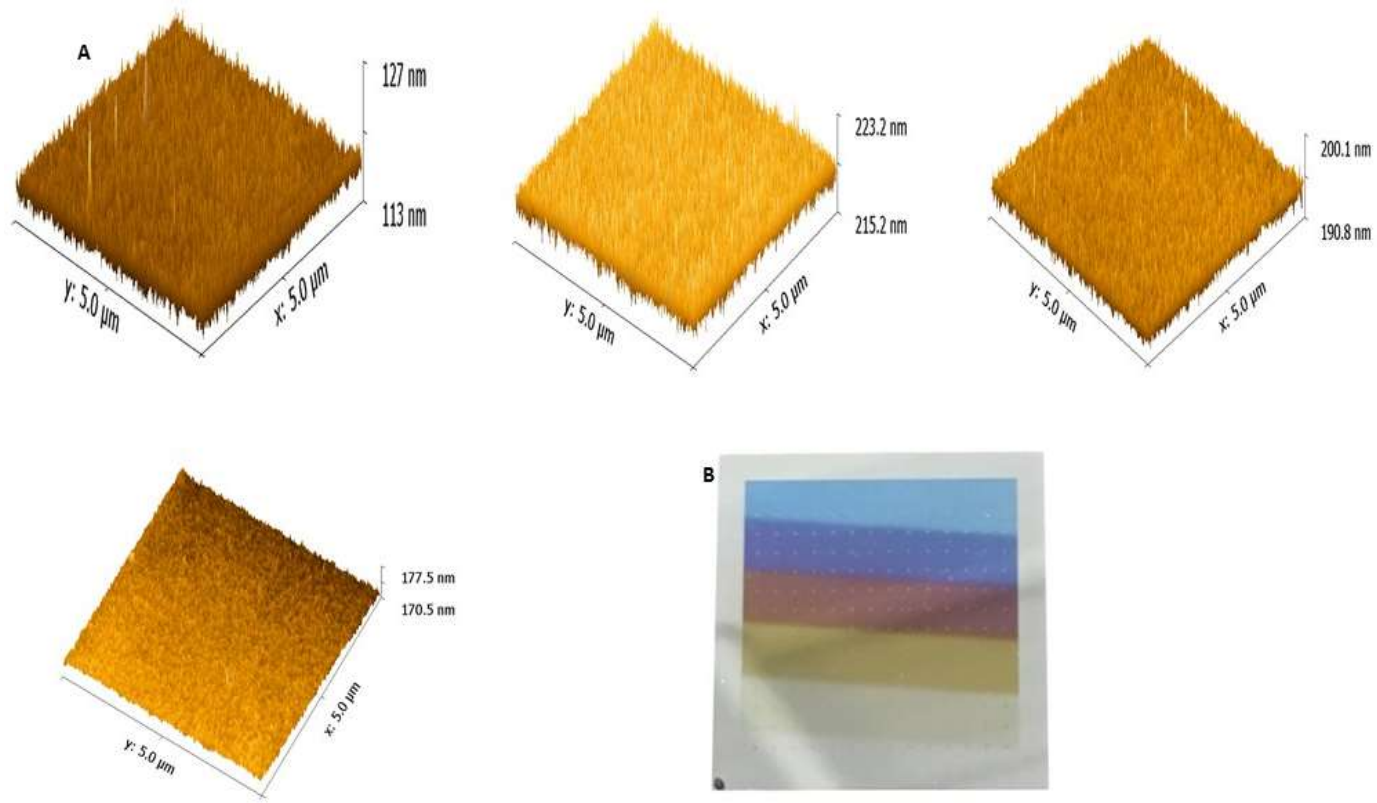

Figure 4.2. (A) AFM topography of anatase titania across different thicknesses (10 to 50 nm, respectively) (B) Sample picture.

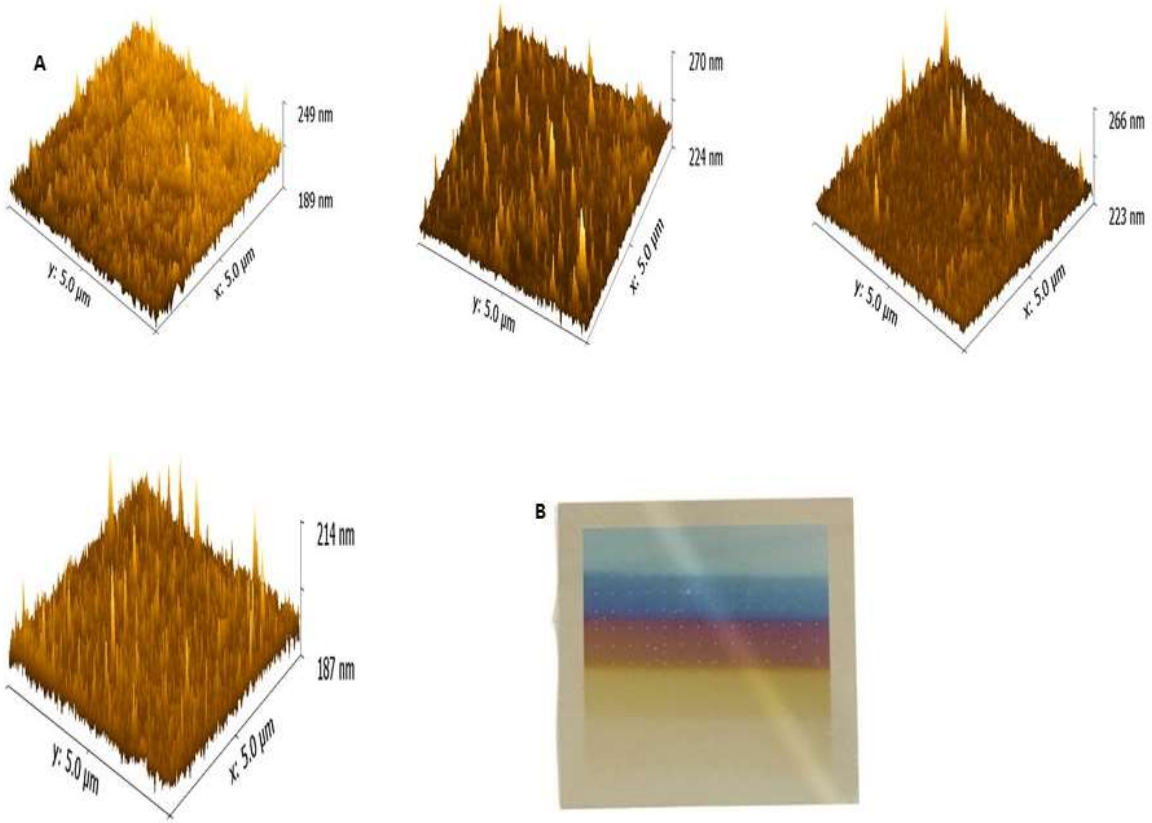

Figure 4.3. (A) AFM topography of rutile titania across different thicknesses (10 to 50 nm, respectively). (B) Sample picture.

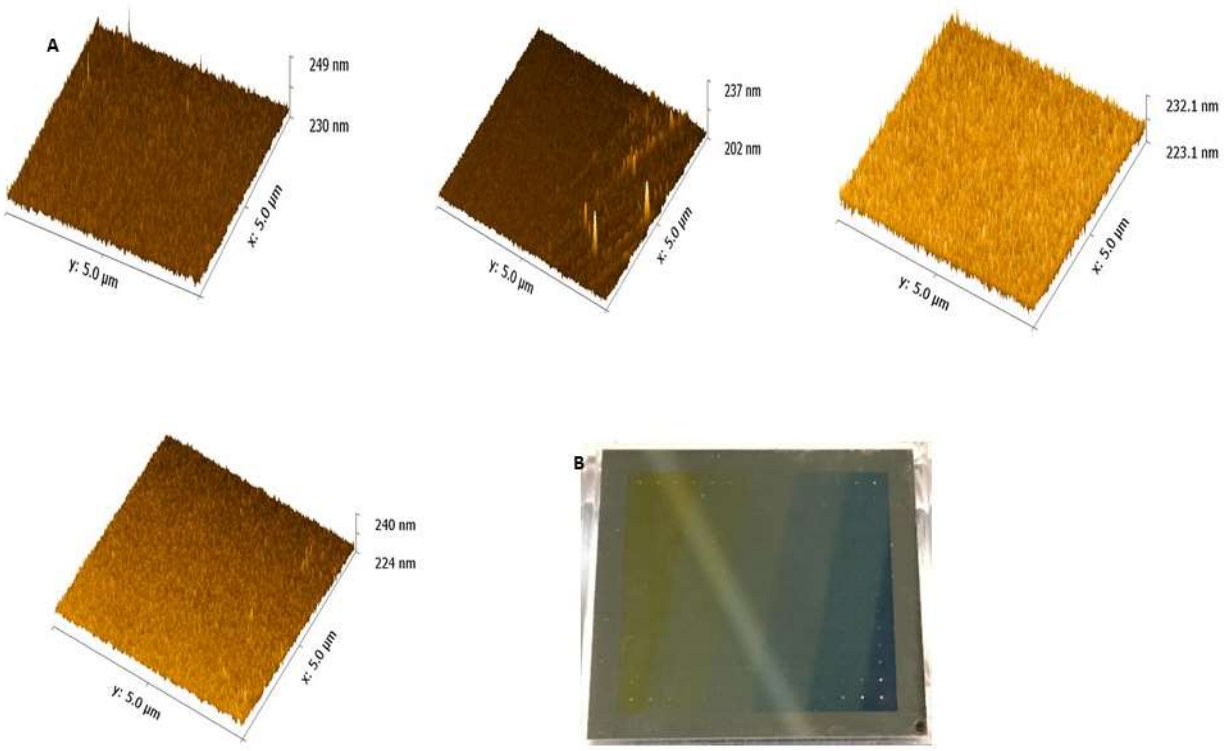

Figure 4.4. (A) AFM topography of composite amorphous titania across different thicknesses (10 to 50 nm, respectively). (**B**) Sample picture.

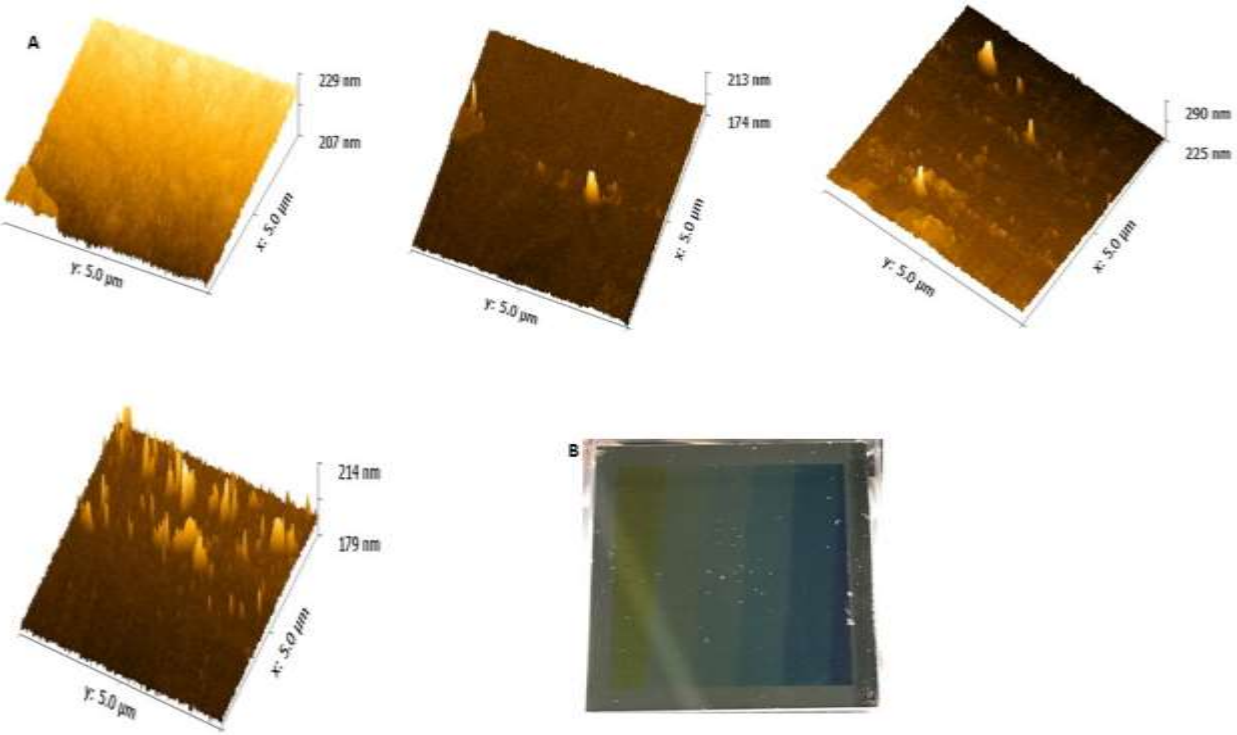

Figure 4.5. (A) AFM topography of composite anatase titania across different thicknesses (10 to 50 nm, respectively). (**B**) Sample picture

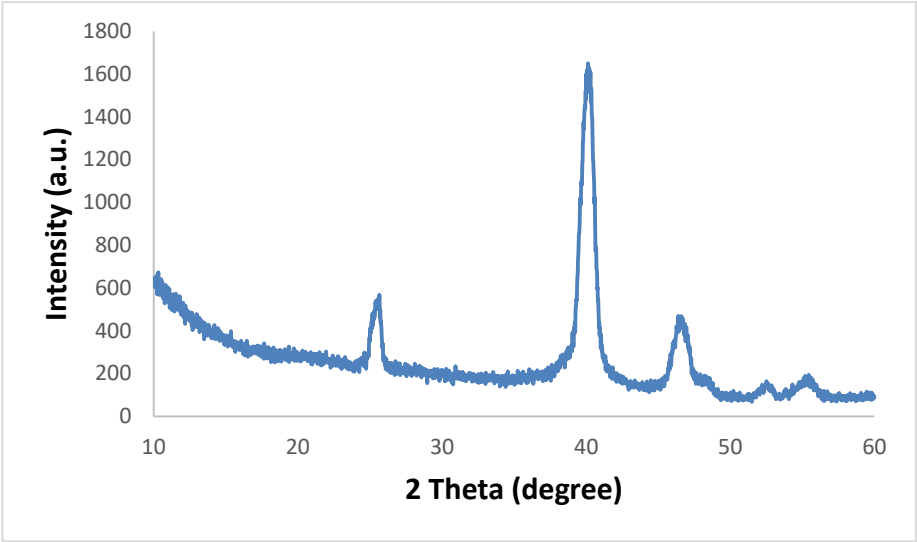

Figure 4.1. XRD data of anatase TiO_2 film with thickness of 40 nm.

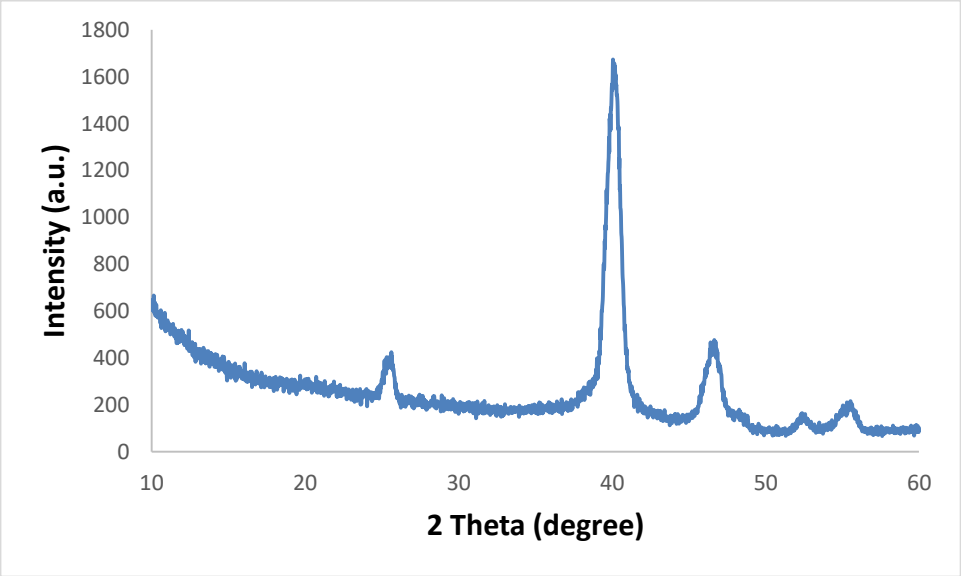

Figure 4.2. XRD data of anatase TiO_2 film with thickness of 30 nm.

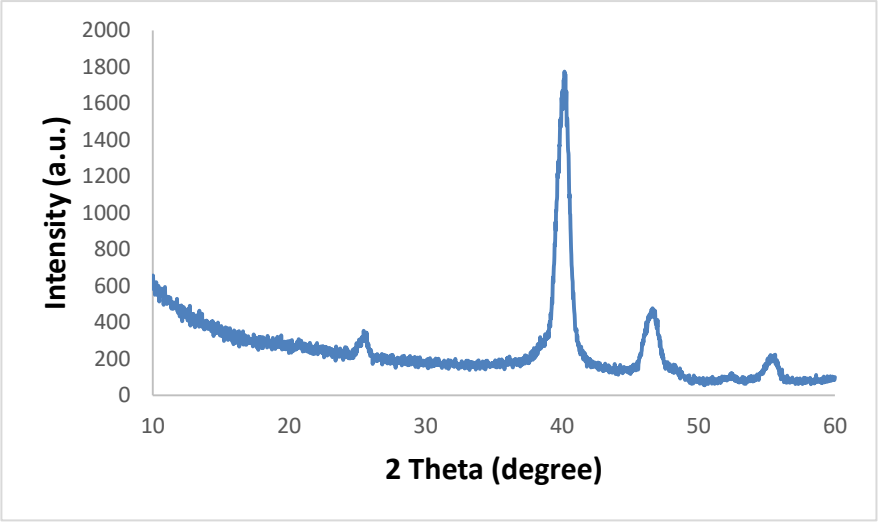

Figure 4.3. XRD data of anatase TiO_2 film with thickness of 20 nm.

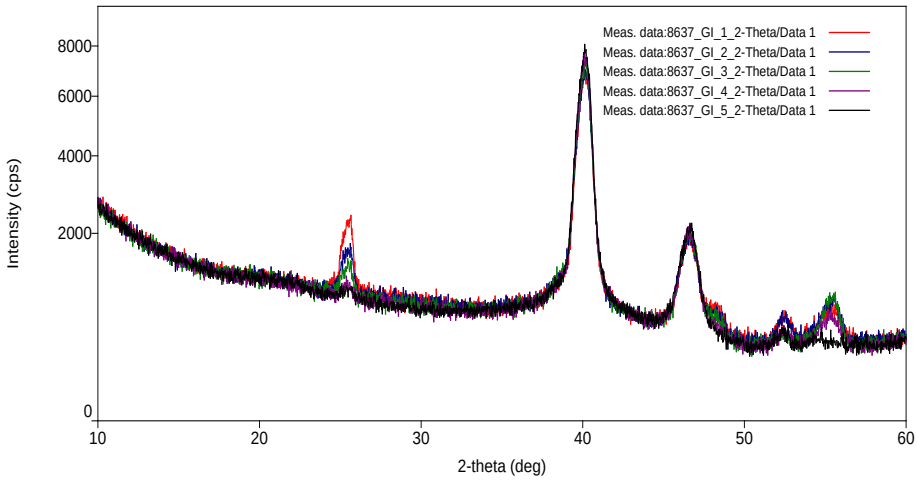

Figure 4.4. Combination of XRD pattern of TiO_2 anatase across thicknesses.

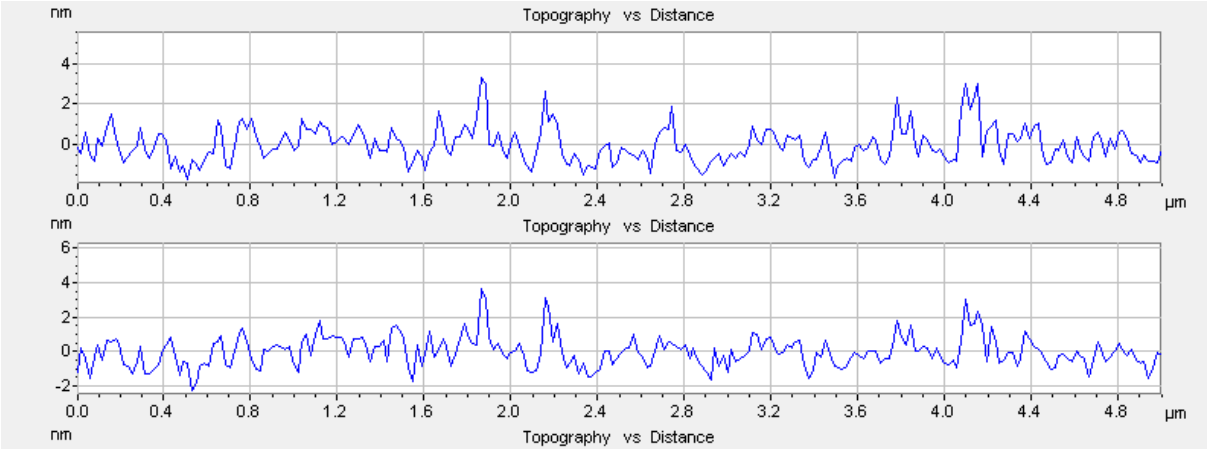

Figure 4.5. AFM frequency scan of amorphous titania.

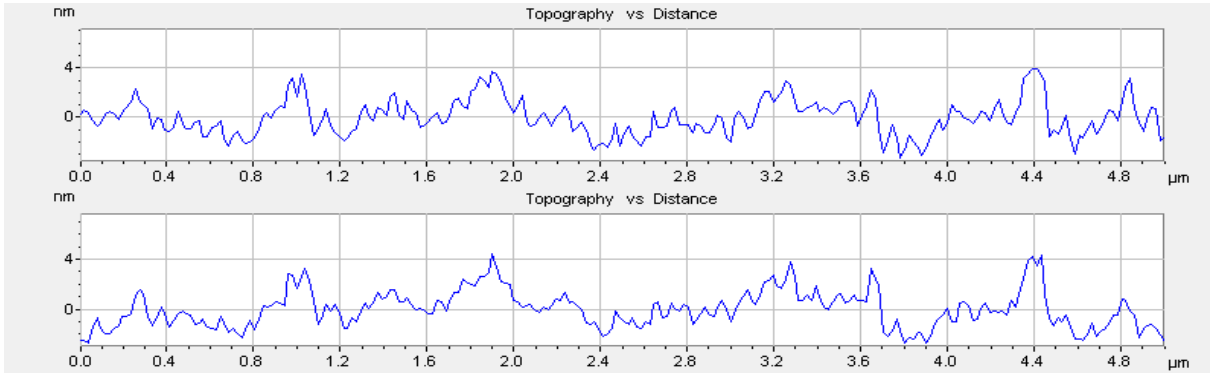

Figure 4.6. AFM frequency scan of anatase titania.

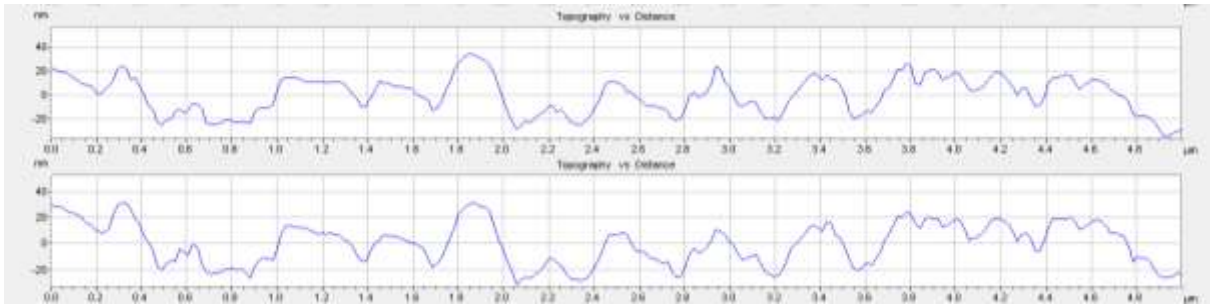

Figure 4.7. AFM frequency scan of rutile titania.

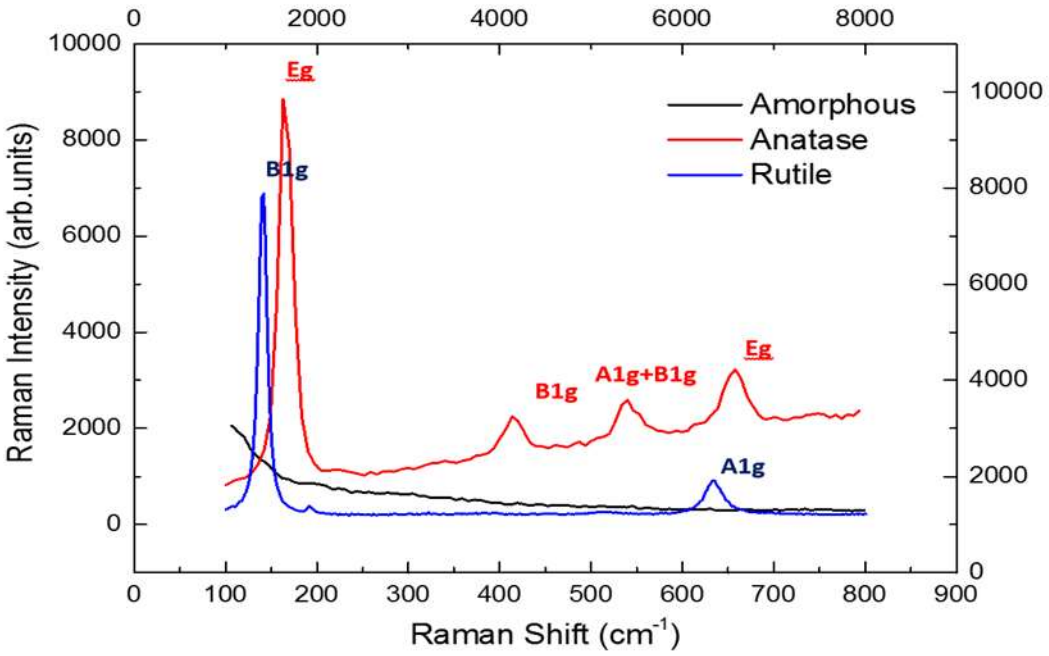

Figure 4.8. Raman spectra of three TiO_2 phases with average thickness of 50 nm being synthesised using HT-PVD

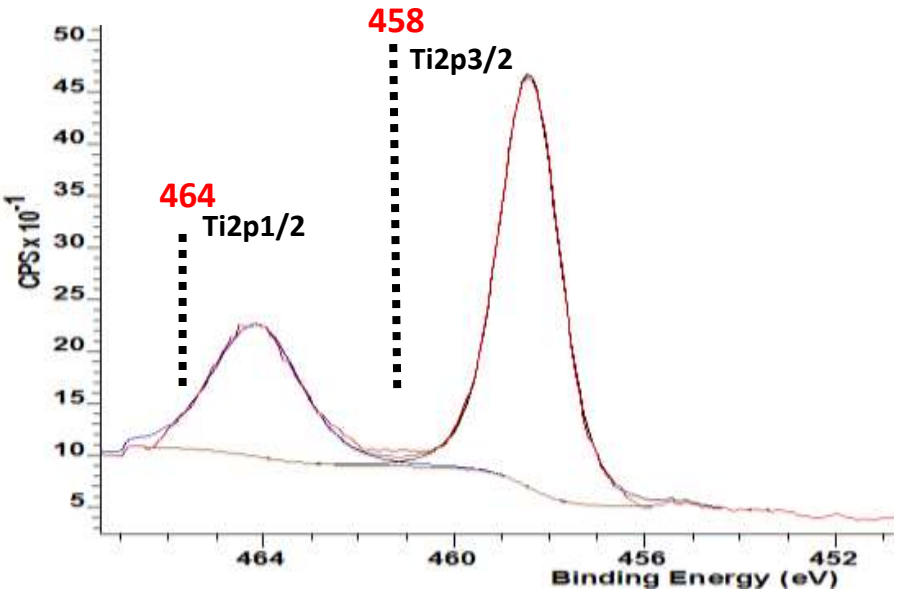

Figure 4.9. XPS spectra for amorphous Ti 2p.

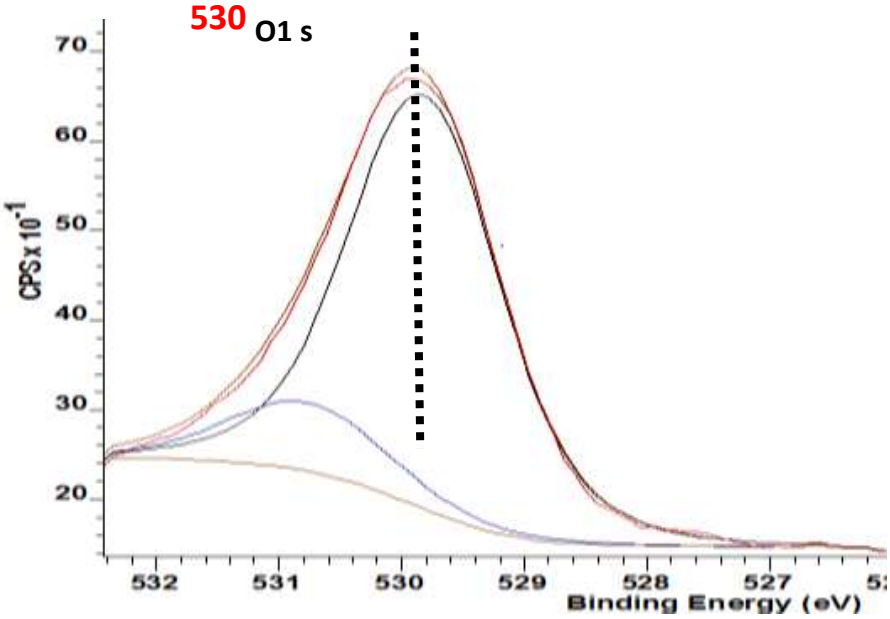

Figure 4.10. XPS spectra for amorphous O 1s.

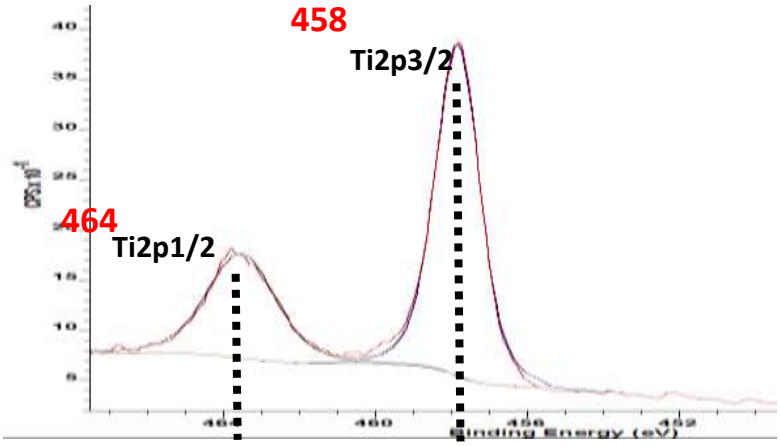

Figure 4.11: XPS spectra for anatase Ti 2p.

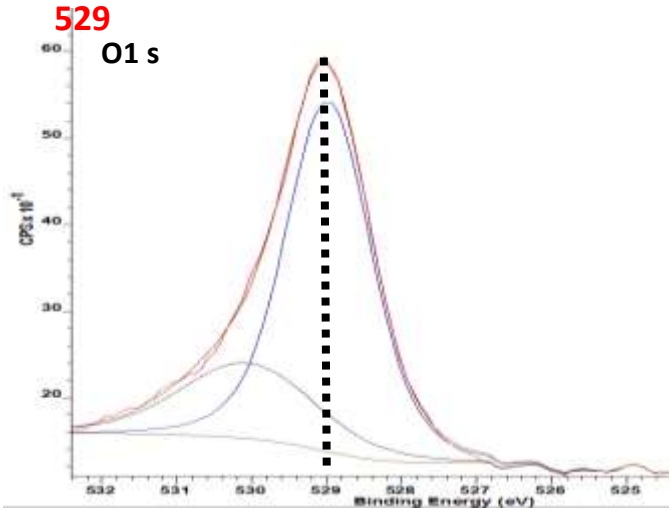

Figure 4.12. XPS spectra for anatase O 1s.

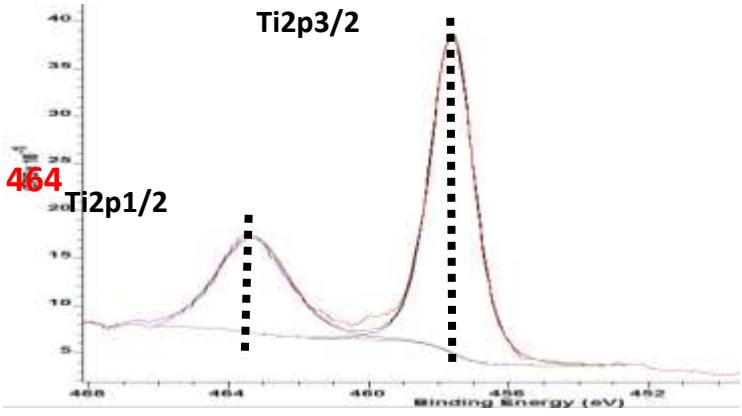

Figure 4.13. XPS spectra for Rutile Ti 2p.

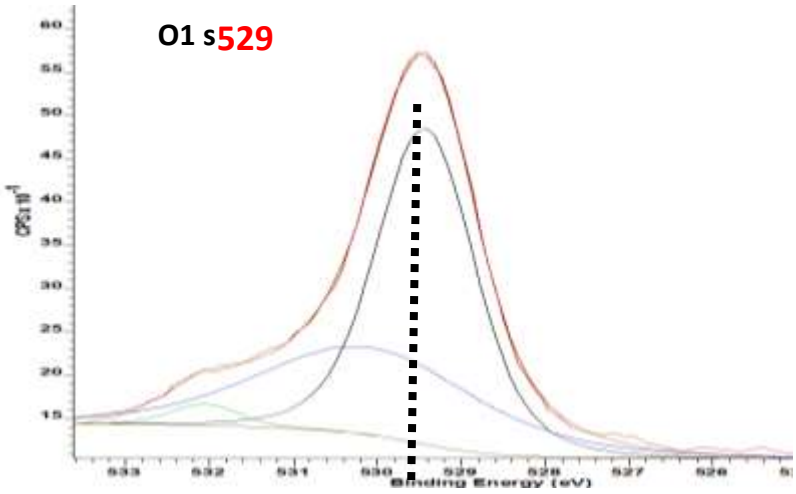

Figure 4.14. XPS spectra for rutile O 1s.

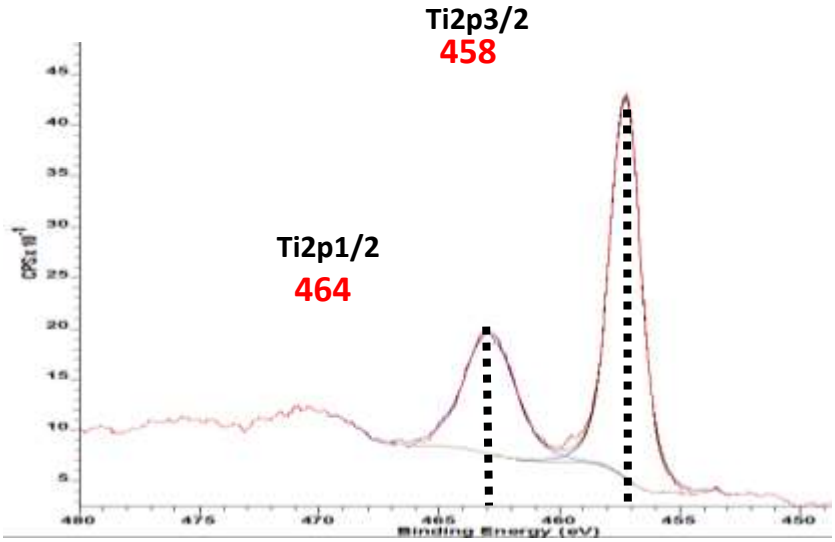

Figure 4.15. XPS spectra for thinner stoichiometric anatase (50nm) Ti 2p.

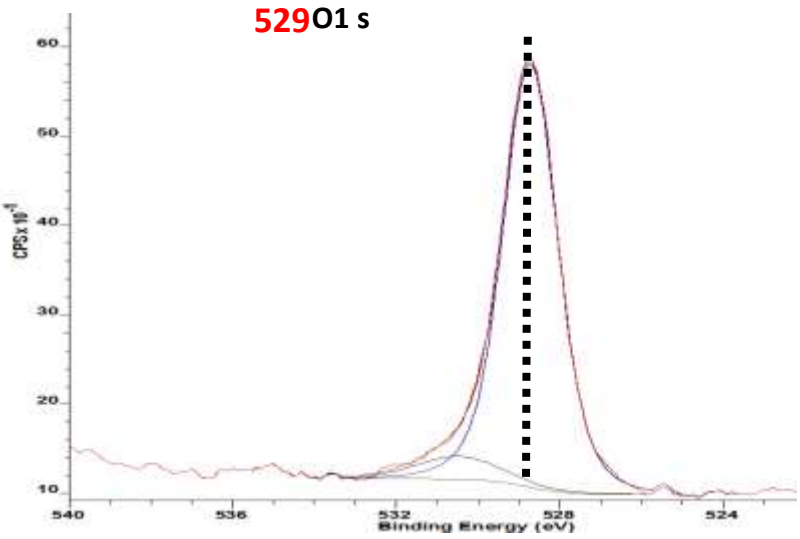

Figure 4.16. XPS spectra for thinner stoichiometric anatase titania O 1s.

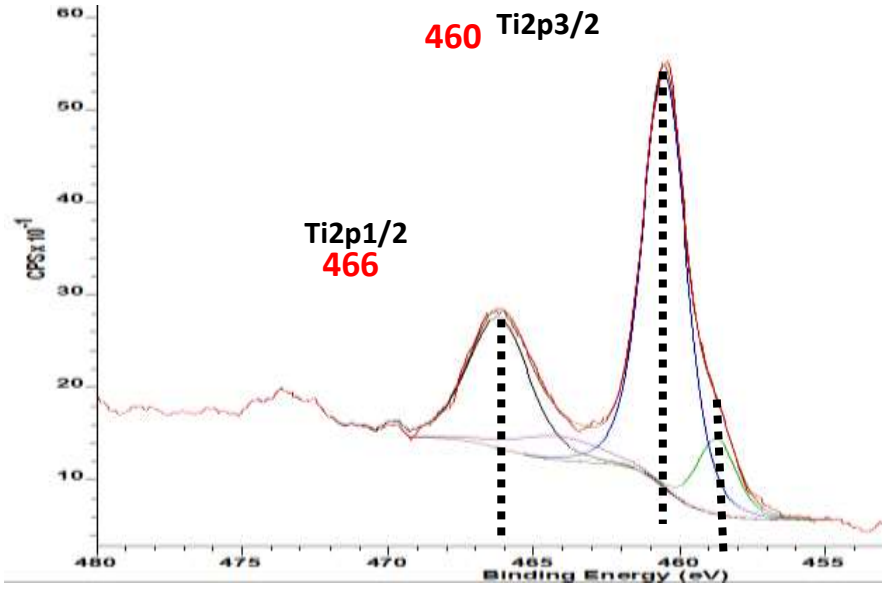

Figure 4.17. XPS spectra for thinner sub-stoichiometric anatase (50nm) Ti 2p.

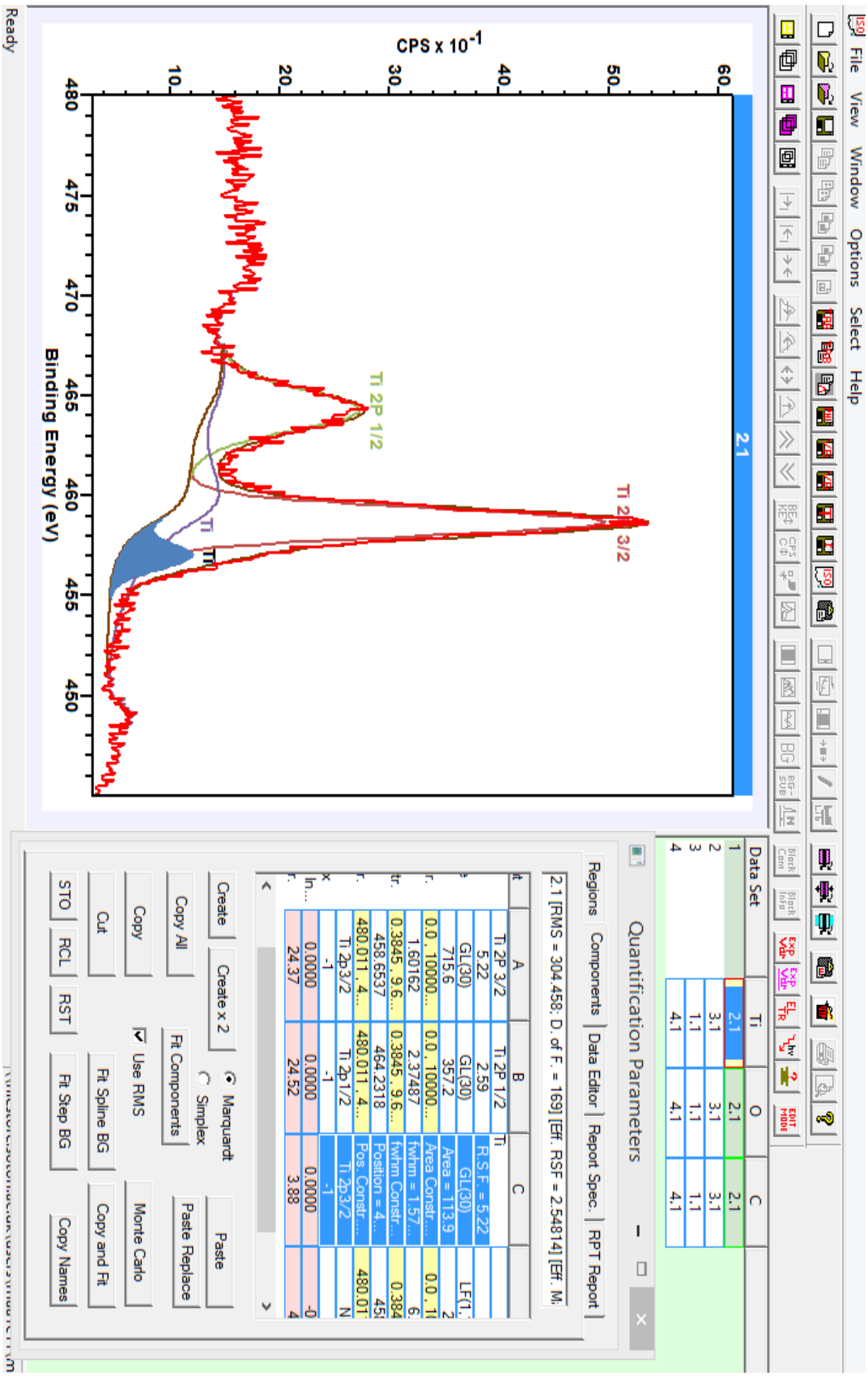

Figure 4.18. Peak area analysis using Casa software.

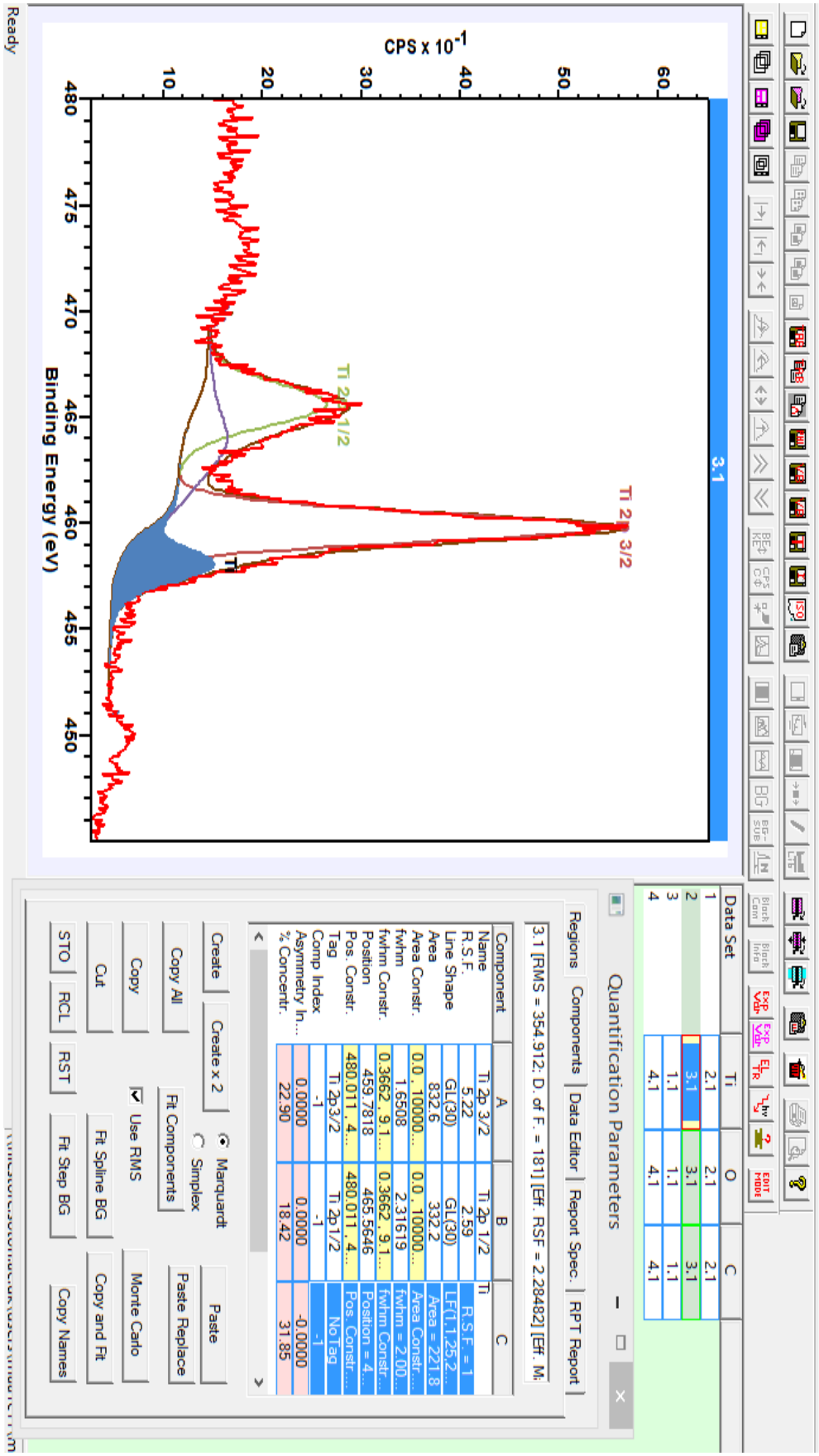

Figure 4.19. Peak area analysis using Casa software.

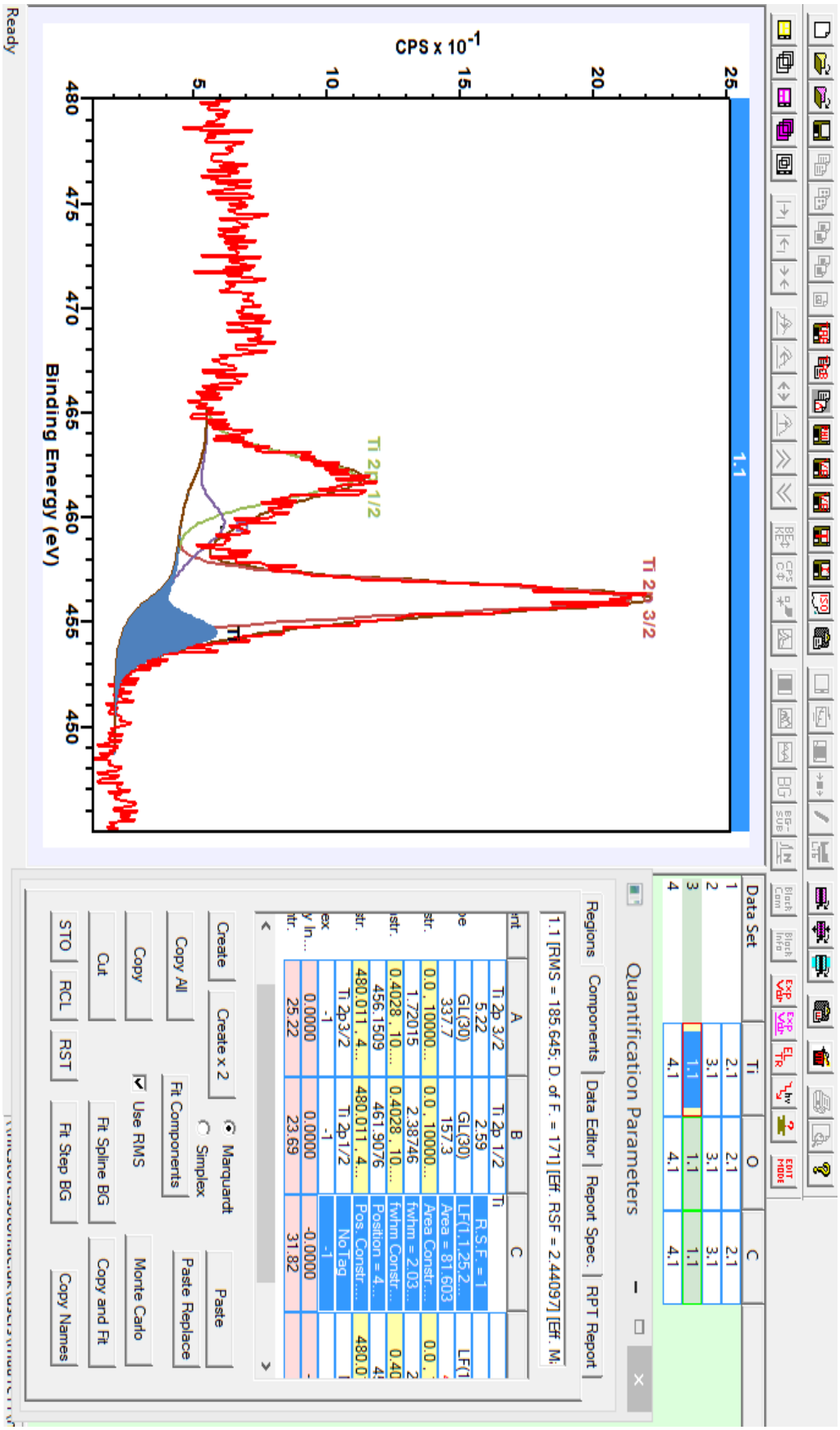

Figure 4.20. Peak area analysis using Casa software.

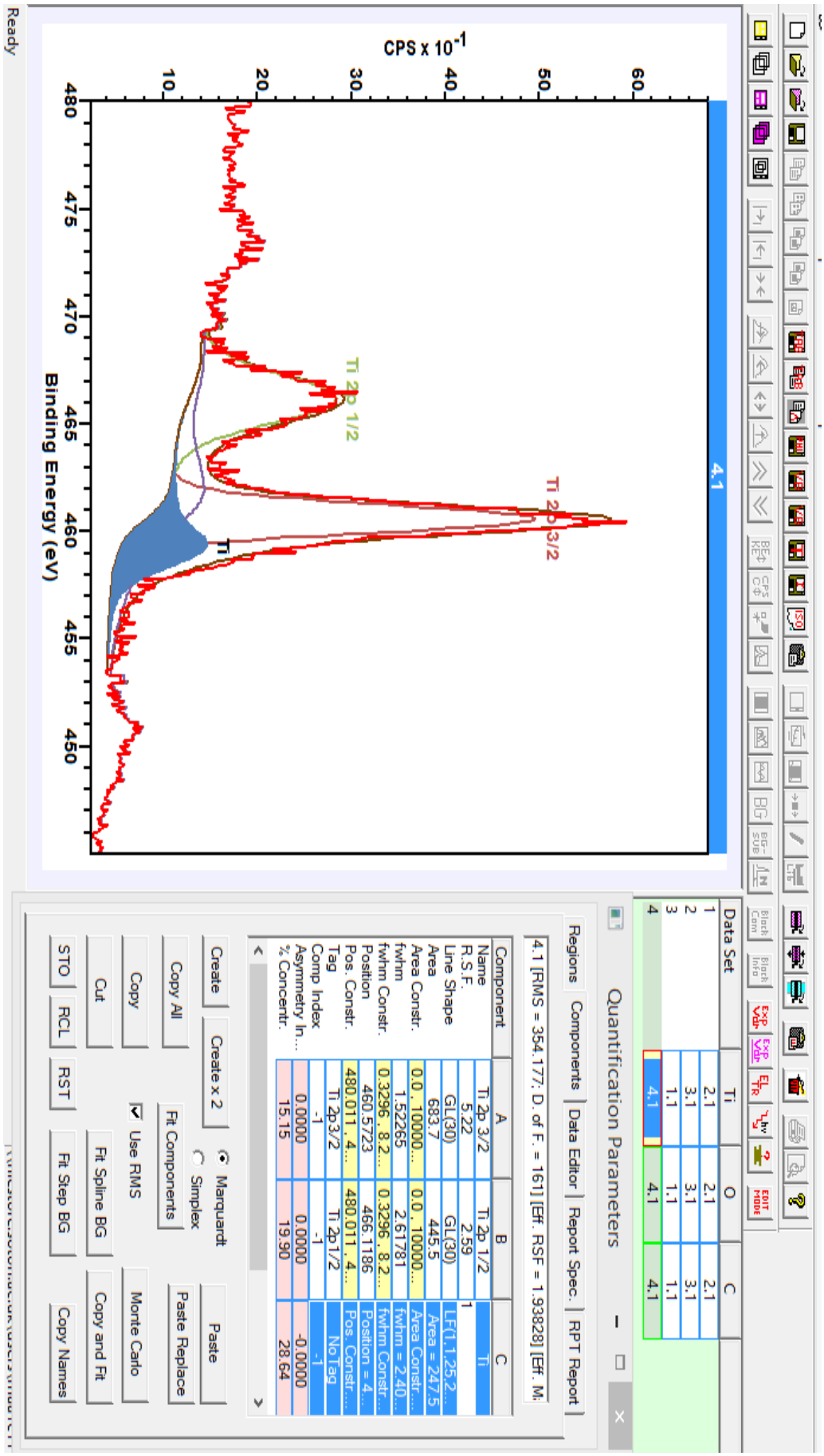

Figure 4.21. Peak area analysis using Casa software.

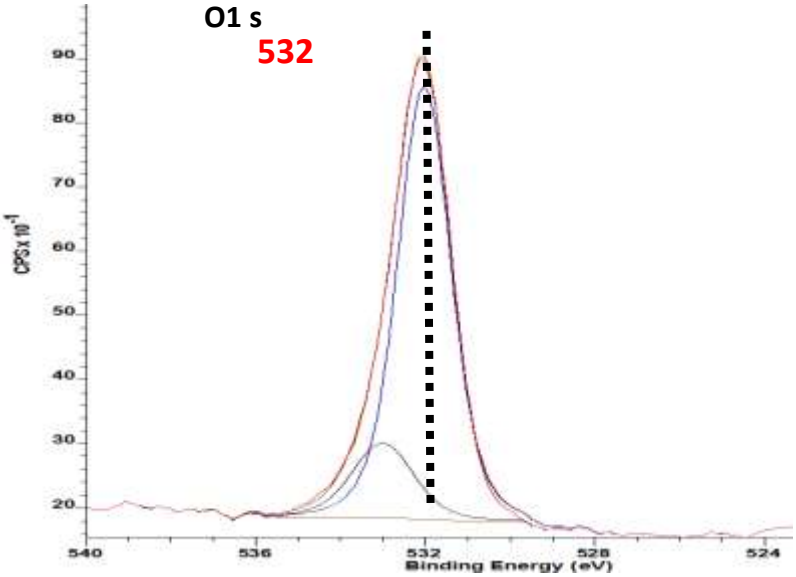

Figure 4.22. XPS spectra for thinner sub-stoichiometric anatase titania O 1s.

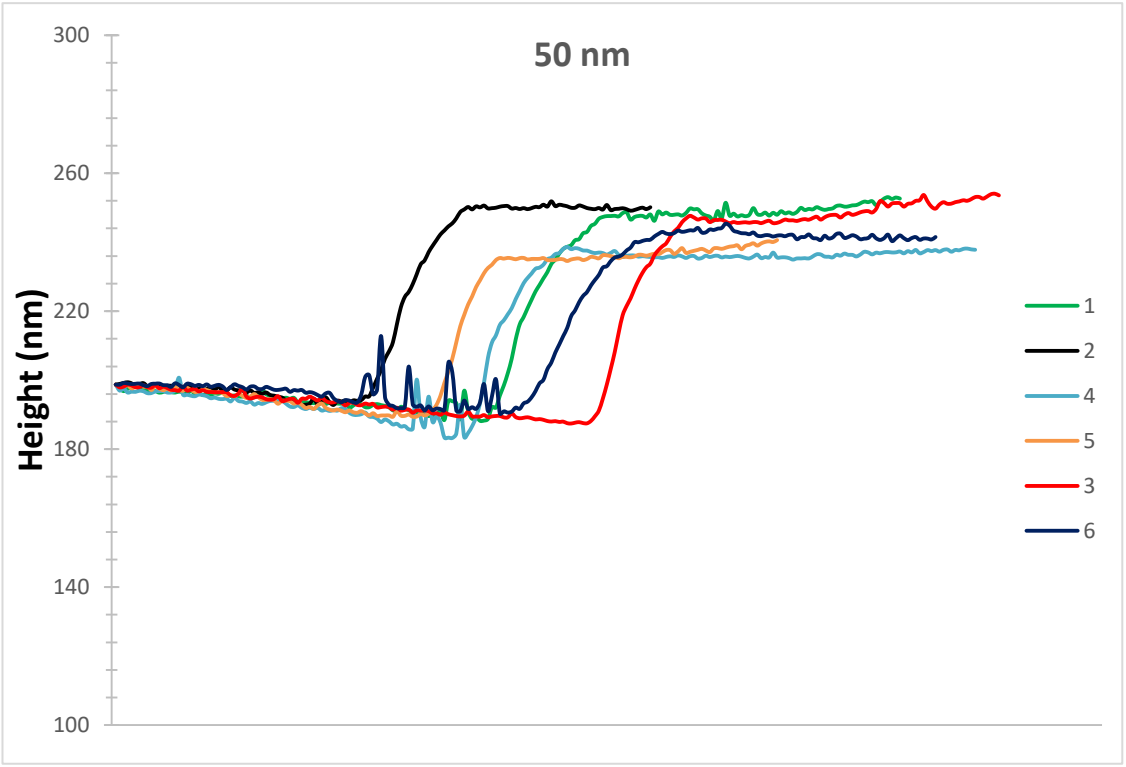

Figure 4.23. Multiple measurement on one strip of thickness (50 nm) for amorphous TiO_2.

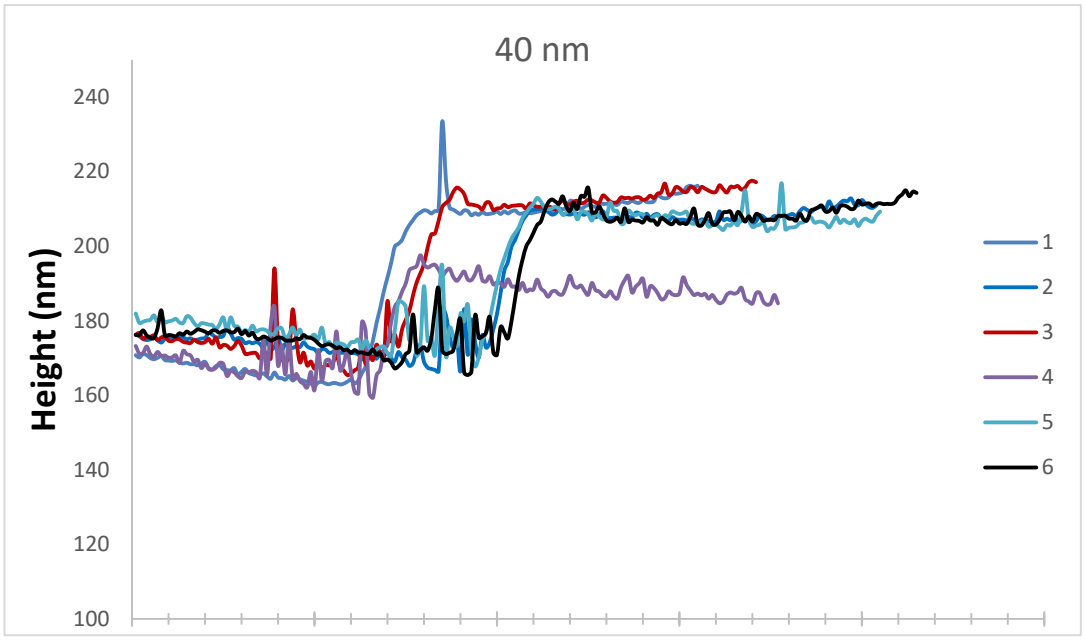

Figure 4.24. Multiple measurement on one strip of thickness (40 nm) for amorphous TiO_2.

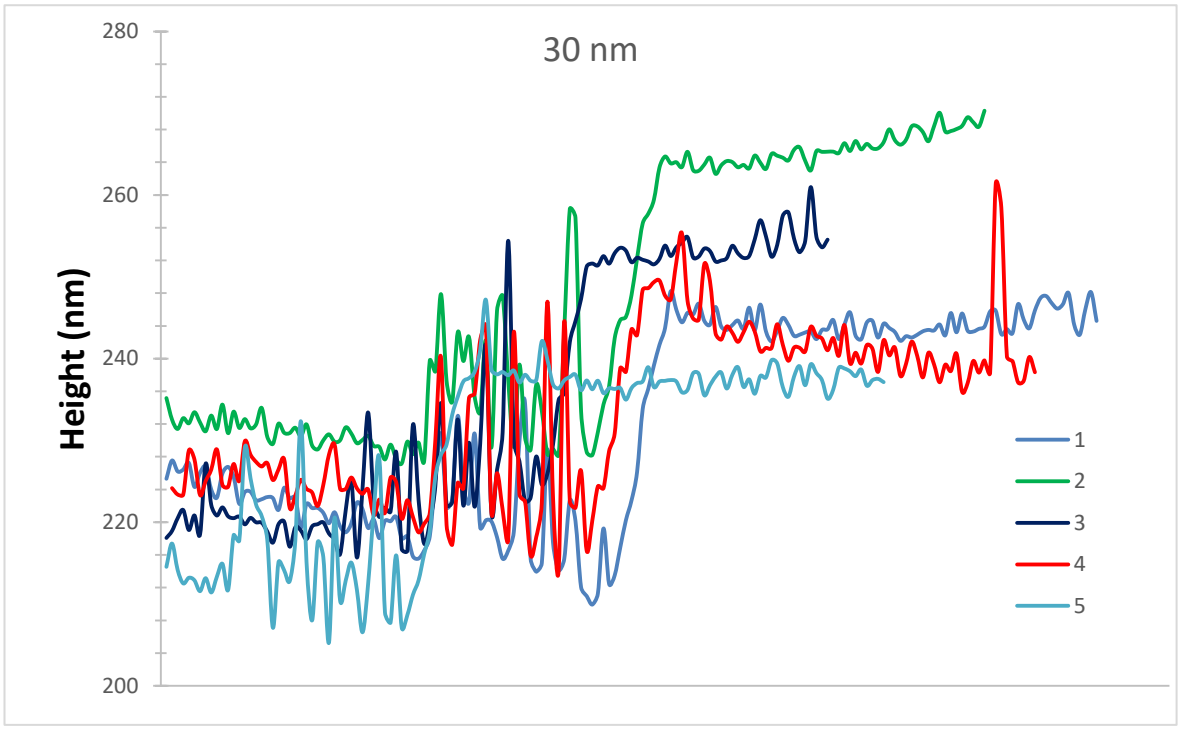

Figure 4.25. Multiple measurement on one strip of thickness (30 nm) for amorphous TiO_2.

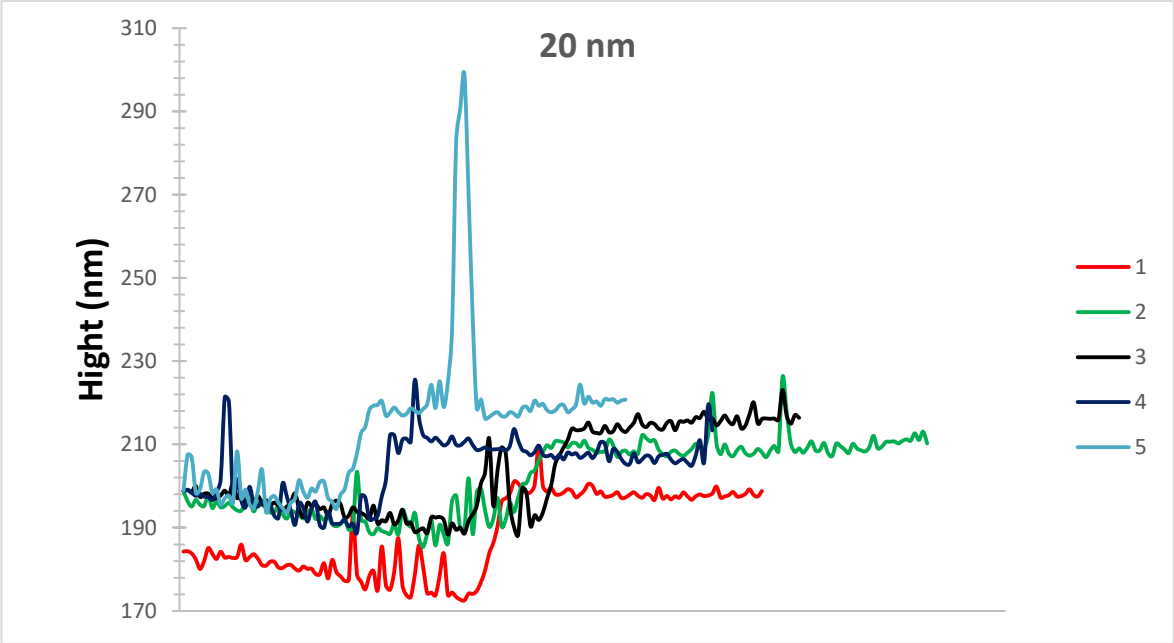

Figure 4.26. Multiple measurement on one strip of thickness (20 nm) for amorphous TiO_2.

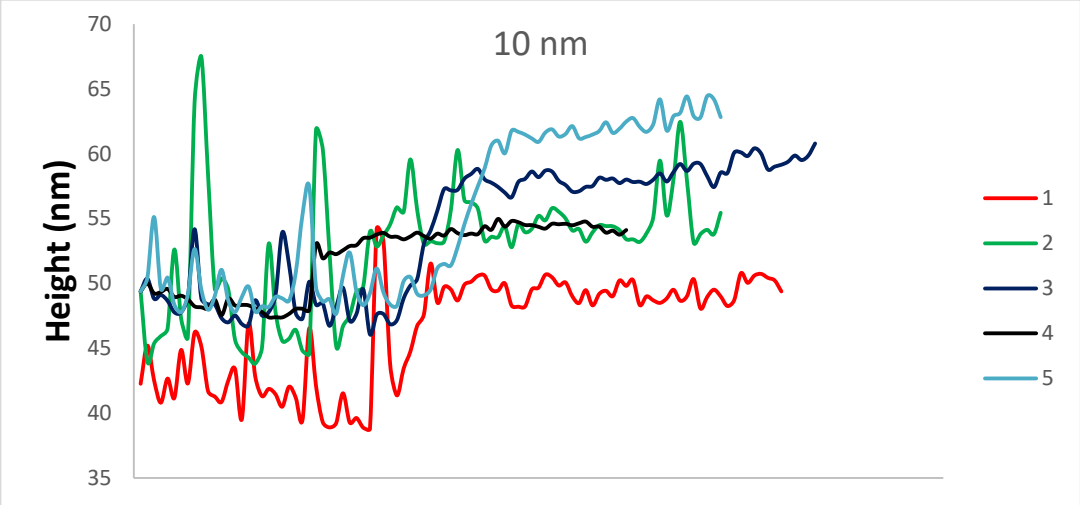

Figure 4.27. Multiple measurement on one strip of thickness (10 nm) for amorphous TiO_2.

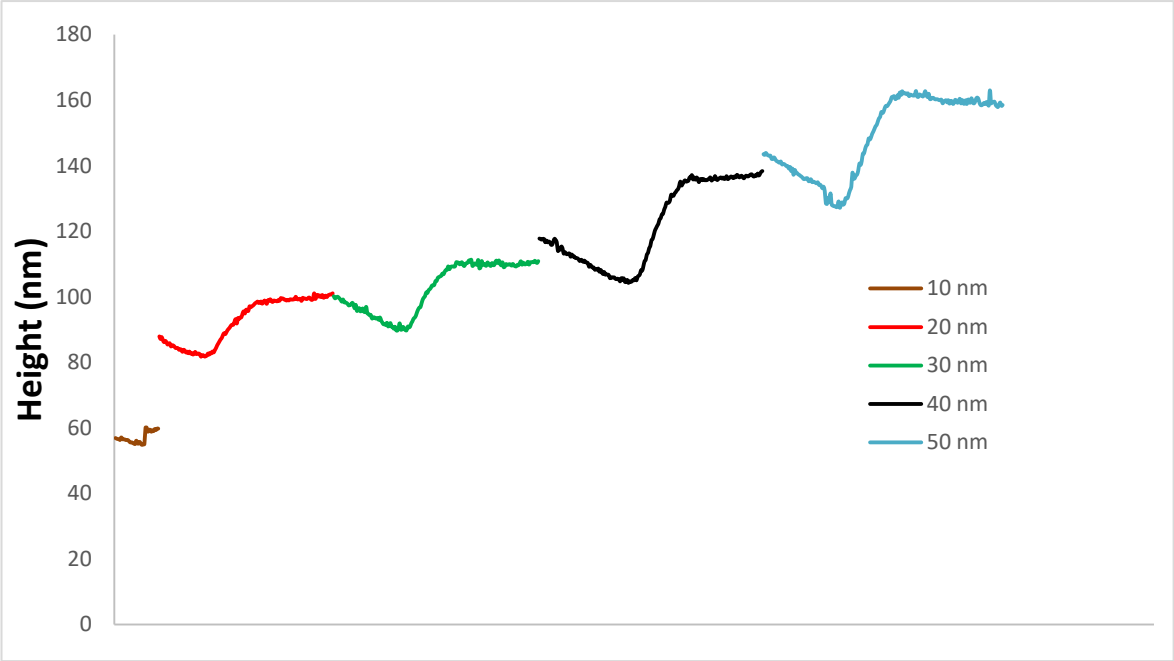

Figure 4.28. Distribution of gradient of thickness for anatase TiO_2 films.

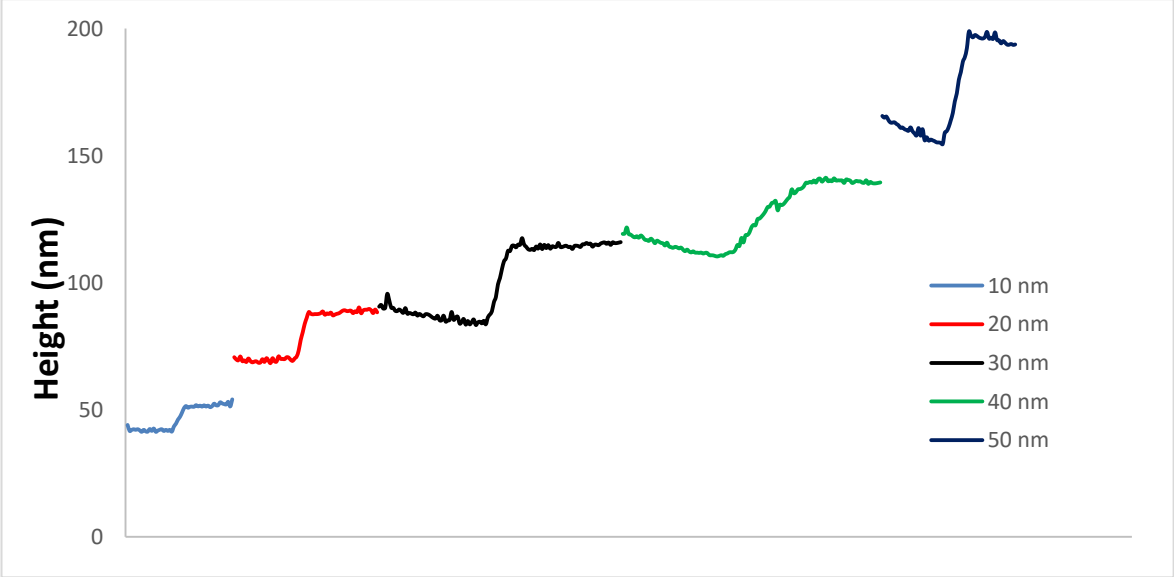

Figure 4.29. Distribution of gradient of thickness for rutile TiO_2 films.

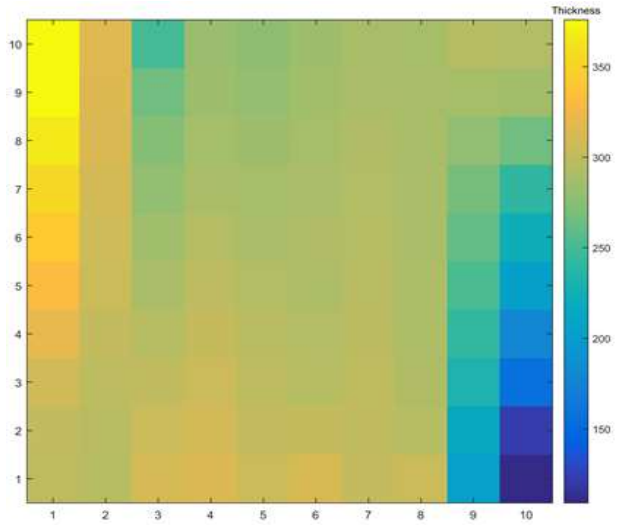

Figure 4.30. Map of thickness distribution of anatase titania prepared by HT-PVD.

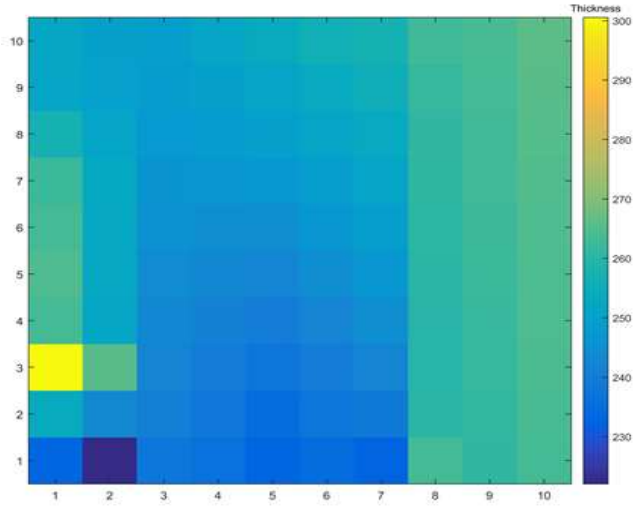

Figure 4.31. Map of thickness distribution of rutile titania prepared by HT-PVD.

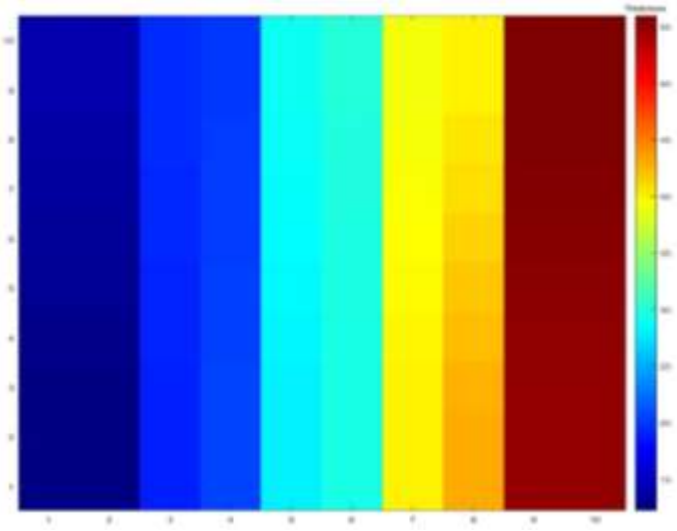

Figure 4.32. Map of step thickness distribution of anatase titania prepared by HT-PVD.

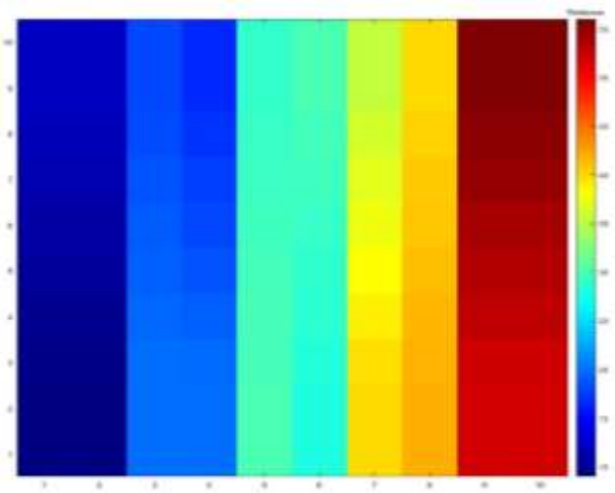

Figure 4.33. Map of step thickness distribution of rutile titania prepared by HT-PVD.

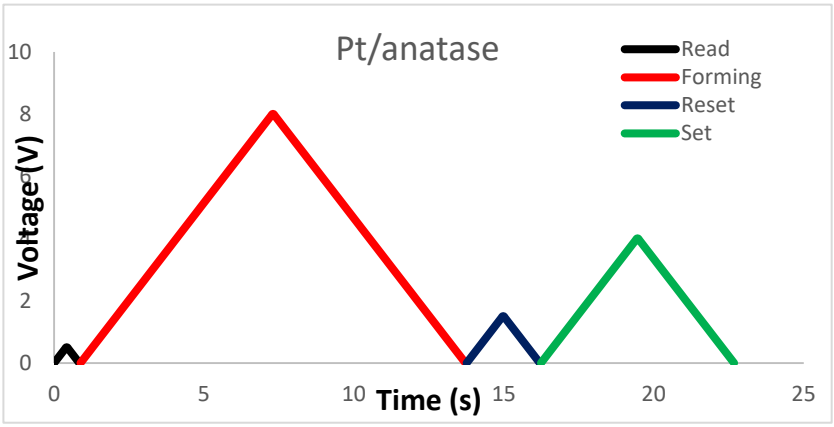

Figure 5.1. Time dependence of Pt/anatase titania/Pt.

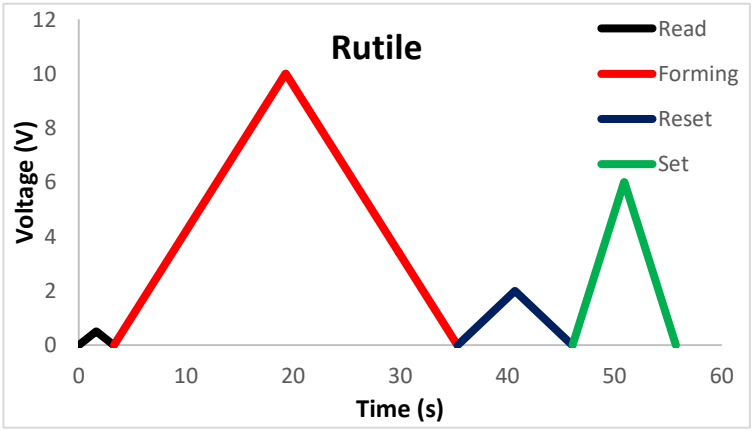

Figure 5.2. Time dependence of Pt/rutile titania/Pt.

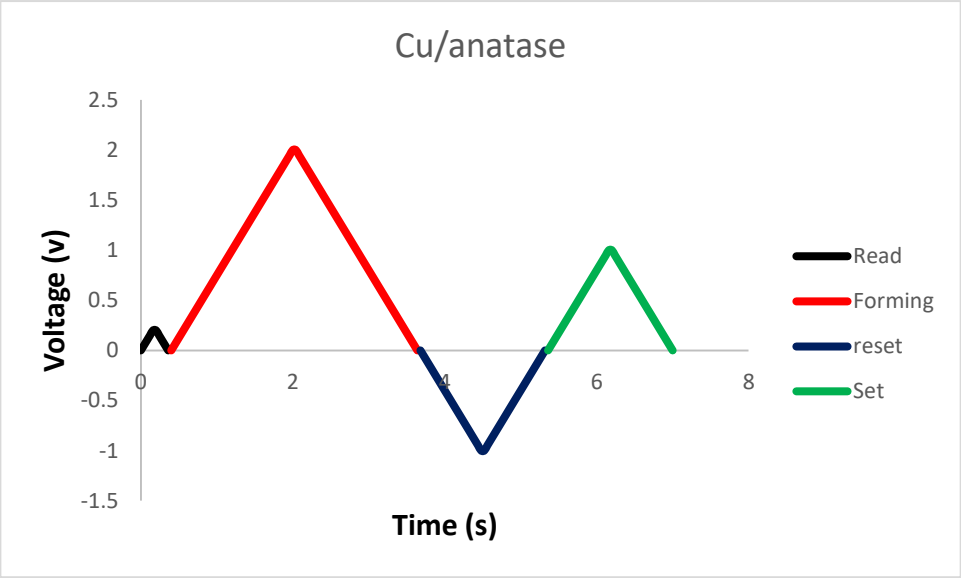

Figure 5.3. Time dependence of Cu/ anatase titania/Pt.

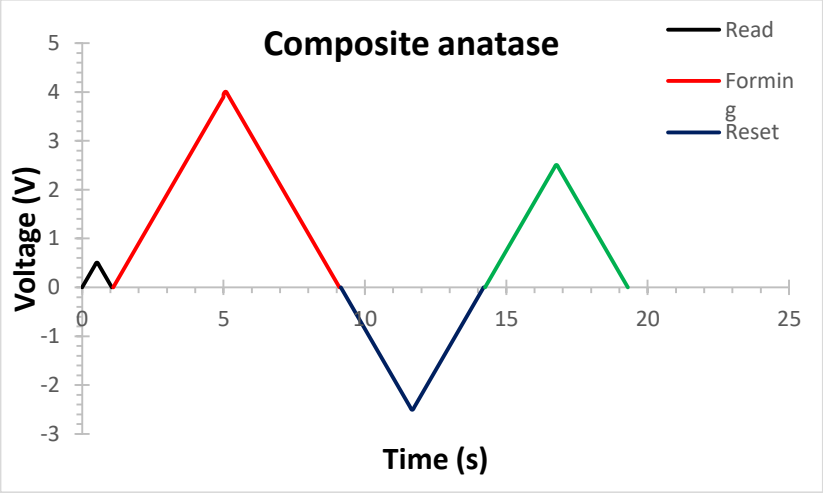

Figure 5.4. Time dependence of anatase composite.

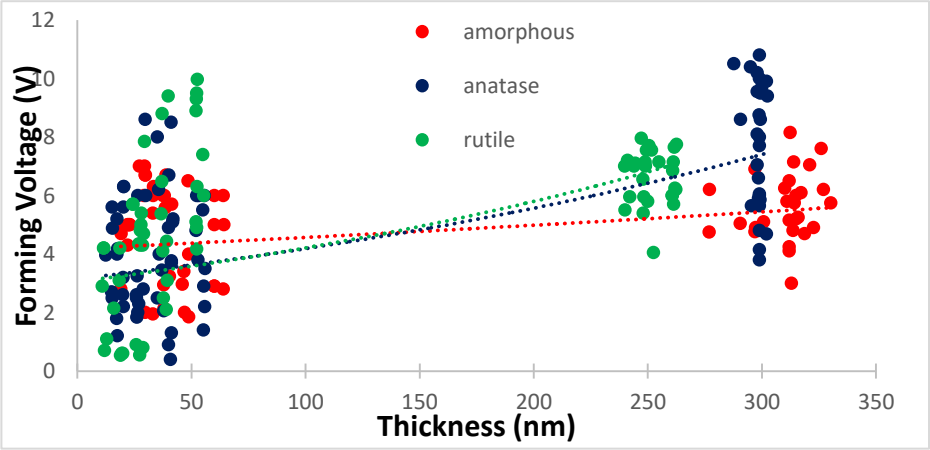

Figure 5.5. Data points of forming voltage across the thickness of three phases of TiO_2.

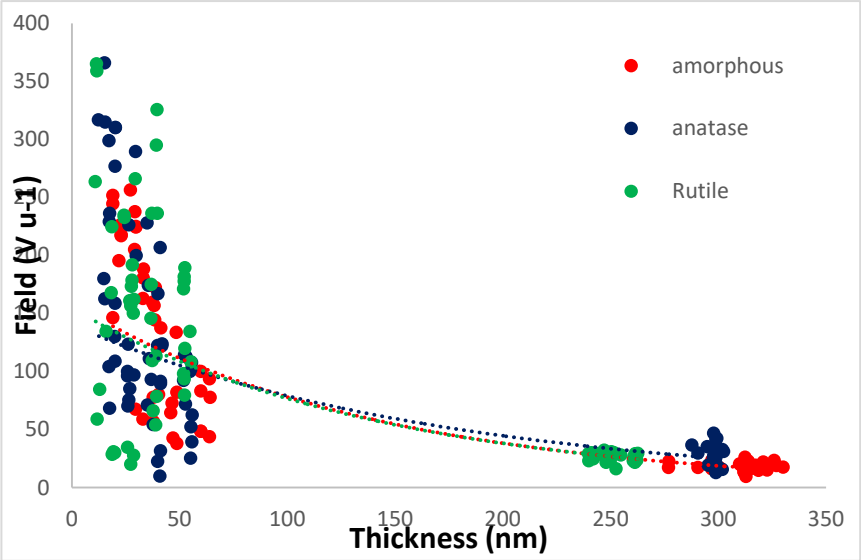

Figure 5.6. Data points of electric field across the thickness of three phases of TiO_2

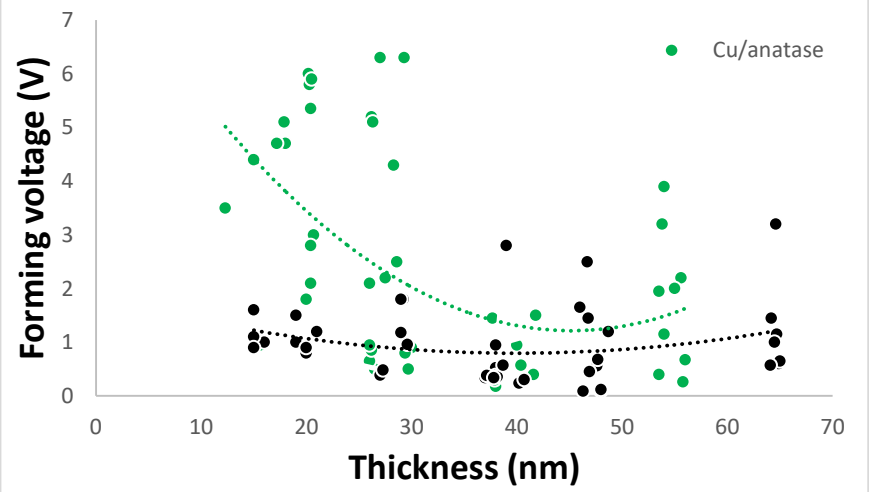

Figure 5.7. Data points of forming voltage across the thickness of Cu/TiO_2/Pt.

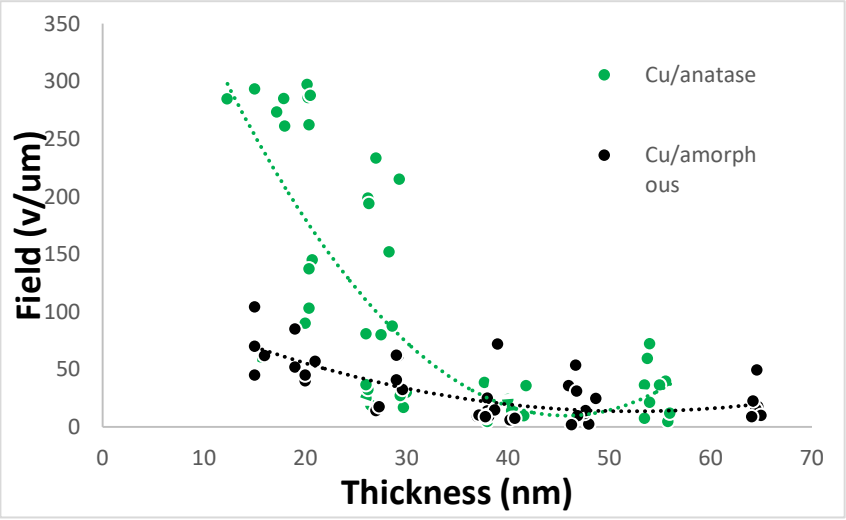

Figure 5.8. Data points of electric field across the thickness of Cu/ TiO_2/Pt.

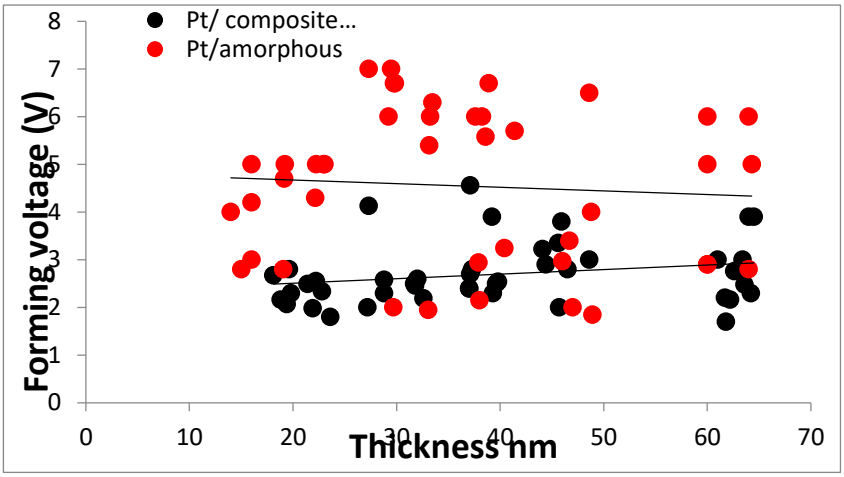

Figure 5.9. Data points of forming voltage across the thickness of $Pt/TiO_2/Pt$ and $Pt/TiO_{2-x}/TiO_2$ amorphous/Pt.

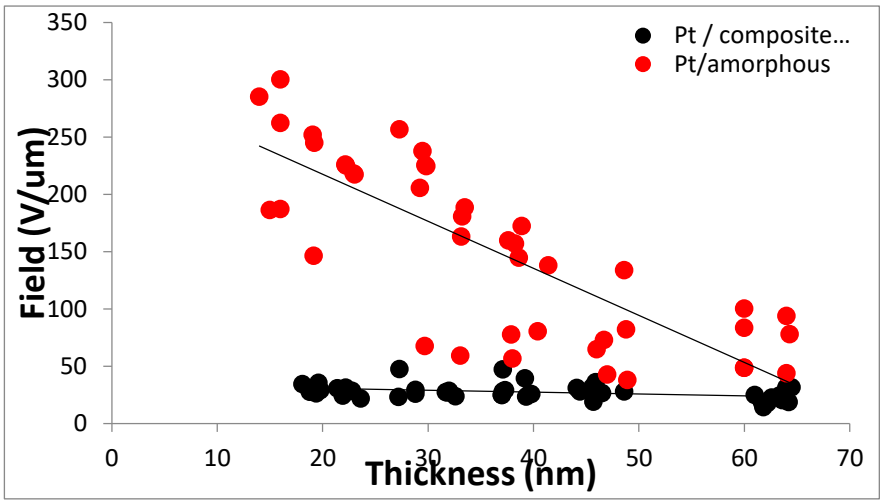

Figure 5.10: Data points of electric field across the thickness of $Pt/TiO_2/Pt$ and $Pt/TiO_{2-x}/TiO_2$ amorphous/Pt.

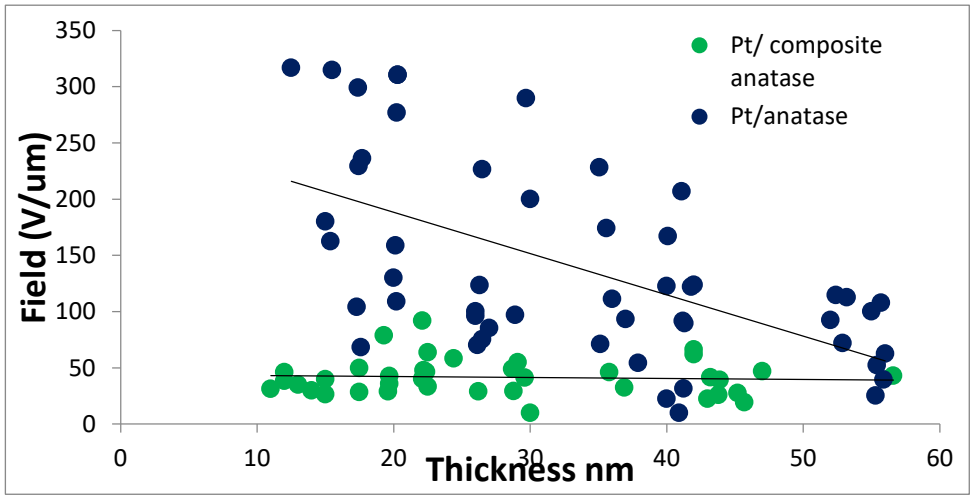

Figure 5.11. Data points of electric field across the thickness of Pt/TiO_2/Pt and Pt/TiO_{2-x}/TiO_2 anatase/Pt.

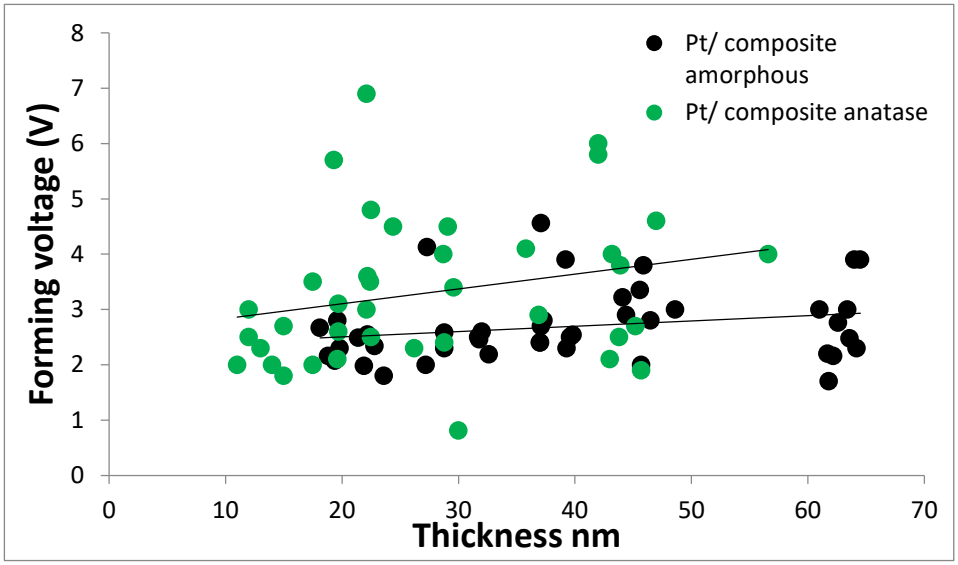

Figure 5.12. Data points of forming voltage across the thickness of Pt/TiO_{2-x}/TiO_2 amorphous /Pt and Pt/TiO_{2-x}/TiO_2 anatase/Pt.

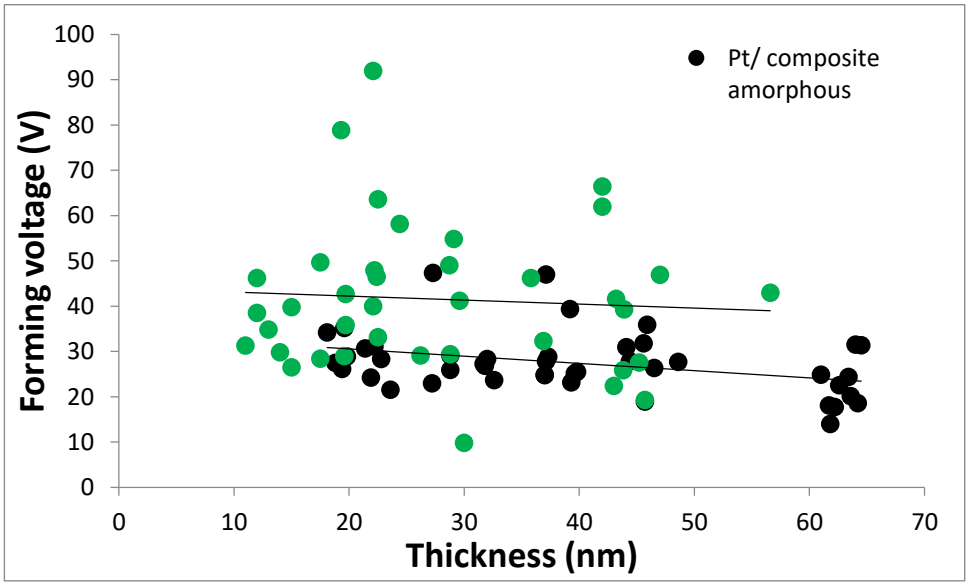

Figure 5.13. Data points of electric field across the thickness of Pt/TiO_{2-x}/TiO_2 amorphous /Pt and Pt/TiO_{2-x}/TiO_2 anatase/Pt.

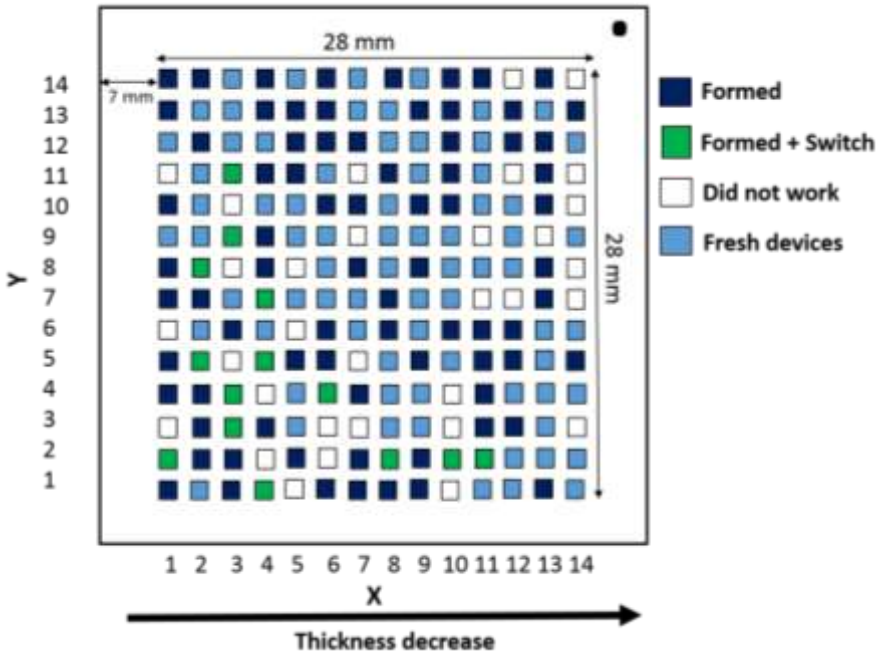

Figure 5.14. High-throughput statistics of device yield of Pt/TiO_2 anatase/Pt; dark blue indicates how many devices are being formed; greens indicate how many devices were formed and rested and set again; white boxes indicate the number of devices that did not form; and light blue are the remaining devices that were not tested.

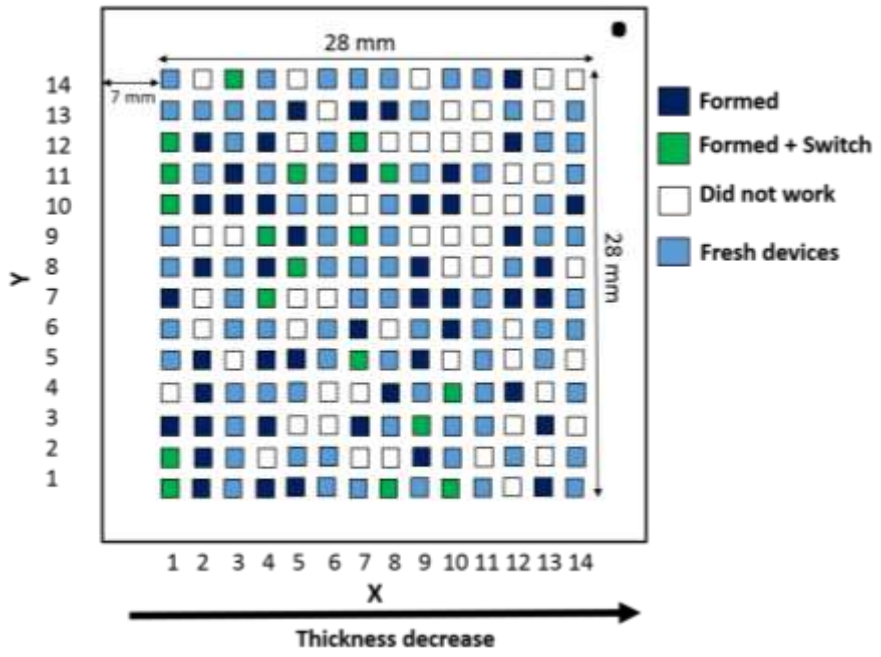

Figure 5.15. High-throughput statistics of device yield of Pt/TiO_2 rutile/Pt; dark blue indicates how many devices are being formed; green indicates how many devices were formed and rested and set again; white boxes indicate the number of devices that did not form; and light blue are the remaining devices that were not tested.

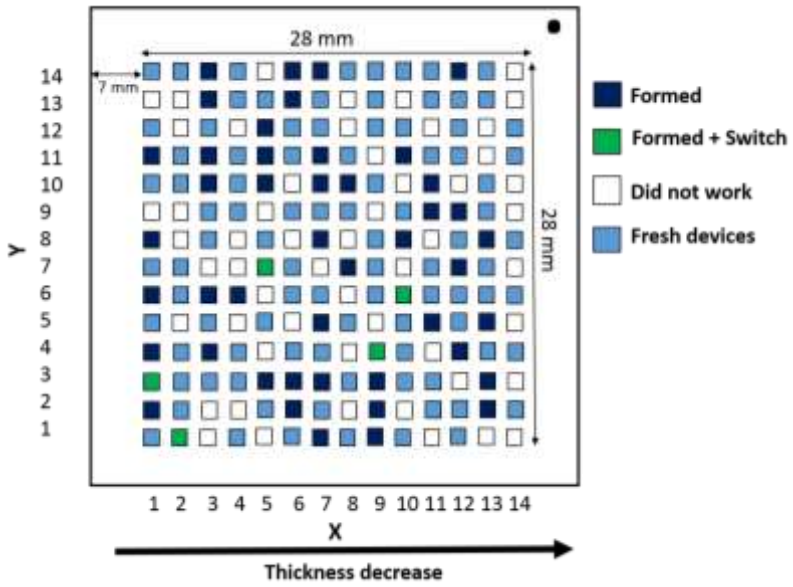

Figure 5.16. High-throughput statistics of device yield of Cu/TiO2 amorphous/Pt; dark blue indicates how many devices are being formed; green indicates how many devices were formed and rested and set again; white boxes indicate the number of devices that did not form; and light blue are the remaining devices that were not tested.

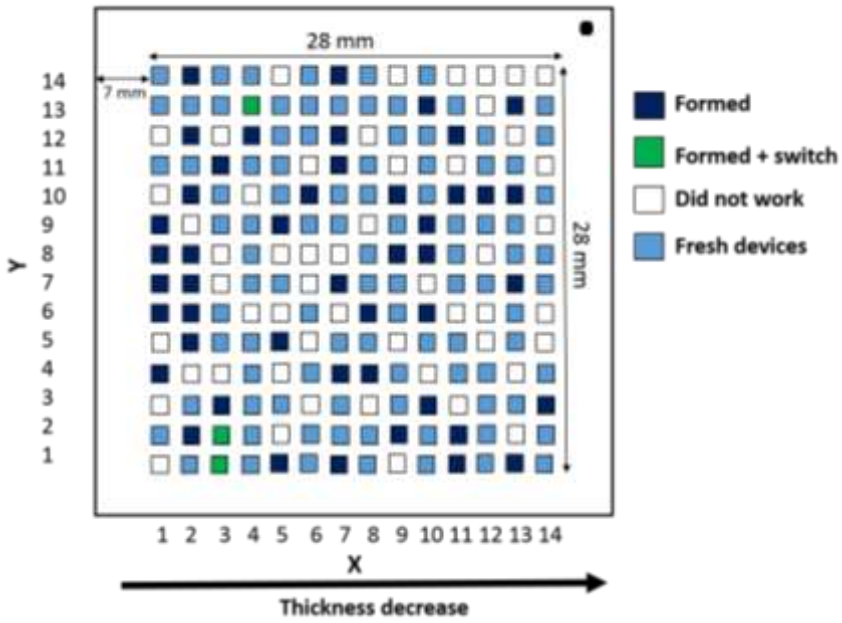

Figure 5.17. High-throughput statistics of device yield of Cu/TiO_2 anatase/Pt; dark blue indicates how many devices are being formed; green indicates how many devices were formed and rested and set again; white boxes indicate the number of devices that did not form; and light blue are the remaining devices that were not tested.

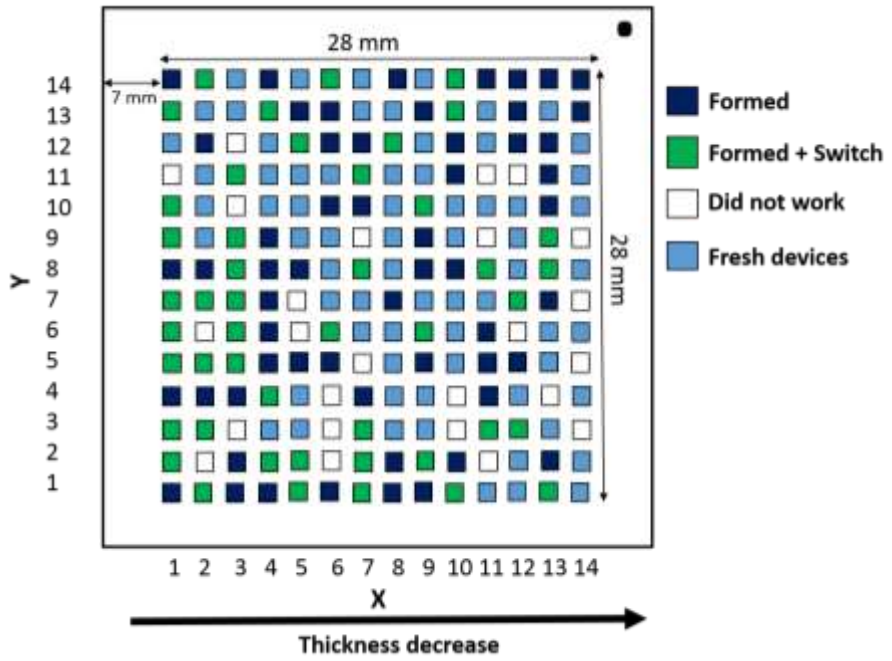

Figure 5.18. Figure 5.18. High-throughput statistics of device yield of Pt/ TiO2-x/TiO2 amorphous/Pt; dark blue indicates how many devices are being formed; green indicates how many devices were formed and rested and set again; white boxes indicate the number of devices that did not form; and light blue are the remaining devices that were not tested.

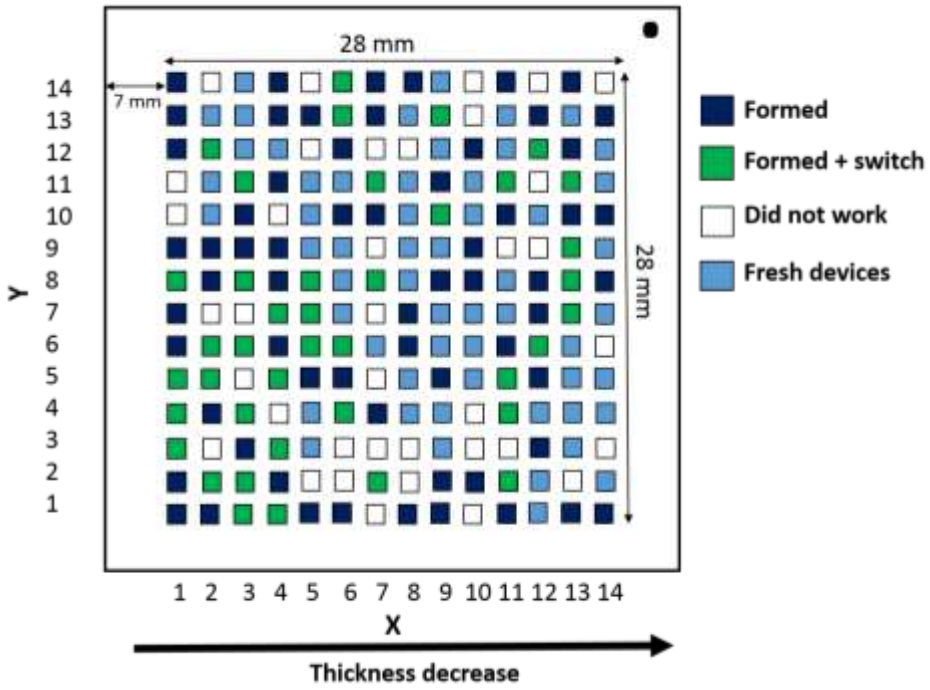

Figure 5.19. High-throughput statistics of device yield of Pt/TiO2-x/TiO2 anatase/Pt; dark blue indicates how many devices are being formed; green indicates how many devices were formed and rested and set again; white boxes indicate the number of devices that did not form; and light blue are the remaining devices that were not tested.

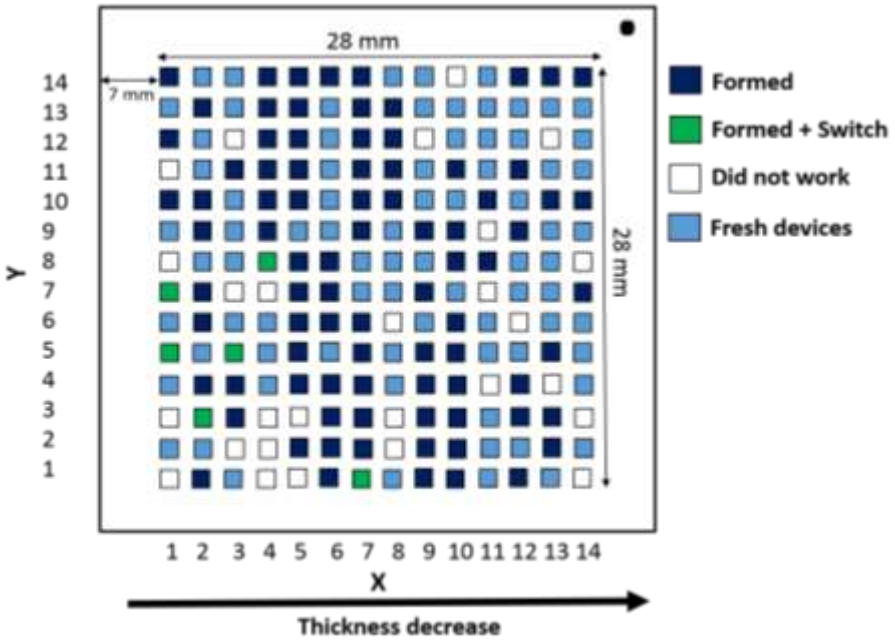

Figure 5.20. High-throughput statistics of device yield of Pt/TiO2 amorphous/Pt; dark blue indicates how many devices are being formed; green indicates how many devices were formed and rested and set again; white boxes indicate the number of devices that did not form; and light blue are the remaining devices that were not tested.

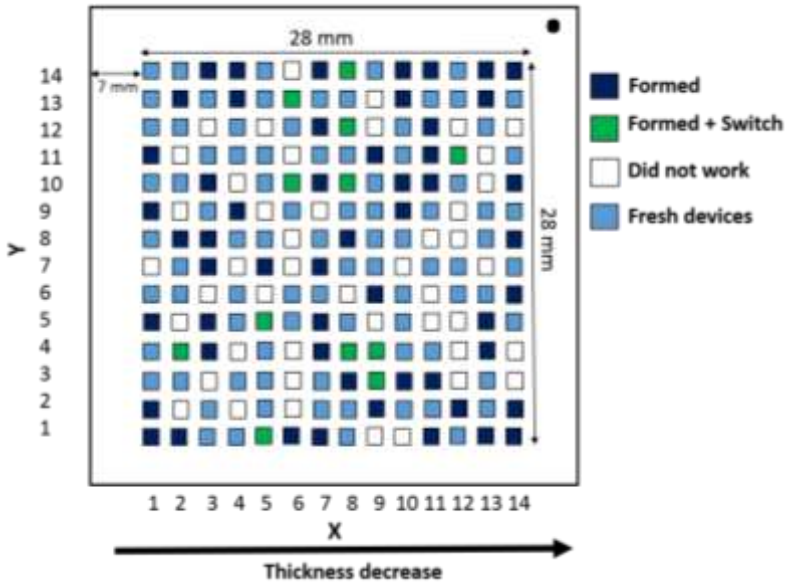

Figure 5.21. High-throughput statistics of device yield of Pt/ TiO2 anatase/Pt; dark blue indicates how many devices are being formed; green indicates how many devices were formed and rested and set again; white boxes indicate the number of devices that did not form; and light blue are the remaining devices that were not tested.

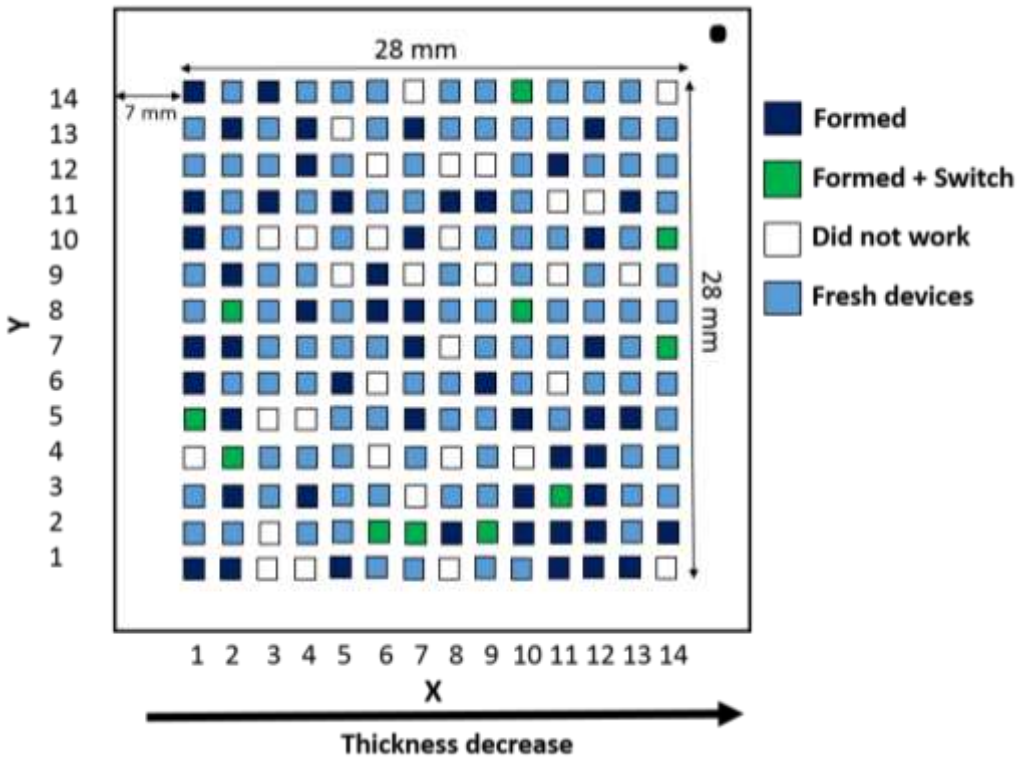

Figure 5.22. High-throughput statistics of device yield of Pt/TiO_2 rutile/Pt; dark blue indicates how many devices are being formed; green indicates how many devices were formed and rested and set again; white boxes indicate the number of devices that did not form; and light blue are remaining devices that were not tested.

Appendix B Tables

Table 3.1. Preparation Conditions for Pt/TiO_2/Pt.

Sample number	**Chamber pressure $(TiO_2)_{torr}$**	**Annealing temperature (°C) (in the chamber)**	**Phase obtained**	**Chamber pressure $(Pt)_{torr}$**	**Mask size for Pt top electrode**
♯8001	2.3×10^{-5}	RT	Amorphous	N/S	N/S
♯8003	2.4×10^{-5}	RT	Amorphous	2.3×10^{-7}	250 micron
♯8004	2.6×10^{-5}	RT	Amorphous	2.3×10^{-7}	50 micron
♯8006	2.6×10^{-5}	450	Anatase	2.3×10^{-7}	50 micron
♯8007	2.5×10^{-5}	450	Anatase	2.4×10^{-7}	250 micron
♯8008	3.5×10^{-5}	450	Anatase	N/S	N/S
♯8025	2.3×10^{-5}	600	Rutile	N/S	N/S
♯8026	2.4×10^{-5}	600	Rutile	2.4×10^{-7}	50 micron
♯8027	2.5×10^{-5}	600	Rutile	2.6×10^{-7}	250 micron

Table 3.2. Preparation Conditions for Pt Contact Pads

Rate	0.8 A/S
Substrate temperature	200 °C before deposition
Time of deposition	60 minutes
Deposition mask size	250 micron, 50 micron
Thickness	80–100 nm

Table 3.3. Description of Deposition Conditions of TiO_2 and Pt Contact Pad (NS = not specified)

Sample number	Mask (mm)	Substrate temperature (°C)	Annealed T	Evaporation source Ti	Evaporation source Pt	Produced phase
♯8003	14×14	RT	N/S	E-gun1	E-gun3	Amorphous
♯ 8007	14×14	RT	450	E-gun1	E-gun3	Anatase
♯8027	14×14	600	600	E-gun1	E-gun3	Rutile
♯8004	W9-4	RT	N/S	E-gun1	E-gun3	Amorphous
♯8006	W9-4	RT	450	E-gun1	E-gun3	Anatase
♯8026	W9-4	600	600	E-gun1	E-gun3	Rutile
♯8001	N/S	RT	N/S	E-gun1	N/S	Amorphous
♯8008	N/S	RT	450	E-gun1	N/S	Anatase
♯8025	N/S	600	600	E-gun1	N/S	Rutile

Table 3.4. Description of Deposition Conditions of TiO_2 and Cu Contact Pad (NS = not specified)

Sample number	Chamber pressure $(TiO_2)^{Torr}$	Annealing temperature (°C) (in the chamber)	Phase obtained	Chamber pressure $(Cu)^{Torr}$	Mask size for Cu top electrode
♯8628	6×10^{-7}	RT	Amorphous	2.1×10^{-7}	50 micron
♯8629	5.9×10^{-6}	RT	Amorphous	N/S	N/S
♯8630	8.5×10^{-7}	RT	Amorphous	3.9×10^{-7}	250 micron
♯8637	6.3×10^{-7}	200	Anatase	N/S	N/S
♯8642	6.4×10^{-7}	200	Anatase	3.8×10^{-7}	50 micron

♯8643	6.1×10^{-7}	200	Anatase	2.2×10^{-7}	250 micron

Table 3.5. Description of Deposition Conditions of TiO_{2-X}/TiO_2 and Cu Contact pad (NS = not specified)

Sample number	**Chamber pressure (TiO_2)**	**Annealed temperature (°C) (in chamber)**	**Phase obtained**	**Chamber pressure (TiO_{2-x})**	**Chamber pressure (Cu)**	**Mask size for Cu top electrode**
♯8634	8.5×10^{-7}	RT	Amorphous	6.7×10^{-7}	3.8×10^{-7}	250 micron
♯8635	6.6×10^{-7}	RT	Amorphous	6.5×10^{-7}	4.1×10^{-7}	50 micron
♯8636	6.5×10^{-7}	RT	Amorphous	6.3×10^{-7}	N/S	N/S
♯8638	6.8×10^{-7}	200	Anatase	6.1×10^{-7}	3.7×10^{-7}	250 micron
♯8639	6.5×10^{-7}	200	Anatase	6×10^{-7}	3.8×10^{-7}	50 micron
♯8641	8.1×10^{-7}	200	Anatase	6.4×10^{-7}	N/S	N/S

Table 4.1. Raman shift and peak assignments of anatase and rutile titania prepared by HT-PVD.

Anatase		**Rutile**	
Raman shift (cm^{-1})	Assignments	Raman shift (cm^{-1})	Assignments
162	Eg	162	B1g
210	Eg	445	Eg
414	B1g	632	A1g
533	A1g+B1g	-------	-------
657	Eg	-------	-------

Bibliography

1. Kincade, K. Big Data = Big Storage Challenges. http://www.nersc.gov/nersc-40/anniversary-news/big-data-big-storage-challenges / (accessed Jul 20, **2016**).
2. Hilbert, M.; López. P. The World's Technological Capacity to Store, Communicate, and Compute Information. *Science* **2011,** *332*, 60-65.
3. Xie, Y., Modeling, Architecture, and Applications for Emerging Memory Technologies. *IEEE Design & Test of Computers* **2011,** *28* (1), 44-51.
4. Blodget, H. IBM Hard Drive Being Loaded onto an Airplane in 1956. Business insider: 2014, http://www.businessinsider.com/picture-of-ibm-hard-drive-on-airplane-2014-1?IR=T (accessed Aug 23, **2017**).
5. Jandeleit, B.; Schaefer Powers, T.; Howard, P.; Turner, H; Weinberg, W. Combinatorial Materials Science and Catalysis. *Wiley Interscience: Germany* **1999,** 111, 2648-2689.
6. Smullen, C.; Mohan, V.; Nigam, A.; Gurumurthi, S.; Stan, M. In *Relaxing Non-volatility for Fast and Energy-efficient STT-RAM Caches*, IEEE International Symposium on High Performance Computer Architecture, **2011**, 50-61.
7. Burr, G.; Kurdi, B.; Scott, J.; Lam, C.; Gopalakrishnan, K.; Shenoy, R. Overview of Candidate Device Technologies for Storage-class Memory. *IBM J. Res. Dev.* **2008,** *52*, 449-464.
8. Jeong, T.; Katiyar, R.; Scott, J.; Kohlstedt, H.; Petraru, A.; Hwang, C. Emerging Memories: Resistive Switching Mechanisms and Current Status. *Rep. Prog. Phys*. **2012**, 75.
9. Liu, M. RRAM-An Emerging Non-Volatile Memory Technology. Institute of Microelectronics China, **2012.**
10. Yang, J.; Strukov, D.; Stewart, D. Memristive Devices for Computing. *Nat. Nanotechnol*. **2013**, *8*, 13-24.
11. Chen, Y.; Li, H. An Overview of Non-Volatile Memory Technology and the Implication for Tools and Architectures; Design, Automation and Test in Europe Conference, France, **2009**.
12. Muller, G.; Happ, T.; Kund, M.; Lee, G.; Nagel, N.; Sezi. R. In *Status and Outlook of Emerging Nonvolatile Memory Technologies,* Electron Devices Meeting IEEE: **2004**.
13. Akinaga, H.; Shima, H. Resistive Random Access Memory (ReRAM) Based on Metal Oxides. Proceedings of Nanodevice Innovation Conference, Japan: IEEE, **2010**.
14. Waser, R.; Dittmann, R.; Staikov, G.; Szot, K. Redox-Based Resistive Switching Memories Nanoionic Mechanisms, Prospects, and Challenges. *Adv. Mater.* **2009**, *21*, 2632-2663.
15. Waser, R. *Nanoelectronics and Information Technology*. 3rd edition, Wiley: **2013**.
16. Mehonic, A. Resistive Switching in Silicon-rich Silicon Oxide. Ph.D. Dissertation, University College London, London, **2013**.
17. Bachtold, A.; Hadley, P.; Nakanishi, T.; Dekker, C. Logic Circuits with Carbon Nanotube Transistors. *Science* **2001**, *294* (5545), 1317-1320.
18. Lu, C.; Lue, H.; Chen, Y. State-of-the-Art Flash Memory Devices and Postflash Emerging Memories. *Sci China Inf Sci.* **2011,** *54*, 1039-1060.
19. MRAM Fact Sheet.http://www.freescale.com/files/memory/doc/fact_sheet/MRAMTECHFS. pdf (accessed Sep 10, **2014**).

20. Hu, J.; Chen, L.; Nan, C. High-density Magnetoresistive Random Access Memory Operating at Ultralow Voltage at Room Temperature. *Nat. Commun.* **2011,** *2*, 1-8.

21. Sheikholeslami, A.; Gulak, P. A Survey of Circuit Innovations in Ferroelectric Random-access Memories, *Proc. IEEE* **2000**, 667-689.

22. Lai, S. Current Status of the Phase Change Memory and its Future, Electron Device Meeting, IEEE, Washington Dec 8-10, **2003**.

23. Micron. Micron Announces Availability of Phase Change Memory for Mobile Devices. http://investors.micron.com/releasedetail.cfm?releaseid=692563 (accessed June 10, **2017**).

24. Hisashiand, S.; Hiroyuki, A. *Basics of RRAM Based on Transition Metal Oxides*; Nanodevice Innovation Research Center, Pdf Report, **2010**.

25. Hickmott, T. Low-Frequency Negative Resistance in Thin Anodic Oxide Films. *J Appl. Phys.* **1962,** *33*, 2669.

26. Strukov, D.; Snider, G.; Stewart, D.; Williams, S. The Missing Memristor Found. *Nat.* **2008,** *453*, 80-83.

27. Panasonic. Panasonic Starts World's First Mass Production of ReRAM Mounted Microcomputers. http://news.panasonic.com/global/press/data/2013/07/en130730-2/en130730-2.html (accessed Sep 20, **2017**).

28. Adesto Technologies. CBRAM®, Adesto's Resistive RAM Technology. http://www.adestotech.com/about-us/technologyip/ (accessed Aug 25, **2017**).

29. Fackenthal, R.; Kitagawa, M.K.; Otsuka, W.; Prall, K.; Mills, D.; Tsutsui, K.; Javanifard, J.; Tedrow, K.; Tsushima, T.; Shibahara, Y.; Hush, G.A. 16Gb ReRAM with 200MB/s Write and 1GB/s Read in 27nm Technology. *International Solid-State Circuits Conference*, IEEE **2014**.

30. Akinaga, H. Recent Advance and Prospects in ReRAM Technology. *Sematech Symposium*, Japan, **2011**.

31. Sawa, A. Resistive Switching in Transition Metal Oxides. *Mater. Today* **2008,** *11* (6), 28-36.

32. Lelmini, D.; Bruchhaus, R.; Waser, R., Thermochemical Resistive Switching: Materials, Mechanisms, and Scaling Projections. *Phase Transitions* **2011**, *84* (7), 570-602.

33. Jeong, D.; Thomas, R.; Katiyar, R.; Scott, J. Overview on the Resistive Switching in TiO_2 Solid Electrolyte. *Korea Institute of Science and Technology* **2011**, *124*, 87-96.

34. Waser, R.; Dittmann, R.D.; Staikov, G.; Szot, K. Prospects and Challenges of Redox-based RRAM Concepts. Imec: **2008**.

35. Tao, L.; ShiBing, L.; Qi, L.; Su, L.; Ming, L. An Overview of Resistive Random Access Memory Devices. *Chinese Sci. Bull.* **2011**, *56*, 3072-3078.

36. Schroeder, H., Jeong, D. Resistive Switching in a Pt/TiO_2/Pt Thin Film Stack – A Candidate for a Non-volatile ReRAM. *Microelectronic Engineering* **2007**, *84*, 1982-1985.

37. Kim, S.; Choi, Y. A Comprehensive Study of the Resistive Switching Mechanism in Al/TiO_x/TiO_2/Al-Structured RRAM. *IEEE Trans. Electron Devices* **2009,** *56*, 3049-3053.

38. Kim, K.; Song, G.; Seok, J.; Lee, M.; Yoon, J.; Hwang, C. Electrically Configurable Electroforming and Bipolar Resistive Switching in Pt/TiO_2/Pt Structures. *Nanotechnology* **2010,** *21*, 305203.

39. Lee, M.; Kim, K.; Song, S.; Rha, S.; Seok, J.; Jung, J.; Kim, G.; Yoon, J.; Hwang, C. Surface Redox Induced Bipolar Switching of Transition Metal Oxide Films Examined by Scanning Probe Microscopy. *Appl. Phys. A* **2011,** *102* (4), 827-834.

40. Choi, D.; Jeong, S.; Kim, S.; Choi, R.; Oh, J.; Kim, H.; Kim, H.; Hwanga, C.; Tiedke, R.; Waser, R. Resistive Switching Mechanism of TiO_2 Thin Films Grown by Atomic-layer Deposition. *Appl. Phys. Lett.* **2005,** *98,* 033715.

41. Rohde, C.; Choi, B.; Jeong, D.; Choi, S.; Zhao, J.; Hwang, C. Identification of a Determining Parameter for Resistive Switching of TiO_2 Thin Films. *Appl. Phys. Lett.* **2005,** *86*, 262907.

42. Lee, C.; Kang, B.; Benayad, A.; Lee, M.; Ahn, S.; Kim, K.; Stefanovich, G.; Park, Y; Yoo, I. Effects of Metal Electrodes on the Resistive Memory Switching Property of NiO Thin Films. *Appl. Phys. Lett.* **2008,** *93*, 042115.

43. Kim, M.; Kim, S.; Choi, E.; Moon, S.; Park, J.; Kim, H.; Park, B.; Jae, M.; Seo, S.; Seo, D.; Ahn, S; Yoo, I., Study of Transport and Dielectric of Resistive Memory States in NiO Thin Film. *Jpn. J. Appl. Phys.* **2005,** *44*, 42-45.

44. Deleruyelle, M.; Muller, C.; Amouroux, J.; Muller, R. Electrical Nanocharacterization of Copper Tetracyanoquinodimethane Layers Dedicated to Resistive Random Access Memories. *Appl. Phys. Lett.* **2010,** *96*, 263504.

45. Kim, J.; Mok, L.S.; Lee, K; Sohnz, H. RESET-first Resistance Switching Mechanism of HfO_2 Films with Ti Electrode, International Technology Conference, USA, IEEE, **2012**.

46. Wu, Y.; Yu, S.; Wong, P.; Chen, S.; Lee, H.; Wang, S.; Gu, P.; Chen, F.; Tsai, M. AlO_x-based Resistive Switching Device with Gradual Resistance Modulation for Neuromorphic Device Application. In *Memory Workshop*, IEEE: Milan, **2012**.

47. Guan, W.; Long, S.; Jia, R.; Liua, M. Nonvolatile Resistive Switching Memory Utilizing Gold Nanocrystals Embedded in Zirconium Oxide. *Appl. Phys. Lett.* **2007,** *91*, 062111.

48. Waser, R.; Szot, K.; Speier, W; Bihlmayer, G. Switching the Electrical Resistance of Individual Dislocations in Single-crystalline $SrTiO_3$. *Nat. Mater.* **2006,** *5*, 312-320.

49. Mojarad, S. Leakage Current and Resistive Switching Mechanisms in $SrTiO_3$. Ph.D. Dissertation, Newcastle University, **2013**.

50. Sun, X.; Li, G.; Zhang, X.; Ding, L.; Zhang, W. Coexistence of the Bipolar and Unipolar Resistive Switching Behaviours in Au/$SrTiO_3$/Pt cells. *J. Appl. Phys.* **2011,** *44*, 12-24.

51. Lenser, C. Investigation of Resistive Switching in Fe-doped $SrTiO_3$ by Advanced Spectroscopy. Ph.D. Dissertation, Aachen University, **2013**.

52. Zeng, B.; Xua, D.; Tanga, Z.; Xiaoa, Y.; Zhou, Y.; Xiong, R.; Tang, M.; Lia, Z.; Zhou, Y. Improvement of Resistive Switching Characteristics in Solution- Synthesized Al, Cr, and Cu-Doped TiO_2 Films. *ECS Solid State Lett.* **2014**, *3*, 59-62.

53. Zhao, L.; Park, S.; Kope, B.; Nishi, Y. Dopant Selection Rules for Desired Electronic Structure and Vacancy Formation Characteristics of TiO_2 Resistive Memory. *Appl. Phys. Lett.* **2013,** *102*, 083506.

54. Janousch, M.; Meijer, G.; Staub, U.; Delley, B.; Karg, S.; Andreasson, B. Role of Oxygen Vacancies in Cr-Doped $SrTiO_3$ for Resistance-Change Memory. *Adv. Mater.* **2007,** *19*, 2232-2235.

55. Hasan, M.; Dong, R.; Choi, D.; Lee, S.; Seong, M.; Pyun, B.; Hwang, H. Effect of Ruthenium Oxide Electrode on the Resistive Switching of Nb-doped Strontium Titanate. *Appl. Phys. Lett.* **2008,** *93*, 052908.

56. Deleruyelle, D.; Putero, M.; Khachroum, O.; Bocquet, M.; Coulet, M.; Boddaert, X.; Calmes, B.; Mullera, C. $Ge_2Sb_2Te_5$ Layer Used as Solid Electrolyte in Conductive-Bridge Memory Devices Fabricated on Flexible Substrate. *Solid-State Electron.* **2013,** *79*, 1-7.

57. Liu, X.; Kim, I.; Siddik, M.; Sadaf, S. Resistive Switching Mechanism of a $Pr_{0.7}Ca_{0.3}MnO_3$-based Memory Device and Assessment of Its Suitability for Nano-scale Applications. *J. Korean Phys. Soc.* **2011,** *59*, 497-500.

58. Zhang, L.; Redolfi, A.; Adelmann, C.; Clima, S.; Radu, I.; Chen, Y.; Wouters, D.; Groeseneken, G.; Jurczak, M.; Govoreanu, B. Ultrathin Metal/Amorphous-Silicon/Metal Diode for Bipolar RRAM Selector Applications. *IEEE Electron Device Lett.* **2014,** *35*, 199-201.

59. Chai, Y.; Takei, K.; Chen, H.; Yu, S.; Chan, P.; Javey, A. Resistive Switching of Carbon-Based RRAM with CNT Electrodes for Ultra-Dense Memory. In *Electronic Device Meeting*, IEEE: San Francisco, **2010**.

60. Huang, J.; Yen, W.; Lin, S.; Lee, C.; Wu, J.; Wang, Z.; Chin, T; Chueh, Y. Amorphous Zinc-doped Silicon Oxide (SZO) Resistive Switching Memory: Manipulated Bias Control from Selector to Memristor. *J. Mater. Chem.* **2014,** *2*, 4401-4405.

61. Do, Y.; Kwak, J.; Bae, Y.; Jung, K.; Im, H.; Hong, J. Hysteretic Bipolar Resistive Switching Characteristics in TiO_2 /TiO_{2-x} Multilayer Homojunctions. *Appl. Phys. Lett.* **2009,** *95*, 093507.

62. Strachan, J.; Yang, J.; Montoro, A.; Ospina, A.; Ramirez, A.; Kilcoyne, A.; Ribeiro, G.; Williams, S. Characterization of Electroforming-free Titanium Dioxide Memristors. *Nanotechnology* **2013,** *4*, 467-473.

63. Lee, D.; Sung, Y.; Sohn, H.; Hong, D; Cho, K. Change of Resistive-switching in TiO_2 Films with Additional HfO_2 Thin Layer. *J. Korean Phys. Soc.* **2012,** *60*, 1313-1316.

64. Lanza, M. A Review on Resistive Switching in High-k Dielectrics: A Nanoscale Point of View Using Conductive Atomic Force Microscope. *Materials* **2014,** *7*, 2155-2182.

65. Willey, R. *Practical Design and Production of Optical Thin Films*. 2nd edition, CRC Press: **1996**.

66. Schiavello, M. *Heterogeneous Photocatalysis*. John Wiley and Sons: **1997**.

67. Hayden, B.; Pletcher, P.; Suchsland, J.; Williams, L. The Influence of Support and Particle Size on the Platinum Catalysed Oxygen Reduction Reaction. *Phys. Chem.* **2009,** *11*, 9141-9148.

68. Guerin, S.; Hayden, B.; Lee, C.; Mormiche, C.; Owen, J.; Russell, A. Combinatorial Electrochemical Screening of Fuel Cell Electrocatalysts. *Comb. Chem.* **2004,** *6*, 149-158.

69. Suchsland, J.; Hayden, B. Partical Size and Substrate Effect in Electrocatalysis. Ph.D. Dissertation, Southampton University, **2007**.

70. Hasan, M.; Dong, R.; Lee, D.; Seong, D.; Choi, H.; Pyun, M.; Hwang, H. A Materials Approach to Resistive Switching Memory Oxides. *Semicond. Sci. Technol.* **2008,** *8*, 66-79.

71. Lin, C.; Wu, Y.; Wu, C.; Lee, T.; Yang, F.; Hu, C.; Tseng, T. Effect of Top Electrode Material on Resistive Switching Properties of ZrO_2 Film Memory Devices. *IEEE Electron Device Lett*. **2007**, *28*, 366-368.

72. Hazra, A. *Resistive Random Access Memory, The New Generation High Speed Switching Non-Volatile Memory Device*. Lambert Academic Publishing: Germany, **2012**.

73. Park, S.; Köpe, B.; Nishi, Y. Impact of Oxygen Vacancy Ordering on the Formation of a Conductive Filament in TiO_2 for Resistive Switching Memory. *IEEE Electron Device Lett.* **2011,** *32*, 197-199.

74. Wang, W.; Fujita, S.; Wong, S. RESET Mechanism of TiO_x Resistance-Change Memory Device. *IEEE Electron Device Lett.* **2009,** *30*, 733-735.

75. Yang, L.; Kuegeler, C.; Szot, K.; Ruediger, A; Waser, R. The Influence of Copper Top Electrodes on the Resistive Switching Effect in TiO_2 Thin Films Studied by Conductive Atomic Force Microscopy. *Appl. Phys. Lett.* **2009,** *95*, 013109.

76. Shim, J.; Hu, Q.; Park, M.; Abbas, Y.; Kang, C.; Kim, J. Resistive Switching Characteristics of TiO_2 Thin Films with Different Electrodes. *J. Korean Phys. Soc.* **2015,** *67*, 936-940.

77. Jeong, D.; Thomas, R.; Katiyar, R.; Scott, J. Overview on the Resistive Switching in TiO_2 Solid Electrolyte. *Integrated Ferroelectrics* **2011**, *124*, 87-96.

78. Kund, M.; Beitel, G.B.; Pinnow, C.; Röhr, T.; Schumann, J.; Symanczyk, R.; Ufert, K.; Mülle, G. Conductive Bridging RAM (CBRAM): An Emerging Non-volatile Memory Technology Scalable to Sub 20nm. Electron Device Meeting, IEEE: Washington, **2005**, 754-757.

79. Prakash, A.; Jana, D.; Maikap, S. TaOx-based Resistive Switching Memories: Prospective and Challenges. *Nanoscale Res. Lett*. **2013**, *8*, 1-17.

80. Sun, H.; Lv, H.; Liu, Q.; Long, S.; Wang, M.; Xie, H.; Liu, X.; Yang, X.; Niu, J.; Liu, M., Overcoming the Dilemma between RESET Current and Data Retention of RRAM by Lateral Dissolution of Conducting Filament. *IEEE Electron Device Letters* **2013**, *34* (7), 873-875.

81. Wouters, D. Resistive Switching Materials and Devices for Future Memory Applications. 43rd IEEE Semiconductor Interface Specialists Conference. SISS, San Diego, **2012**.

82. Keithley, K. Pulse I-V Characterization of Non-Volatile Memory Technologies; **2013.**

83. Hiro, A.; Hisashi, S. Forum on 2020 Semiconductor Memory Strategies: Processes, Device and Architectures. Singapore: **2008**.

84. Xu, N.; Liu, L.; Sun, X.; Liu, X.; Han, D.; Wang, Y.; Han, R.; Kang, J.; Yub, B. Characteristics and Mechanism of Conduction/Set Process in TiN/ZnO/Pt Resistance Switching Random-access Memories. *Appl. Phys. Lett.* **2008**, *92*, 232112.

85. Guan, W.; Long, S.; Liu, Q.; Liu, M.; Wang, W. Nonpolar Nonvolatile Resistive Switching in Cu Doped ZrO_2. *IEEE Electron Device Lett* **2008**, *29*, 434-437.

86. Sun, B.; Liu, Y.; Liu, L.; Xu, N.; Wang, Y.; Liu, X.; Han, R.; Kang, J. Highly Uniform Resistive Switching Characteristics of TiN/ZrO_2/Pt Memory Devices. *J. Appl. Phys.* **2009**, *105*, 061630.

87. Peng, S.; Zhuge, F.; Chen, X.; Zhu, X.; Hu, B.; Pan, L.; Chen, B.; Li, R. Mechanism for Resistive Switching in an Oxide-based Electrochemical Metallization Memory. *Appl. Phys. Lett.* **2012**, *100*, 072101.

88. Seo, J.; Park, J.; Lim, K.; Yang, J.; Kang, S. Transparent Resistive Random Access Memory and its Characteristics for Nonvolatile Resistive Switching. *Appl. Phys. Lett.* **2008**, *93*, 223505.

89. Chang, W.; Lai, Y.; Wu, T.; Wang, S.; Chen, F.; Tsai, M. Unipolar Resistive Switching Characteristics of ZnO Thin Films for Nonvolatile Memory Applications. *Appl. Phys. Lett.* **2008**, *92*, 022110.

90. Sakamoto, T.; Banno, N.; Iguchi, N.; Kawaura, H.; Sunamura, H.; Fujieda, S.; Terabe, K.; Hasegawa, T.; Aono, M. A Ta_2O_5 Solid-electrolyte Switch with Improved Reliability. International Symposium on VLSI Technology Digest of Technical Papers, **2007**.

91. Chen, X.; Wu, G.; Bao, D. Resistive Switching Behavior of Pt/$Mg_{0.2}Zn_{0.8}O$ /Pt Devices for Nonvolatile Memory Applications. *Appl. Phys. Lett.* **2008**, *93*, 093501.

92. Ta, L.; Bing, L.; Bing, H.; Qi, L.; Qin, W.; Yan, W.; Sen, Z.; Tai, L.; Su, L.; Ming, L. Investigation of Resistive Switching Behaviours in WO_3-Based RRAM Devices. *Chin. Phys. B* **2011**, *20*, 017305.

93. Shin, J.; Kim, I.; Biju, K.; Jo, M.; Park, J.; Lee, J.; Jung, S.; Lee, W.; Kim, S.; Park, S.; Hwang, H. TiO_2 based Metal-Insulator-Metal Selection Device for Bipolar Resistive Random Access Memory Cross-point Application. *J. Appl. Phys.* **2011**, *109*, 033712.

94. Carta, D.; Salaoru, I.; Khiat, A.; Regoutz, A.; Mitterbauer, C.; Harrison, N.; Prodromakis, T. Investigation of the Switching Mechanism in TiO_2 Based RRAM: A Two-Dimensional EDX Approach. *ACS Appl. Mater. Interface* **2016**, *8*, 19605-19611.

95. Trapatseli, M.; Carta, D.; Regoutz, A.; Khiat, A.; Serb, A.; Gupta, I.; Prodromakis, T. Conductive Atomic Force Microscopy Investigation of Switching Thresholds in Titanium Dioxide Thin Films. *Phys. Chem.* **2015**, *119*, 11958-11964.

96. Lim, K.; Park, J.; Kim, S.; Choi, S. Effect of Oxygen Content on Resistive Switching Memory Characteristics of TiO_x Films. *J. Korean Phys. Soc.* **2012**, *60*, 791-794.

97. Oh, S.; Jung, H.; Lee, H. Effect of the Top Electrode Materials on the Resistive Switching Characteristics of TiO_2 Thin Film. *J. Appl. Phys.* **2011**, *109*, 124511.

98. Chae, S.; Lee, S.; Choi, W.; Lee, S.; Chang, S.; Shin, H.; Kahng, B.; Noh, T. Multilevel Unipolar Resistance Switching in TiO_2 Thin Films. *Appl. Phys. Lett.* **2009**, *95*, 093508.

99. Carta, D.; Guttmann, P.; Regoutz, A.; Khiat, A.; Serb, A.; Gupta, I.; Mehonic, A.; Buckwell, M.; Hudziak, S.; Kenyon, A.; Prodromakis, T. X-ray Spectromicroscopy Investigation of Soft and Hard Breakdown in RRAM Devices. *Nanotechnology* **2016**, *27*, 791-794.

100. Cortese, S.; Trapatseli, M.; Khiat, A.; Prodromakis, T. A TiO_2 based Volatile Threshold Switching Selector Device with 10^7 Non Linearity and Sub 100 pA Off Current, International Symposium of System and Application, IEEE, **2016**.

101. Carta, D.; Hitchcock, A.; Guttmann, P.; Regoutz, A.; Khiat, A.; Serb, A.; Gupta, I.; Prodromakis, T. Spatially Resolved TiOx Phases in Switched RRAM Devices Using Soft X-ray Spectromicroscopy. *Nat. Sci. Rep.* **2016**, *6*, 21525.

102. Choi, B.; Jeong, D.; Kim, S.; Rohde, C.; Choi, S.; Oh, J.; Kim, H.; Hwang, C.; Szot, K.; Waser, R.; Reichenberg, B.; Tiedke, S. Resistive Switching Mechanism of TiO_2 Thin Films Grown by Atomic-layer Deposition. *Appl. Phys.* **2005**, *98*, 033715.

103. Li, Y.; Long, S.; Zhang, M.; Liu, Q.; Shao, L.; Zhang, S.; Wang, Y.; Zuo, Q.; Liu, S.; Liu, M. Resistive Switching Properties of Au/ZrO_2/Ag Structure for Low-Voltage Nonvolatile Memory Applications. *IEEE Electron Device Lett.* **2010**, *31*, 117-119.

104. Prakash, A.; Maikap, S.; Chen, W.; Lee, H.; Chen, F.; Tien, T.; Lai, C.; Tsai, M. Device Size-Dependent Improved Resistive Switching Memory Performance. *IEEE Trans. Nanotechnol.* **2014**, *13*, 409-417.

105. Diebold, U. The Surface Science of Titanium Dioxide. *Surf. Sci. Rep.* **2003**, *48*, 53-229.

106. Swamy, V.; Dubrovinsky, L.; Dubrovinskaia, N.; Simionovici, A.; Drakopoulos, M.; Dmitriev, V.; Weber, H. Compression Behavior of Nanocrystalline Anatase TiO_2. *Solid State Comm.* **2003**, *125*, 111-115.

107. Jeong, D.S. Resistive Switching in Pt/TiO_2/Pt. Ph.D. Dissertation. Aachen University, Germany, **2008**.

108. Dorian, A.; Hanaor, H.; Sorrell, C. Review of the Anatase to Rutile Phase Transformation. *J. Mater. Sci.* **2011**, *46*, 855-874.

109. Austin, R. H.; Lim, S.-F., The Sackler Colloquium on Promises and Perils in Nanotechnology for Medicine. *Proceedings of the National Academy of Sciences* **2008**, *105* (45), 17217-17221.

110. Wu, J., Cao, J., Han, W.-Q., Janotti, A., Kim, H. Functional Metal Oxide Nanostructures, *Springer Series in Mat. Sci.* **2012**.

111. Seitz, F.; Turnbull, D. *Solid State Physics.* Academic Press: New York, **1956**, 307.

112. Tilley, D. Nonstoichiometry, Diffusion and Electrical Conductivity in Binary Metal Oxides. **1975**, 159-163.

113. Sze, S.; Kwok, Ng. *Physics of Semiconductor Devices.* 2nd edition, John Wiley & Sons: **2006**.

114. Kim, K.; Jo, S.; Gaba, S.; Lua, W. Nanoscale Resistive Memory with Intrinsic Diode Characteristics and Long Endurance. *Appl. Phys. Lett.* **2010**, *96*, 053106.

115. Bally, A. Electronic Properties of Nano-crystalline Titanium Dioxide Thin Film. Ph.D. Dissertation, Lasanne University, **1999**.

116. Cronemeyer, D. Electrical and Optical Properties of Rutile Single Crystals. *Phys. Rev.* **1952**, *87*, 876-886.

117. Hayfield, P. *Development of a New Material : Monolithic Ti_4O_7 Ebonex Ceramic*. RCS Publishing **2002**.

118. Vinokurova, B.; Avvakumov, G.; Gusev, A. Synthesis of Ti_4O_7 Magneli Phase Using Mechanical Activation. *Science of Sintering* **2003**, *35*, 141-145.

119. Hanak, J. The "Multiple-Sample Concept" in Materials Research: Synthesis, Compositional Analysis and Testing of Entire Multicomponent Systems. *J. Mater. Sci.* **1970**, *5*, 964-971.

120. Bergh, S.; Guan, S. Low Cost, Efficient Catalyst Identification and Optimization for High Throughput Combinatorial Chemistry, **2000**.

121. Green, M.; Takeuchi, I.; Simpers, J. Applications of High Throughput (Combinatorial) Methodologies to Electronic, Magnetic, Optical, and Energy-related Materials. *Appl. Phys. Lett*. **2013**, *113*, 231101.

122. Persidis, A. Combinatorial Chemistry. *Nat. Biotechnol.* **1998**, *16*, 691-693.

123. Saalfrank, J.; Maier, W. Doping, Selection and Composition Spreads, a Combinatorial Strategy for the Discovery of New Mixed Oxide Catalysts for Low-temperature CO Oxidation. *C. R. Chimie* **2004**, *7*, 483-494.

124. Hayden, B.; Guerin, S. Physical Vapor Deposition Method for the High-Throughput Synthesis of Solid-State Material Libraries. *Comb. Chem.* **2006**, *8*, 66-73.

125. Gopal, V.; Chiang, T. P.; Hashim, I.; Higuchi, R. J.; Huertas, R. A.; Pham, H.; Wang, Y., Methods and Vehicles for High Productivity Combinatorial Testing of Materials for Resistive Random Access Memory Cells. Google Patents: **2014**.

126. Beck, A.; Bednorz, J.; Gerber, C.; Rossel, C.; Widme, D. Reproducible Switching Effect in Thin Oxide Films for Memory Applications. *Appl. Phys. Lett.* **2000**, *77*, 139-141.

127. Yoshida, C.; Tsunoda, K.T.; Noshiro, H.; Sugiyama, Y. High Speed Resistive Switching in $Pt/TiO_2/TiN$ Film for Nonvolatile Memory Application. *Appl. Phys. Lett.* **2007**, *91*, 223510.

128. Yoshida, C.; Kinoshita, K.; Yamasaki, T.; Sugiyama, Y. Direct Observation of Oxygen Movement during Resistance Switching in NiO/Pt Film. *Appl. Phys. Lett.* **2008**, *93*, 042106.

129. Bousoulas, P.; Giannopoulos, J.; Giannakopoulos, K.; Dimitrakis, P.; Tsoukalas, D. Memory Programming of TiO_{2-x} Films by Conductive Atomic Force Microscopy Evidencing Filamentary Resistive Switching. *Appl. Surf. Sci.* **2015**, *332*, 55-61.

130. Magyari, B.; Tendulkar, M.; Park, S.; Lee, H.; Nishi, Y. Resistive Switching Mechanisms in Random Access Memory Devices Incorporating Transition Metal Oxides: TiO_2, NiO and $Pr_{0.7}Ca_{0.3}MnO_3$. *Nanotechnology* **2011**, *20*, 254029.

131. Guerin, S.; Hayden, B.; Lee, C.; Mormiche, C.; Russell, A. High-Throughput Synthesis and Screening of Ternary Metal Alloys for Electrocatalysis. *Phys. Chem.* **2006**, *110*, 14355-14362.

132. Guerin, S.; Hayden, B.; Smith, D. High-Throughput Synthesis and Screening of Hydrogen-Storage Alloys. *Comb. Chem.* **2008**, *10*, 37-43.

133. Simpson, R.; Hewak, D.; Guerin, S.; Hayden, B.; Purdy, G. High Throughput Synthesis and Screening of Chalcogenide Materials for Data Storage. International Chemistry Conference, Singapore, **2005**.

134. Beal, M.; Hayden, B.; Gall, T.; Lee, C.; Lu, X.; Mirsaneh, M.; Mormiche, C.; Pasero, D.; Smith, D.; Weld, A.; Yada, C.; Yokois, S. High Throughput Methodology for Synthesis, Screening, and Optimization of Solid State Lithium Ion Electrolytes. *ACS Comb. Sci.* **2011**, *13*, 375-381.

135. Aljohani, T.; Hayden, B.; Anastasopoulos, A. The High Throughput Electrochemical Screening of the Corrosion Resistance of Ni–Cr Thin-film Alloys. *Electro. Chem. Acta.* **2012**, *76*, 389-393

136. Darby, M.; Guerin, S.; Hayden, B.; Schreiner, H.; Yakovlev, S. High Throughput Physical Vapour Deposition and Dielectric and Ferroelectric Screening of (Bi,Na)TiO_3 Thin-film Libraries. *Appl. Phys.* **2013**, *113*, 014104.

137. David, A.; Guerin, S.; Hayden, B.; Noble, R.; Soulié, J.; Vian, C.; Koutsaroff, I.; Higai, S.; Tanaka, N.; Konoike, T.; Ando, A.; Takagi, H.; Yamamoto, T.; Fukura, T.; Leki, H. High-throughput Synthesis and Characterization of $(Ba_xSr_{1-x})_{1+y}Ti_{1-y}O_{3-\delta}$ and $(Ba_xSr_{1-x})_{1+y}Ti_{1-y}O_{3-z}N_z$ Perovskite Thin Films. *Cryst. Growth Des.* **2013**, *14*, 523-532.

138. Al-Odail, F; Anastasopoulos, A.; Hayden, B. The Hydrogen Evolution Reaction and Hydrogen Oxidation Reaction on Thin-film PdAu Alloy Surfaces. *Phys. Chem.* **2010**, *12*, 11398-11406.

139. Hu, C.; McDaniel, M. D.; Posadas, A.; Demkov, A. A.; Ekerdt, J. G.; Yu, E. T., Highly Controllable and Stable Quantized Conductance and Resistive Switching Mechanism in Single-crystal TiO_2 Resistive Memory on Silicon. *Nano Lett.* **2014**, *14* (8), 4360-4367.

140. Cerri, I.; Nagami, T.; Davies, J.; Mormiche, C.; Vecoven, A.; Hayden, B. Innovative Catalyst Supports to Address Fuel Cell Stack Durability. *International. J. of Hydrogen Ener.* **2013**, *38*, 640-645.

141. Hannah, L. The High Through-put Synthesis & Screening of Electrocatalysts for the Reduction of Nitrate in Groundwater and Waste Streams. Ph.D. Dissertation. University of Southampton, **2012**.

142. Emmanuel, J. A High-Throughput Thermographic Screen for Model Heterogeneous Catalysts. Ph.D. Dissertation, University of Southampton, **2014**.

143. Kobayashi, S.; Inaba, K., X-ray Thin-film Measurement Techniques. Mass Spectroscopy Equipped with a Skimmer-type Interface **2012**, 8.

144. Mitsunaga, T. X-ray Thin-film Measurement Technique. *Rigaku J* **2009**, *25*, 7-12.

145. Long, D. A., The Raman Effect: A Unified Treatment of the Theory of Raman Scattering by Molecules. West Sussex, **2002**.

146. Frank, O.; Zukalova, M.; Laskova, B.; Kurti, J.; Koltai, J.; Kavan, L. Raman spectra of titanium dioxide (anatase, rutile) with identified oxygen isotops (16, 17, 18). Phys. Chem. Chem. Phys., **2012**, 14, 14567-14572.

147. Zhang, Y.; Harris, C. X.; Wallenmeyer, P.; Murowchick, J.; Chen, X., Asymmetric Lattice Vibrational Characteristics of Rutile TiO_2 as Revealed by Laser Power Dependent Raman Spectroscopy. *J. Phys. Chem. C* **2013**, *117* (45), 24015-24022.

148. Giessibl, F. J., Advances in Atomic Force Microscopy. *Rev. Phys.* **2002**, 23.

149. Pietrasanta, H. L. Atomic force Microscopy and other Scanning Probe Microscopies; **1998**, 579-584.

150. Watts, J. F.; Wolstenholme, J. An Introduction to Surface Analysis by XPS and AES. **2003**.

151. Biesinger, M. C.; Payne, B. P.; Grosvenor, A. P.; Lau, L. W.; Gerson, A. R.; Smart, R. S. C., Resolving Surface Chemical States in XPS Analysis of First Row Transition Metals, Oxides and Hydroxides: Cr, Mn, Fe, Co and Ni. *Appl. Surf. Sci.* **2011**, *257* (7), 2717-2730.

152. Zhang, C.; Grass, M. E.; McDaniel, A. H.; DeCaluwe, S. C.; El Gabaly, F.; Liu, Z.; McCarty, K. F.; Farrow, R. L.; Linne, M. A.; Hussain, Z., Measuring Fundamental Properties in Operating Solid Oxide Electrochemical Cells by Using in situ X-ray Photoelectron Spectroscopy. *Nat. Mater.* **2010**, *9* (11), 944.

153. Miccoli, I.; Pfnur, F.; Tegenkamp, E., The 100th Anniversary of the Four-point Probe Technique: The Role of Probe Geometries in Isotropic and Anisotropic Systems. *J. Phys* **2015**, *27*.

154. Russ, J. C., Fundamentals of Energy Dispersive X-Ray Analysis: Butterworths Monographs in Materials. Butterworth-Heinemann: **2013**.

155. Zhang, W.; He, Y.; Zhang, M.; Yin, Z.; Chen, Q., Raman Scattering Study on Anatase TiO_2 Nanocrystals. *J. Phys. D: Appl. Phys.* **2000**, *33* (8), 912.

156. Mazza, T.; Barborini, E. B.; Piseri, P.; Cattaneo, M.; Bassi, L., Bottani, C.; Ducati, C. Raman Spectroscopy Characterization of TiO_2 Rutile Nanocrystals. *Phys. Rev*. **2007,** *75*, 045416.

157. Kelly, S.; Polak, F.; Tomkiewicz, M. Raman Spectroscopy as a Morphological Probe for TiO_2 Aerogels. *Phys. Chem.* **1997,** *101*, 2730 - 2734.

158. Wypych, A.; Bobowska, I.; Tracz, M.; Opasinska, A.; Kadlubowski, S.; Kaliszewska, A.; Grobelny, J.; Wojciechowski, P. Dielectric Properties and Characterisation of Titanium Dioxide Obtained by Different Chemistry Methods. *J. Nanomater.* **2014,** *9*, 124814.

159. Kwon, D.; Kim, K.; Jang, J.; Jeon, J.; Lee, M.; Kim, G.; Li, X.; Park, G.; Lee, B.; Han, S.; Kim, M.; Hwang, C. Atomic Structure of Conducting Nanofilaments in TiO_2 Resistive Switching Memory. *Nat. Nanotechnol.* **2010,** *5*, 148-153.

160. Acharyya, D.; Hazra, A.; Bhattacharyya, P. A Journey Towards Reliability Improvement of TiO_2 Based Resistive Random Access Memory: Rev. *Microelec.* **2014,** *54*, 541-560.

161. Cho, E.; Han, S.; Ahn, H.; Lee, K.; Kim, S.; Hwang, C. First-principles Study of Point Defects in Rutile TiO_{2-x}. *Phys. Rev.* **2006,** *73*, 193202.

162. Marlasca, G.; Ghenzi, N.; Rozenberg, M.; Levy, P. Understanding Electroforming in Bipolar Resistive Switching Oxides. *Appl. Phys Lett.* **2011,** *98*, 042901.

163. Valov, I.; Waser, R.; Jameson, J.; Kozicki, M. Electrochemical Metallization Memories – Fundamentals, Applications, Prospects. *Nanotechnology* **2011**, *22,* 254003.

164. Jeong, D.; Schroeder; H., Waser, R. Mechanism for Bipolar Switching in a Pt/TiO_2/Pt Resistive Switching Cell. *Phys. Rev.* **2009**, *79*, 195317.

165. Zhu, X.; Shang, J.; Li, R. Resistive Switching Effects in Oxide Sandwiched Structures. *Mater. Sci.* **2012**, *6*, 183-206.

166. Bertaud, T.; Walczyk, D.; Walczyk, C.; Kubotsch, S.; Sowinska, M.; Schroeder, T.; Wenger, C.; Vallée, C.; Gonon, P.; Mannequin, C.; Jousseaume, V.; Grampeix, H. Resistive Switching of HfO2-Based Metal Insulator Metal Diodes: Impact of the Top Electrode Material. *Thin Solid Films* **2012**, *520*, 4551-4555.

167. Carta, D.; Mountjoy, G.; Regoutz, A.; Khiat, A.; Serb, A.; Prodromakis, T. X ray Absorption Spectroscopy Study of TiO_{2-x} Thin Films for Memory Applications. *Phys. Chem.* **2015**, *119*, 4362-4370.

168. Lee, J.; Shin, J.; Lee, D.; Lee, W.; Jung, S.; Jo, M.; Park, J.; Biju, K. P.; Kim, S.; Park, S. In Diode-less Nano-scale ZrO_x/HfO_x RRAM Device with Excellent Switching Uniformity and Reliability for High-density Cross-point Memory Applications, Electron Devices Meeting (IEDM), IEEE: **2010**.

169. Yoon, K.; Lee, M.; Kim, G.; Song, S.; Seok, J.; Han, S.; Yoon, H.; Kim, K.; Hwang, C. Memristive Tri-stable Resistive Switching at Ruptured Conducting Filaments of a Pt/TiO_2/Pt Cell. *Nanotechnology* **2012,** *23*, 185202.

170. Marucco, J.; Lemasson, P.; Gautron, J. Thermogravimetric and Electrical Study of Non-Stoichiometric Titanium Dioxide TiO_{2-x}, Between 800 and 1100°C. *J. Phys. Chem. Solids* **1981,** *42* (5), 363-367.

171. Stoneham, A.; Hayes, W. *Defect and Defect Process in Nonmetallic Solids*. Wiley: New York, **1985**.

172. Yang, J.; Strachan, J.; Miao, F.; Zhang, M.; Pickett, M.; Ti, W.; Ohlberg, D.; Riberiro, M.; Williams, R. Metal/TiO_2 Interfaces for Memristive Switches. *Appl. Phys.* **2011,** *102*, 785-789.

173. Siddik, M.; Jung, S.; Lee, W.; Shin, J.; Park, S.; Lee, D.; Kim, I.; Hwang, H. Thermally Assisted Resistive Switching in $Pr_{0.7}Ca_{0.3}MnO_3$/Ti/$Ge_2Sb_2Te_5$ Stack for Nonvolatile Memory Applications. *Appl. Phys.* **2011,** *99*, 063501.

174. Yang, J.; Miao, F.; Pickett, M.; Ohlberg, D.; Stewart, D.; Lau, C.; Williams, R. The Mechanism of Electroforming of Metal Oxide Memristive Switches. *Nanotechnology* **2009,** *20*, 215201.

175. Kim, W.; Rhee, S. Effect of the Top Electrode Material on the Resistive Switching of TiO_2 Thin Film. *Microelectron Eng.* **2010,** *87* (2), 98-103.

176. Nardi, F. Electrical Characterization and Physical Modeling of Unipolar/Bipolar Resistive Switching Materials. Ph.D. Dissertation, Milano University, **2011**.

177. Hosoi, Y.; Tamai, Y.; Ohnishi, T.; Ishihara, K.; Shibuya, T.; Inoue, Y.; Yamazaki, S.; Nakano, T.; Ohnishi, S.; Awaya, N.; Inoue, I.; Shima, H.; Akinaga, H., Takagi, H.; Akoh, H.; Tokura, Y. High Speed Unipolar Switching Resistance RAM (RRAM) Technology. Electron Device Meeting, IEEE: San Francisco, **2006**.

178. Kim, K.; Choi, B.; Hwang, C. Localized Switching Mechanism in Resistive Switching of Atomic-layer-deposited TiO_2 Thin Films. *Appl. Phys. Lett.* **2007,** *90*, 242906.

179. Kim, S.; Kim, K.; Jeong, D.; Jeon, W.; Jean, K.; Hwang, C. Titanium Dioxide Thin Films for Next-generation Memory Devices. *Mater. Res. Soc.* **2013,** *28*, 313-325.

180. Kim, K.; Choi, B.; Shin, Y.; Choi, S.; Hwang, C. Anode-interface Localized Filamentary Mechanism in Resistive Switching of TiO_2 Thin Films. *Appl. Phys. Lett.* **2007,** *91*, 012907.

181. Kinoshita, K.; Tamura, T.; Aoki, M.; Sugiyama, Y.; Tanaka, H. Bias Polarity Dependent Data Retention of Resistive Random Access Memory Consisting of Binary Transition Metal Oxide. *Appl. Phys. Lett.* **2006,** *89*, 103509.

182. Yang, J.; Pickett, M.; Li, X.; Ohilberg, D.; Stewart, D.; Williams, S. Memristive Switching Mechanism for Metal/Oxide/Metal Nanodevices. *Nat. Nanotechnol.* **2008**, *3*, 429-433.

183. Fujiwara, K.; Nemoto, T.; Rozenberg, M.; Nakamura, Y.; Takagi, H. Resistance Switching and Formation of a Conductive Bridge in Metal/Binary Oxide/Metal Structure for Memory Devices. *Jpn. J. Appl. Phys.* **2008,** *47*, 6266-6271.

184. Gupta, I.; Serb, A.; Khiat, A.; Zeitler, R.; Vassanelli, S.; Prodromakis, T., Real-time encoding and compression of neuronal spikes by metal-oxide memristors. *Nat. Comm.* **2016,** *7*, 12805.

185. Chen, A., Memory selector devices and crossbar array design: a modeling-based assessment. *J. Computational Electronics* **2017,** *16* (4), 1186-1200.

186. Lv, H.; Xu, X.; Liu, H.; Liu, R.; Liu, Q.; Banerjee, W.; Sun, H.; Long, S.; Li, L.; Liu, M., Evolution of conductive filament and its impact on reliability issues in oxide-electrolyte based resistive random access memory. *Sci. Rep.* **2015,** *5*, 7764.

187. Huang, Y.-C.; Lin, H.-M.; Cheng, H.-C. In *Superior resistive switching characteristics of Cu-TiO_2 based RRAM cell*, Nanoelectronics Conference (INEC), 2013 IEEE 5th International, IEEE: **2013**; pp 236-239.

188. Hayden, B. E.; Rogers, F. K., Oxygen reduction and oxygen evolution on $SrTi_{1-x}Fe_xO_{3-y}$ (STFO) perovskite electrocatalysts. *J. Electroanalytical Chem.* **2017**.

189. Yada, C.; Lee, C. E.; Laughman, D.; Hannah, L.; Iba, H.; Hayden, B. E., A high-throughput approach developing lithium-niobium-tantalum oxides as electrolyte/cathode interlayers for high-voltage all-solid-state lithium batteries. *J. Electrochemical Society* **2015,** *162* (4), A722-A726.

190. Bakaimi, I.; Guerin, S.; Hayden, B. E. et al. Unpublished Manuscript **2018**.